Muon Spin Relaxation Study of MnGe and Development of Pair Distribution Function Methods

Zizhou Gong

Submitted in partial fulfillment of the

requirements for the degree

of Doctor of Philosophy

in the Graduate School of Arts and Sciences

COLUMBIA UNIVERSITY

2018

ABSTRACT

Muon Spin Relaxation Study of MnGe and Development of Pair Distribution Function Methods

Zizhou Gong

The first half of the thesis presents our experimental study of a helical magnet MnGe. In a non-centrosymmetric magnetic structure, a type of magnetic exchange interaction, usually called the Dzyaloshinskii-Moriya interaction, was allowed to exist in addition to ferromagnetic interaction. Unlike the ferromagnetic interaction which tends to align the spin along the same direction, the Dzyaloshinskii-Moriya interaction tends to align the neighboring spins to be perpendicular to each other. Therefore in a magnetic structure where the ferromagnetic and the Dzyaloshinskii-Moriya interaction coexist, the ordered phase could acquire a helical spin order which. Within specific temperature and magnetic field range, the helical order could evolve into a lattice of vortex-like, topologically nontrivial spin structures called Skyrmion. Among these materials, MnSi and MnGe have been shown experimentally to exhibit spin fluctuation and dynamic critical behaviors. This makes them suitable for muon spin relaxation (μSR) study. As a sensitive probe to local magnetism, the μSR technique gives information about the temporal correlation of the dynamic local field through tracking the rotation and relaxation of the muon spin under the influence of the local magnetic environment.

In this study, we apply μSR technique to study the dynamic as well as the static magnetism in MnGe. Our key findings are as follows. From the muon dynamic relaxation $1/T_1$ results, no apparent critical behavior or anomaly was observed at the boundary between paramagnetic and the induced-ferromagnetic regions. Our study revealed linear relation between the transverse field relaxation rate and the static magnetization. Furthermore, their ratio, which can be regarded a form of hyperfine coupling constant, is very similar in the induced ferromagnetic region and the paramagnetic region. This suggest that the Z component of the Mn moment is static in both regions. On the other hand, the single relaxation rate in the transverse spectra suggest that the internal field is highly homogeneous in the induced ferromagnetic region. We therefore speculate that the induced ferromagnetic region and the paramagnetic region are not separate phases, but rather a single phase with different tendencies as temperature decrease. With decreasing temperature, the paramagnetic region is marked with the winning of the tendency towards ferromagnetic ordering over random ordering, and the induced ferromagnetic region is marked with the winning of the tendency towards the helical order over ferromagnetic order.

At lower temperature, we observed dynamic critical behavior in the boundary between the induced ferromagnetic region and the Skyrmion region. Specifically, in low fields, the $1/T_1$ relaxation rate behaves qualitatively different from the prediction of SCR theory for itinerant ferromagnet for large temperature regime above T_c. In high fields, on the other hand, the system recovers the SCR itinerant ferromagnetic behavior. Through analyzing field effect on spin fluctuation and phase transition in the low and high field regimes, we speculate that this could be due to the suppression of helical fluctuation into ferromagnetic-like fluctuation by large magnetic fields. Our μSR results, which show 2nd order signature for the transition between the induced ferromagnetic region into the Skyrmion region, is consistent with considerations based on the topology of the magnetic structure in each phase. At low

temperatures within the Skyrmion region of MnGe, our analysis of the transverse field data shows that all the three components of the Mn moment is frozen. The quadratic temperature dependence of $1/T_1$ at low temperatures suggest the two-magnon spin wave to be the dominant spin excitation in the Skyrmion region. This is similar to those seen in localized moment magnets and is qualitatively different from the linear temperature dependence predicted from SCR theory for itinerant ferromagnets.

The second half of the thesis present our derivation of the structure function and the pair distribution function (PDF) for textured materials. We also derive the analytical form of the PDF for a few special cases of texture. The PDF is derived from Fourier transforming the scattering structure function, and it reveals the local atomic arrangement within the material. The theory of the pair distribution function has been well established under the assumption that the sample is isotropic, meaning that the crystallites within the sample has equal probability to be along each and every orientation. While the isotropic PDF has been applied to a variety of samples and have successfully unveiled their local structure, in reality there're many cases where the sample itself has strongly preferred orientation, or samples with texture. In such cases the isotropic PDF might become less accurate for these textured samples. In this study, we start from the general form of a 3D structure function and derive the general and orientationally averaged form of the structure function and PDF for textured samples. In particular for a thin film sample with fibre texture, our formalism gives the result known as the 2 dimensional PDF. We developed open-software that calculates the 2 dimensional PDF for a textured thin film, and showed that the experimental PDF was well fitted using the model.

On the other hand, the PDF method could be extended to an energy-dependent form, which could reveal explicitly the effect of lattice dynamics on the local arrangement of the atoms.

This is usually called the dynamic PDF method. In this thesis we derive the analytical form of the dynamic PDF for a simple molecule that contains two identical atoms. And we interpret the mathematical results with physical consideration of the lattice dynamics. In addition, we also propose a new definition for the dynamic PDF which can be shown to reduce to the atomic PDF by integrating over energy. This new definition of the dynamic PDF incorporates the contribution from multi-phonon scattering effects, and can be computed conveniently from inelastic neutron scattering.

Table of Contents

List of Figures

xi

Acknowledgments

First and foremost, I would like to express my gratitude to my two research advisors, Tomo Uemura in the Department of Physics and Simon Billinge in the Department of Applied Physics and Applied Mathematics. They demonstrated to me the highest level of intellectual endeavor, which is at the heart of scientific research. The joy of doing scientific research will never came to me without their enlightening mentorship. After all, I was most impressed by their immensely generous and upright personality. Their deeply kind and benevolent thoughts will shine in my heart forever. Thank you, Tomo and Simon.

My PhD journey would be impossible without the generous and wholehearted support from all the Uemura and the Billinge group members. Dr. Benjamin Frandsen and Dr. Sky Cheung helped me to have a smooth settle-down to the environment and research topics in the group. The fruitful and often joyous conversations with Dr. Zurab Guguchia has elevated my research to a whole new level. I deeply appreciate his dedication to his beloved family and to his everyday work. The significant computational task in this thesis work wouldn't be realized without the solid support from Dr. Pavol Juhas. I am extremely grateful for having the generous support from Soham Banerjee, Chia-Hao (Tim) Liu, Maxwell Terban, Long Yang, Elizabeth Culbertson, Christopher Wright. The experience of working with you all has been so enjoyable and memorable.

To my parents, Jing and Yue.

To my advisors, Tomo and Simon.

Chapter 1

Introduction to the Skyrmion Materials

1.1 Generic aspects of Skyrmion systems

1.1.1 Magnetic phases in Skyrmion system

Here we introduce the generic phases in 2-dimensional Skyrmion system. The presence of the energy scales in various Skyrmion materials has resulted in a rather universal phase diagram, as shown in Figure 1.1. Very similar phase diagram was observed in Skyrmion materials that are metal, semiconductor, and insulator, with MnGe being perhaps the single known exception which will be discussed in detail in a separate section Seidel [2016].

1.1.1.1   The induced magnetic phase

In the temperature regime above the Skyrmion transition, an induced magnetic phase can be achieved under large external magnetic field. In MnSi, this state is believed to be purely ferromagnetic and thus can be continuously tuned into the conical state by decreasing the magnetic field at fixed temperature. The induced (ferro-) magnetic state is characterized by the saturation of the Mn magnetic moment at around 0.4 μ_B as the system enters the induced magnetic state from the conical state Stishov and Petrova [2011]. The crossover from the paramagnetic state to the induced magnetic state at high temperature is identified from susceptibility and magnetization measurements Bauer and Pfleiderer [2012]; Bauer *et al.* [2013]; DiTusa *et al.* [2014]. For example in MnGe and FeGe, the large low field contribution to magnetization is characteristic of a ferromagnetic phase with little hysteresis DiTusa *et al.* [2014]. To our knowledge, detailed experimental study of the induced magnetic phase is still lacking. In this thesis, this will be presented through a study of MnGe.

1.1.1.2   The Skyrmion phase

The Skyrmion phase, as marked by the small pocket region right below the transition temperature in the phase diagrams, consisting of a locally spiral spin state that is topologically inequivalent to either the conical, helical or the ferromagnetic state. Regarded as being stabilized by its unique spin topology, the Skyrmion phase is first established experimentally via small angle neutron scattering on single crystal MnSi Mühlbauer *et al.* [2009], where the 6-fold symmetric scattering pattern was observed in the Skyrmion phase, indicating the formation of the hexagonal Skyrmion lattice. This study also shows, with computer simulation, that the stabilization of the Skyrmion phase against the conical phase can be assisted by the large thermal fluctuations near the phase transition. This point has been corroborated via

a subsequent simulation study, which uses classical Monte Carlo (MC) method and incorporates the thermal fluctuation effect with a non-perturbative approach Buhrandt and Fritz [2013]. In fact the energy of the 2D Skyrmion state is close to the conical state even without thermal fluctuations Mühlbauer *et al.* [2009], and thus the interplay between thermal agitation and topological stability becomes significant in some Skyrmion materials. The mean lifetime, energy landscape and stability of the Skyrmion phase against the external magnetic field has been studied numerically in Hagemeister *et al.* [2015]; Sampaio *et al.* [2013], and experimentally in Oike *et al.* [2016]. It is found from the experimental study that through rapid cooling the system enters the metastable Skyrmion state inside the conical phase, and have a typical lifetime of 10^4 seconds at a temperature of 23 K with external field of 0.22 T in MnSi Oike *et al.* [2016].

1.1.1.3 Evolution of the magnetic phases in external field

At high temperature the Skyrmion system exhibit paramagnetic behavior with a large fluctuating moment enhanced by strong ferromagnetic exchange interaction, as revealed by the μSR experiment Ishikawa *et al.* [1985]. At low temperature and low field, a helical, or stripe-like, phase has been observed in various materials Zhao *et al.* [2016]; Romming *et al.* [2015]; Milde *et al.* [2013]. In the helical phase the spin rotates along the magnetic propagation vector, which at low field is fixed to the easy axis of the material determined by the crystal magnetic anisotropy. Within the helical phase, if we fix the temperature and increase the field until it is comparable to the strength of the magnetic anisotropy in the system, then the field would decouple the spin helix from the magnetic anisotropy axis and align the magnetic propagation vector along the direction of the field. Up to this point the external field competes with and has overcome the magnetic anisotropy. For convenience of notation
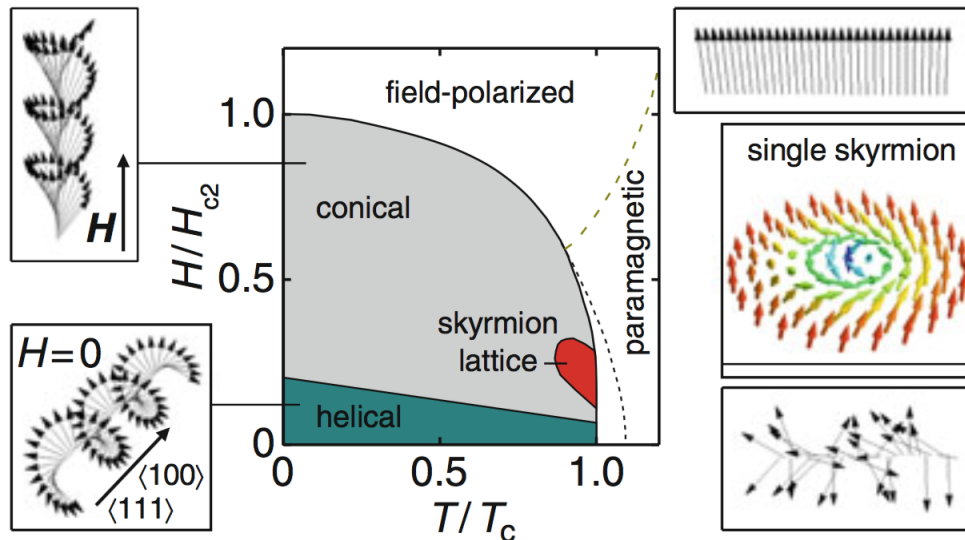
Figure 1.1: Generic magnetic phases diagram in Skyrmion systems. Also shown are the spin configurations of different phases, including the helical, conical, paramagnetic, field-polarized and the Skyrmion phase. The y and x axes were normalized using the upper critical field and the critical temperature, respectively. Figure reproduced from Seidel [2016].

we refer to this field as H_{c1}. We see that H_{c1} is the critical value beyond which the magnetic propagation decouples from the crystal axis, and the helical phase transforms into a lower symmetry state. Furthermore, as the field continues to increase beyond H_{c1}, it starts to compete with the next stronger interactions in the system, the DM interaction, and starts to tilt the spins in the spiral towards the field direction. This tilted spin spiral state is referred to as the conical state. As the field continues to increase beyond a certain critical value, H_{c2}, the spin becomes fully aligned with the field, and the system enters the field-polarized (ferromagnetic) state. Therefore we see that H_{c2} is the field value beyond which the external field completely win over the DM interaction. The influence of external field on the stability of the various phases is studied in both experiments and calculations with a focus on the field-dependent size of the (2D) Skyrmion Romming *et al.* [2015]. Intuitively, in the 2D

Skyrmion state the ferromagnetic exchange energy is minimized in the background region, where spins are totally aligned with the field, and the DM exchange energy is minimized within the Skyrmion region, where the period of the spin spiral is shorter than in the conical phase in the nearby region of the phase diagram (namely the consecutive spins are aligned more perpendicularly) and therefore further reduces the DM interaction. Figure 1.2 gives an illustration of the evolution of the Skyrmion under magnetic field. As the external field increases, the 'background' ferromagnetic region expand, and the edge of the Skyrmion correspondingly shrinks towards the center. Since the spins on the outer edge of the Skyrmion are more aligned with the FM background, it is clear that increasing the external field along the polarization direction the background spin would shrink the Skyrmion by aligning more of its edge spins along the field. From a theoretical perspective (see Ch.2 in Seidel [2016]), the tilt angle of the spin within a Skyrmion follows:

$$\theta(\rho) \approx \begin{cases} \pi - c_1 \kappa \rho & \text{for } \rho \to 0 \\ \frac{c_2}{\sqrt{\kappa \rho}} e^{-\kappa \rho} & \text{for } \rho \to \infty. \end{cases} \tag{1.1}$$

where $\kappa^2 \sim H/J$, thus as the field increase, the size of the Skyrmion shrinks in order to reduce the magnetic energy Seidel [2016]. On the other hand, theory requires that Skyrmion takes a minimal size (the critical size of Skyrmion) against external field at certain temperature, beyond which the Skyrmion will become unstable and collapse into the ferromagnetic phase Siemens *et al.* [2016].

1.1.1.4 Real space observations

Various real space observation has been applied in the observation of the helical and Skyrmion state in different compounds. Figure 1.3 (a) shows the direct observation of Skyrmion via magnetic field microscopy Milde *et al.* [2013], in which the dot-like objects are Skrymions
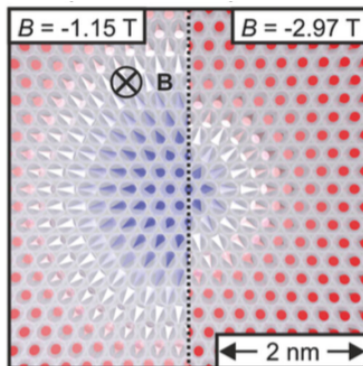
Figure 1.2: Simulation on the field dependence of the size of Skyrmion. The field is applied along the spins in the background outside the Skyrmion region. As the field increases, the background ferromagnetic region expands due to more spins being aligned by the field, while the Skyrmion region shrinks from the edge. Figure reproduced from Romming *et al.* [2015].

and the stripe-like order is the helical phase. This study shows that the Skyrmions break and merge with each other to form local stripe-like magnetic object, which then further connect with each other and establish the long-range helical phase. Evolution of the helical phase across the Skyrmion phase into the ferromagnetic phase is also demonstrated in similar studies using Lorentz transmission electron microscopy (LTEM) and other techniques Yu *et al.* [2012, 2010]; Zhao *et al.* [2016]; Heinze *et al.* [2011]; Park *et al.* [2014], where the spin textures within the observed phases were mapped out. The decrease of the Skyrmion size under increasing external field, as discussed above, has been clearly observed from the LTEM image, see Figure 1.3 (b). In a separate study using LTEM Nagao *et al.* [2015], helical phases with multiple wave vectors were observed in the vicinity of the field-driven Skyrmion phase transition (see Figure 1.5). By monitoring the temporal evolution of this multi-Q vector state this study demonstrates that Skyrmions annihilate with a time scale of 30 seconds.
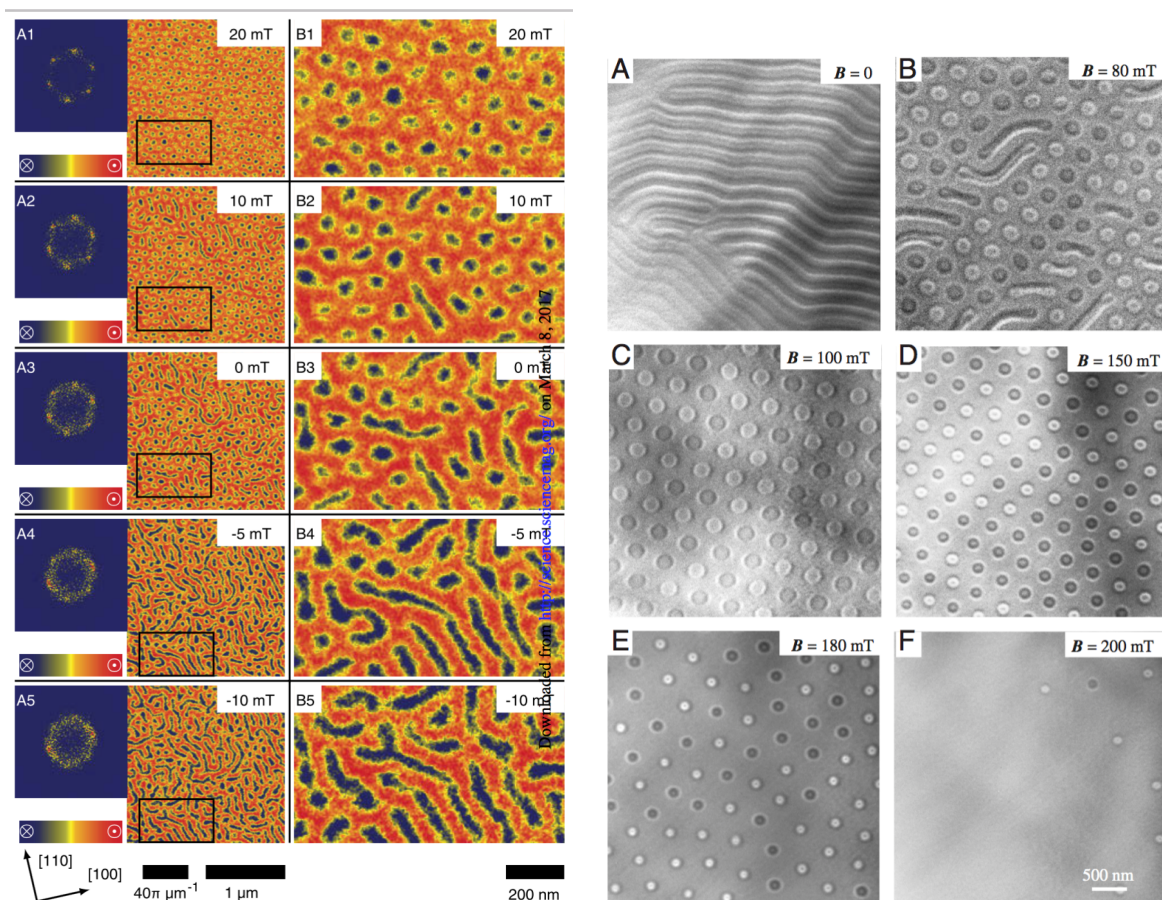
(a) Magnetic force microscopy   (b) Lorentz TEM

Figure 1.3: (a) Magnetic force microscopy images of Skyrmion material $Fe_{0.5}Co_{0.5}Si$ under different external fields. As the field decreases from 20 mT to -20 mT, the system changes gradually from the Skyrmion phase into the helical phase. The pair-annihilation of Skyrmion and the creation of stripe-like helical order can be clearly seen from the intermediate fields B3, B4. Figure reproduced from Milde *et al.* [2013]. (b) Lorentz TEM image of $BaFe_{12-x-0.05}Sc_xMg_{0.05}O_{19}$, x = 0.16. As the field increases, the stripe-like helical phase first evolves into the Skyrmion phase, which were then stabilized and subsequently shrink and disappears into the ferromagnetic phase. Figure reproduced from Yu *et al.* [2012].
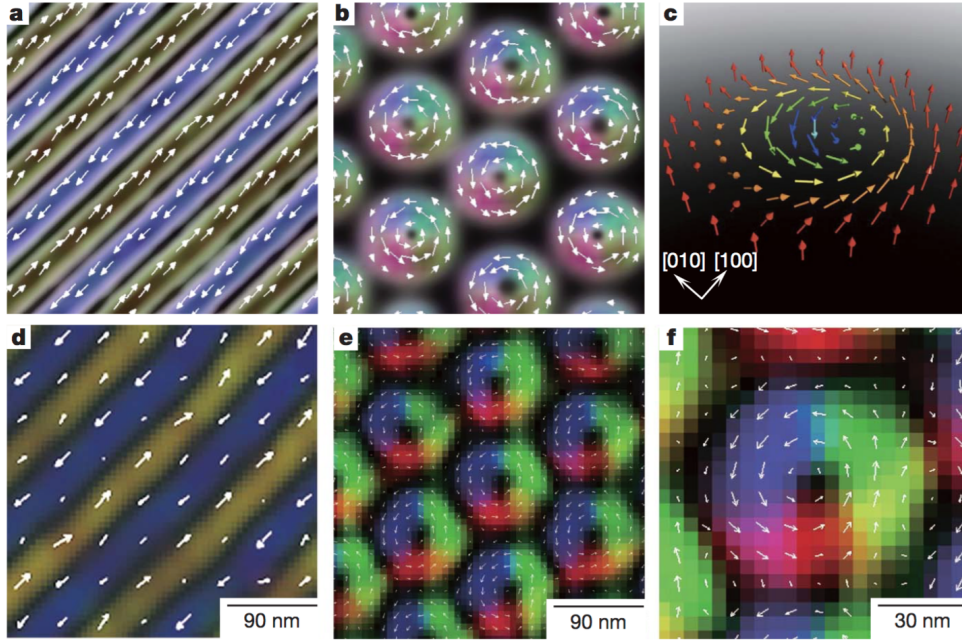
Figure 1.4: Lorentz TEM image of $Fe_{0.5}Co_{0.5}Si$. As the field increases, the stripe-like helical phase evolves into the Skyrmion phase. The experimental data (lower panels) were fitted and interpreted well with the theoretical calculation (corresponding upper panels). Figure reproduced from Yu *et al.* [2010].

1.1.2   Energy scales in Skyrmion system

The formation of the helical and Skyrmion state originates from the competition of 3 distinct energy scales. The largest energy scale, corresponding to the strongest interaction, in Skyrmion system is the ferromagnetic exchange (FM) interaction which favors parallel spin alignment. At the presence of other interactions in the Skyrmion system, the FM interaction still forcibly aligns the spin on short spatial scales. The second largest energy scale comes from the isotropic Dzyaloshinskii- Moriya (DM) spin-orbit interaction. The DM interaction is a result of the lack of inversion symmetry in the crystal structure, and takes the following
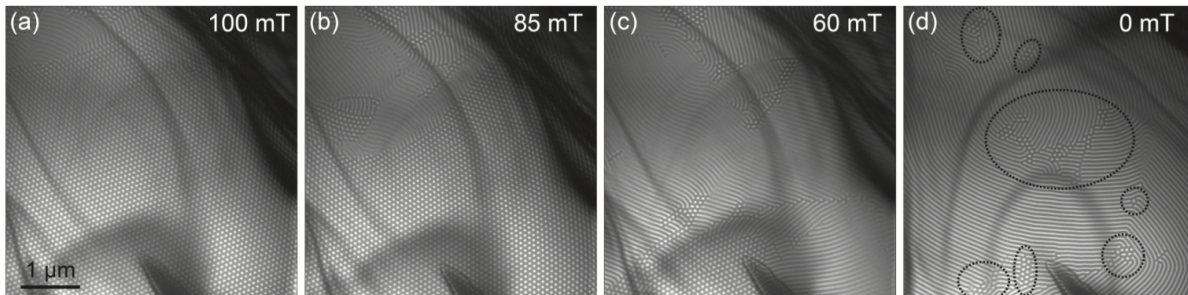
Figure 1.5: Fresnel image series of FeGe at 200 K, with field decreasing from 100 mT to 0 mT. As the field decreases, stripe-like helical order with different orientations grows longer, and finally intersect at the Skyrmion regions. Figure reproduced from Nagao *et al.* [2015].

form

$$- D \int d\mathbf{r} \mathbf{M} \cdot (\nabla \times \mathbf{M}) . \tag{1.2}$$

Intuitively the DM interaction favors perpendicular spin alignment. Thus within certain temperature and magnetic field condition, the competition of the FM and DM interaction stabilizes a spin configuration with spiraling spins. This can be a helical, conical or even a topologically-nontrivial spin structure called the Skyrmion. The wave vector Q of such helical spin order can be estimated as $Q \sim D/J$, where D and J stands for the strength of the ferromagnetic and DM interactions. Finally, the smallest energy scale comes from the higher order spin-orbit interactions in the system. These interactions are usually referred to as either the crystal electric field effect or cubic anisotropy, and determines the direction of propagation of the helical modulation Seidel [2016].

The above energy hierarchy is closely related to the nature of the critical thermal fluctuation in the above mentioned Skyrmion system. At above T_c, decreasing the temperature reduces the thermal disruption to the system, which subsequently develops stronger magnetic correlations. In a system with multiple levels of spin interaction, this implies that as temperature decreases the spin interactions become dominant according to their relative strength, and
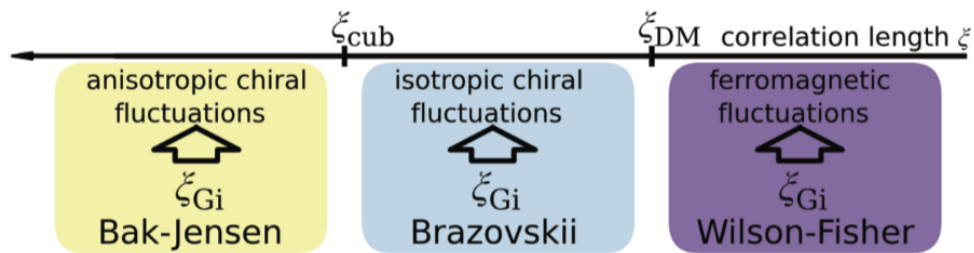
Figure 1.6: Energy scale and correlation lengths in the Skyrmion system. Figure reproduced from Janoschek *et al.* [2013].

forming dynamic spin correlations on the scale of the correlation length ξ determined by the temperature of the system. Thus it is convenient to associate each energy scale (interaction) in the system with a corresponding spatial correlation length ξ_E, with the intuition that it is only when the temperature is low enough and the thermal correlation length ξ is equal or larger than ξ_E that the interaction with energy scale of E becomes effective and dominant. In other words, the stronger the interaction, the larger its energy scale, and the smaller the associated length scale, and thus the easier for it to be effective at a certain temperature and correlation length ξ. We conveniently use ξ_{cub}, ξ_{DM} and ξ_{FM} as the correlation length for the cubic, DM and the ferromagnetic interaction, as illustrated in 1.6. Since the FM interaction is much stronger than the other two, ξ_{FM} is usually smaller than the other two length scales and thus its effect is constantly present around the phase transition. We therefore consider the effective onset of the other interactions as temperature decreases towards T_c.

Specifically, at $T \gg T_c$ the fluctuation is essentially ferromagnetic-like since the correlation length ξ is relatively short compared with the helical/Skyrmion period ($\xi \sim J/D$). Furthermore, as temperature decrease and the correlation length becomes comparable to the helical period, the magnetic fluctuation tends to form spin spirals with a wave vector of $Q \sim D/J$. At this stage fluctuation of these spin spirals are highly isotropic and tends to occupy a

spherical area in the reciprocal space Mühlbauer *et al.* [2009]. As the temperature further decreases, the cubic anisotropy interaction finally sets in. These anisotropy interaction tends to fix the magnetic fluctuations to the (energetically preferred) easy axis of the crystal.

Beyond the above 3 energy scales that are responsible for the formation of the helical/Skyrmion phase, the 4th energy scale of the system is set by the interaction between the fluctuating helical modes. The length scale for this interaction is the Ginzburg length Chaikin [1995], ξ_{Gi}. The strength of the interaction can be measured by comparing the thermal correlation length with ξ_{Gi}, and can be treated differently in each case. For example the system is considered strongly interacting if $\xi \gtrsim \xi_{Gi}$, and can be treated as weakly interacting if $\xi \ll \xi_{Gi}$. The relative strength of the interaction of helical fluctuations with respect to that of the other interactions in the Skyrmion system sets the nature of the phase transition, e.g. its order (1ˢᵗ or 2ⁿᵈ). The specific case where

$$\xi_{cub} \gg \xi_{Gi} \gg \xi_{DM} \tag{1.3}$$

corresponds to the case considered by Brazovskii Brazovskiĭ [1975]. In this case the helical fluctuations becomes strongly interacting when they're still fluctuating isotropically, and the phase transition, which a mean-field theory predicts to be 2ⁿᵈ order, driven by the tendency to reduce the strong interaction energy, turns out to be 1ˢᵗ order.

1.1.3   Models of magnetic fluctuations

1.1.3.1   Localized electron model of magnetism

Historically, magnetism was explained first by regarding a magnetic material as composed of small local magnetic moment with a fixed size. Under external field, a set of atoms with

fixed magnetic moment would, with statistical averaging, align with the field and gives rise to the Curie law of magnetic susceptibility Moriya [1985]

$$\chi_{\text{Curie}} = \frac{C}{T},$$ (1.4)

where C is the Curie constant and T is temperature. After introducing the concept of an interaction between atomic magnetic moment, using mean molecular field as an approximation Moriya [1985], Weiss has successfully explained the existence of ferromagnetic phase, with the susceptibility behaving like

$$\chi_{\text{Curie-Weiss}} = \frac{C}{T - T_c},$$ (1.5)

with T_c being the ferromagnetic transition temperature. Equation 1.5 is usually called the Curie-Weiss law of magnetic susceptibility, and is commonly observed in nearly all ferromagnets.

Despite its success in many aspects, the classical theory of magnetism has several intrinsic difficulties that remains to be resolved Moriya [1985]. For example it assumed without concrete proof the existence of atomic magnetic moment with constant magnitude. Furthermore, the magnitude of the molecular field required to reproduce the observed T_c is about three orders larger than the estimation based on magnetic dipole-dipole interaction. These mysteries were resolved by the quantum theory of magnetism.

According to quantum mechanical laws, electrons in the atom goes into their eigenstate and thus have quantized orbital and spin-angular momentum. The quantized unit for electron magnetic moment is known as the Bohr magneton, which equals to $\mu_b = e\hbar/2mc$. On the other hand, the existence of the Weiss molecular field was clarified by introducing the quantum-mechanical exchange interaction between adjacent atoms. In particular, as a phenomenological model, the Heisenberg model has proved to be a very important model

in explaining a variety of properties of magnetic materials. By specifying the sign of the exchange constant, antiferromagnetism, ferrimagnetism and even helical magnetism has all been successfully derived. It also provides valuable insights into the elementary excitations in magnetic material and introduced the concept of spin wave.

1.1.3.2   Itinerant electron model of magnetism

Alongside the localized moment picture is the itinerant electron theory of ferromagnetism. The basic idea is that the exchange interaction between the up and down electrons within the same energy band turns out to shift the two spin-subbands by an energy difference of the order of the exchange interaction. The occupation number in each spin sub-band thus becomes unequal, effectively introducing ferromagnetism into the material. The predictions of the itinerant electron model of ferromagnetism turns out to be consistent with the observed magnetization in transition metals with non-integer Bohr magneton, although it does experience some difficulty in explaining the Curie-Weiss law of magnetic susceptibility and some other observed trends in many ferromagnets.

From a wholistic point of view, the localized and the itinerant electron model of magnetism starts with opposing states of the electron. And since most real cases tend to fill out the full spectrum instead of the extreme limiting cases, controversies has arisen for a long time about using the two models Moriya [1985]. By far it become clear that the d electrons, a primary contribution to magnetic moment in material, should be regarded as more localized in magnetic insulators, and behaves more like itinerant electrons in transition metals.

1.1.3.3 Random-Phase Approximation theory of spin fluctuation

Random-phase approximation, or RPA, was among the efforts to unify the above mentioned opposing pictures of magnetism. In his seminal work on spin waves, Slater Slater [1937] emphasized the importance of the interaction between the excited electrons and holes. Subsequently, Herring and Kittle Herring and Kittel [1951]; Herring [1952] developed the microscopic spin wave theory of ferromagnetic metals. Finally, the random-phase approximation was introduced by Izuyama in his attempt to solve the general spin fluctuation problem, including paramagnetic and critical fluctuations Izuyama *et al.* [1963]. The RPA theory, however, turns out to be inconsistent with some of the experimental observations. And this is expected since it didn't include the effect of spin fluctuation on the calculated thermal equilibrium state of the system. In other words, a theory is needed, which accounts for the spin fluctuation effects in a self-consistent fashion. One attempt at this, which is proved to be quite successful, is the self-consistent renormalization, or SCR, theory of itinerant electron magnetism.

1.1.3.4 Self-Consistent Renormalization theory of spin fluctuation

As mentioned in the previous section, the SCR theory calculates at the same time the thermal equilibrium state and the spin fluctuations in a self-consistent fashion Moriya [1985]. In other words, the interacting modes of the spin fluctuation was accounted for self-consistently. Along this line of thought, Murata and Doniach Murata and Doniach [1972] developed the phenomenological mode-mode coupling theory of spin fluctuations for a weak ferromagnetic metal, and the quantum mechanical treatment of the self-consistent renormalization of spin fluctuation was finally proposed by Moriya Moriya and Kawabata [1973].
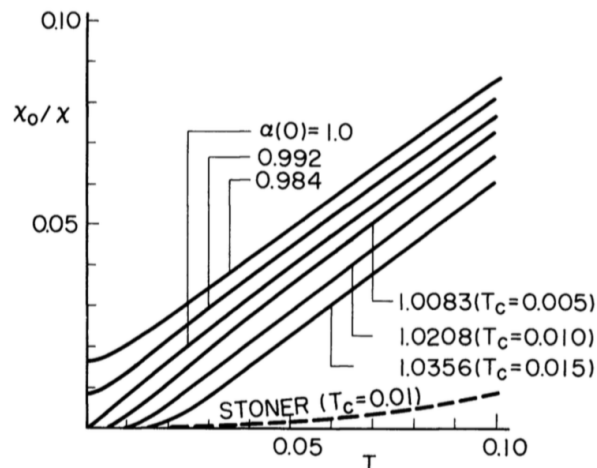
Figure 1.7: Temperature dependence of the inverse magnetic susceptibility calculated from the SCR theory (solid line) and from the Stoner model (dash line). Figure reproduced from Moriya [1985].

Experimental results has since then supported the SCR theory in many aspect and properties of the material, as well as the temperature and field dependence of the spin fluctuation condition Moriya [1985]. Among the many successful predictions of the SCR theory, the most important one is considered to be the new mechanism proposed for the Curie-Weiss law of susceptibility.

For detailed development of the theory, we direct the readers to Moriya [1985, 1982] and references therein. Here we briefly introduce and discuss the results of the theory, with a focus on the Curie temperature and magnetic susceptibility above T_c. As a self-consistent treatment of spin fluctuation, the SCR theory calculates the dynamic susceptibility and the free energy at the same time Moriya [1985]. The calculated magnetic susceptibility is plotted in Figure 1.7. From Figure 1.7 it is clear that the SCR susceptibility follows an approximate Curie-Weiss law, in stark contrast with the result calculated from the Stoner model. This indicates that the Curie-Weiss law of magnetic susceptibility of ferromagnetic

metals should be explained as primarily due to the self-renormalization effects from the strong spin fluctuation in the system, and is thus different from the local moment. The Curie constant of the CW law turns out to be determined by the band structure at the Fermi surface. Meanwhile, SCR theory predicts that the CW behavior should hold even when the paramagnetic metal is close to the ferromagnetic phase boundary.

In particular, SCR theory predicts that at a very small region near T_c, the inverse susceptibility becomes quadratic in $(T - T_c)$ for weakly ferromagnet metals. The theory for this special behavior was presented on page 57 in Moriya [1985]. Such important deviation from the CW law around T_c is observed in MnSi only recently, owing to the enhanced temperature resolution and stability of the μSR experimental facility Gat-Malureanu *et al.* [2003]. This deviation is later found to be related to the 1$^{\text{st}}$ order nature of the topological phase transition at zero field Janoschek *et al.* [2013].

According to SCR theory, the mean square local amplitude of the fluctuating spin decreases linearly with temperature above the transition temperature, and this results in the Curie-Weiss behavior of the susceptibility Moriya [1985]. Furthermore, in weak ferromagnetic metals, the Curie-Weiss law holds only for very small q values for χ_q. This is in contrast with the local moment picture, which predicts that χ_q obeys the Curie-Weiss law for all q values. After all, in weak ferromagnetic metals the dominant spin fluctuations are of long-wave length character, and thus the spatial spin correlation is also expected to be long-ranged Moriya [1985].

1.1.3.5   SCR theory of weakly ferromagnetic metals and spin relaxation

As revealed by SCR theory, the nature of the spin fluctuations in ferromagnetic metals is different from materials with local moment Moriya [1985]. The spin fluctuation in local

moment system consists of randomly flipping local moment as a form of thermal excitation, and can be regarded as a short-range correlation between nearby moments. On the other hand, the spin fluctuation in weak ferromagnetic metals are long-range (long-wavelength) spin fluctuations which cannot be properly accounted for in the local moment picture Moriya [1985]. This is evidenced by the fact that the local spin amplitude in weakly ferromagnetic metals varies (linearly) with temperature.

As has been introduced before, the random phase approximation is able to provide a good enough description of the ground state excitations since the interaction effect between the excited modes are weak at low temperatures. As the spin excitation becomes increasingly populated at higher temperatures, the coupling effect between the fluctuating spin modes becomes significant and gives rise to renormalization effects that needs to be accounted for in order to have a reasonable theory. The nature of the mode mode interaction in weakly ferromagnetic metals is the increased kinetic energy due to the spatial overlapping of the fluctuating modes Moriya [1985].

Ueda and Moriya calculated the muon spin dynamic relaxation rate, $1/T_1$ using the SCR result for the dynamical susceptibility Moriya [1963]; Moriya and Ueda [1974]; Ueda and Moriya [1975]. It is found that the relaxation rate at low temperatures is linear in T. At temperatures close yet still below T_c, the relaxation rate diverges quickly as $T \to T_c$. At above T_c, $1/T_1$ and the susceptibility is related by

$$1/T_1 \sim T\chi \sim \frac{T}{T - T_c} \tag{1.6}$$

Since χ essentially follows the Curie-Weiss law for temperatures above and not too close to T_c, $1/T_1$ tends to remain constant for temperatures much higher above T_c. In a seminal study by Hayano *et al.* [1978], the $T/(T - T_c)$ behavior of $1/T_1$ was clearly observed in the itinerant ferromagnet MnSi via μSR as shown in Figure 1.9.
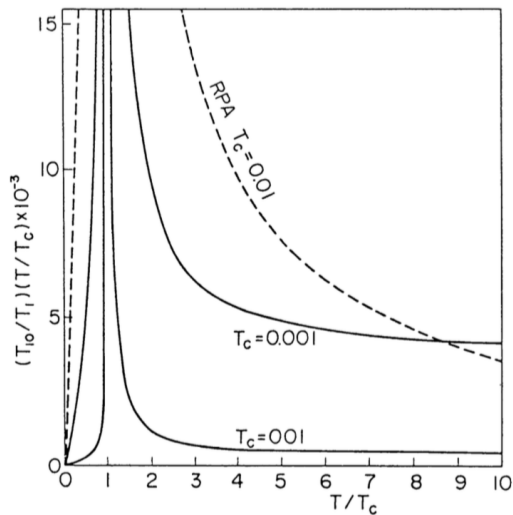
Figure 1.8: Nuclear $1/T_1$ dynamic relaxation rate for weakly ferromagnetic metals with electron-gas band, calculated using SCR theory. Figure reproduced from Moriya and Ueda [1974].

These results have also been observed in a wide variety of itinerant ferromagnetic metals (e.g. Masuda *et al.* [1977]; Masuda [1983]; Mochizuki [2012]; Alloul and Mihaly [1982]; Takagi *et al.* [1981]; Kitaoka and Yasuoka [1980]; Katayama *et al.* [1977]; Akimoto *et al.* [1975]), further demonstrating the power of SCR theory.

1.1.4 Technical applications of Skyrmion materials

In recent years Skyrmionic materials have received increasing attention from researchers due to potential applications for data storage and information transportation Jiang *et al.* [2015]; Iwasaki *et al.* [2013]; Woo *et al.* [2016]; Büttner *et al.* [2015]; Boulle *et al.* [2016]; Koshibae *et al.* [2015]; Li *et al.* [2014b]; Shibata *et al.* [2013]. Excellent reviews on this topic is readily available Kang *et al.* [2016]; Wiesendanger [2016]; Koshibae *et al.* [2015], and therefore here
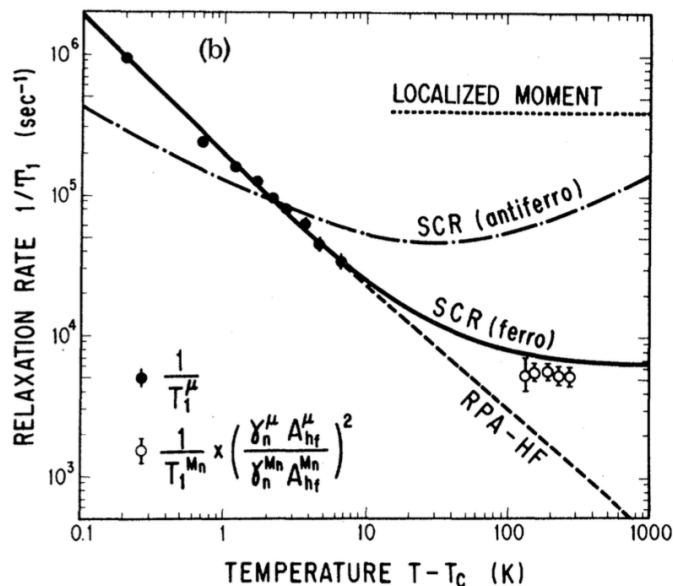
Figure 1.9: Muon $1/T_1$ dynamic relaxation rate and NMR data for weakly ferromagnetic metal MnSi, plotted as a function of $(T - T_c)$. Results from theoretical calculations based on localized and itinerant ferromagnet and itinerant anti-ferromagnet model with SCR theory were plotted comparison. It is clear that the experimental μSR and NMR data agrees well with the SCR theory for itinerant ferromagnet. Figure reproduced from Hayano *et al.* [1978].

we only give a brief survey of the present works, and encourage the reader to refer to these works to further explore this topic.

It is well known that the properties of the nano magnetic particles widely used in traditional magnetic hard disk suffer from loss of stability after being decreased below a critical size. This single factor has severely limited the storage volume of the magnetic storage from further increasing, given the sizes of the device Krause and Wiesendanger [2016]. Magnetic Skyrmions are considered, among many other candidates, as one of the promising solution for solving this problem. Owing to their stable topological protection for the spin configuration, some of the species remain stable even at room temperature. Stable, isolate Skyrmion as small as

50 nm has been successfully realized at room temperature in laboratory Woo *et al.* [2016]. In another recent experiment, Skyrmions are found to be expanding or shrinking under different external currents. Furthermore, the demonstrate of current-driven transformation from magnetic stripes to Skyrmions indicates new potential for Skyrmion spintronics Jiang *et al.* [2015].

Skyrmions has also been realized at room temperature in ultra-thin nano materials, without even the stabling force of an external magnetic field. The extreme thinness as well as the high sensitivity of the Skyrmion to the nano structure configuration opens up new paths for designing devices of exotic property and extreme geometry Boulle *et al.* [2016]. Furthermore, through applying external current/fields, Skyrmions can be controlled in a variety of ways. For example, by applying transient electric current pulses, individual Skyrmions can be efficiently driven along a magnetic track Woo *et al.* [2016]. By careful manipulation of the central vortex through external field, Skyrmion can be controlled to switch between different topological states, or between the on and off state Li *et al.* [2014b]. The tunability of the Skyrmionic state further expands the potential of Skymions in the application of logic circuits and memory devices.

1.2 Phase transitions and topology in Skyrmion systems

1.2.1 Helical fluctuation-driven phase transition

Recent studies have shown that the magnetic transition in MnSi behaves weakly 1st order in zero field due to the strong and interacting spin fluctuations, and becomes 2nd order as

the spin fluctuations is suppressed under external magnetic field Janoschek *et al.* [2013]; Bauer *et al.* [2013]. Theories of magnetic phase transitions driven by spin fluctuation has been proposed by Brazovskii and other researchers Brazovskiĭ [1975]; Murata and Doniach [1972]; Schmalian and Turlakov [2004], and have been successfully applied to explain the experimental data on MnSi.

It is first shown by Brazovskii Brazovskiĭ [1975] that a classical 2nd order magnetic phase transition becomes 1st order if the magnetic soft modes, which proliferates at temperatures close to T_c, has a non-zero wave vector. For systems with Dzyaloshinskii-Moriya interaction, due to the competition between the DM interaction and the Ferromagnetic interaction, the magnetic soft modes takes the form of short-ranged helical spin order, and acquires a finite wave vector. As has been studied in Schmalian and Turlakov [2004], such large wave vector and thus phase space of the magnetic fluctuation results in singularity in the density of state for the fluctuating modes. Thus the interaction energy (self-energy) of these fluctuating modes becomes enormous as the system approaches the phase transition. Intuitively, the large self-energy can be understood as due to the large Ferromagnetic interaction in the system. The wave vectors of these fluctuating modes occupy a spherical phase space and therefore the spin configuration largely deviates from Ferromagnetic configuration, and thus may induce large energy gain compared with Ferromagnetic spin configuration. Furthermore, it turns out that in this case the free energy of the ordered phase, due to the reduction of the fluctuating mode and thus their interaction energy, becomes lower than that of the paramagnetic phase. Therefore as the temperature approaches T_c, driven by energy and entropy gain, the system circumvents the large interaction energy between the proliferate fluctuating modes by avoiding the 2nd order transition and enters the ordered state via a 1st order transition. As a result, the correlation length of the system does not diverge, and the order parameter varies discontinuously. Furthermore, close to the theory of the fluctuation-
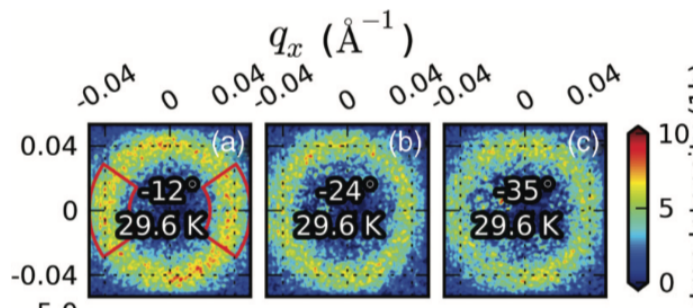
Figure 1.10: Magnetic fluctuations from neutron scattering, measured for a single crystal MnSi sample at different rocking angles ω up to ± 35 degrees for T $= 29.6$ K. This shows that right above the transition temperature the critical fluctuation is highly isotropic. Figure reproduced from Ref. Janoschek *et al.* [2013].

drive 1st order transition, the wave vectors of the fluctuating modes above the transition should occupy the entire spherical phase space, and thus the fluctuation is largely isotropic.

In MnSi, such isotropic magnetic fluctuation has been identified through neutron scattering experiment on a single crystal sample of MnSi Janoschek *et al.* [2013]. In this experiment, neutron diffraction patterns has been obtained at 3 different rocking angles at a temperature above but very close to T_c of MnSi. As shown from plot 1.10, the magnetic intensity distribution at these different angles are all consists of a homogeneously distributed ring with the same radius. This demonstrates that the wave vectors of the fluctuating magnetic modes around the phase transition is indeed homogeneously distributed on a sphere in phase space, and thus provide strong evidence for the presence of a fluctuation-drive 1st order phase transition. The 1st order nature of the magnetic transition in MnSi has been demonstrated unambiguously through specific heat and magnetic susceptibility measurements Bauer *et al.* [2013]; Stishov *et al.* [2007, 2008]. It is clear from Figure 1.11 that the magnetic phase transition is associated with a very sharp peak in specific heat. Moreover, the peak is seen to be suppressed as we increase the magnetic field, indicating that the transition shifts from
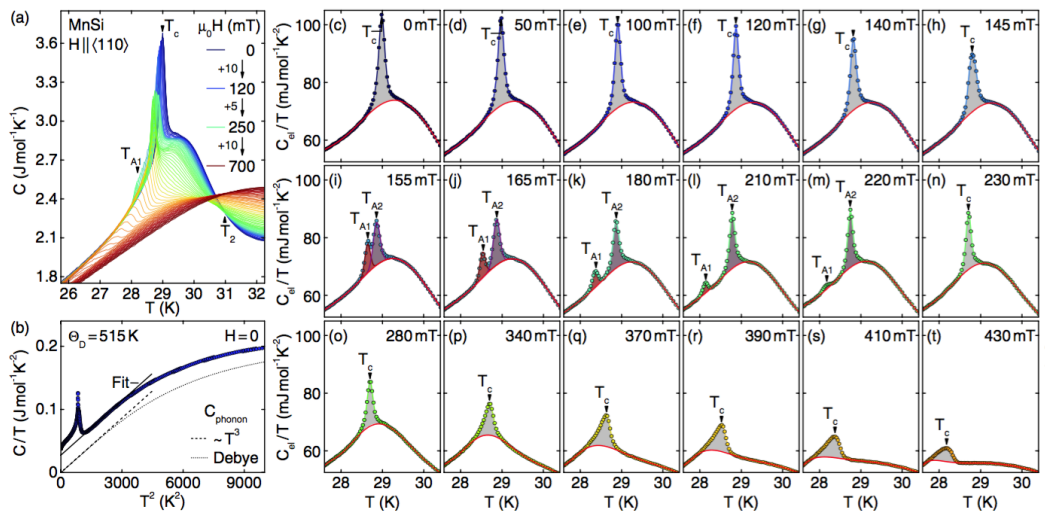
Figure 1.11: Specific heat of MnSi as a function of temperature for magnetic fields up to 0.7 T. The sharp peak which indicates a 1st order transition is seen from fields up to 280 mT, and is essentially suppressed for fields beyond 430 mT, where the fluctuation phase was suppressed by the field Bauer *et al.* [2013]. Figure reproduced from Ref. Bauer *et al.* [2013].

1st order to 2nd order. Therefore we see that in weak itinerant ferromagnet MnSi, due to the presence of strong spin fluctuations, the continuous 2nd order magnetic phase transition becomes 1st order at low fields.

This evolution of the phase transition can be better understood by studying the effect of the external field on the spin fluctuations in MnSi, which will be discussed in detail in the spin fluctuations section.

1.2.2 Topological descriptions of Skyrmion

1.2.2.1 topology and winding number

Mathematically, objects with certain geometric shape cannot be transformed continuously to those with different topological sectors without breaking. Conversely, objects of the sample topological sector are always able to be transformed to each other via continuous variation. Those topological objects that are able to deform continuously into each other are referred to as belonging to the same homotopy class. For each homotopy class, or the collection of topologically equivalent objects, a 'fingerprint' can be defined that characterizes uniquely the configuration belong to one and the same homotopy class. The general expression of winding number can be found in Braun [2012]. Intuitively, the winding number of a smooth curve is the number of complete turns the tangent vector to the curve makes as it passes around the curve once Mcintyre and Cairns [1993].

Next we introduce the concept of critical points as examples of topological objects in different homotopy classes, and consider the winding number for some of them. For a vector field, if each point of the surface is equipped with a vector tangent to the surface at that point, and depend continuously on the points where their tails are attached, it is usually referred to as a (continuous) tangent vector field on the surface. In such a vector field there exist different types of critical points that corresponds to singular field distribution at certain location (see for example Effenberger and Weiskopf [2010]). Figure 1.12 shows the field configuration of different types of critical points. Spin configurations that well resembles these critical points has been observed in various Skyrmionic materials. For example, periodic lattice consisting of the saddle-point-like object in Figure1.12 (a), also known as the meron-antimeron lattice Lee and Han [2015], has been predicted in Park and Han [2011] and observed in Heinze *et al.*
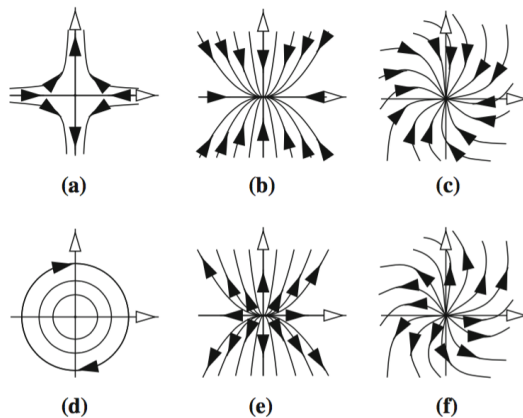
Figure 1.12: Types of local singularities in a vector field. (a) saddle point. (b) attracting node. (c) attracting focus. (d) center. (e) repelling node. (f) repelling focus. The 3D Hedgehog and Anti-Hedgehog structure as speculated to exist in MnGe corresponds to the attracting and the repelling node, respectively. Figure reproduced from Effenberger and Weiskopf [2010].

[2011]. The 3D version of this saddle point, known as the Hedgehog lattice, was recently observed in MnGe Tanigaki *et al.* [2015]. As we will see below, the Skyrmion line and Hedgehog structures found in real materials can be regarded (mathematically) as critical points in a smooth vector field, and thus can be classified with their winding number. For such vector field we know the theorem that, consider a surface and a vector field having no critical points on the surface, the winding number of the surface equals the sum of the indices of the critical points lying inside the domain bounded by the surface. As we will see below, this theorem requires that the Hedgehog and Antihedgehog must appear with equal number in order to exist in a ferromagnetic background.

For a vortex-type configuration in 2 dimensions, the winding number along a closed loop enclosing such vortex structure is expressed as:

$$w = \frac{1}{2\pi} \int_0^{2\pi} d\tau \partial_\tau \phi \tag{1.7}$$

Here $\mathbf{m}(\tau) = (\cos\phi(\tau), \sin\phi(\tau))$ is the vector field on the loop, and $\phi(\tau)$ specifies the orientation of the spin at each angle τ ($0 < \tau < 2\pi$). The various configurations in Figure 1.14 can be easily calculated using this formula. More generally, for the vector field in a 2D Skyrmions, we have Nagaosa and Tokura [2013]:

$$w = \frac{1}{4\pi} \int\int d\mathrm{x} d\mathrm{y}\, \mathbf{m} \cdot (\partial_x \mathbf{m} \times \partial_y \mathbf{m}) \tag{1.8}$$

For a Hedgehog as a 3D topological object, the winding number is given by

$$w = \frac{1}{4\pi} \int \mathbf{b} \cdot d\mathbf{S} \tag{1.9}$$

$$\mathbf{b} = \frac{1}{|M|^3} \left[\mathbf{m} \cdot \partial_y \mathbf{m} \times \partial_x \mathbf{m}, \mathbf{m} \cdot \partial_z \mathbf{m} \times \partial_x \mathbf{m}, \mathbf{m} \cdot \partial_x \mathbf{m} \times \partial_y \mathbf{m} \right], \tag{1.10}$$

Intuitively, the winding number counts how many times the unit vector $\mathbf{n}$, representing the orientation of the spin in the Skyrmion, wraps the circle. It has been proven mathematically that the winding number is always an integer if $|\mathbf{m}| = 1$, namely the vector $\mathbf{m}$ lying on the unit sphere (see Chapter 3 in Rajaraman [1982]).

More generally, the winding number of a critical point can be calculated by counting the number of different type of sectors in it. An illustration of different types of sectors are shown in Figure 1.13 de Floriani and Spagnuolo [2008]. It turns out that, since different sectors are topologically separate objects, the number of each of these sectors can be counted separately. The winding number of a critical point can be calculated using the following equation de Floriani and Spagnuolo [2008]:

$$w = 1 + \frac{n_e - n_h}{2}. \tag{1.11}$$

Here in Eq. 1.11, n_e stands for the number of elliptic sector, and n_h the number of hyperbolic sector. As mentioned before, intuitively the index can be understood as the number of counterclockwise turns made by the vectors while traveling counterclockwise on a closed curve around the critical point.
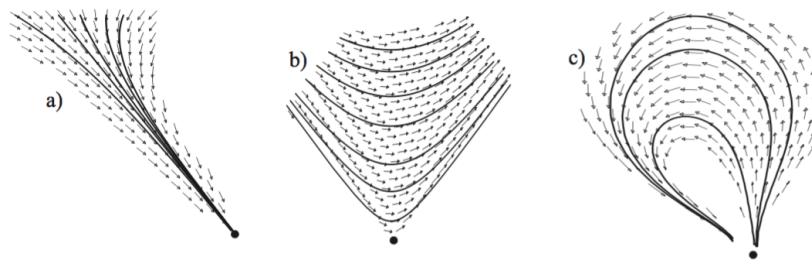
Figure 1.13: Different types of sectors of a critical point. (a) parabolic sector; (b) hyperbolic sector; (c) elliptic sector. Figure reproduced from de Floriani and Spagnuolo [2008].

1.2.2.2 Skyrmion as topological object

Here we briefly introduce the description of Skyrmionic spin configuration as a topological object. The discussion in this section closely follows that from Braun [2012]. The magnetic field in a Skyrmion can be reasonably approximated by a tangent vector field if considered at scales larger than the size of the helix. Under this assumption the Skyrmion itself can be described mathematically as a continuous geometric object with non-zero topological winding number. Furthermore, the magnitude of the magnetization is temperature-dependent, and can be assumed to be fixed for considerations on the topological structure Braun [2012]. Furthermore, within the ordered phase, it would be very energy-costly to suppress the local magnetic field to zero Mühlbauer *et al.* [2009], and thus the transformation between topologically inequivalent magnetic configurations remains physically unrealizable when the system is far enough from the phase boundary. Therefore at steady state, the local spin configuration of a topological spin state will be oriented specifically to minimized the energy, namely to stay at the ground state. At the presence of small perturbations, although its local configuration might undergo moderate reorientations, the topology of the overall spin state will not change due to this high energy barrier to break the topology. Thus after the perturbation has vanished, the same topological spin state will again reorganize and go back

to its ground state configuration. In other words, although the state itself may vary upon external perturbation, the topological structure of the state is firmly protected by a large energy barrier and is thus a stable feature of the system.

We emphasize the different nature of the 2D Skyrmion and the 3D Hedgehog. The 2 dimensional Skyrmion can be regarded as a continuous classical spin field and can be described mathematically by a continuous vector field. It is a continuous topological object existing in a 2D continuous field. The Hedgehog is a singular object embedded in a 3D discrete lattice. It requires the suppression of local magnetic moment and is thus not contained in a continuum theory. In other words, the creation and existence of Hedgehog structure have to resort to the discreteness of the lattice model. Although as a topological object in a continuous field Skyrmion is not allowed to dissociate (via continuous reorientation of the field), the Hedgehog itself is defined via the discreteness of the lattice and readily dissipate at the presence of a small hole punched at its very center Abanov and Pokrovsky [1998]; Tretiakov and Tchernyshyov [2007]; Yang *et al.* [2016], possibly through strong thermal fluctuation or pinning to defects in the sample Milde *et al.* [2013].

If we regard the sample itself as a topological object, then it is the Skyrmion within it that contribute to the total topological winding number of the system. If the system has nonzero winding number, then since the ferromagnetic state has a zero winding number, the magnetic configuration of the system cannot be transformed continuously to ferromagnetic configuration without breaking the Skyrmion, or equivalently, overcame large energy barrier and suppress the local magnetic moment, or resort to lattice discreteness Braun [2012] or the thermal instability of the state near phase transition. Therefore in a Skyrmionic state away from the phase boundary, the Skyrmions remain stable due to the its topologically non-trivial magnetization field distribution and the robustness of the local magnetization within it. In
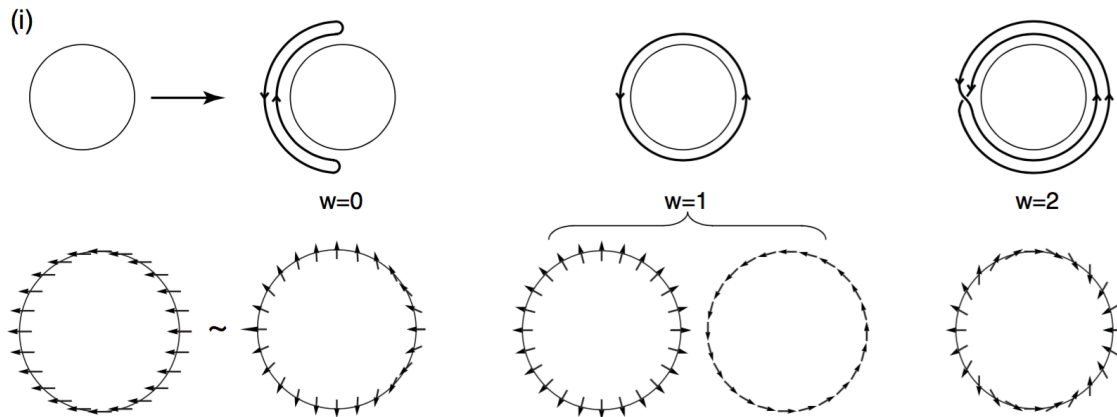
Figure 1.14: Spin vortex configurations with different topological winding number. Figure reproduced from Braun [2012].

other words, the Skyrmions are protected by the vector field topology of its magnetization configuration. This turns out to have significant implications on the properties of the system, in particular its phase transitions as will be discussed in detail in a separate section.

We take the 2-dimensional spin vortex state as an example to illustrate the concept of winding number and topological equivalence. Here the winding number w is calculated to be how many times that the spin rotates around 360 degrees around the circular configuration of the vortex. From Figure 1.14 we see that for $w = 0$ the spin first rotates clockwise from 9 to 12 position on the circle, and then rotates counter-clockwise from 12 to 3 position, and then repeat this from 3 to 9. Therefore around the circle the spin has rotated by a total degree of 0, and thus having a winding number of zero. It is apparent that this state can be transformed to the ferromagnetic state by continuously varying the spins within it, and thus verified that the latter also has zero winding number. For $w = 1$, the spins rotates consistently clockwise around the circle and complete a full rotate as it recovers its starting location. It is clear that in this case there's no way to transform the spin configuration

(a) Helical and (b) Skyrmion   (c) Hedgehog and Anti-Hedgehog
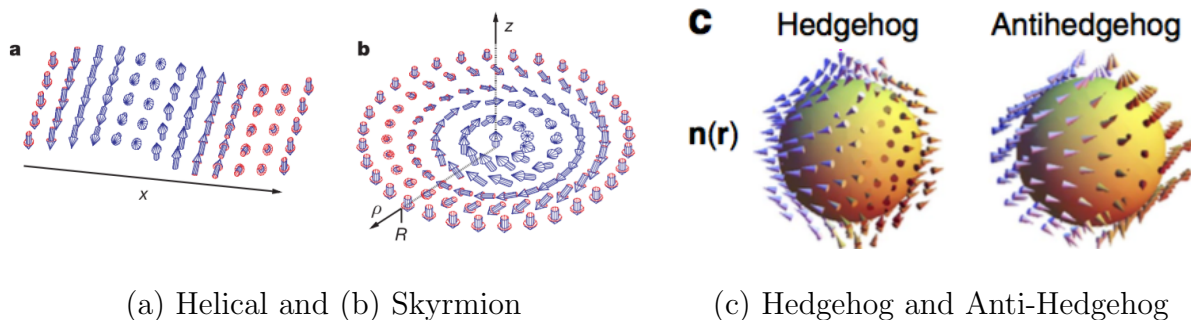
Figure 1.15: Illustration of the local moment distribution in (a) the helical state with winding number 0, (b) the Skyrmion state with winding number 0, and (c) the Hedgehog and Anti-Hedgehog state with winding number 1 and -1, respectively. Figure reproduced from Robler *et al.* [2006] and Kanazawa *et al.* [2016].

continuously to that in the $w = 0$ case without locally breaking the spin chain. Similar argument applies to the case of $w = 2$.

Figure 1.15 (a) and (b) shows the spin configuration of the helical state and the 2D Skyrmion. As seen from the illustration the helical state can be formed by rotating each layer of spin in a ferromagnetic state by a slight degree relative to its neighbor on one side, and therefore is topologically equivalent to the ferromagnetic state. On the other hand, the Skyrmion has its center spin opposite to that of the ferromagnetic background, and thus is topologically inequivalent to the latter. Flipping the spin in a Skyrmion by 180 degrees produces the Anti-Skyrmion, whose spin at the center and the edge might have the same orientation as that in a Skyrmion, but is topologically inequivalent to the latter. Furthermore, since the Skyrmion has all its edge spins aligned along the same direction, it can exist alone without the paring of an Antiskyrmion in a ferromagnetic background, and the same for Antiskrymion. As will be discussed below, for the case of Hedgehog, it is not allowed by topology to exist alone in a ferromagnetic background, unless paired with an Antihedgehog.

Figure 1.15 (c) show the Hedgehog and Anti-hedgehog as examples of 3D topological objects. As shown from the figure in a Hedgehog the spin orients towards left and right on the left and right side (outwardly) , and points down and up on the up and down side (inwardly), respectively. By extending the spin configuration as plotted on the edge towards the center, we can see that the center magnetization of the Hedgehog must be zero due to symmetry reasons. In other words there's a magnetic singularity inside each Hedgehog (and also Anti-Hedgehog). Meanwhile, we note that while a strict magnetic singularities would be very energy-costly to realize in a physical system, the spins in the material may, instead, remain reasonably 'soft' and thus absorbing some of the neighboring spins Robler *et al.* [2006]; Park and Han [2011]. In such case forming a Hedgehog would cost much less energy and can thus be physically realizable. The Anti-hedgehog configuration can be realized by simply reversing the orientation of the spins in a Hedgehog. Therefore from Eq. 1.8 we see that the Skyrmion number of the Hedgehog and the Anti-Hedgehog must be opposite. In fact from calculation they equal to $+1$ and -1, respectively.

1.2.3 Topological phase transition in Skyrmion systems

1.2.3.1 Concepts of topological phase transiton

Topological phase transition refers to a phase transition between two topological spins states of a system. Here we consider the details of a topological phase transition between 2 spin ordered state, including how the spin configuration transforms microscopically around such transition. Thus these topological transitions involving stable phases consisting of long-range ordered topological structures are different in nature from those in which disordered

topological object participates as the topological excitations assisting the phase transition (see e.g. Kosterlitz and Thouless [1973]; Haldane [1988]).

Furthermore, since thermal topological transitions at low field usually involve strong spin fluctuation and interaction effect Brazovskiĭ [1975], we focus on the field-induced topological transition at relative high field, where spin fluctuations are largely suppressed and so that the transition is dominated by topological consideration. Meanwhile, we take the vortex (antivortex) structure Hertel and Schneider [2006], which has been observed in many materials including MnSi, as the example to illustrate the evolution of continuous (nodeless) topological objects, and take the Hedgehog structure as example of nodal topological structure.

From the discussion about topology we know that topologically inequivalent states cannot transform to each other via continuous variation without breaking or resorting to discreteness of the lattice, and vice versa. It is well established that the collapsing of 2 Skyrmion in to 1 Skyrmion corresponds to a change in the total topological number, which has to be assisted by the emergent magnetic Hedgehog. As has been studied in detail in the seminal work of Haldane Haldane [1988] and following studies Senthil *et al.* [2004]; Thiaville *et al.* [2003]; Tretiakov and Tchernyshyov [2007]; Milde *et al.* [2013], due to the continuous nature of the topological object, any change in the topological sector requires the presence of a singular point in space where the magnetic field vanishes to zero, namely a Hedgehog or Antihedgehog.

From the parameter space point of view, if we map each topological object onto a sphere, then the sphere of a continuous topological object would also be continuous, whereas the sphere of an actual spin field defined on discrete lattice will be discretized into an elastic mesh. The change in topological sector, for example the merging of 2 Skyrmions, corresponds to the dilation of a single mesh through which a topological charge (the Hedgehog in parameter

space) enters the sphere Haldane [1988]. Thus we see that this mesh discretization of the order-parameter sphere, as an reflection of the discreteness of the lattice, is essential for the merging of Skyrmions to occur.

Therefore, the phase transition between two topologically inequivalent spin states cannot be 2nd order (or, have to be 1st order) since it cannot be accomplished via continuous variation of the spins. By definition a phase transition is $1^{st}/2^{nd}$ order if the order parameter varies discontinuously/continuously. This is reflected in the case in MnSi, where the (field-induced) phase transition between the topologically equivalent states, namely the helical, conical and the ferromagnetic state, are shown to be 2nd order, whereas that between them and the topologically inequivalent (2D) Skyrmion state is 1st order (see for example Bauer *et al.* [2013]). On the other hand, for MnGe, it has equal amount of Hedgehog and Anti-Hedgehog in the Skyrmion state and thus having a total of zero winding number. This means that the Skyrmion state in MnGe is topologically equivalent to the ferromagnetic state, and thus a 2nd order transition is allowed between the two states. Meanwhile, experiment has also shown evidence for such 2nd order topological transition in MnGe Kanazawa *et al.* [2016].

At the presence of Antiskrymion, the winding number should also account for the orientation of the center spin Skyrmion, which determines the sign of the topological number Tretiakov and Tchernyshyov [2007]. This has been observed in a recent simulation on Skyrmion-Antiskyrmion annihilation Hertel and Schneider [2006]. Furthermore, because of the continuity of the annihilation process of Skyrmion-Antiskyrmion pair, to define a strict point at which the transition occur would be conceptually invalid. In this sense the continuous topological phase transition (between topologically inequivalent phases) is different in nature from the regular second order phase transition, although signatures of the later has been observed from experiments. As will be discussed below, the second order signature of such

topological transition might come from the self-annihilation of the Hedgehog as by product of the annihilation process.

1.2.3.2 Evolution of the spin configuration in Skyrmion transition

In the following we discuss the microscopic picture of the evolution of the spin configuration as the system cross the phase boundary with increasing magnetic field. We first consider the case of 2D Skyrmion and analyze the prototypical system of MnSi. As shown from Figure 1.16, for the topological transition between the helical and the 2D Skyrmion state, the Skyrmion lines first meet and merges with each other at a local spot, where the spin configuration then constitutes a Hedgehog. And then the edges of the two 2D Skyrmions continuous to merge into each other, which is accompanied and accomplished by the movement of the Hedgehog along the edge of the 2D Skyrmion. Finally, as the Hedgehog reaches either end of the Skyrmion line and become separated and eventually disappear due to instability, the two Skyrmions are totally merged. The merging of many such 2D Skyrmions form stripe-like spin order which eventually becomes the helical spin state.

If we zoom into the region where the two Skyrmions merge, we realize that the spins at the edge of the two 2D Skyrmions are always along the opposite direction, and so were the spin in the ferromagnetic background and at the middle of a 2D Skyrmion. This intuitive implies that since the local spin structure has been superimposed onto each other at where the 2D Skyrmions meet and merge, the local spin structure at this meeting point must contain a singular point where the magnetization vanishes. In other words, the creation of a Hedgehog at where the two Skyrmion lines merge is required by the conservation of topological winding number of the system, and that the winding number of a Skyrmion can vary only at singular points where magnetization vanishes. Specifically, since the merging
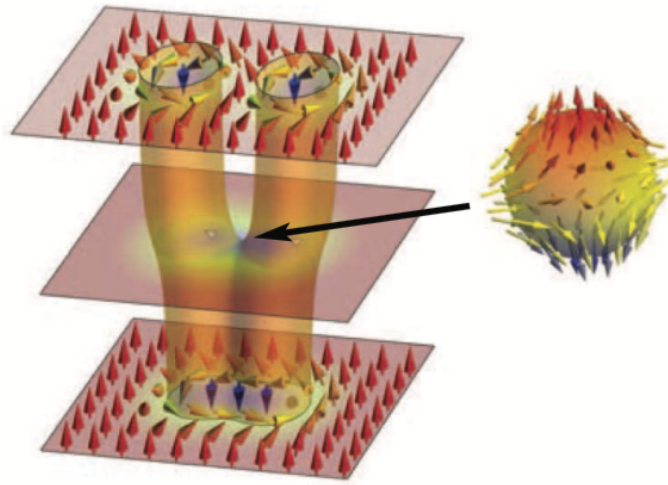
Figure 1.16: Illustration of the merging and unwinding process of two 2D Skyrmions. At the beginning stage, one Hedgehog structure was segregated from the contacting region of two Skyrmions, where the spins starts to align smoothly. Subsequently, more spins from the edge of the two Skyrmions start to align and merge with each other as the Hedgehog structure moves along the edge region. Eventually the two Skrymions completely merges into one, with the Hedgehog structure being isolated into the background (and then annihilated due to instability). Figure reproduced from Milde *et al.* [2013].

of the two 2D Skyrmions coincides with the creation of 1 Hedgehog, and that the winding number of a Skyrmion and a Hedgehog are the same, we see that during the merging of the 2D Skyrmions the total winding number of the system remains the same. In fact we note that the winding number for the two 2D Skyrmions that are partially merged (not including the Hedgehog) equals that of a single Skyrmion. It is apparent that the two objects can be transformed into each other (except the Hedgehog part). It is at the final stage where the Hedgehogs as by-products of such merging process disappear due to thermal instability that the winding number of the system as a whole is diminished (and finally suppressed to 0 as the system fully enters the helical state).

The annihilation of a single 2D Skyrmion line has also been studied via simulation in Schütte and Rosch [2014]; Lin and Saxena [2016]. In such case the Skyrmion breaks up in the middle and by creating a Hedgehog and Anti-hedgehog pair, which has zero winding number in total. And the left two parts of the Skyrmion diminishes in their length as the Hedgehog/Anti-Hedgehog moves along it, and finally disappears as the Hedgehogs reach the surface of the sample and annihilate due to thermal instability. Physically this corresponds to the encroaching of the Skyrmion region by the ferromagnetic background, driven by the thermal creation and fluctuation of the Hedgehog-Antihedgehog pair Schütte and Rosch [2014]. In specific, the motion of the Hedgehog corresponds to the reduction of the topologically nontrivial region in the material. Furthermore, it is also shown from simulation that the annihilation of an Skyrmion-Anti-Skyrmion pair in 2 dimension also involves the creation of Hedgehog/Bloch points at where the two object merge Hertel and Schneider [2006].

For a 2D Skyrmion line that is, instead of extending to the real surface of a ferromagnetic system, enclosed inside a ferromagnetic background of spins, then at its very ends there must exist Hedgehog or Anti-Hedgehog. This is due to the topological inequivalence of the spin structure inside the Skyrmion and that of the ferromagnetic state. For such an 'enclosed' Skyrmion line, it's inherent topological winding number cannot be nonzero without introducing additional magnetic singular points inside it. In other words, at the two ends of such Skyrmion there much be one Hedgehog and one Anti-Hedgehog. Following this line, we know that during the self-annihilation process of such Skyrmion, after breaking up into 2 segments from the middle due to the creation of the Hedgehog-Anti-Hedgehog pair, the part that has one end with an Hedgehog (Anti-Hedgehog) must be associated with an Anti-Hedgehog (Hedgehog) at the broken end, so that (after the original Skyrmion break up) the winding number for each Skyrmion segment also has zero winding number and thus can be created without introducing more singularities within each segment.

1.2.3.3 Order of the Skyrmion transition

Regarding the phase transition, we argue that it is the abrupt annihilation of the Hedgehogs (Anti-Hedgehogs) at the end of the merging process of two Skyrmions that accounts for the 1st order nature of the Skyrmion transition. First of all, the creation of the Hedgehogs corresponds to the superposition of the local spin textures at where the two Skyrmions meet. Since as analyzed above this process conserves the total winding number, it can be realized via smooth reorganization of the local spin and thus does not contribute to the discontinuity of the transition. Furthermore, at the end of the merging process, the Hedgehog reach the end of each Skyrmion line while the latter has merged with each other and formed the stripe-like helical phase. The current state is thus a helical state decorated with individual Hedgehogs, and therefore the Hedgehogs will have to disappear in order to realize the real helical state. This annihilation of the Hedgehog, since no Anti-Hedgehog is present and thus no smooth pair-annihilation process available, has to occur via the abrupt self-annihilation of each Hedgehog, which we argue is the physical origin of the 1st order nature of this topological transition. According to the above reasoning, the creation of Hedgehogs and the merging of the Skyrmions should happen during the immense thermal fluctuation before the phase boundary is reached, and the real transition happens at when the Hedgehog undergoes annihilation. After the transition there should be only helical spin state, and no Hedgehog should be left, according to the nature of the phase transition. This in principle can be checked via imaging experiments around the phase transition.

Similar argument applies to the case of the self-annihilation of a single 2D Skyrmion Schütte and Rosch [2014]. This corresponds to a transition between Skyrmion state and the ferromagnetic state. This case differ from the merging case in that it is accompanied by the creation and separation of Hedgehog-Antihedgehog pairs. In such case the Hedgehog (Anti-
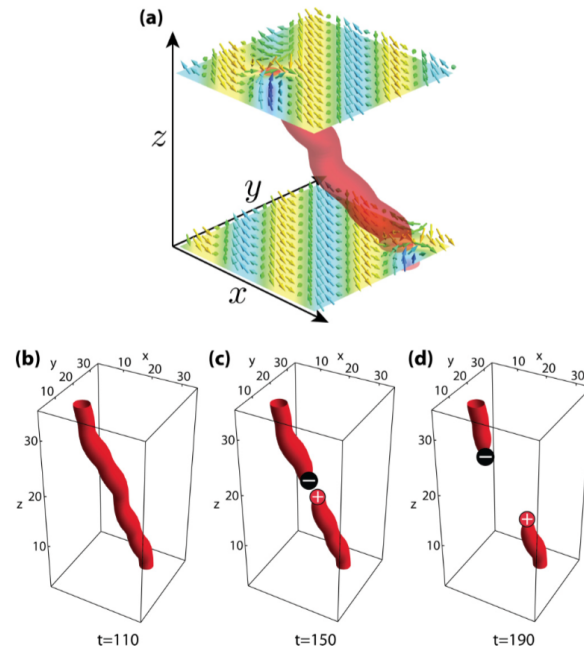
Figure 1.17: Simulation result of the creation of the Hedgehog-Antihedgehog pair during the annihilation of a single Skyrmion. The Hedgehog-Antihedgehog structure has a total winding number of zero, and thus the total topological number of the system is conserved during the process breaking of a Skyrmion line into two. The disappearance of each Skyrmion is marked with the encounter and annihilation of the Hedgehogs at the end of the contraction of each Skyrmion line. Figure reproduced from Schütte and Rosch [2014].

hedgehog) annihilate as they reach the either end of the Skyrmion line. And since there's no cancelling topology for a 2D Skyrmion and a 3D Skyrmion, the annihilation must correspond to an abrupt annihilation of the topological configurations in the system, and thus gives a 1st order transition. Again the underlying reason of the 1st order nature is the topological inequivalence of the Skyrmion state and the ferromagnetic state. We can also think about this process in reverse and consider the formation of the Skyrmion state out of the helical state. An illustration of the microscopic picture can be found in Figure 1.18. This process is also assisted by the formation of Hedgehog at where the stripe spin order in the helical phase

bifurcates. Skyrmion state becomes more energetically favorable over the helical state as the magnetic field increases Park and Han [2011]. Intuitively, (e.g. in MnSi) as the external field increases, the ferromagnetic background tends to encroach the stripe spin order and approach to its center. Energetically, this is likely realized first at a point location on the stripe (instead of encroaching the whole stripe altogether). This process cuts a spin stripe into large segments, and a Hedgehog was thus created at where the spin stripe was broken. These extended spin stripe segments in fact have the same topological number as the Skyrmion. They can be seen as an enlarged and extended Skyrmion within the x-y plane, and are therefore topologically protected. Then after the long spin stripes in the helical state are broken up into segments, each segment as a deformed Skyrmion, although protected by topology, may deform continuously and finally, minimizing the energy of the system, forms the circular Skyrmion with proper size.

1.2.3.4   Evolution of spin configuration in Hedgehog transtion

Below we analyze the topological transition involving only Hedgehog and Antihedgehog in 3 dimensions. As an example, MnGe is known to host a 3 dimensional periodic magnetic structure consisting of alternating Hedgehog and Antihedgehogs Kanazawa *et al.* [2011, 2012]; Tanigaki *et al.* [2015]; Kanazawa *et al.* [2016]. Recent experimental results have suggested that at temperatures below 170 K, MnGe undergoes a 2nd order transition from the Hedgehog (3D Skyrmion) state to the ferromagnetic state with increasing field Kanazawa *et al.* [2016]. Here by summarizing existing results, we attempt to clarify the microscopic evolution of the spin configuration crossing the phase boundary.

It can be seen from the simple geometric analysis that a ferromagnetic background cannot exist with only 1 Hedgehog/Antihedgehog in it. In order for the ferromagnetic background to
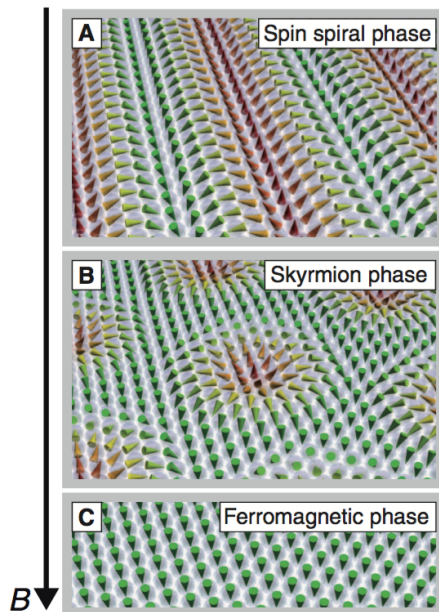
Figure 1.18: Illustration of the effect of external field on the spin configuration in a Skyrmion system. It is clear that the stable phase in higher external fields has larger ferromagnetic region. Figure reproduced from Romming *et al.* [2013].

exist, the number of Hedgehog and Antihedgehog must be equal. In case a field is applied in the direction of the ferromagnetic direction, the Hedgehog and Antihedgehog will be pushed towards each other to form a configuration with lower energy under the field. Eventually the Hedgehog and Antihedgehog undergo the merging process, leaving behind a pure ferromagnetic state with a winding number of zero. This is guaranteed by the theorem mentioned before, which requires that the winding number on a closed smooth surface equals the sum of winding number of the critical points it encloses. In other words a Hedgehog configuration is realizable in a ferromagnetic background only if there exist an Antihedgehog within the ferromagnetic domain. Thus the topological structure of MnGe suggested in Kanazawa *et al.* [2016], consisting of equal number of Hedgehog and Antihedgehog, is consistent with its interpretation of the field-induced polarization process involving a ferromagnetic background. If

this is the case, then the modeling of any 3D Skyrmionic structure using superposition of helical order is assuming a state that is topologically equivalent to the ferromagnetic state, and thus the field induced evolution and transition would necessarily consists of and be achieved through the motion and annihilation of the Hedgehog-Antihedgehog pairs. Meanwhile, the co-existence of Hedgehog and Antihedgehog is also more energetically favorable compared to the isolated Hedgehog (Antihedgehog) Yang *et al.* [2016]. In other words the existence of Hedgehog-Antihedgehog pair in a ferromagnetic background can be a requirement from both energetic and topological consideration.

A closely related question is whether a superposition of any 3 helical structure will still give a spin configuration that is topologically equivalent to the ferromagnetic state. It is clear that any helical order individually is topologically equivalent to a ferromagnetic state.

With the above preparation the topological transition in MnGe can be readily understood. For MnGe, the spin state in one unit cell is composed of a nearly ferromagnetic background decorated with 4 Hedgehog-Antihedgehog pairs, and is thus topologically equivalent to the ferromagnetic state Kanazawa *et al.* [2012, 2016]. This is not surprising considering that the spin state is a superposition of 3 helical configurations, each of which separately is topologically equivalent to the ferromagnetic state. While these Hedgehogs minimizes the DM interaction energy, the background region minimizes the ferromagnetic interaction energy. As has been shown from simulation Kanazawa *et al.* [2016], as the field increases below the critical field, the total total magnetization of the system increase steadily while the Hedgehogs remain intact. Considering that the Hedgehogs does not contribute to any macroscopic moment if remained intact by the field, the increasing magnetic moment of the system implies that the background spins outside the Hedgehogs are gradually polarized by the field as the it increases in magnitude. As the background polarizes, the Hedgehogs and Antihedgehogs

move along certain paths within the system to minimize the total magnetic energy. The critical field corresponds to the situation in which the Hedgehog and Antihedgehog meet and annihilation with each other in space, and subsequently forms the ferromagnetic state. Since the total winding number of a pair of Hedgehog and Antihedgehog equals to that of the ferromagnetic state (0), a smooth transition or crossover between the Hedgehog and the ferromagnetic state is allowed by topological consideration.

1.2.3.5   Order of the Hedgehog transtion

As has been discussed already, a fundamental difference between the 2D Skyrmion state in MnGi and the 3D Skyrmion state in MnGe is that, while the former is composed of solely Skyrmion and therefore non-zero winding number, the latter consists of equal number of Skyrmion and Anti-Skyrmion and thus a total winding number of 0 (for calculation see supplementary information in Kanazawa *et al.* [2016]). Therefore the 3D Hedgehog state in MnGe is topologically equivalent to the ferromagnetic state, and thus a smooth transition is allowed from topological analysis.

However, we note that neither the microscopic picture nor the knowledge and evidence about its physical mechanism of the annihilation of Hedgehog-Antihedgehog pair, or more generally the 2D Skyrmion with in-plane nodes Heinze *et al.* [2011]; Lee and Han [2015], is known at the moment, and the nature of the dissipation process of the nodal points in a spin texture remains to be studied.

Chapter 2

The Muon Spin Relaxation (μSR) Technique

Muon spin relaxation (μSR) has been one of the most sensitive probe of the magnetic field distribution within condensed matter materials. μSR experiment detects the relaxation of spin in time domain, and can be effectively performed in zero and tiny external fields Uemura *et al.* [1999]. The large magnetic moment of the muon makes it capable of detecting magnetic fields as small as 10^{-5} T Blundell [1999]; Frandsen [2016]. Meanwhile, as a sensitive local probe for magnetism, μSR is also very useful in studying materials with short-range or even random magnetic order. It also yields important information about the dynamics of the local field. These unique features of μSR stands it aside the existing techniques of nuclear magnetic resonance (NMR) or electron spin resonance (ESR), and make it a highly efficient and unique experimental tool for probing the magnetism inside materials Uemura *et al.* [1999]. This chapter introduces the μSR technique and its application to magnetic materials, in particular MnSi and MnGe in the Skyrmion systems.

2.1 Muon: a local probe of the magnetic field

After being implanted into the specimen, a positive muon with prescribed polarization direction quickly looses its kinetic energy (usually within 1 ns) during its interaction with the sample. The muon then stop moving and, usually, rests at an interstitial site without further displacement. During the muon stopping process the magnetic interaction between the muon and the material is known to be negligible. Therefore the precession of the muon due to interaction with the magnetic field within the material starts effectively as it arrives at one of the interstitial sites in the material. After the muon implantation, the average polarization of the muon spin at time t is defined as the muon spin relaxation function, $G(t)$ Uemura *et al.* [1999]. Since the muon precession is chiefly determined by the distribution of the internal field of the material, detecting and modeling the muon spin relaxation spectra, $G(t)$, allows us to study the details of the magnetism within it. The local magnetic field that the muon experiences arises predominantly from the dipolar magnetic interaction of the muon spin with the nuclear spin, the electronic spin, the contact hyperfine field or a combination of them Uemura *et al.* [1999].

For a local magnetic field, $\mathbf{B}$ the muon spin, $\mathbf{S}_\mu$, undergoes the Larmor precession around the field, following the temporal evolution determined by the equation of motion

$$\frac{d\mathbf{S}_\mu}{dt} = \gamma_\mu \mathbf{S}_\mu \times \mathbf{B}, \tag{2.1}$$

where γ_μ is the gyromagnetic ratio of the muon ($\gamma_\mu = 851.6$ rad μs^{-1}T^{-1}). By solving the above equation of motion of the muon spin, it turns out that the projection initial muon spin polarization that is initially parallel to the external field remains unchanged, while the projection that is perpendicular precesses with time around the field with an angular frequency of $\omega = \gamma_\mu B$, where B is the magnitude of the field. In other words, it is the

projection of the precession of the entire muon spin on to different axes that gives the projected asymmetry, which is being detected in an µSR experiment.

From a more realistic perspective, the nuclear dipolar moment within the material usually composes of several static nuclear moments with random orientations, located around the muon. Given the fact that the number of muons that were implanted into the sample is usually large, and that in principle the signal detected comes from all the muons within the sample, the distribution of the average internal field experienced by the muon can usually be well approximated by a Gaussian distribution and/or a Lorentzian distribution Uemura *et al.* [1999].

2.2 µSR experimental geometry and relaxation functions

2.2.1 Local field geometry and the muon precession

In an actual µSR experiment the initial polarization of the muon, meaning the polarization of the muon as it was injected into the sample at time $t = 0$, can be tuned to rotate by 90 degrees by a spin rotator located in the upstream of the beam. As discussed below, this would allow us to perform experiment in the longitudinal and transverse configuration and to probe the static components as well as the dynamic fluctuation of the local field. Figure 2.1 presents the relation between the local field geometry and the precession of the muon polarization. For the case where the muon initial polarization is along the direction of the (static) local field, as shown in Figure 2.1 (a) (left), the muon polarization does not have transverse component with respect to the field and therefore does not rotate or relax at

(a) Longitudinal field only

(b) Transverse and longitudinal field
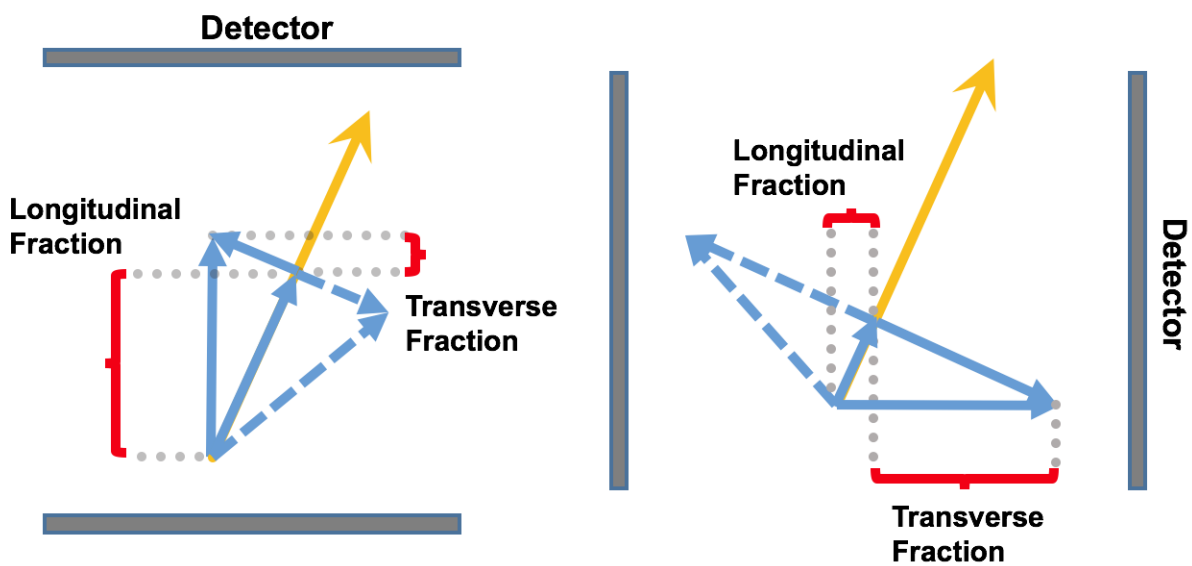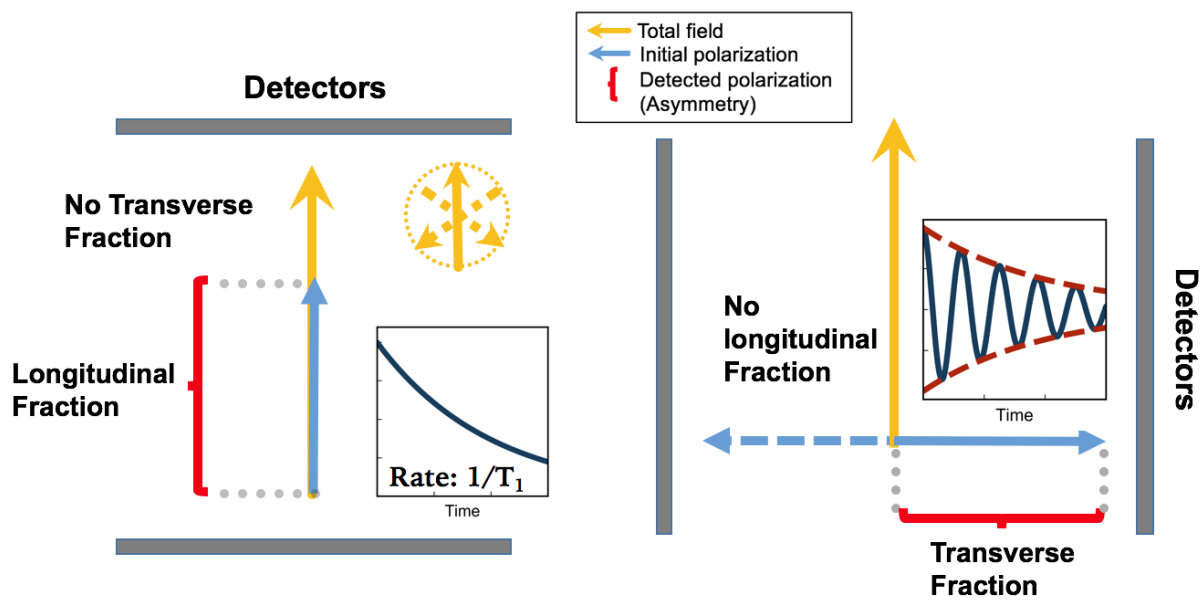
Figure 2.1: Muon spin precession in (a) field with only only longitudinal component and (b) field with both longitudinal and transverse component. The inset in Figure (a) shows spectra for the corresponding geometry.

all if the local field is purely static. In this case the muon polarization could, however, relax under the influence of the fluctuating local field. The fluctuating part of the local field does not change the average direction of the field over long time, but it does change the direction of the local field at each time segment. If the fluctuation of the local field is fast enough, this will cause the muon spins to flip it direction defined by the static (Zeeman) levels. This process corresponds to the dynamic relaxation of the muon, and is often referred to as the T_1 process. Meanwhile, if in an experiment the muon polarization was along the external field, which gives a total field highly aligned with the external field and therefore the muon polarization, the relaxation rate of the muon polarization contains information about the time scale of the fluctuation of the local field.

On the other hand, if the muon initial polarization was perpendicular to the local field, as shown in Figure 2.1 (a) (right), then the muon would feel the full strength of the static local field and start to precess around it. In this case, the frequency and relaxation rate of the muon precession would give information about the strength and width of the static internal field, as determined by Equation 2.1. In reality, the relaxation of the muon in a transverse field is influenced by both the inhomogeneity of the static field and the dynamic relaxation (T_1 process). The relative magnitude of these contribution need to be analyzed specifically for different cases.

In real cases, the local field and the muon polarization is usually neither 0 or 90 degree, but something in between. In such case, as shown in Figure 2.1 (b), the muon dynamic would contain finite longitudinal and transverse (oscillating) fraction in both geometries. Specifically, the longitudinal and transverse (oscillating) fraction of the polarization for one muon initial polarization would become the transverse and longitudinal fractions of the muon polarization if the muon initial polarization is rotated by 90 degrees. This problem, however,
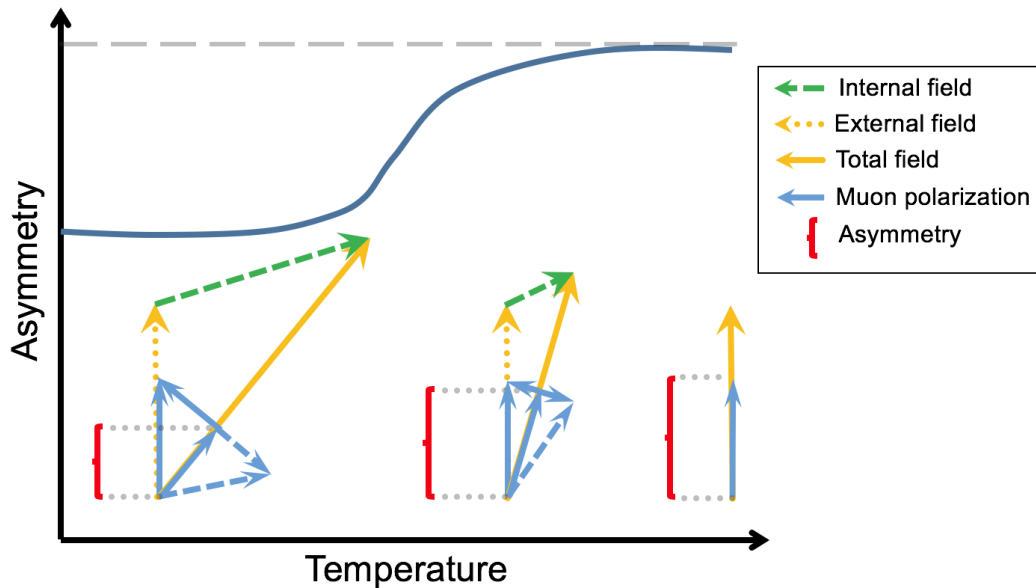
Figure 2.2: Evolution of the muon initial polarization and the corresponding local field direction.

can be partially resolved by applying an external field along one of the muon polarization directions. The external field would gives a totally field that is approximately aligned or perpendicular to the two muon polarization, and thus allows the muons with different initial polarization to detect separate (dynamic or static) properties of the local field.

Following the above analysis, we now give an example of the evolution of the muon polarization in different internal field conditions determined by temperature. For a magnetic material with increasing static internal field as temperature goes down, the evolution of the muon asymmetry usually looks like Figure 2.2. The initial polarization of the muon was chosen to be along the external field direction. At high temperature, the internal moment is very small compared with the applied external field. In this case the total field will be approximately aligned with the external field, and therefore the dynamic (or longitudinal) fraction of the muon polarization, which were experimentally detected, would equal to the

muon initial polarization. As the temperature goes down, the internal field becomes stronger and thus contribute to the transverse component of the total field. In this case the dynamic fraction of the muon asymmetry would becomes smaller than the muon initial polarization. At even lower temperature, the local field is further deviated from the muon initial polarization direction, and thus results in a even smaller asymmetry of the muon.

2.2.2   Zero field µSR experiment

As discussed above, µSR experiments can be conducted in zero or an applied external magnetic field. In the latter case, the external field is usually applied either in the longitudinal direction (longitudinal field, or LF), parallel with with the muon spin polarization at $t = 0$, or in the transverse direction (transverse field, or TF) perpendicular to the muon polarization direction. As will be explained in detail below, both the orientation and the strength of the external field has a unique influence on the internal field of the material and thus also the precession of the muon spin. And the choice for the external field is usually determined by the experimental question of interest.

In zero field experiment, the local field at the muon sites consists of only the internal field within the sample. Suppose that the local field is random at different sites of the muon but has a fixed magnitude $B = \sqrt{B_x^2 + B_y^2 + B_z^2}$, then the z component of the muon spin polarization, $\sigma_z(t)$, can be written as

$$\sigma_z(t) = \frac{B_z^2}{B^2} + \frac{B_x^2 + B_y^2}{B^2} \cos(\gamma_\mu B t) = \cos^2 \theta + \sin^2 \theta \cos(\gamma_\mu B t). \tag{2.2}$$

In the above expression, θ stands for the tilting angle of the internal magnetic field with respect to the z axis (the muon polarization direction). The first term, $\cos^2 \theta$, represents the time averaged z projection of the initial muon polarization along the field. The second term,

$\sin^2\theta\cos(\gamma_\mu Bt)$, represents the time-dependent part of the z component of the muon spin. This term comes from the projection of the periodic precession of the muon spin around the local field onto plane perpendicular to the field.

As mentioned above, instead of a single value, in real materials the magnetic field at different muon sites is usually described by the distribution function of a vector field. In such case the muon spin relaxation function, $G(t)$, can be calculated by averaging $\sigma_z(t)$ over the distribution function Uemura *et al.* [1999]. For a field distribution that has the same magnitude but different orientations (Ω) at different muon sites, if we assume that the field has equal probability (namely, $1/4\pi$) to be along each spatial orientation, then the muon relaxation function can be calculated to be

$$G_z(t) = \int \sigma_z(t)\frac{d\Omega}{4\pi} = \frac{1}{3} + \frac{2}{3}\cos(\gamma_\mu Bt). \tag{2.3}$$

Here in Equation 2.3 the constant component ($1/3$) comes from the average of the longitudinal component $\cos(\theta)$. In specific, for a vector field with isotropic orientation distribution and uniform magnitude, the average projection of the field along any particular direction would be one-third of its magnitude. Similarly, for a Gaussian field with distribution

$$P(H_i) = \frac{\gamma_\mu}{(2\pi)^{1/2}\Delta}\exp\left(-\frac{\gamma^2 B_i^2}{2\Delta^2}\right), \quad i = x, y, z, \tag{2.4}$$

the relaxation function turns out to be Uemura *et al.* [1999]

$$G(t) = \frac{1}{3} + \frac{2}{3}\left(1 - \Delta^2 t^2\right)\exp\left(-\frac{1}{2}\Delta^2 t^2\right). \tag{2.5}$$

This is known as the Kubo-Toyabe function, which is derived first by Kubo and Toyabe in 1967 Blinc [1967]. By fitting the experimental muon relaxation spectra with Equation 2.5 we can obtain an estimation of the width of the internal field from parameter Δ.

2.2.3 Weak transverse field µSR experiment

According to Equation 2.2, in circumstances where the magnitude of the local field changes drastically from site to site, the temporal dynamics (e.g. frequency) of the muon at different locations can be very different. Although the detected signal is the superposition of the signal from every muon within the sample, area/phases with very different field distributions could produce visibly different signal containing, e.g. significantly different oscillating frequencies and relaxation rates. These distinct signals can usually be distinguished by fitting the data with known muon relaxation functions. From such fitting knowledge about the magnitude and distribution of the local field can usualy be derived. Furthermore, since the muons are approximately uniformly distributed within the sample volume, the weight of different signals in $G(t)$ is roughly proportional to the volume of the phases in the sample under the experimental condition if the system is spontaneously decomposed into multiple phases.

Since the muon relaxation function within the paramagnetic phase turns out to be slowly relaxing and cannot be accurately distinguished with the signal from an ordered phase with large local field (except for the difference in the relaxing asymmetry), in actual µSR experiments a weak magnetic field is usually applied to the sample in a direction perpendicular to the muon polarization (i.e. the transverse direction) to induce visibly oscillatory signal from the paramagnetic fraction of the sample. In case the internal field is much stronger than and therefore not affected by the applied external field, the muon relaxation function can be approximated by

$$G(t) = f \cdot \left(\frac{1}{3} + \frac{2}{3} \cos(\gamma_\mu B_{\text{int}} t) \right) + (1 - f) \cdot \cos(\gamma_\mu B_{\text{ext}} t), \tag{2.6}$$

where f stands for the fraction of the volume of the ordered phase, B_{int} and B_{ext} are the magnitude of the internal field (in the ordered phase) and the external field, respectively.

Intuitively, Equation 2.6 describes the case where the muon within the ordered phase experiences field with uniform magnitude and isotropic distribution, and muons within the paramagnetic phase experiences the external field. Through refinement of the f factor, a good estimation of the volume fraction of different phases within the sample can be obtained. In reality, due to the finite width of the distribution and the fluctuation of the local field, the signal from the paramagnetic phase usually turns out to be a damped oscillation. On the other hand, since with the same field width the rate of damping is faster for a larger field magnitude, the fast-oscillating signal from the ordered phase also damps out much faster than that from the paramagnetic phase.

This technique of applying a weak transverse field (wTF) is thus very useful, especially in the study of phase transition, where the evolution of the relative volumes of the competing phases is closely connect with the order of the transition Uemura *et al.* [2007]; Frandsen *et al.* [2016]. As is different from a 2nd order transition where one phase is completely replaced with another after crossing the transition temperature, a 1st order phase transitions can be associated with the separation of the two phases within a finite temperature regime below the transition temperature. Therefore information about the temperature evolution of the volume fraction of the phases from the µSR wTF measurement can provide information related to the order of the phase transition.

2.2.4 Transverse field µSR experiment

The difference between a wTF and a TF µSR experiment is that the field strength in a typical TF experiment can be comparable to or larger than the internal field of the material. In the case the local field is dominated by the transverse field, the muon will precess with a frequency set by the external field, and the finite spread of the local field, due to the presence

of the internal field, will only introduce damping to the signal. On the other hand, if the applied transverse field is comparable to the internal field, then as the material enters the ordered phase, the local field at the muon site undergoes significant change, and a shift of the muon precession frequency is expected.

2.2.5 Longitudinal field μSR experiment

Since the local field is a vector sum of the internal and the external magnetic field, applying a longitudinal field parallel with the initial muon polarization (i.e. along the z axis) tends to align the (total) local field to the muon polarization direction. Moreover, applying a longitudinal field would decrease the ratio of the width and the magnitude of the local field. Therefore since only the perpendicular projection of the muon polarization will precesses around the local field, applying a longitudinal field would effectively reduce the magnitude of the precession, which is then reflected in the reduced damping rate in the measured relaxation spectra.

From Equation 2.2 it is clear that decreasing the angle between the directions of the muon spin and the local field would result in the reduction of the magnitude of the precessing component of the relaxation spectra. For an isotropic gaussian internal field, the static relaxation function becomes Uemura *et al.* [1999]

$$G(t) = 1 - \frac{2\Delta^2}{\omega_0^2} \left[1 - \exp\left(-\frac{1}{2}\Delta^2 t^2\right) \cos\omega_0 t \right] + \frac{2\Delta^4}{\omega_0^3} \int_0^t \exp\left(-\frac{1}{2}\Delta^2\tau^2\right) \sin\omega_0\tau d\tau \quad (2.7)$$

where $\omega_0 = \gamma_\mu B_{ext}$ is the typical precession frequency, determined by the magnitude of the external field. In this case, the magnitude of the relaxation is closely related to the ratio of the longitudinal and the transverse component of the local field. For a large external field, the value of Δ/ω_0 can be very small. This means that the transverse component of

the muon polarization, which in this case is responsible for the oscillation and relaxation of the muon spin, is very small. Therefore intuitively, the fraction of the muon spin which undergoes oscillation would be small. This can be an intuitive explanation for Equation 2.7. In case the external field is vanishingly small, it is easily verified that Equation 2.7 reduces to Equation 2.5.

In the discussion above, the internal field is assumed to remain unchanged, i.e. static, during the precession of the muon. Now we consider the case in which the internal field is dynamic in nature. The fluctuating local field comes from the electron spin, which undergoes constant fluctuation and therefore induce fluctuating fields. The relaxation caused by the transition between Zeeman levels assisted by spin-lattice interaction is commonly referred to as the T_1 process, with the corresponding relaxation rate being $1/T_1$ Uemura *et al.* [1999]. A finite-width distribution of the local field (and thus multiple precession frequencies) introduces damping in the muon precession, and the fluctuation of the field gives rise to dephasing process during the precession. The observed muon spin relaxation is a consequence of both (static) damping and (dynamic) dephasing process. Mathematically, this gives rise to the Kubo-Toyabe type of relaxation function, with an exponential envelope function signifying the effect of field fluctuation.

In the case of fluctuating field, the precession and thus relaxation process of the muon will depend on the relation of 2 time scales. The first time scale is the oscillation frequency, ω_0, determined by the strength of the static local field, and the second is the fluctuation rate $1/\tau$. Intuitively, if the oscillation frequency is much larger than the hopping rate, it means that the muon would effectively have sufficient time to precess under a stable local field environment at a fixed site, and this would result in similar oscillation and relaxation behavior of the muon as if in a static field environment.

At the other limit, where the hoping rate of the muon is much larger than its precession frequency, what happens is that there won't be sufficient time for the muon to precess around the field at one site before it jumps to another location. In other words, the local field that the muon experiences within a give time window has been constantly changing frequently in both magnitude and orientation. Thus in this case the muon spin can be seen as doing a nearly random walk around its initial polarization, with the step size proportional to the ratio of the precession frequency and the hopping rate. Intuitively, the more often the muon jumps between different sites (and therefore less time it spends at each site), the slower the muon precess around the local field, the smaller will be the change of the muon polarization during its stay at each site. Since the field distribution at each site is assumed to be random, the direction of the change in the muon orientation is also random, resulting in a random-walk like evolution of the muon polarization. A detailed analysis of this behavior based on the strong collision approximation (SCA) can be found in Uemura *et al.* [1999].

Meanwhile, we analyze the interplay between the width (distribution) and the temporal fluctuation of the local field. The random (temporal) fluctuation of the random (spatial) field tend to homogenize the field as the muon precesses. The theory of brownian motion says that with a constant speed, less frequent but larger step tends to reach further compared with frequent but smaller step motion within fixed time period. Mathematically, this is seen through the square-root dependence on the step number of the expectation value of the distance in a brownian motion. Physically, this reflects the inefficiency in the accumulation of total displacement in the random Brownian motion. In our case this means that, assuming a constant rate of change (product of step size and rate), the local field appears to be more stable with smaller step size (and larger fluctuating frequency). In other words, muon tends to relax faster in fields with less-frequent but large fluctuations than in fast-changing but small temporal fluctuations.

Following this analysis, we see that more frequent temporal fluctuation gives less cumulative change in the local field, and thus suppresses the effect of dephasing on muon spin relaxation. In fact, a more randomized field tends to have narrower width (e.g. from Lorentzian to Gaussian), and thus the relaxation becomes slower due to the narrowed frequency spectrum (according to the static field relaxation formula, Equation 2.5).

Therefore considering only the field distribution/with and the hopping, it turns out that faster temporal fluctuation of the field would (instead of stagnating as from the analysis with field strength and hopping rate) accelerates the relaxation of the muon. The seemingly contradictory conclusions from the above analyses can be resolved by realizing that (a) the damping due to finite width of the static field and that (b) the dephasing due to field fluctuation are both mechanisms that causes the relaxation of the muon spin. These mechanisms all act coincidentally upon the same local field and their effect need to be considered simultaneously rather than separately.

In general, we know that

- the dephasing process describes the effect of temporal fluctuation (due to thermal/quantum and/or other physical origins) of the local field on the relaxation of an individual muon spin.

- the damping process is due to the spatially/frequency averaging of the relaxation of all the muons within the sample.

Random fluctuation will, in addition to contributing to the dephasing process, randomizes the field distribution as the system evolves. As randomization means narrowing the width while yielding a more Gaussian distribution of the local field, which yields slower relaxation, the temporal fluctuation thus slows down the relaxation (via changing the field distribu-

tion). Thus for field distribution the temporal fluctuation process can be seen as a kind of thermalization of the initial distribution towards a gaussian distribution, with the temperature/thermalization rate being the rate of local field fluctuation.

Furthermore we notice that faster fluctuation, while rendering the dephaing process less efficient (as discussed previously), implies faster randomization of the field distribution. Thus for an initial field distribution,

- if it is close to the equilibrium gaussian distribution, then the effect of fluctuation will mostly be dephasing the spin dynamics, and

- if it is far away from the equilibrium distribution, then the temporal fluctuation affects the relaxation via both the dephasing process and affecting the damping process (through change the field distribution).

In reality since the system is always assumed to be in thermal equilibrium condition, the effect of temporal fluctuation on the field distribution can be minimal. This is somewhat different from the conclusions in Section 4.1 in Uemura *et al.* [1999]. Dephasing is usually much more efficient than damping (e.g. in MnSi Uemura *et al.* [1999]) and turn out to be the dominant contribution to the muon spin relaxation in dynamic field systems.

The muon relaxation function is the superposition of all muon dynamics. Since dephasing causes each individual muon to lose its phase in the dynamics, and that the damping of the integrated μSR signal depends critically on the coherence of the dynamics of all the muons (i.e. having approximately the same phase), dephasing will thus hamper the coherent damping process and slow down the muon relaxation. Following this analysis the reason that temporal fluctuation results in slower relaxation is randomizing, instead of the field, the

phase of the dynamite muon, or equivalently, hampering the coherence of the precession of the muons inside the sample.

The actual relaxation rate in the fast fluctuation limit turns out to be the ratio of the field width (damping efficiency) over the dephasing rate (dephasing efficiency), (see Equation 17 in Uemura *et al.* [1999]), which reflects the fact that the actual relaxation is a result of the competition of the damping and dephasing process. This is clearly reflected in the smear out of the characteristic behavior of the Kubo-Toyabe function in Figure 14 in Uemura *et al.* [1999], which is replaced by the exponential decay exemplifying the decoherence caused by fast fluctuation. In the slow fluctuation limit, the fluctuation of the longitudinal field, which produces the persistent 1/3 signal, causes the 1/3 signal to decay, and the decay rate is determined by the dephasing rate. Furthermore, since in the slow fluctuation case dephasing occurs essentially after the damping has saturated to its 1/3 limit, the initial characteristic behavior of the Kubo-Toyabe function is preserved.

When static and fluctuating local fields coexist, the relaxation function turns out to be the product of the relaxation functions at the presence of each field individually. As we assume that the static field and the fluctuating fields are highly decoupled from each other and respond to external field independently, the behavior of the total signal can be interpreted by analyzing the muon relaxation under each of these fields separately. A good example is the MnSi data discussed in Uemura *et al.* [1999].

Above we considered the interplay of the field strength and the field width, of the field strength (precession frequency) and the hopping rate, and of the field width and the hopping rate, respectively. A more detailed analysis is required to consider the interplay of all 3 factors and its effect on the muon relaxation.

According to the above discussion, the longitudinal field (LF) μSR measurement can be applied to address unique physical questions.

First of all, it can help to distinguish between static and dynamic internal field. Since the precession induced by the longitudinal field is usually orders of magnitude slower than the rate of the spin fluctuation, the muon dephasing process caused by spin fluctuation can remain unaffected by the LF. In contrast, in the case of static field where muon relaxation is caused by frequency superposition, a longitudinal field shifts the center of the field distribution to non-zero value and thus induces oscillatory behavior in the relaxation process. Thus in this case the muon spin relaxation can be quite sensitive to the LF. As mentioned in Uemura *et al.* [1999], the characteristics of the LF-dependence of the muon relaxation spectra can be used to distinguish between static and dynamic spin system.

Secondly, LF can be used to decouple the static and dynamic relaxations. It is known that the static internal field usually consists of the nuclear dipolar field, while the dynamic field is mainly contributed by the fluctuating electron spins. Since the static field can be aligned by a strong enough longitudinal field, and that the dynamic fluctuation of the field is largely independent of the LF, we can in principle suppress the relaxation due to static field by applying a large enough LF, and thus monitor the relaxation due solely to the fluctuating field caused by electrons. MnSi as an example is discussed in detail in Uemura *et al.* [1999].

Thirdly, LF μSR measurements are frequently used to characterize the field fluctuation around phase transition. In an itinerant magnetic system like MnSi, the ferromagnetic exchange interaction propagates within the sample via the itinerant electrons. As a result, the fluctuation of the local field is mainly a result of the thermal fluctuation of the electrons. Namely in this case the magnetic fluctuation is thermal fluctuation in nature, and thus can exhibit exotic behavior as the temperature across thermal phase transition T_c. In fact as

the system reach its transition point, the fluctuation of the itinerant electron slows down significantly (critical slowing down) due to the diverging electron-electron correlation length, namely the fluctuation of the local field is suppressed near thermal phase transition. This is manifested as the divergence of the muon spin relaxation rate for the case of MnSi, which implies spin freezing across the transition Uemura *et al.* [1999].

In contrast, in localized moment systems the magnetic field fluctuation is in nature the quantum fluctuation of the spins, and thus in principle should not depend on temperature for the general cases.

2.3 μSR studies of helical magnets

2.3.1 μSR studies of MnSi

As an itinerant weak-ferromagnet, MnSi has, since 1980s', been studies extensively in the μSR community for the study of itinerant ferromagnetism and spin fluctuation phenomena. As temperature drops below 30 K, MnSi enters a helimagnetic state with long and incommensurate helical modulation to the spins. As shown in Figure 2.3(a), μSR experiments at zero field detects the emergence of internal field at below the transition temperature. Figure 2.3(b) shows the $1/T_1$ as a function of temperature for MnSi. According to room temperature μSR results Hayano *et al.* [1980, 1978] the electron spin fluctuation remains very fast at room temperature, and the μSR $1/T_1$ relaxation process of the muon has a period longer than the detection capacity of the instrument. As the temperature goes down, the fluctuation of the spin and thus the local field begin to slow down, allowing for a more stable local field for the muon. The $1/T_1$ relaxation of the muon thus becomes more visi-
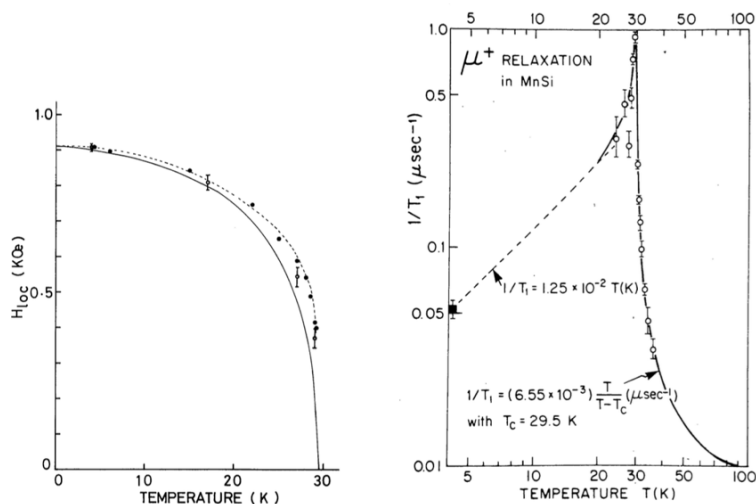
Figure 2.3: (a) (Left) Temperature dependence of the magnitude of the local magnetic field. (b) (Right) Observed μSR $1/T_1$ relaxation rate as a function of temperature. The solid curve is the best fit to the SCR theory. Figure taken from Takigawa *et al.* [1980]; Hayano *et al.* [1980].

ble. At temperatures around (and above) the magnetic phase transition, due to the critical slowing down of the spin fluctuation the internal field also slows down significantly, and thus the $1/T_1$ relaxation of the muon is much enhanced near the transition. Below the transition temperature, the $1/T_1$ relaxation rate drops quickly as temperature decreases. This is understood as due to the quick increase and stabilization of the local moment within the ordered phase.

From Figure 2.3 it is seen that the behavior of $1/T_1$ as a function of temperature can be well described by the self-consistent renormalization (SCR) theory Moriya [1985]. For weak ferromagnets, the SCR theory predicts that the $1/T_1$ follows

$$\frac{1}{T_1} \propto \frac{T}{T - T_c} \tag{2.8}$$

for temperatures above and close to the transition Moriya [1985]. For low temperatures deep inside the ordered phase, the SCR theory predicts that

$$\frac{1}{T_1} \propto T. \tag{2.9}$$

These predicted behaviors of $1/T_1$ over different temperature regimes has been observed from several independent μSR studies on MnSi Takigawa *et al.* [1980]; Hayano *et al.* [1978, 1980]; Kadono *et al.* [1990], and have thus established MnSi as an weak itinerant ferromagnet sufficiently described by the SCR theory.

Despite these consistent results from the earlier measurements, with much higher instrument resolution for μSR since 2000, exciting new physics has been revealed for the magnetic phase transitions in MnSi Gat-Malureanu *et al.* [2003]; Yaouanc *et al.* [2005]; Uemura *et al.* [2007]. Figures taken from Gat-Malureanu *et al.* [2003]. In a recent μSR study on MnSi Gat-Malureanu *et al.* [2003], with the aid of improved temperature resolution ($\pm$ 0.02 K), it is found that, although $1/T_1$ follows the predicted behavior of SCR theory up at temperatures well above and below the transition, for temperatures close to T_c it is found that $1/T_1$ follows

$$\frac{1}{T_1 T} \propto \frac{1}{(T - T_c)^2}, \tag{2.10}$$

which cannot be explained by the formal SCR theory. In fact it is found that as long as the enhanced interactions between the fluctuating helical modes at around the transition is properly taken into account Moriya [1985], the SCR theory is able to reproduce the $1/(T - T_c)^2$ behavior of $1/(T_1 T)$ as observed from μSR experiment. These findings are corroborated by following independent μSR studies (see e.g Yaouanc *et al.* [2005]). shed light upon the role of mode-mode interaction in such weak ferromagnets with helical modulation, which has been further established in subsequent studies using neutron scattering and other techniques Brazovskiĭ [1975]; Janoschek *et al.* [2013]; Bauer *et al.* [2013]; Schmalian and Turlakov [2004].
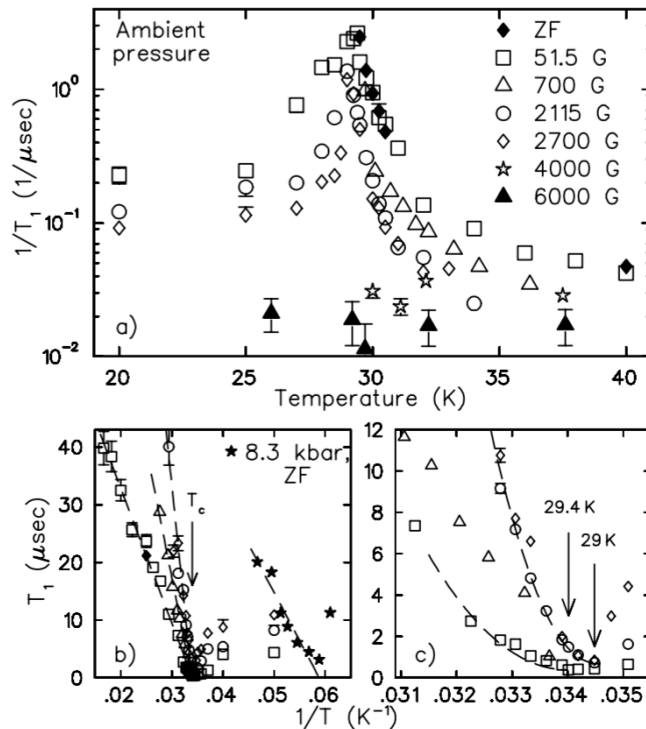
Figure 2.4: (a) Temperature dependence of $1/T_1$ relaxation rate in MnSi for longitudinal field $B_L = 0 - 6000$ G. (b) Plot of T_1 versus $1/T_1$ for MnSi at ambient pressure and under $p = 8.3$ kbar (star symbol). (c) T_1 versus $1/T_1$ at around $T_c = 29.5$ K, together with fits to $TT_1 \propto (T - T_c)^2$.

Recently there has been several µSR studies focusing on determining the details of the spin configuration and the local field in the ordered phase of MnSi Amato *et al.* [2014]; Lian and Uemura [2017]; Dalmas de Réotier *et al.* [2016, 2017].

2.3.2   µSR studies of MnGe

Due to practical difficulties in for example high pressure sample synthesis, µSR studies of MnGe started only in recent years Martin *et al.* [2016]; Yaouanc *et al.* [2017]. From
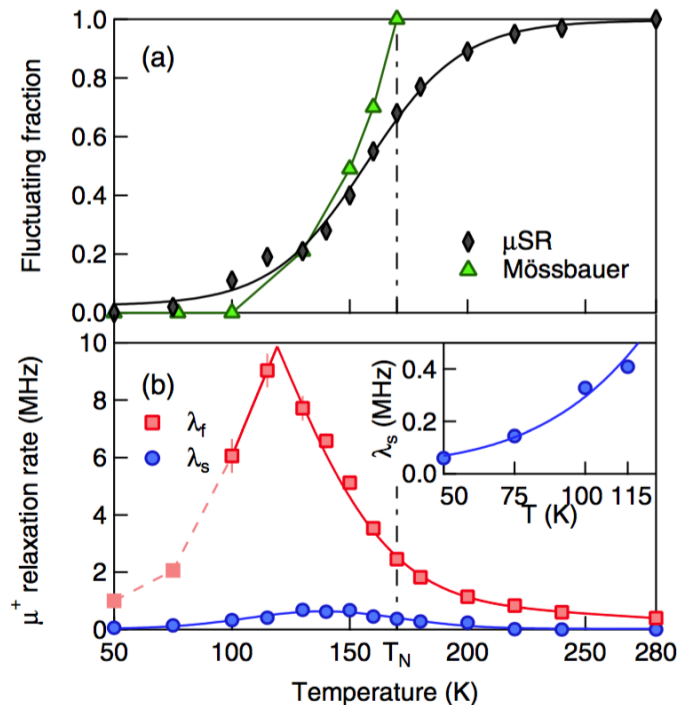
Figure 2.5: (a) Fluctuating phase fraction derived from a fit to the μSR spectra, in comparison with paramagnetic fraction from Mossbauer spectroscopy. (b) Relaxation rates obtained from the same fitting using fast and slowing relaxing components. Figure taken from Martin *et al.* [2016].

an experimental study by Martin *et al.* [2016], the $1/T_1$ relaxation rate in MnGe displays a seemingly sharp divergence at the magnetic phase transition in zero field as shown in Figure 2.5. Meanwhile, the large fluctuating fraction in the material quickly stablize below the Skyrmion transition T_c. The divergent behavior of $1/T_1$ is reminiscent of that observed in MnSi, and calls for further study and analysis using e.g. the SCR theory. The effect of external field on spin fluctuation and the $1/T_1$ relaxation rate is yet to be studied. On the other hand, there isn't enough data at the temperature range where crossover from the paramagnetic to ferromagnetic region occur. In this study the static local field distribution deep inside the Skyrmion phase was approximated by a shifted Overhauser Function Amato

(a) μSR spectra in zero field

(b) Internal field versus moment
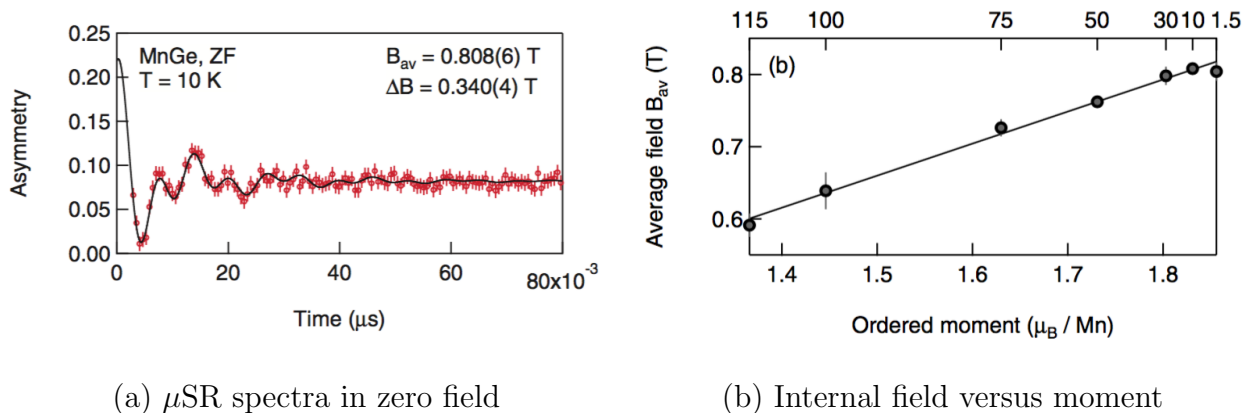
Figure 2.6: (a) Time-dependent μSR spectra of MnGe, measured at 10K in zero external field. The solid curve is a fit to the data based on a Overhauser field distribution. B_{av} and ΔB refers to the center and width of the field distribution. (b) Internal field versus Mn moment from neutron scattering. Figures taken from Martin *et al.* [2016].

et al. [2014] with sharp frequency cutoffs. Using lattice constant, Mn ion site and the helical wavelength obtained from neutron experiment, the shifted Overhauser field distribution was successfully reproduced by assuming a random phase factor associated with the position of the muon. The magnetic structure in the Skyrmion phase was studied in more detail in a separate μSR study Yaouanc *et al.* [2017], where the canonical helimagnetic structure was identified.

Alongside the existing μSR results, MnGe appear to be very different from MnSi in many aspects. These differences also serves as motivation to further the study of MnGe. For example, Figure 2.7 is a table that compares the basic properties of MnGe and MnSi. It is clear from the table that the helical pitch, static moment and transition temperature of MnGe is about 5 times larger than that of MnSi. If we assume that T_c is roughly proportional to the ferromagnetic interaction, J, then J_{MnGe} would also be 5 times larger than J_{MnSi}. As will be introduced later, the small angle neutron scattering result also shows possibility of

Property	MnGe	MnSi	Ratio
Helical Pitch (4K)	**2.3 nm^{-1}**	0.35 nm^{-1}	6.5
Static Moment (2K)	**2.2 μ_B**	0.4 μ_B	5.5
T_c (0 T)	**170 K**	30 K	5.6
$B_{\text{upper critical}}$ (2K)	**130 kG**	6.2 kG	20.9

Figure 2.7: Table with experimental parameters for MnGe and MnSi from various studies. Data taken from Martin *et al.* [2016]; Kanazawa *et al.* [2012]; Makarova *et al.* [2012]; Gat-Malureanu *et al.* [2003]; Seki and Mochizuki [2016]; Bauer *et al.* [2013]

a Hedgehog-like magnetic structure within the ordered phase Kanazawa *et al.* [2012], which is topologically distinct from the 2 dimensional Skyrmion in MnSi. These properties make MnGe attractive for investigations using various techniques including µSR.

Chapter 3

Muon Spin Relaxation Study of MnGe

Muon spin dynamic relaxation rate $1/T_1$ has been measured in longitudinal magnetic field up to 5 T for the Skyrmion material MnGe. We discovered strong dependence of $1/T_1$ on the applied longitudinal field, and the non-SCR behavior of the spin fluctuation ($TT_1 \propto (T - T_c)^2$) over large temperature range above T_c. The results were analyzed using the self-consistent renormalization (SCR) theory. Except for the low field regime, the behavior of MnGe generally agrees with SCR theory and is similar to that of MnSi. With increasing magnetic field, the Skyrmion transition possibly experiences a crossover from helical fluctuation-induced transition to a ferromagnetic fluctuation driven transition, with the ferromagnetic critical fluctuation being first enhanced and then suppressed by the field. Within the Skyrmion region, the relaxation rate follows $1/T_1 \propto T^2$, which suggests the two-magnon spin wave from localized moment as the dominant spin excitation at low temperature. On the other hand, no apparent critical behavior was observed in the boundary bewteen the paramagnetic

and the induced ferromagnetic regions. By combining our transverse field and longitudinal field μSR data, we found that the Z component of Mn to be static and the in-plane (X and Y) components of the moment to be fluctuating both in the paramagnetic and the induced ferromagnetic regions. The static Z moment in the induced ferromagnetic region is found to be homogeneous.

3.1 Introduction

Spin fluctuation effects in itinerant magnetic systems are usually associated with interesting physical phenomena. As one example, Manganese Silicide (MnSi) as an itinerant ferromagnet with strong spin fluctuations displays a rich phase diagram and has been extensively studied over decades with various technique. MnSi is known for hosting the 2-dimensional magnetic Skyrmion within a finite field-temperature pocket on the phase diagram Skyrme [1962]; Tonomura *et al.* [2012]; Mühlbauer *et al.* [2009]; Robler *et al.* [2006]; Bauer and Pfleiderer [2012]; Nagaosa and Tokura [2013]. In zero magnetic field, MnSi enters a helical magnetic state below the magnetic transition temperature $T_c = 29.5$K, with a helical pitch of 18 nm and static Mn moment of $0.4\mu_B$ at T = 0K Ishikawa *et al.* [1976]; Mühlbauer *et al.* [2009]. In particular, several studies show that this magnetic transition behaves weakly 1st order in zero field, possibly due to the strong interaction of the helical spin fluctuations, and becomes 2nd order as the helical fluctuations is suppressed by external magnetic field Schmalian and Turlakov [2004]; Janoschek *et al.* [2013]; Bauer *et al.* [2013]; Zhang *et al.* [2015].

The presence of strong spin fluctuations in MnSi and its sensitivity to external field have also been identified from muon spin relaxation (μSR) studies Kadono *et al.* [1990]; Hayano *et al.* [1980]; Gat-Malureanu *et al.* [2003]; Uemura *et al.* [2007]; Takigawa *et al.* [1980]. The

muon spin dynamic relaxation rate $(1/T_1)$ is known as an effective measure of the electronic spin fluctuations Uemura *et al.* [1999]. In the paramagnetic phase above T_c, as a result of the Curie-Weiss behavior of susceptibility, the $1/T_1$ relaxation rate follows $T/(T - T_c)$, which is in good agreement with the prediction of the self-consistent renormalization (SCR) theory Moriya [1985]. On the other hand, behavior of $1/T_1$ is shown to be strongly modified by spin fluctuations within a small temperature range (the so-called fluctuating regime) above T_c, which exhibits signature of a fluctuation-driven 1st order transition, first introduced by Brazovskii in 1975 Brazovskiĭ [1975]. The temperature regime for this helical fluctuation regime is about 2K above T_c in zero field, which continuously reduces to zero with increasing external field up to 0.4 T Bauer *et al.* [2013].

More recently, another B20-type magnet, Manganese Germanium (MnGe), has gained popularity due to evidence of hosting a stable 3-dimensional Skyrmion phase with high T_c and Skyrmion density Tanigaki *et al.* [2015]; Kanazawa *et al.* [2016, 2012, 2011]; Deutsch *et al.* [2014]; Makarova *et al.* [2012]. At temperatures below 170 K in zero field, a magnetic lattice composed of alternating magnetic monopole and anti-monopoles has been identified in MnGe from transmission electron microscopy and topological hall effect Tanigaki *et al.* [2015]; Kanazawa *et al.* [2011]. Compared with the 2D Skyrmion in MnSi, the much smaller pitch (3nm vs 18 nm) and higher T_c (170 K vs 30 K) of the 3D monopole lattice indicate a much stronger ferromagnetic exchange interaction, Dzyaloshinskii-Moriya (DM) as well as spin-orbit interactions in MnGe Makarova *et al.* [2012]. In particular, recent neutron scattering Altynbaev *et al.* [2014], μSR Martin *et al.* [2016] and magnetization DiTusa *et al.* [2014] studies on MnGe have shown signatures of strong spin fluctuations over extended temperature range well above T_c, reminiscent of that in MnSi. Although the experimental results on MnGe are relatively limited (possibly due to difficulty in sample synthesis), the existing results suggest intimate correlation as well as fundamental differences between MnGe and

MnSi, and thus necessitates further study to understand the peculiarity of MnGe. In parallel with a previous μSR study on MnSi Gat-Malureanu *et al.* [2003], here we report the study of how external field influences the spin fluctuations and the static magnetism in MnGe.

We present the results of the muon spin dynamic relaxation rate $1/T_1$ in longitudinal magnetic fields up to 5 T and additional transverse field measurement on a polycrystalline sample of MnGe. Our key discoveries are as follows (a) strong dependence of $1/T_1$ on applied longitudinal field, (b) crossover from non-SCR to SCR behavior of $1/T_1$ over large temperature range above T_c as B_L increases, (c) T^2 dependence of $1/T_1$ at low temperature, indicating two-magnon spin-wave excitations of local moment, and that (d) in the induced ferromagnetic region, only the polarized Z component of the Mn moment is homogeneous and static under applied field, and the in-plane X-Y moment remains fluctuating. Our analysis also suggest similar nature of the induced ferromagnetic region and the paramagnetic region. The ZF and LF data were compared with the predictions from the SCR theory along with existing results on MnGe, and were discussed in parallel with existing results on MnSi. The $1/T_1$ and the transverse field results were combined in the discussion on the induced ferromagnetic region.

3.2 Experimental details

The polycrystalline samples of MnGe were synthesized under high pressure using methods introduced in Ref. Kanazawa *et al.* [2011], and were shaped into rectangles with a size of about 4 by 4 mm^2, suitable for μSR measurements. The μSR experiments were carried out at the M15 and M20 Channels of TRIUMF, Canada using the HiTime, Helios and the LAMPF spectrometers, together with the Pandora dilution refrigerator. A gas-flow

cryostat was used for all measurements, providing access to temperatures from 2K to 320 K with excellent stability ($\leq$0.03K). The μSR time spectra were analyzed using the software package μSRFIT Suter and Wojek [2012]. More details on the μSR time spectra and the fitting functions are to be presented along with the analysis.

3.3 Muon $1/T_1$ relaxation and dynamic magnetism

3.3.1 Temperature evolution of the $1/T_1$ relaxation in zero field

Figure 3.1 (b) shows the μSR spectra at five different temperatures in zero field (ZF). Pronounced $1/T_1$ dynamics was observed consistently for the measured temperature and field values. After time-binning, the fast oscillation, due to the large static Mn moment in the Skyrmion region, becomes a sharp dip and accounts for the loss of initial asymmetry in the early times. It is clear that as temperature goes down, the $1/T_1$ rate experience a maximum at around the Skyrmion transition temperature T_c. This peaking behavior of the muon $1/T_1$ relaxation rate is a result of the critical spin fluctuation in the system, and is observed for all the field values measured.

Figure 3.2 and Figure 3.3 (b) shows the asymmetry, $1/T_1$ relaxation rate and the internal magnetic field $\mu_0 H$ from the fitting of the above ZF μSR spectra. In specific, the zero field μSR spectra were analyzed using an exponential function with a single damping rate. In the Skyrmion region, the spectra were analyzed using the relaxation function corresponding to an incommensurate magnetic field distribution, similar to previous works Amato *et al.* [2014]; Martin *et al.* [2016]:

$$P(t) = \frac{2}{3} J_0(\gamma_\mu \Delta B t) \cos\left(\gamma_\mu B_{\mathrm{av}} t + \phi\right) e^{-\lambda_a t} + \frac{1}{3} e^{-\lambda_b t}, \qquad (3.1)$$
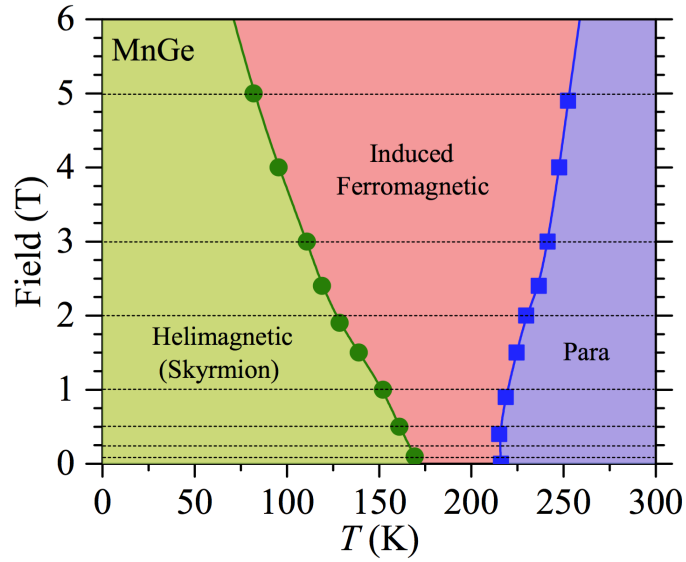
(a) Phase diagram
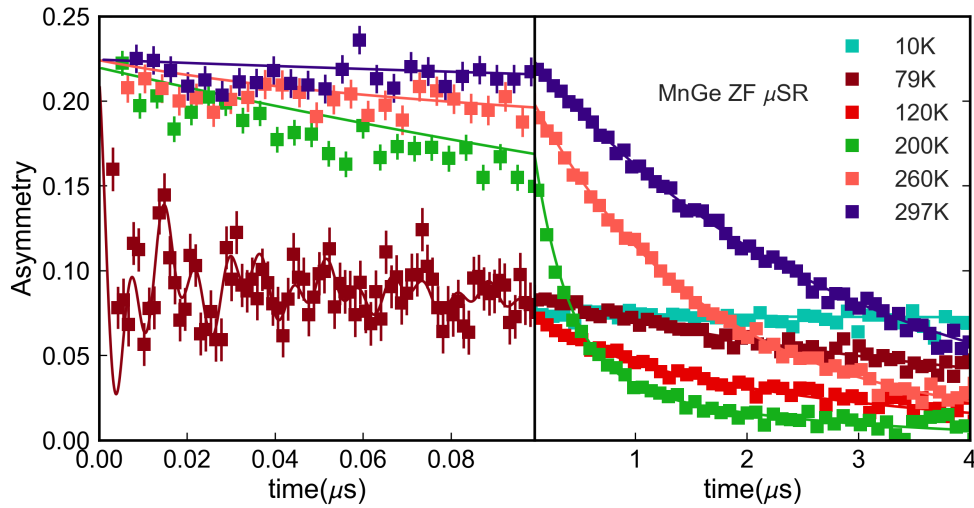
(b) Spectra

Figure 3.1: (a) Field-temperature phase diagram of MnGe up to 6T, derived from dc magnetization measurement by Dr. Kanazawa from the University of Tokyo. The dashed lines indicate the field values measured in this study. (b) Zero field muon spin relaxation spectra at different temperatures plotted in separate time range of 0 - $0.1\mu S$ and 0.1 - $4\mu S$.
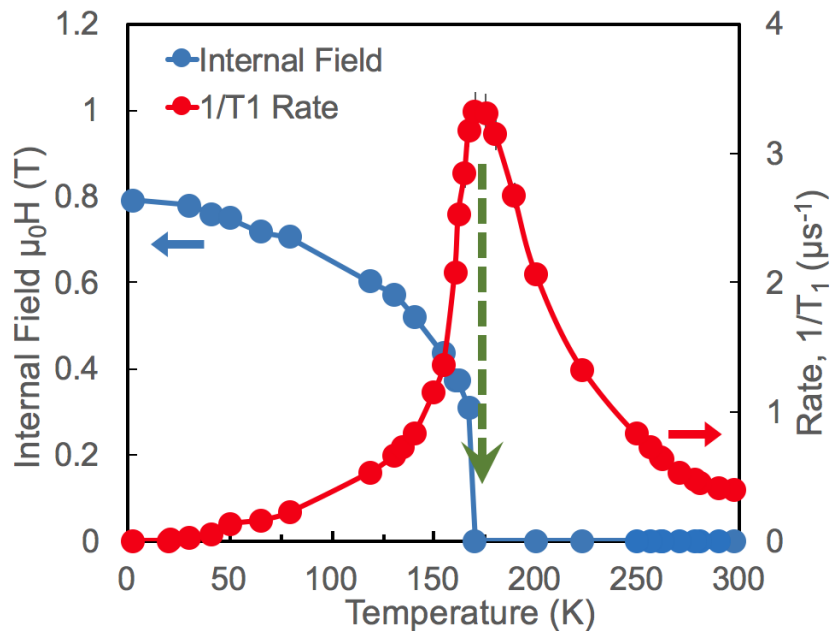
Figure 3.2: Temperature dependence of the $1/T_1$ relaxation rate and the internal magnetic field $\mu_0 H$ for MnGe, determined from the zero-field μSR experiments. The dashed arrow (green) marks the transition temperature T_c to the helical state. The solid lines are the guides to the eyes. The size of the error bars for most temperature points are either comparable or smaller than that of the dots, and therefore is not obviously seen in the plot.

where J_0 is a Bessel function of the first kind, ϕ is a phase term. ΔB and B_{av} are the average and the width of the internal magnetic field at the muon site. They are defined through the upper and lower cutoffs of the field distribution, B_{max} and B_{min}: $B_{\mathrm{av}} = (B_{\mathrm{max}} + B_{\mathrm{min}})/2$, $\Delta B = (B_{\mathrm{max}} - B_{\mathrm{min}})/2$. γ_μ is the muon gyromagnetic ratio. The finite width of the field comes from the incommensurability of the helical spin order with the lattice period. As has been analyzed in previous studies Amato *et al.* [2014]; Martin *et al.* [2016], the distribution of the internal field in the Skyrmion region can be approximated by a shifted Overhauser funtion:

$$D(B) = \frac{1}{\pi} \frac{1}{\sqrt{(B_{\mathrm{max}} - B)(B - B_{\mathrm{min}})}}. \tag{3.2}$$
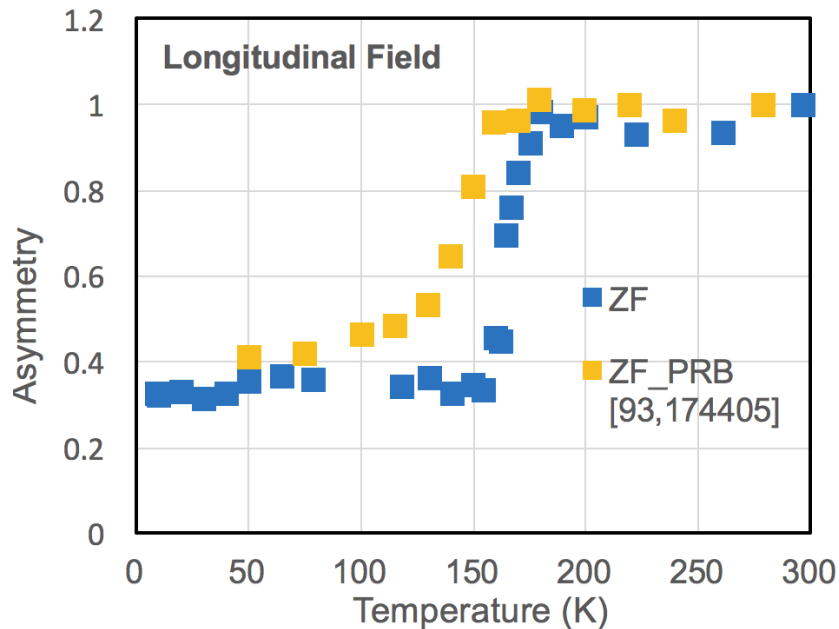
Figure 3.3: Temperature dependence of the initial asymmetry for MnGe, determined from the zero-field μSR experiments. The data were plotted in parallel with the result from a published study by DiTusa *et al.* [2014].

As shown from the plot, the asymmetry in our data displays a sharp dip across the Skyrmion phase transition. The drop of the initial asymmetry as temperature goes down below the Skyrmion transition temperature turns out to be much sharper than that from the other μSR study of MnGe by Martin *et al.* [2016]. Our result thus demonstrates higher T_c and the quality of our sample as compared with that used in Martin *et al.* [2016]. The temperature dependence of the internal field is similar to that found in MnSi Takigawa *et al.* [1980]; Kadono *et al.* [1990], with a sharp rise at $T_c \approx 170$K. $1/T_1$ exhibits a sharp reduction coincidental with the rise in the internal field. The T_c identified here is in good agreement with the Skyrmion transition temperature measured from dc susceptibility on MnGe. Furthermore, the value of T_c is either close to or higher than those reported from previous studies Martin *et al.* [2016]; Altynbaev *et al.* [2014]; DiTusa *et al.* [2014], again pointing to the high qual-

ity of our sample. The increase of $1/T_1$ relaxation rate as temperature approach T_c from above is due to the critical slowing-down of the spin fluctuations and the development of longer spatial correlation of such fluctuation. The decrease in $1/T_1$ below T_c indicate the transformation of the dynamic spin correlations into static long-range order. In particular, no apparent critical behavior was seen around 270K, where the dynamic magnetization data from exhibit a sharp jump DiTusa *et al.* [2014]. The absence of critical behavior around this temperature is also confirmed from the $1/T_1$ data in small and big longitudinal fields, as will be presented below. At temperatures above but very close to T_c, the peaking behavior of $1/T_1$ slows down and shows a saturated plateau behavior instead of a sharp peaking. Over large temperature range above T_c, the $1/T_1$ data in zero field results in a $(T - T_c)^2$ behavior of $T_1 T$, which is different from the prediction of SCR theory ($T_1 T \sim (T - T_c)$). This will be analyzed and discussed with longitudinal field data.

The observed deviation from ferromagnetic SCR theory for $T \lesssim T_c$ might be understood from similar μSR studies on MnSi. As analyzed in Ref. Takigawa *et al.* [1980], according to SCR theory the helical spin fluctuations within a small region around the magnetic vector Q becomes the dominant spin fluctuation near T_c. In particular, these helical fluctuations are more anti-ferromagnetic-like when the correlation length is larger than a few helical pitch, which is realized at $T \sim T_c$. Therefore, at temperatures close to T_c, MnSi is expected to be described better with SCR theory for antiferromagnet (instead of ferromagnet) Moriya [1985]; Moriya and Kawabata [1973].

For the case of MnGe, due to stronger DM exchange interaction, the helical spin fluctuations are expected to have shorter spatial period compared with MnSi, and is therefore more antiferromagnetic-like rather than ferromagnetic. This could render the system at $T \sim T_c$ to behave as an itinerant antiferromagnet instead of ferromagnet. Meanwhile, magnetic

susceptibility measurements show that MnGe displays a broad antiferromagnetic peak at the Skyrmion transition Kanazawa *et al.* [2011]; Viennois *et al.* [2015]. Thus the effect of the strong helical spin fluctuations observed in MnSi at $T \lessapprox T_c$, which is considered to be responsible for the deviation from the ferromagnetic SCR behavior Takigawa *et al.* [1980], could also be expected in MnGe. This could be one possibly explanation for the observed deviation between T/H^2 and $1/T_1$ around T_c.

On the other hand, we note that the systematic deviation of $1/T_1$ at lower temperature $(T \ll T_c)$ from SCR theory is present in all the field values we measured. The quadratic temperature dependence of T_1 observed here is qualitatively different from the SCR behavior of either ferromagnet or antiferromagnet, and requires understanding beyond the SCR scheme. These low temperature $1/T_1$ data will be presented later in Figure 3.9 (a) and discussed in detail. Meanwhile, from Figure 3.2 it is seen that $1/T_1$ exhibit a smooth plateau, instead of a sharp peak, at temperatures immediately around T_c. This smooth hump in $1/T_1$ suggests the suppression of ferromagnetic critical behavior. This behavior of $1/T_1$ is also accompanied by the sharp rise in the internal field at T_c, as seen in Figure 3.2, and will be analyzed in the following with finite field data in Figure 3.4.

3.3.2 $1/T_1$ relaxation in longitudinal fields

To study how external magnetic field influences the spin fluctuations in MnGe, we measured the temperature dependence of $1/T_1$ in external longitudinal fields up to B_L=5T. The results are presented in Figure 3.4. Here the sharp drop of the initial asymmetry as the system enters the Skyrmion region from the induced ferromagnetic region is due to the transformation of the fluctuating longitudinal moment into the static transverse moment in the ordered phase. As the longitudinal field increases, the static longitudinal moment is enhanced and the static
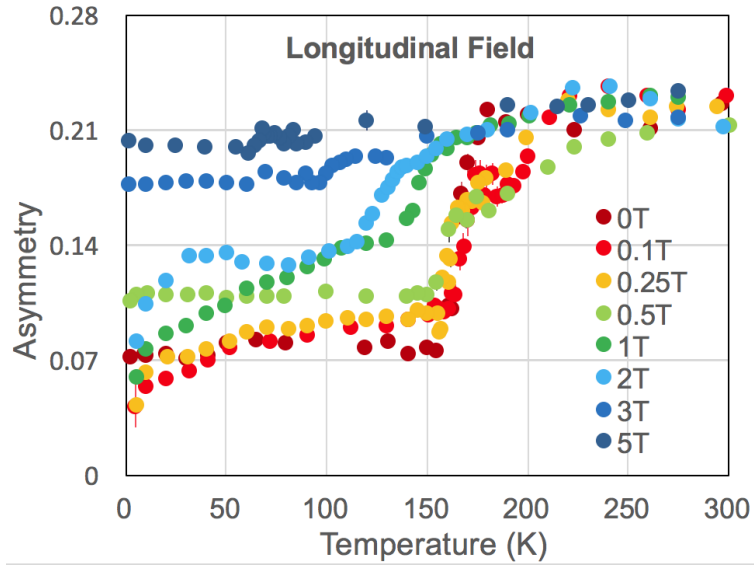
(a) Initial asymmetry
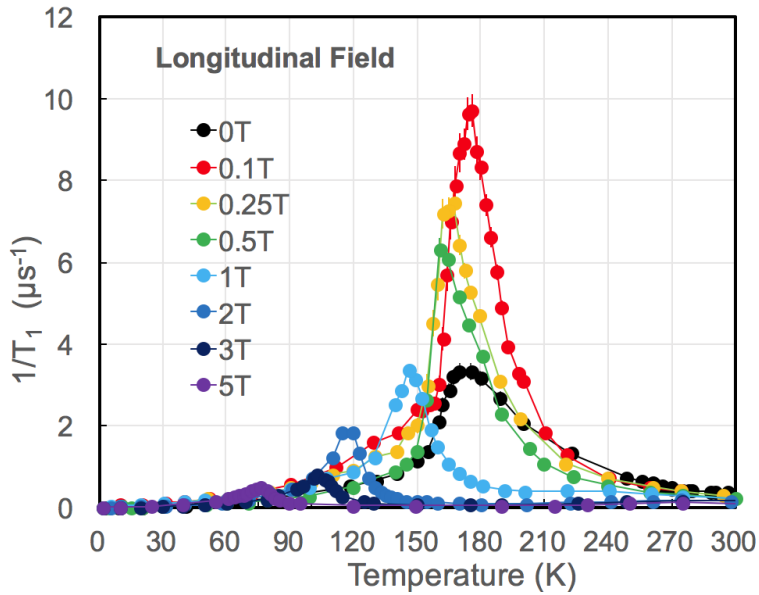
(b) Relaxation rate

Figure 3.4: (a) Temperature dependence of the initial asymmetry for MnGe in different longitudinal fields B_L up to 5 T. (b) Temperature dependence of the $1/T_1$ dynamic relaxation rate in different longitudinal fields B_L up to 5 T.

transverse moment reduced, therefore the difference of the initial asymmetry before and after the Skyrmion transition becomes smaller and smaller. The rise of $1/T_1$ as temperature approach T_c from above reflects the emergence of correlation between the randomly fluctuating spins which then becomes dynamic correlations with increasing correlation length near the Skyrmion phase transition. This is associated with the critical slowing-down of the fluctuation. Meanwhile, the shape of the peak in both $1/T_1$ and susceptibility transforms from right-skewed to left-skewed as B_L increases above 1T. The presence of a sharp peak at T_c is an indication of divergence of magnetic correlation time. As the applied field increases from zero to 5T, except for a board hump with $1/T_1$ values generally much smaller than the value near T_c, no apparent signature was observed at the boundary between the paramagnetic and the ferromagnetic region. These observations are consistent with the phase diagram as shown in Figure 3.1, as well as with our transverse field data as will be presented below.

For all the eight fields we measured, the magnetic transition is marked with a clear peaking in $1/T_1$, and T_c as a function of field, and the result is in good agreement with the dynamic susceptibility data measured by DiTusa *et al.* [2014]. In particular, the temperature dependence of $1/T_1$ from our μSR measurement and that of the susceptibility χ measured in DiTusa *et al.* [2014]show very similar trend over the measured temperature and field range, especially around T_c. For example, both $1/T_1$ and χ displays a smooth hump in 0 T but a sharp, asymmetric peak in 1T. According to SCR theory, the relaxation rate $1/T_1$ and magnetic susceptibility χ are expected to follow the relation of Moriya [1963, 1985]:

$$\frac{1}{T_1 T} \propto \chi. \tag{3.3}$$

The agreement of $1/T_1$ with the susceptibility data measured from DiTusa *et al.* [2014] implies good consistency of our results with existing measurements. This point will be revisited in more detail in a later section.

We noticed that the $1/T_1$ rate is significantly enhanced at around T_c as the field increases from 0T to 0.1T, and then starts to decrease as the field further increases beyond 0.1T up to 5T. This is seen clearly from Figure 3.6, where we plot T_c and the value of $1/T_1$ rate at T_c as a function of external field. The x axis was plotted on log scale to display the low field regime. The suppression of $1/T_1$ by strong applied fields (above 0.1T) is reminiscent of that observed in MnSi, and is probably due to the suppression of the long wave ($q = 0$) component of the spin fluctuations along the external field Gat-Malureanu *et al.* [2003]; Takigawa *et al.* [1980]. On the other hand, T_c starts to drop as the field increases above 0.1T. This could be due to the fact that at fixed temperature, in higher magnetic field the helical fluctuation becomes more less favorable than ferromagnetic fluctuation, and therefore lower temperature is required for the proliferation of helical fluctuation and thus the transition into the Skyrmion phase.

On the other hand, the smooth peaking in $1/T_1$ in zero field evolves into a sharp peak as the field increases to 0.1T. Such peaking remains sharp for fields up to 5T. This divergent behavior at the Skyrmion phase transition is also identified from ultrasound and magnetoresistance measurements on MnGe Kanazawa *et al.* [2011, 2016]. As will be discussed further below, this enhancement of critical behavior in low field might be related to the evolution from a (helical) fluctuation-driven Brazovskii transition to an ordinary phase transition driven by critical fluctuation. It is worth noting that although the Brazovskii phase transition is shown to be weakly 1st order, the temperature range above T_c where strong interactions between the helical fluctuations occur remains small, and therefore at temperatures not too close to T_c, regular critical behavior was also expected from the Brazovskii. Therefore it is expected that the peaking critical behavior of μSR $1/T_1$ data alone would be insufficient to determine the order of the phase transition (e.g. 1st or 2nd). On the other hand, the possible different nature was revealed in an later analysis of the behavior of T_1T, as will be shown in a later section.

The helical fluctuation-driven phase transition from the paramagnetic region to the helical region has been identified in MnSi from multiple neutron scattering Janoschek *et al.* [2013]; Pappas *et al.* [2016, 2017] and specific heat measurements Bauer *et al.* [2013]. It is understood as the result of the strong spin fluctuation in low fields Janoschek *et al.* [2013]; Schmalian and Turlakov [2004]. Without strong enough alignment from the external magnetic field, the fluctuating helical modes above T_c has no preference for orientation and thus occupies a large spherical area in the phase space. Furthermore, the interaction energy between these degenerate modes become huge as they populate at $T \sim T_c$. Thus a weakly 1st order transition becomes energetically more favorable as it avoids the large critical fluctuation and the associated energy increase. Applying a magnetic field is expected to fix the orientation of the helical fluctuations and thus brings the transition back to a 2nd order transition driven by ferromagnetic fluctuation Schmalian and Turlakov [2004].

3.3.2.1 Effect of high longitudinal field on $1/T_1$ dynamics

To further understand the effect of large longitudinal field ($B > 1$T) on the spin fluctuation, we plot the $1/T_1$ relaxation rate as a function of longitudinal field square for different normalized temperatures T/T_c in Figure 3.5. Here we choose the normalized temperature T/T_c in consideration of the different transition temperatures for different fields. With the same normalized temperature, it is expected that the level of thermal critical fluctuation, in some sense the effective temperature to the phase transition, is similar, and therefore the difference in the $1/T_1$ rate can be treated as due to external field.

It is clear from Figure 3.5 that the $1/T_1$ rate decreases linearly with increasing external field squared. This behavior, as mentioned above, has also been observed in MnSi, and therefore suggest that the behavior of $1/T_1$ might be explained by essentially the same model as
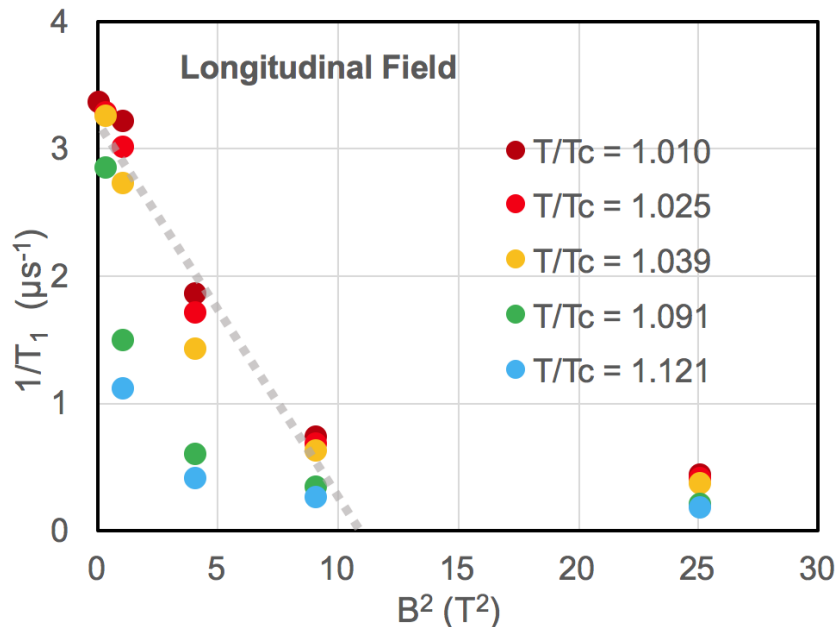
Figure 3.5: $1/T_1$ as function of longitudinal field square at different normalized temperatures T/T_c for high fields up to 5T. The normalized temperatures are chosen to be above but close to the helical transition (where $T/T_c = 1$).

proposed by Gat-Malureanu *et al.* [2003]. In specific, the muon dynamic relaxation comes from the fluctuating local field that is perpendicular to the muon initial polarization (the transverse component). Under an external field along the initial polarization of the muon, the fluctuating local moment and thus the fluctuating local field will be gradually stabilized and aligned with the field. The reduction of the fluctuating transverse field will thus slow down the $1/T_1$ relaxation as the field increases up to a threshold of $B_{\max}$. The transverse fluctuating component is nearly fully suppressed for $B > B_{\max}$.

In MnSi and MnGe, this perpendicular, or transverse, component of the fluctuating local moment comes from the strong helical fluctuation. Thus the the larger value of $B_{\max}$ also suggest stronger DM interaction in MnGe as compared with that of MnSi. This is consistent with other measurements on MnGe.
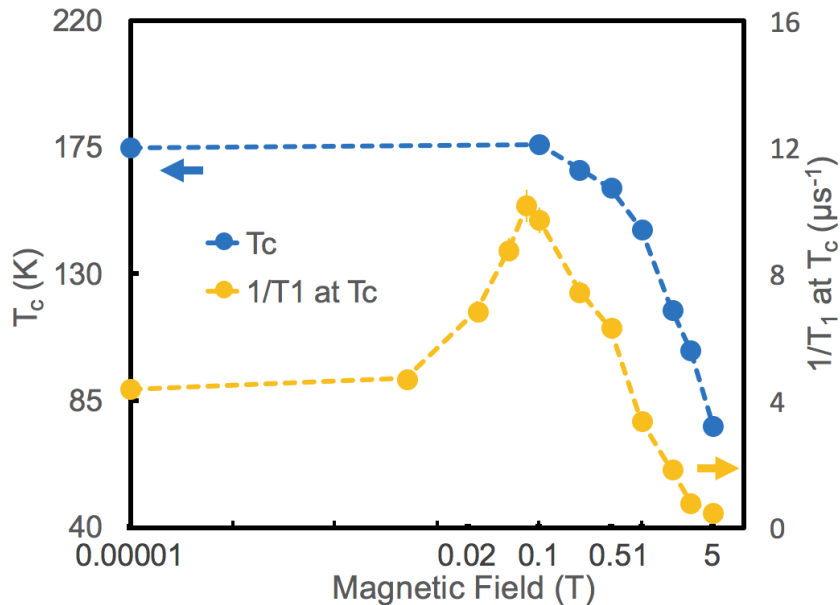
Figure 3.6: Skyrmion transition temperature T_c and the $1/T_1$ rate at T_c as a function of applied longitudinal field B_L. The x-axis (B_L) is plotted in logarithmic scale to display the variation in the low field regime.

3.3.2.2 Peculiarity of the low field regime

To further investigate the distinctiveness of the field regimes above and below 0.1T, we plot the transition temperature T_c and the $1/T_1$ relaxation rate at T_c as a function of external longitudinal field in Figure 3.6. It is clear that while T_c remains essentially unchanged for fields under 0.1T, the peaking value of $1/T_1$ first rises to a maximum at 0.1T, and then starts to drop at higher fields. Figure 3.6 clearly marks 0.1T as the boundary that separates the low field and high field regime in the phase diagram of MnGe. Meanwhile we noticed that from a magnetization measurement by DiTusa *et al.* [2014], the magnetization within the ordered phase is abruptly suppressed as the external field becomes greater than 0.1T. It is interesting to note that in MnSi, T_c also remained unchanged in the low field regime where the transition was shown to be 1st order, and then start to decrease at higher fields where the

transition becomes 2nd order Bauer *et al.* [2013]. On the other hand, to our knowledge the enhancement of $1/T_1$ in the low field regime as seen from Figure 3.4 and Figure 3.6 has not been observed in other Skyrmion materials like MnSi or Cu_2OSeO_3, where $1/T_1$ is found to be monotonically suppressed by external field Gat-Malureanu *et al.* [2003]; Lian and Uemura [2017]. In the following discussion we propose an understanding to the distinct behavior of MnGe in these two field regimes.

3.3.3   Analysis of the field dependence of the $1/T_1$ relaxation rate

The crossover from smooth plateau to sharp peaking in the temperature dependence of $1/T_1$ relaxation rate revealed the influence of the external magnetic field on spin fluctuations. Previous studies on MnSi suggest that magnetic field influences both the orientation and the magnitude of the helical spin fluctuation Grigoriev *et al.* [2006b,a]; Gat-Malureanu *et al.* [2003]; Janoschek *et al.* [2013]; Bauer *et al.* [2017]. Under relatively small magnetic field (e.g. 0.1T for MnGe, 0.13T for MnSi), while the magnitude of the fluctuation remains largely unaffected, the orientation of the fluctuating short-range helical magnetic correlation is much more sensitive to magnetic anisotropy and start to align with the field Schmalian and Turlakov [2004]. Thus a transition assisted by ferromagnetic fluctuation becomes more favorable compared with helical phase transition at the presence of magnetic field. This explains the rise of the sharp peaking of $1/T_1$ at T_c, as a signature of ferromagnetic SCR critical behavior, from the smooth hump in zero field as the field increases up to 0.1T. This picture is also supported by the temperature dependence of T_1T as presented in Figure 3.7, and will be explained in the following section. As the field increases beyond 0.1T, while the orientation of the fluctuating helical correlation remains fixed, the magnitude of the fluctuation will be gradually suppressed Gat-Malureanu *et al.* [2003]. Thus the value of $1/T_1$

around T_c decreases monotonically as the field further increases beyond 0.1T. The monotonic decrease of $1/T_1$ in high field is also expected from SCR theory Moriya [1985]; Kontani *et al.* [1976]: due to the suppression of the spin fluctuation by the applied magnetic field, the magnetic susceptibility χ follows $\chi \propto 1/(h/H + H^2)$, with h being the external field and H the internal field, and thus $1/T_1$ follows $1/T_1 \propto T/(h/H + H^2)$ and is reduced monotonically with increasing field h. Similarly, below the Skyrmion transition T_c, the suppression of $M(T)$ for $H \geq 0.1$T might be due to the stabilization of the fluctuating spin into antiferromagnetic-like helical order at higher fields.

For an itinerant ferromagnet, SCR theory concludes that at $T \gg T_c$, the uniform susceptibility follows the Curie-Weiss behavior $\chi \propto 1/(T - T_c)$, which results in $T_1 T \propto 1/\chi \propto (T - T_c)$. In the critical regime around T_c, due to the proliferation of the interacting helical spin fluctuations, the behavior of the susceptibility starts to deviate from the Curie-Weiss law and behaves as $\chi \propto 1/(T - T_c)^2$, and $T_1 T$ in this case behaves as $T_1 T \propto (T - T_c)^2$ (for details, see page 57 in Moriya [1985]). The non-Curie-Weiss behavior of the susceptibility comes from the Brazovskii renormalization of the Curie-Weiss susceptibility due to the interactions among the fluctuating helical modes, which becomes significant along with the proliferation of the magnetic fluctuation around T_c Moriya [1985]; Brazovskiĭ [1975]; Janoschek *et al.* [2013]; Yaouanc *et al.* [2005]. Thus the quadratic temperature dependence of $T_1 T$ indicates the presence of strong helical spin fluctuations and deviation from the mean field/SCR behavior. Correspondingly, this deviation also marks the crossover of a ferromagnetic fluctuation-assisted phase transition with diverging correlation length, to a helical fluctuation-assisted transition.

To further understand the effect of external field on the spin fluctuations in MnGe, we performed fitting to $T_1 T$ and analyze its temperature dependences in different fields. Figure 3.7
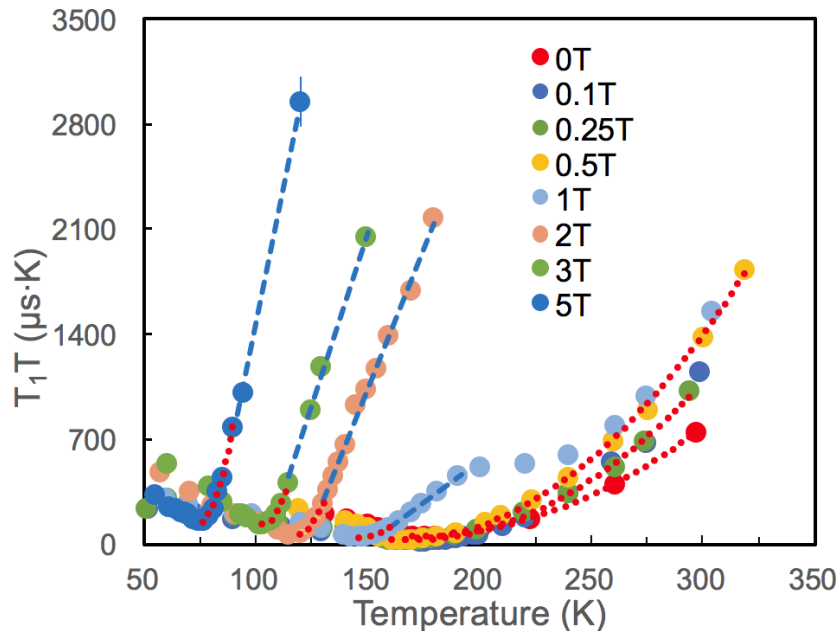
Figure 3.7: Temperature dependence of T_1T for different longitudinal fields. The dotted and the dashed lines are fits using quadratic ($y = ax^2 + bx + c$) and linear ($y = kx + b$) functions to show the corresponding temperature dependences of T_1T in the temperature range of $T \geq T_c$ in each fields.

shows the temperature dependence of T_1T in longitudinal magnetic fields. The dotted lines are fits to the quadratic regime of the data, and the dashed line for linear regime of the data. It is clear from the fits that for all measured field values, T_1T display quadratic behavior near T_c. In particular, while in high (0.5T to 5T) fields T_1T is quadratic in T only for temperature up to 20K above T_c, in low (0T to 0.5T) field T_1T remains quadratic for temperature extending to 150 K above T_c (nearly 300K). Thus in low field the behavior of T_1T in MnGe is in stark contrast with that of MnSi, where T_1T remains quadratic up to only 10 K above T_c Gat-Malureanu *et al.* [2003]; Kadono *et al.* [1990]; Yaouanc *et al.* [2005]. Interestingly, in a magnetic field of 1T, we see the evolution of the temperature dependence

of T_1T from quadratic to linear behavior as temperature cools down from room temperature to T_c.

The presence of strong magnetic spin fluctuation over extended temperature regime in MnGe is also identified from neutron scattering Altynbaev *et al.* [2014]; Deutsch *et al.* [2014] and ultrasound Kanazawa *et al.* [2016] experiment on MnGe. In other words, while MnSi deviates from SCR behavior only at $T \sim T_c$ due to critical helical fluctuation Takigawa *et al.* [1980]; Kadono *et al.* [1990], the effects of the helical fluctuations in MnGe can be much stronger and results in deviation of the system from SCR behavior even for temperatures well above T_c especially in fields below 1T.

One possible origin for the enhanced effect of helical spin fluctuations in MnGe is the stronger DM interaction with much shorter helical pitch in MnGe (3 nm) compared with that of MnSi (18 nm). First of all, the phase space and therefore density of state for the helical fluctuations is much larger with a larger Q vector, which comes from a shorter pitch length of the helix. This allows larger number of fluctuating helical modes to exist and interact with each other. On the other hand, with a smaller pitch the fluctuating helical modes can be formed with a shorter correlation length of the system, and thus can be realized at higher temperature. Thirdly, a shorter pitch can be attributed to stronger DM interaction, which also makes these fluctuating short range order more robust and difficult to align by field. According to these considerations, a much stronger helical fluctuations and interaction, extending to higher temperatures can be expected in a system with shorter helical pitch length. This is exactly what has been observed from our $1/T_1$ results of MnGe as compared with that of MnSi Gat-Malureanu *et al.* [2003]; Yaouanc *et al.* [2005]. Therefore, the presence of the interaction of strong helical spin fluctuations could be responsible for both (1) the deviation of the behavior of spin fluctuations from SCR theory at $T > T_c$, (2) the evolution of the

dominant spin fluctuation from helical to ferromagnetic as with increasing external field, and (3) the possible deviation from ferromagnetic SCR to anti-ferromagnetic SCR behavior at $T \lesssim T_c$. This argument applies to both MnGe and MnSi.

On the other hand, applying a strong magnetic field can significantly alter the nature of the spin fluctuation and the behavior of the system. A strong enough magnetic field (e.g. 1T for MnGe) can significantly suppress the transverse component of the spin fluctuations Gat-Malureanu *et al.* [2003]. As it is shown above that B_{max} in MnGe is about 15 times larger than that in MnS. If we assume that the field needed to generally suppress the transverse (helical) magnetic fluctuation in MnGe is also about 15 times that of MnSi Gat-Malureanu *et al.* [2003], which gives $0.07 \times 15 \approx 1T$. This value agrees with the analysis of $1/T_1$ as shown below.

A strong field could also change the helical fluctuation to a ferromagnetic-like spin fluctuation by fixing the direction of the spins. Meanwhile, it is known from SCR theory that the $q = 0$ ferromagnetic spin fluctuations play an important role at temperature above T_c, while at $T \sim T_c$ the helical fluctuations become dominant Takigawa *et al.* [1980]. With these, one can expect that under strong enough magnetic field the system recovers from a transition driven by helical fluctuation (weakly 1st order, non-SCR behavior), to a transition driven by ferromagnetic fluctuation both around and above at T_c (SCR behavior). Together with the field evolution of the temperature dependence of $1/T_1$ as shown in Figure 3.4, it becomes clear that the recovery of the ferromagnetic SCR behavior above T_c, i.e. the linear temperature dependence of $T_1 T$, coincides with the sharp critical behavior of $1/T_1$ at T_c. To further verify this, we notice that according to the SCR theory, the dynamic susceptibility should be proportional to the $1/T_1$ relaxation rate Moriya [1985]. We therefore compared our $1/T_1$ data with a known study of MnGe using dynamic susceptibility DiTusa *et al.* [2014]. It is
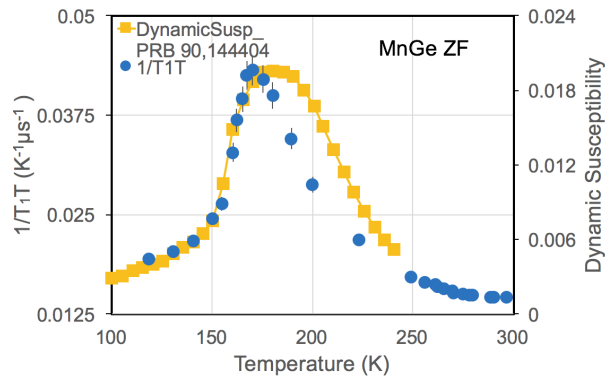
(a) Zero field
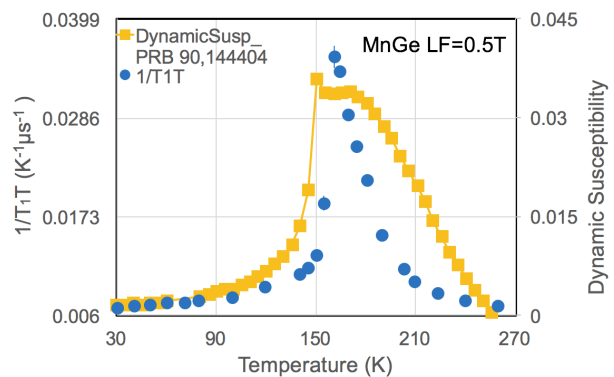
(b) 0.5T
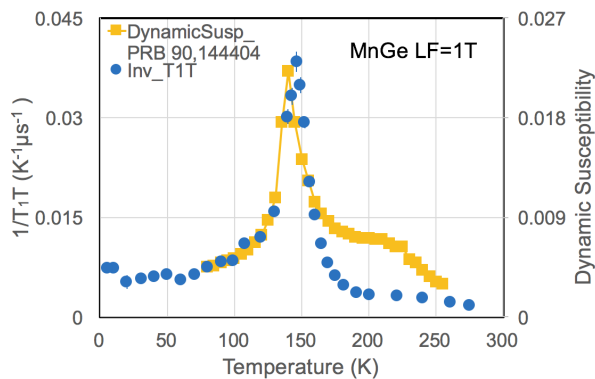
(c) 1T
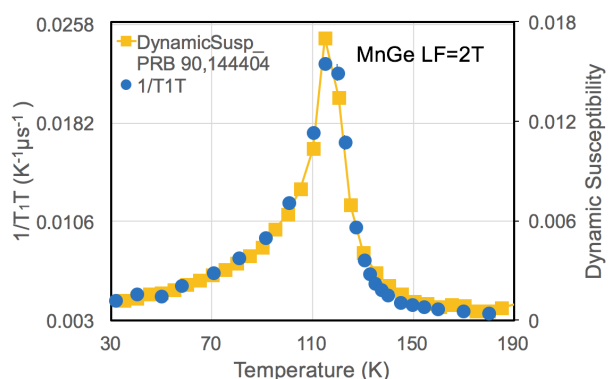
(d) 2T

Figure 3.8: Comparison of $1/T_1$ relaxation rate with dynamic susceptibility data in (a) zero (b) 0.5T (c) 1T and (d) 2T longitudinal magnetic fields. The upper and lower limits of the dynamic susceptibility data were chosen to show its overlapping with the $1/T_1$ data. The temperature axis is the same for all data sets. The dynamic susceptibility data were reproduced from a published study on MnGe by DiTusa *et al.* [2014].

clearly seen from Figure 3.8 in low fields (e.g. 0T and 0.5T) the $1/T_1$ rate deviates from the dynamic susceptibility around T_c, whereas in high fields they generally agree with each other. This is another strong evidence that the system deviates from SCR behavior in low fields, and recovers SCR behavior in high fields. It is noteworthy that in low fields, although don't follow closely with each other, the $1/T_1$ and dynamic susceptibility do exhibit similar temperature variation especially around T_c. For example in zero field, both $1/T_1$ and dynamic susceptibility exhibit smooth plateau around T_c, which could imply the missing of critical divergence.

The above analysis of $1/T_1$ shows clearly that in low fields the spin fluctuation in MnGe is dominated by strong helical fluctuations for temperatures above and around T_c, which likely results in a helical fluctuation-driven phase transition. Furthermore, as the helical spin fluctuations align and stabilize in high magnetic field, the system (although still dominated by helical, antiferromagnetic-like spin fluctuations at $T \sim T_c$) largely recovers the ferromagnetic SCR behavior and undergoes a transition with sharp critical fluctuation.

3.3.4 $1/T_1$ relaxation at low temperature

The temperature dependence of the muon spin $1/T_1$ relaxation rate at low temperatures ($T \ll T_c$) offers insight into the dominant type of spin excitations in the Skyrmion region. Figure 3.9 (a) shows $1/T_1$ as a function of T^2 down to 2 K. Clearly, $1/T_1$ exhibit T^2 behavior at $T \ll T_c$ for all the field values we measured. This is in sharp contrast with MnSi, where $1/T_1$ depends linearly on T in zero field, as confirmed from several μSR experiments Kadono *et al.* [1990]; Lian and Uemura [2017]; Yaouanc *et al.* [2005]; Takigawa *et al.* [1980].

From SCR theory of itinerant ferromagnet, one possible mechanism for the linear T dependence of $1/T_1$ below T_c is the spin flip excitations of an electron-hole pair near the Fermi
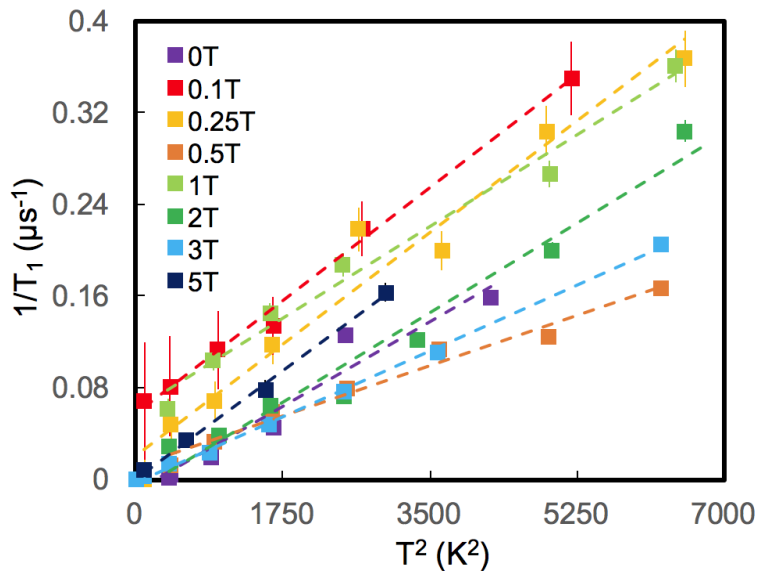
(a) MnGe
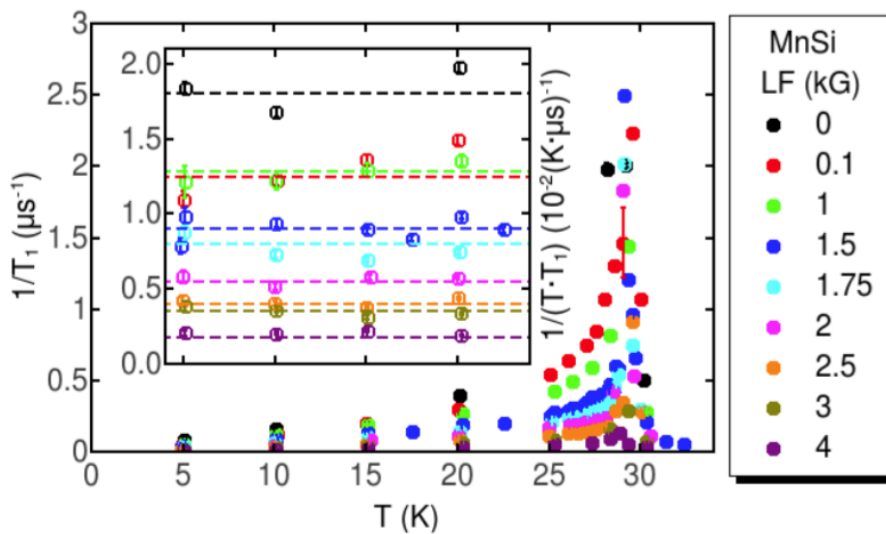
(b) MnSi

Figure 3.9: (a) $1/T_1$ dynamic relaxation rate of MnGe versus temperature square at low temperature ($T \ll T_c$) for different longitudinal fields up to 5T. The quadratic temperature dependence of $1/T_1$ is clearly seen in all the measured fields. (b) $1/T_1$ dynamic relaxation rate of MnSi versus temperature for different longitudinal fields. The inset shows $1/T_1 T$ versus temperature.

surface Lian and Uemura [2017]. In this case SCR theory predicts $1/T_1$ to be proportional to T/H^2, and thus $1/T_1 \propto T/H(T)^2 \propto T$ as the internal magnetization $H(T)$ saturates at low temperature, as is the case for MnSi Lian and Uemura [2017]; Yaouanc *et al.* [2005]; Moriya [1985]; Moriya and Ueda [1974]. On the other hand, under strong magnetic field the spin fluctuations are largely suppressed and the system becomes dominated by localized spins, entering a ferromagnetic-like state with static Mn moment Demishev *et al.* [2012]. Correspondingly, the spin-hole excitation reduces to spin wave excitation from local moments, which is well understood from the Heisenberg model Ishikawa *et al.* [1977]. Furthermore, in the ordered state of a Heisenberg ferromagnet, due to the presence of magnetic anisotropy which gaps out the spin-wave spectrum, the single-magnon excitation energy turns out much larger than the muon spin Zeeman energy associated with the muon spin flip process Lian and Uemura [2017]. In such case the two-magnon (Raman) process becomes the dominant contribution to the muon spin dynamic relaxation process, which gives the quadratic temperature dependence of the relaxation rate Dalmas de Réotier and Yaouanc [1995]; Beeman and Pincus [1968]; Yaouanc and Reotier [1991]; Mitchell [1957].

In addition, the strength of the magnetic anisotropy in MnGe can be estimated to be much larger than that in MnSi, which is in favor of the two-magnon excitation in the Skyrmion region. Here we use J for the ferromagnetic interaction, and D for the DM interaction. For both MnGe and MnSi, the magnetic anisotropy is mainly induced by the DM interaction, with spatial scale being the size of the Skyrmion, proportional to J/D. Considering that the saturation moment (1.9 μ_B) Altynbaev *et al.* [2014] and T_c (170K) of MnGe is approximately 5 times larger than that of MnSi (0.4 μ_B, T_c=29K), the strength of the ferromagnetic exchange J in MnGe is likely about 5 times stronger than that of MnSi. Meanwhile, since the size of the Skyrmion in MnGe (3 nm) is about 6 times larger than that of MnSi (18 nm), the DM interaction D in MnGe is estimated to be about 30 times stronger than that

of MnSi. Thus the magnetic anisotropy energy in MnGe, approximately D/J^2, can be of 180 times larger than that of MnSi. Appropriate were the above estimations, the low energy spin excitations, including 1 magnon processes, would be more severely suppressed in MnGe compared with MnSi. This is in favor of the 2-magnon process as the dominant contribution to spin excitation in the Skyrmion region in MnGe.

Therefore, our results suggest that in MnGe the spins freeze into localized moments at $T \ll T_c$ and the system behave as a Heisenberg ferromagnet in the Skyrmion region. This behavior is qualitatively different from that of MnSi, in which electron-hole pair excitation from the strong spin fluctuations remains dominant in zero field even at low temperature. These findings are also supported by recent experimental results. A neutron scattering experiments on MnGe Deutsch *et al.* [2014] shows that the magnetic state become nearly 100 percent magnetic at temperature below 100 K within the Skyrmion phase, indicating the stabilization of spin fluctuations into static local moments. Another experiment shows that the saturation moment of MnGe is much larger than that of MnSi Altynbaev *et al.* [2014]. Together, Figure 3.4 and Figure 3.9 (a) explains the evolution of the shape of the $1/T_1$ peak with increasing field, as seen in Figure 3.2: the reduction of the weight on the high temperature side of the peak reflects the evolution of $T_1 T$ from quadratic to linear (or, non-SCR to SCR) behavior, and the gain of the weight on the low temperature side is because of the T^2 behavior of $1/T_1$ in the Skyrmion region begins to dominate as T_c moves to lower temperature and the critical fluctuation further suppressed by the increasing magnetic field.

3.4 Muon transverse relaxation and static magnetism

3.4.1 Transverse field (TF) μSR spectra

Figure 3.10 shows the transverse field μSR spectra for 0.5 Tesla and 3 Tesla. The time axes were set differently for different fields to show the evolution of the initial dynamics with changing temperature in each fields, respectively. Above T_c, the relaxation rate is expected to increase with decreasing temperature due to the formation of field-induced static Z component of the Mn moment and the increase of the width of the static internal field at the muon site generated by these Mn moments. For example in both 0.5 T and 3 T, as the system enters the induced ferromagnetic phase from high temperature paramagnetic phase, the time spectra exhibit significant change in both relaxation rate and oscillation frequency. Meanwhile, we noticed that in the Skyrmion region the 0.5 T spectra exhibit an abrupt shift of frequency as well as an increase in the relaxation rate as temperature decreases below the Skyrmion transition, whereas in 3 T both the relaxation rate and oscillation frequency of the spectra changes smoothly. As analyzed below, the different behaviors in the spectra in 0.5 T and 3 T are due to their difference in the ratio of the width of the static internal field from Mn and the magnitude of the external field.

First of all, we define θ to be the angle between the static internal field and the applied field direction. In MnGe, due to the small but finite (static) internal field, the total static field, which equals the vector sum of the internal and the external field, is not completely parallel to the external field. With a relatively homogeneous external field, the total static field itself will also acquire the width equal to that of the internal field.

(a) 0.5T   (b) 3T early time   (c) 3T longer time
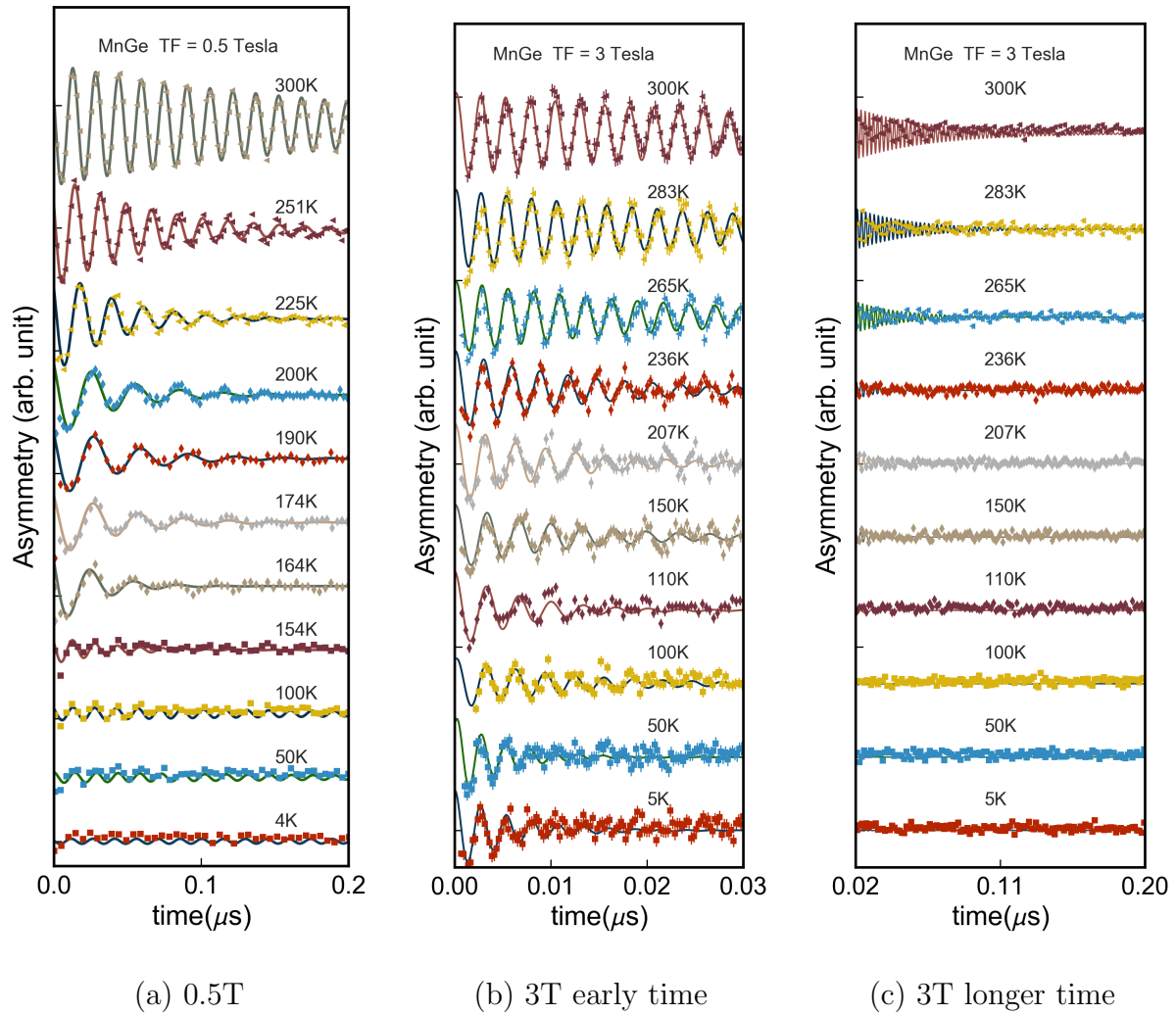
Figure 3.10: Transverse field μSR spectra in different temperatures, plotted for 0.5 T and 3 T. The spectra in the paramagnetic, induced ferromagnetic, and the Skyrmion phase are plotted with triangle, rhombus and square shape, respectively. The early time (0 - 0.03μS) and long time (0.02 - 0.2μS) dynamics were plotted separately with different binning of time in Figure (b) and (c).

In the ordered Skyrmion phase, especially in low external fields, since that the internal field distribution will largely remain unchanged by the external field and that the external field is small compared with the internal field, the internal field will remain dominant in the material. Considering the helical nature of the internal moment, the direction of the static moment from Mn as seen by the muons can be regarded as random. In such case, θ would be equal to 90 degrees. From the analysis of the zero field μSR data, the internal field strength in MnGe is about 0.5 Tesla (about 4 times that in MnSi Gat-Malureanu *et al.* [2003]). Thus as a rough estimation, the width of the internal field would also be on the order of 3-5 kilo Gauss (kG). For an external field of 5 kG, such width of the internal field is almost comparable with the magnitude of the averaged field. If we measure the uniformity of the field by the ratio of its width and magnitude, then the small uniformity of the field in the 0.5T case would cause the spectra to damp without apparent initial oscillation (which only comes from the precession of the muon in a relatively uniform internal field). Furthermore, with a width of 3 kG, we expect relaxation rate to be around 300 inverse microsecond, which will depolarize the transverse field signal within about 20-30 nano second.

Therefore since the 0.5 T transverse field spectra were fitted with a single component of damped oscillation with fitting time range up to 200 nano second, it is expected that the fast damping in the spectra cannot be picked up by the fit. In fact, the fit for the TF spectra in the Skyrmion region in 0.5 T only catches the small long-live component with the frequency set by the applied field, which possibly comes from the small fluctuating volume deep inside the Skyrmion region. In other words, the 0.5 T spectra shows almost no initial asymmetry in the Skyrmion region due to the large width of the total internal field compared with the field strength.

On the other hand, for the 3 T transverse field spectra, the external field of 3 T is significantly larger than the width of the internal field in the Skyrmion region (about 3-5 kG). Thus in the 3 T case the center frequency of the muon precession is much larger than the width of the frequency. This would result in a more uniformed precession of the muon around the center frequency of 3 T. Therefore we would expect clear oscillation to be seen in the 3 T spectra even in the Skyrmion region. In other words, the 3 T spectra exhibits clear oscillation due to the fact that the internal field in the Skyrmion region was heavily polarized by a much stronger external field and is thus more uniform.

3.4.2   Analysis of the TF μSR spectra

To get more insights into the field induced ferromagnetic phase of MnGe, in Figure 3.11 we present the analysis result for the relaxation rate and internal field shift in different transverse fields. The relaxation rate of the 0.5 T data drops down sharply as the system enters the Skyrmion region. As has been discussed above, this is due to the fact that the early time signal is not resolved because of fast depolarization of the muon spin induced by the strong inhomogeneous internal field. The relaxation rate of the 3 T data continues to rise as temperature decreases. Considering that the early time oscillation in the 3T data was well-fitted, this implies that the width of the internal field has been rising continuously as temperature goes down. On the other hand, for all the field values we measured, the field shift experiences a generally smooth transition as the system enters the induced ferromagnetic region from the paramagnetic region. This suggest that the induced ferromagnetic region and the paramagnetic state are potentially very similar in property, and is connected more likely via a smooth crossover rather than a sharp phase transition. This is further consolidated in the following analysis.
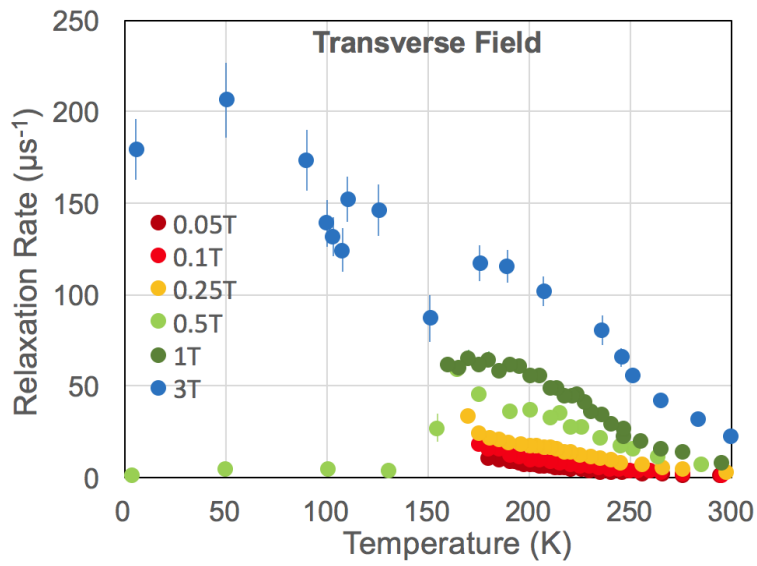
(a) Relaxation rate
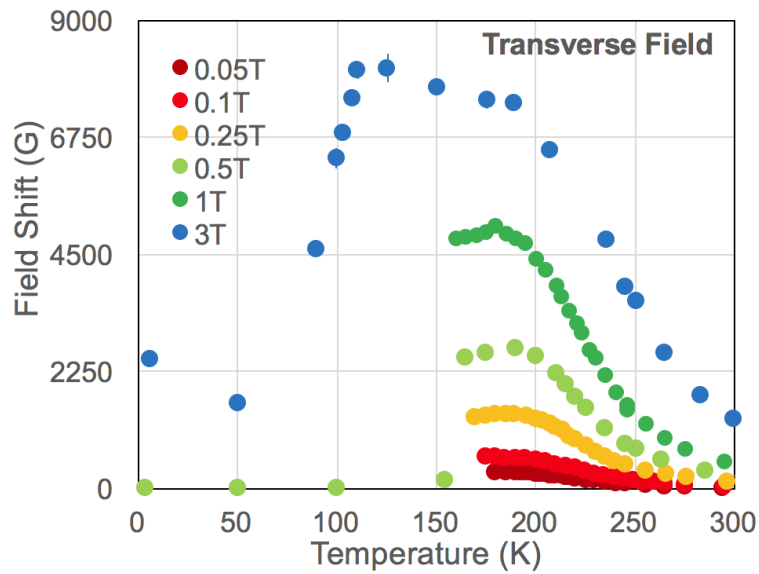
(b) Field shift

Figure 3.11: Temperature evolution of the relaxation rate (a) and internal field shift (b) of the transverse field μSR spectra in fields up to 3 T. The internal field shift is defined as the external field minus the detected field.
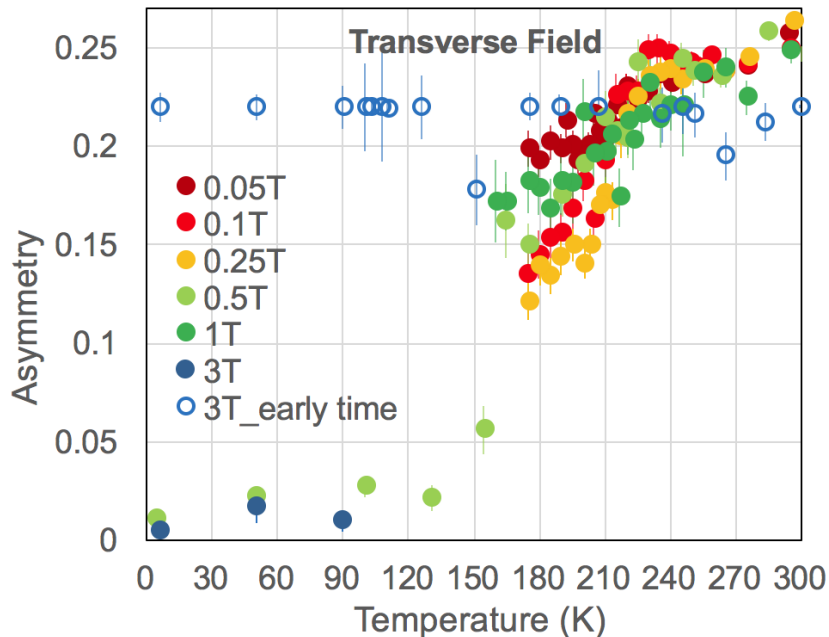
Figure 3.12: Temperature evolution of the initial asymmetry of the TF μSR spectra in different transverse fields up to 3 T. For the early time data (plotted in open circle) the upper limit of 0.22 were used in the fitting to avoid artifacts in data processing.

To further understand the difference between the induced ferromagnetic region and the paramagnetic state, we plot the temperature dependence of the initial asymmetry in different transverse fields in Figure 3.12. As has been analyzed in the discussion of the TF time spectra, the sharp drop of the asymmetry after the Skyrmion transition in 0.5T is a natural result of our choice for the fitting function. To show the difference, we plotted the fitting of the 3T data using only the early time (0 - 0.03 μS) spectra in open circle in Figure 3.12, which shows nearly constant initial asymmetry as plotted in the spectra. It is clear from Figure 3.12 that, especially in low fields of 0.1T and 0.25T, the asymmetry nearly remains constant in the paramagnetic phase, and starts to drop steadily as the system enters the induced ferromagnetic phase. This is possibly due to the build-up of the internal field in the induced ferromagnetic phase, as discussed below.
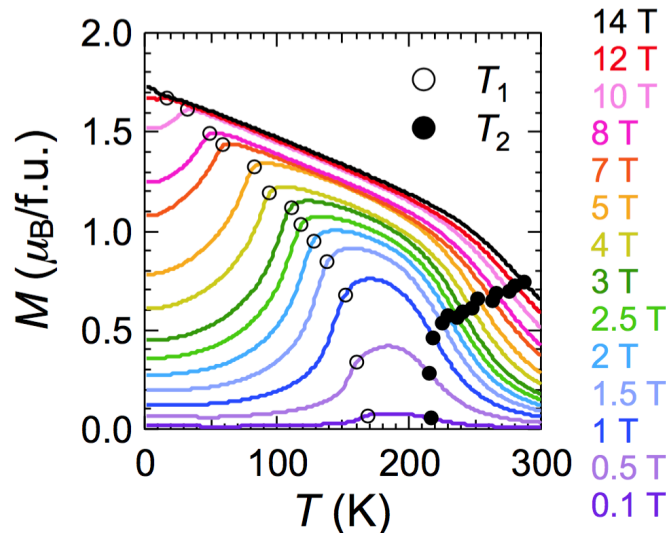
Figure 3.13: Temperature evolution of the magnetization in different transverse fields up to 3 T. The data was normalized to show average Mn moment per formula unit. Figure from Dr. Naoya Kanazawa (the Tokura lab) of Tokyo University.

The static field at the muon site is a vector sum of the internal field and the external (applied) field. In an absolutely non-magnetic state, the local field will be equivalent to the external field and is therefore perpendicular to the muon spin direction in a transverse field μSR experiment. In this case the muon precession would give the largest (full) asymmetry. On the other hand, as the system becomes magnetic, the local field will start to deviate from the external field, and that the angle between the muon spin and the local field is no longer 90 degrees. And this would result in the reduction of the muon precession asymmetry, which could be calculated using the angle between the muon polarization and the local field and with simple trigonometric relations. Therefore the reduction of the asymmetry in the induced phase could come from the build-up of the static magnetic field as the system enters the induced ferromagnetic phase.

In fact, as the magnetization data in Figure 3.13 show, under the same field, the magnetization (susceptibility) is significantly larger in the induced ferromagnetic phase than in the paramagnetic phase. The behavior of the magnetization could be understood as follows. As the temperature decrease and the system enters the induced ferromagnetic region from the paramagnetic region, the magnetic correlation length ξ of the system remains much smaller than the helical correlation length ξ_{DM}. Therefore the dominant correlation remains ferromagnetic within the paramagnetic region and the higher temperature part of the induced ferromagnetic region. Under the same external field the moment from ferromagnetic region is larger than that from the paramagnetic region due to larger correlation length in the latter.

Within the induced ferromagnetic region, as the temperature decreases the correlation length gradually becomes comparable with the helical correlation length ξ_{DM}. As noted in Janoschek *et al.* [2013], in such case the helical correlation come into existence and starts to compete with the ferromagnetic correlation. This possibly corresponds to the slowing-down in the increase of the magnetization as temperature decreases within the ferromagnetic region. The 1$^{\text{st}}$ derivative of the field shift shows peaking at the paramagnetic to induced ferromagnetic region transition, which also indicates the slowing-down of the increase of magnetization as temperature decreases. With further decreasing temperature the helical correlation gradually becomes comparable with the ferromagnetic correlation, and this could correspond to the saturation of the magnetization at temperatures close to the helical transition T_c. Eventually, the helical correlation wins over the ferromagnetic correlation and induces the transition from the induced ferromagnetic order into the helical order.

It is noteworthy that, as seen from Figure 3.13, the boundary of the paramagnetic and the induced ferromagnetic region remains nearly unchanged for fields below 1T, and starts to shift to higher temperature as the field increases beyond that. Meanwhile, as analyzed

previously, 1T is also the field value beyond which the transverse (helical) fluctuation of the system is suppressed. Therefore we suspect that in low field the helical fluctuation is preventing the formation of ferromagnetic moment in the induced ferromagnetic region. In high fields, the helical fluctuation was suppressed and thus the transition of the paramagnetic order into ferromagnet order becomes realizable at higher temperature as the field increases.

3.4.3   Magnetism in the induced ferromagnetic region

By comparing Figure 3.4.3 and Figure 3.4 it is apparent that in the induced ferromagnetic region the TF rate is much larger than the LF rate. This means that the muon spin transverse relaxation is mostly caused by the static field. As a consequence, the relaxation rate of the transverse field μSR spectra can be used as an estimation for the width of the static field. The fact that the TF relaxation rate is proportional to the static field width is discussed in detail in Appendix C.

The static field width is composed of the Z component along the external field direction and the X-Y component perpendicular to the field. On the other hand, magnetization gives a measure of the Z component of the static Mn moment. Meanwhile, we know that the width of the static field distribution is roughly proportional to the size of the static Mn moment. Therefore the relation between the TF relaxation rate and the magnetization could reveal important information about whether each component of the Mn moment is static or dynamic. In Figure 3.14 we plot the TF relaxation rate as a function of the Mn magnetization for different temperatures. The magnetization data were reproduced with permission from the Tokura lab in the University of Tokyo. It is clear that for the the selected temperatures, the relaxation rate is roughly proportional to the Z moment size measured from magnetization. In other words, the static internal field width goes up linearly with
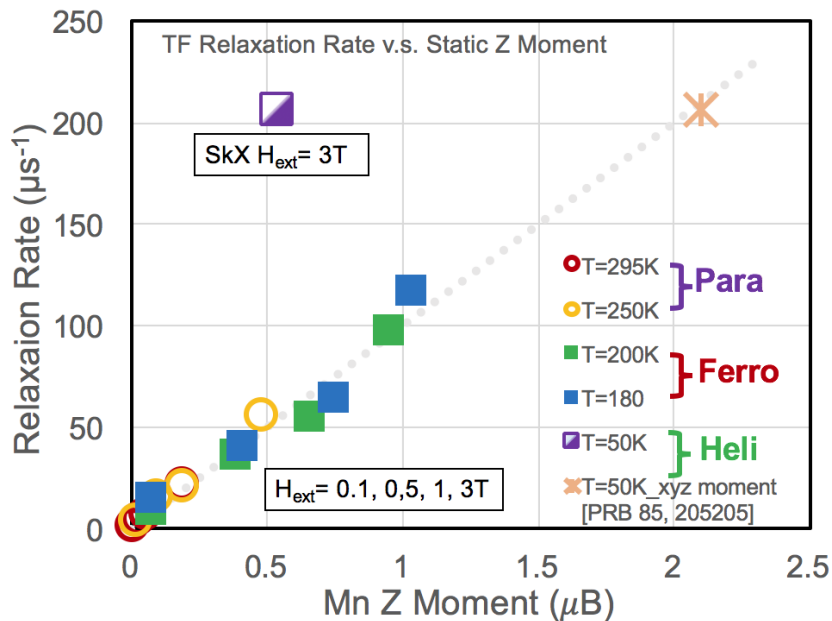
Figure 3.14: Transverse field μSR relaxation rate as a function of Mn moment measured from magnetization for different temperatures. Linear behavior is seen in both the paramagnetic and the induced ferromagnetic phase, suggesting that the static internal field is mainly contributed by the Z moment. Similar values for the slope suggest that the hyperfine coupling constant is similar in the two phases.

the static Z moment of Mn. The ratio between the moment and the relaxation rate (and thus the static field width) defines a form of hyperfine coupling constant. Meanwhile, it is obvious that in the paramagnetic phase, only the Z component is being polarized by the external field and is thus the only component that contributes to the internal field width. It is clear that the hyperfine coupling constant derived from Figure 3.14 is essentially the same for the induced ferromagnetic phase and the paramagnetic phase. This suggests that in the induced ferromagnetic phase, only the Z component of the Mn moment is being polarized by the external field, just as in the paramagnetic phase.

Correspondingly, we know that in the induced ferromagnetic phase the X-Y component of the Mn moment remain unpolarized and do not contribute to the static field width. Meanwhile, we recall that in our $1/T_1$ dynamic relaxation results the induced ferromagnetic region exhibit large spin fluctuation. These evidences suggest that while the Z moment is static, the X-Y component of the Mn moment is highly dynamic in the induced ferromagnetic phase, and is thus responsible for the muon $1/T_1$ dynamic relaxation.

To further verify this, we plot the TF rate versus moment at 50K within the Skyrmion phase. It is clear that the point has 3-4 times larger relaxation rate compared with the para or induced state with the same moment. This is because in the ordered Skyrmion phase, not only the Z component of the Mn moment but also the X-Y component of the Mn moment has become static and is all contributing to the muon TF relaxation. If we plot the same relaxation rate versus the full size (including X,Y and Z component) of the Mn moment obtained from a neutron scattering study Makarova *et al.* [2012], then the data point share the same slope as the high temperature phases. This further confirms that the X-Y components of the Mn moment in the induced ferromagnetic region is dynamically fluctuating and not contributing to the static field. The fact that the full moment data point also obeys on the linear relation with the same slope simply means that the coupling between the static internal field and the static Mn moment is similar for all the phases of the material, which is what we expected. With the above analysis, our data from Figure 3.14 shows clearly that the coupling strength (and possibly coupling mechanism) between the Mn moment and the local field could be similar for the induced ferromagnetic phase and the paramagnetic phase.

Meanwhile, the fact that the transverse relaxation spectra in the induced and the paramagnetic phase can be fitted with a single exponentially damped cosine function, as shown in

Figure 3.10, suggest that the internal field is highly uniform in the induced ferromagnetic phase, just as the paramagnetic phase (otherwise, the drastically different internal fields would cause the TF spectra to have 2 or more relaxation rates that can be seen in different time ranges). Therefore we see that the induced ferromagnetic phase and the paramagnetic phase could both have highly homogeneous and disordered internal field distribution, with similar coupling to the external field. This suggest that the two states have similar microscopic interaction between the spins. In this sense, they have very similar nature, with only the quantitative difference in that the Mn moment is larger in the induced ferromagnetic region, and therefore the same external field would result in larger moment polarization and internal field shift, as shown in the transverse data in Figure and in the magnetization data in Figure 3.13. Due to the similar nature of the two states, it is reasonable that the transition between the paramagnetic state and the induced state could be more of a smooth crossover than a sharp phase transition, as have been shown in the transverse relaxation rate and field shift data. This is further corroborated by the the temperature evolution of the asymmetry data in Figure 3.12. A continuous crossover/transition between the two regions is also allowed from a topological point of view since the two regions have the same winding number 0.

As a short remark, we note that the difference between a 'real' ferromagnetic state and the induced ferromagnetic magnetic state lies in several aspects. First of all, the regular ferromagnetic phase originates from the strong exchange coupling between the neighboring spins, and its formation was a result of the competition between the exchange coupling and the thermal fluctuation. The ferromagnetic state is thus a quantum state in which the wave functions of the neighboring spins are highly coherent with each other. Furthermore, the direction of the spins in the ferromagnetic state is largely determined by the configuration of the exchange interaction. The induced ferromagnetic region, on the other hand, can be

regarded as a 'polarized paramagnetic state' in which the fluctuating moment along the field direction was stabilized and aligned by the external field instead of the exchange interaction between them. Consequently, these stabilized component of the spins in the induced ferromagnetic region, although aligned with each other and appearing as a ferromagnetic state, remains (quantum-mechanically) incoherent. In other words, while the ferromagnetic state is characterized by long-range ferromagnetic order, the induced ferromagnetic state only contains short range ferromagnetic order. Therefore, while the paramagnetic state could be connected with the ferromagnetic state only through a statistical phase transition, it could evolve into the induced ferromagnetic region via a smooth crossover.

3.5 Comparison of MnGe and MnSi

In this chapter we compare the published results on MnSi and MnGe with our MnGe results. Specifically, the comparison of the published μSR result on MnSi with our result on MnGe shows striking similarity between the two materials.

3.5.1 Neutron scattering

Figure 3.15 shows the small angle neutron scattering results for MnSi and MnGe. The plotted momentum range is much smaller for MnSi compared with MnGe, and this indicate a longer helical pitch in MnSi. It is clear that critical helical fluctuation, as demonstrated by the scattering intensity at the Skyrmion pitch q vector, was present in both MnSi and MnGe. We note that since MnGe have much shorter helical pitch and thus much larger helical momentum vector, the scattering intensities around the center beam at temperatures above the transition is not necessarily ferromagnetic but helical-like fluctuations. These fluctuation
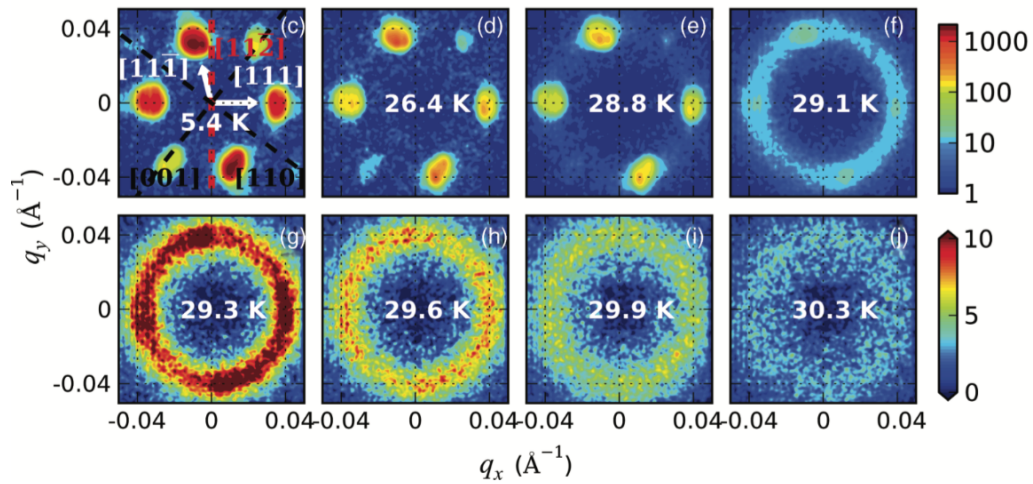
(a) MnSi
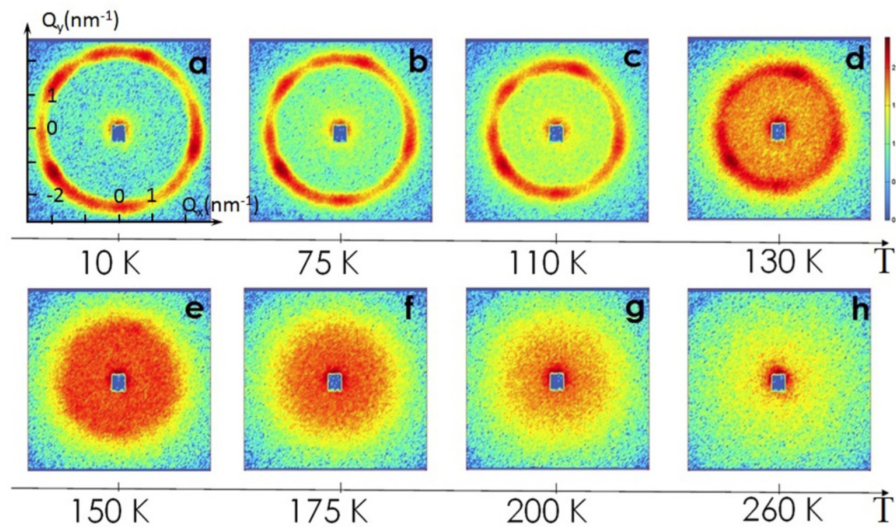
(b) MnGe

Figure 3.15: Temperature evolution of the small angle neutron scattering patterns of (a) single crystalline MnSi and (b) polycrystalline MnGe in zero magnetic field. Figures reproduced from Janoschek *et al.* [2013] and Kanazawa *et al.* [2012]. The q vectors for the scattering patterns of MnSi and MnGe were plotted on different scale.

above the helical transition is more ferromagnetic-like in MnSi as they have much smaller moment vector and thus much larger spatial scale.

3.5.2 Muon spin relaxation

Figure 3.16 compares the $1/T_1$ relaxation rate at low temperatures for MnGe and MnSi. While for MnSi the $1/T_1$ rate is generally linear in low temperatures and thus agrees with the prediction of the SCR theory, the $1/T_1$ rate of MnGe displays quadratic behavior in low temperatures.

Figure 3.17 plots T_1 versus inverse temperatures in different longitudinal fields for MnSi and MnGe. At temperatures close to the helical transition, T_1 in both MnSi and MnGe displays quadratic behavior $T_1 \sim 1/(T - T_c)^2$ and therefore deviates from the prediction of SCR theory which predicts that $T_1 \sim 1/(T - T_c)$. At temperatures much higher than the helical transition T_c, T_1 of MnSi recovers the SCR behavior of $T_1 \sim 1/(T - T_c)$. This indicates that in MnSi the helical fluctuation is dominant only as the critical fluctuation around the helical transition, and gives its place to ferromagnetic fluctuation at higher temperatures. On the other hand, at high temperatures, the non-SCR behavior of MnGe persists well above the helical transition up to 300K in low fields (<1T). It only recovers SCR behavior in high fields (>1T). This may be due to the stronger helical tendency induced by the stronger DM interaction in MnGe. Overall, these results agree with our analysis in the text.

Figure 3.18 plots $1/T_1$ rate versus T_c-normalized temperature $(T - T_c)/T_c$ for MnSi and MnGe. While SCR theory predicts the behavior of $1/T_1 \sim (T - T_c)/T_c$ for $T \geq T_c$, both MnGe and MnSi exhibit non-SCR behavior around the helical transition. At temperatures further above the helical transition T_c, MnSi starts to display SCR behavior as shown in
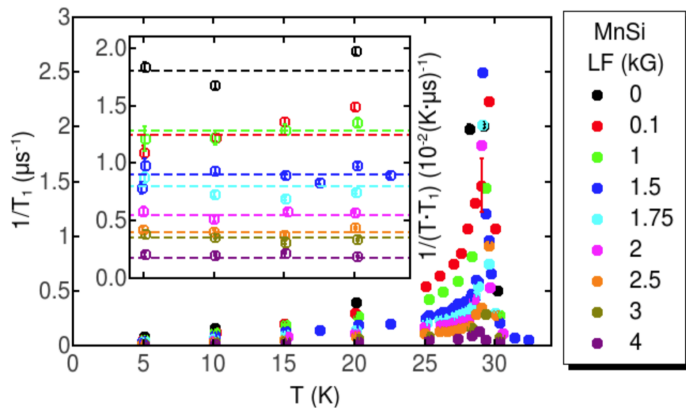
(a) MnSi
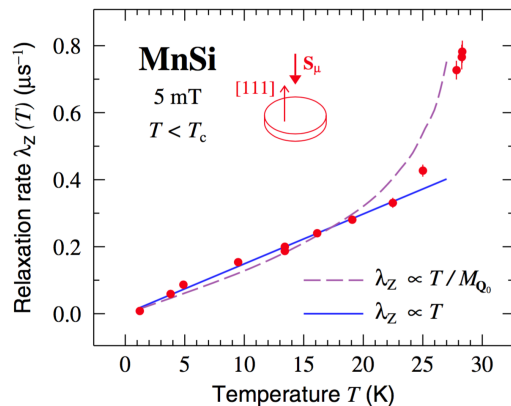
(b) MnSi
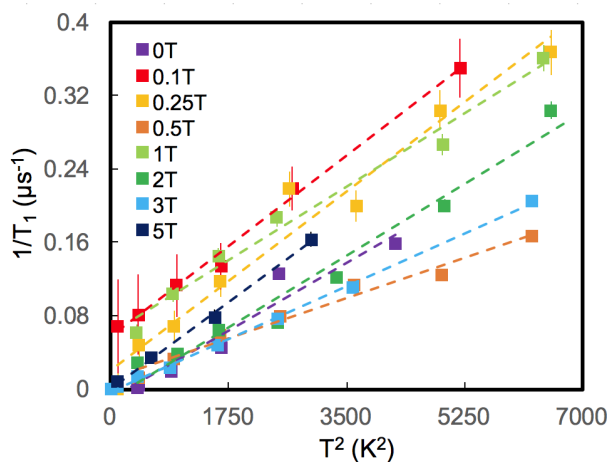
(c) MnGe

Figure 3.16: (a)$1/T_1$ rate of MnSi as function of temperature in different longitudinal fields. The inset shows linear behavior of $1/T_1$ rate as function of temperature at low temperatures within the Skyrmion phase. (b)$1/T_1$ rate of MnSi as function of temperature in longitudinal field of 5 mT. (c) $1/T_1$ rate of MnGe as function of temperature at low temperatures in different longitudinal fields. Figure (a) and (b) reproduced from Lian and Uemura [2017] and Yaouanc *et al.* [2005].
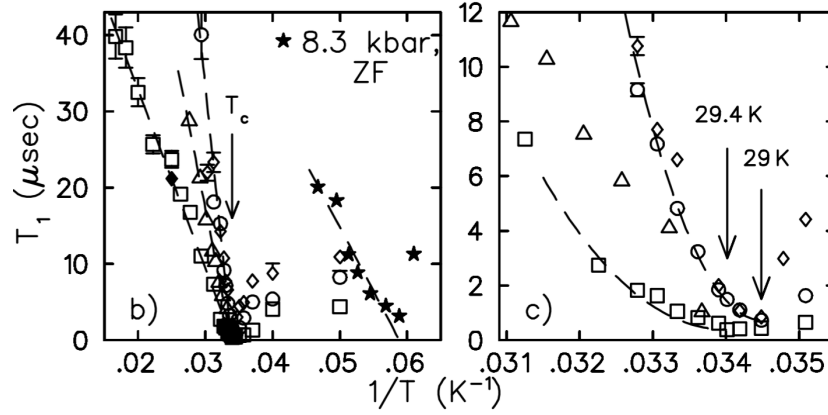
(a) MnSi
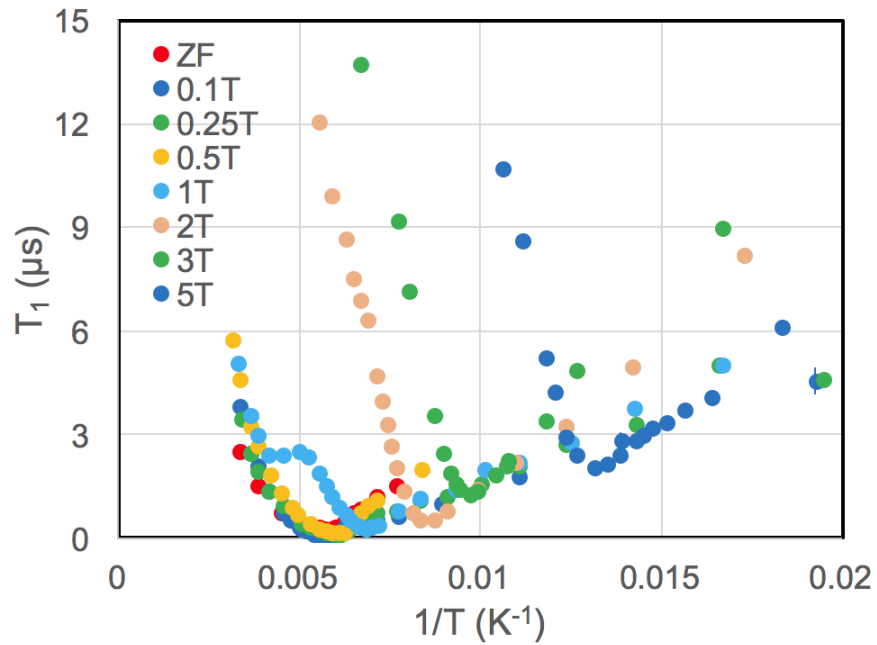
(b) MnGe

Figure 3.17: T_1 as function of inverse temperature $1/T$ in different longitudinal fields for (a) MnSi and (b) MnGe. Figure (a) reproduced from Gat-Malureanu *et al.* [2003].

(a) MnSi

(b) MnGe
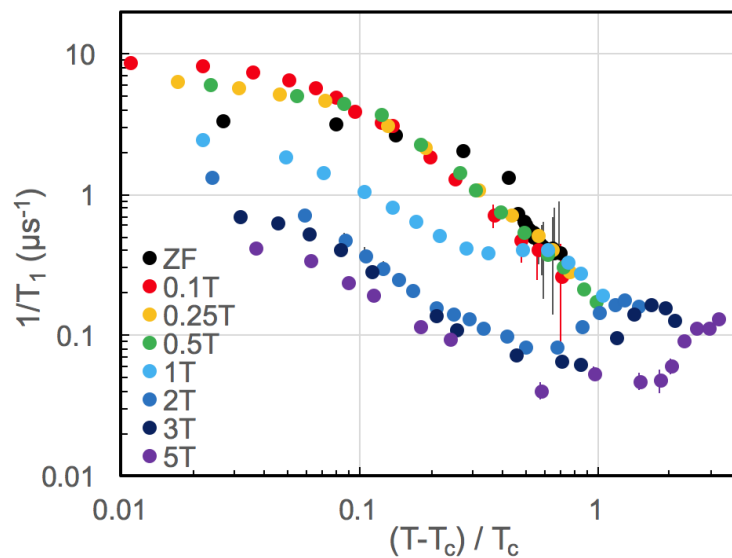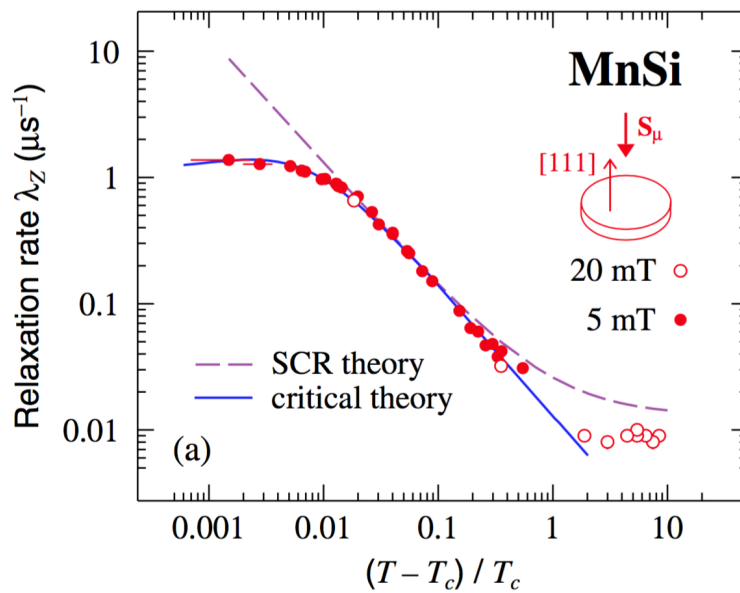
Figure 3.18: (a) $1/T_1$ as function of normalized temperature $(T-T_c)/T_c$ for MnSi in longitudinal fields of 5 mT and 20 mT. (b) $1/T_1$ as function of normalized temperature $(T-T_c)/T_c$ for MnGe in different longitudinal fields. Figure (a) reproduced from Yaouanc *et al.* [2005].

Figure 3.18 (a). For MnGe, in low fields the non-SCR behavior of $1/T_1$ persists up to 300K, in high fields the SCR behavior was recovered. This is consistent with our previous analysis.

Figure 3.19 shows $1/T_1$ as function longitudinal field square for MnSi and MnGe. The external field is expected to promote the Z component and thus reduce the X and Y component of the spin fluctuation. This explains the decrease of $1/T_1$ with increasing field. From the figure we derived the B_{max} of MnGe to be around 3.3T, which is about 15 time larger than that of MnSi. As analyzed before, this suggest stronger helical spin fluctuation in MnGe. The linear behavior of $1/T_1 \sim B^L$ is similar to that of MnSi. This suggest that the behavior of $1/T_1$ in MnGe in high fields might be explained by the same model for MnSi as proposed in Gat-Malureanu *et al.* [2003].

3.5.3   Summary of comparison

Critical behavior at the boundary between the Skyrmion phase and the induced ferromagnetic region was seen in both MnSi and MnGe. By comparing the μSR results, it appears that MnGe is in fact similar to MnSi at least from μSR point of view. On the other hand, critical behavior in MnSi has been studied extensively by neutron scattering in MnSi, which, together with specific heat results, gives the evidence of a 1st order phase transition for the helical transition. Such measurements are yet to be carried out for MnGe.

3.6   Potential connections with topology

In this section we discuss the possible connections of our μSR results on MnGe with the concept of topological phase transition. As has been introduced in Chapter 1, a continuous static magnetic structure can be modeled mathematically as a continuous vector field, about which
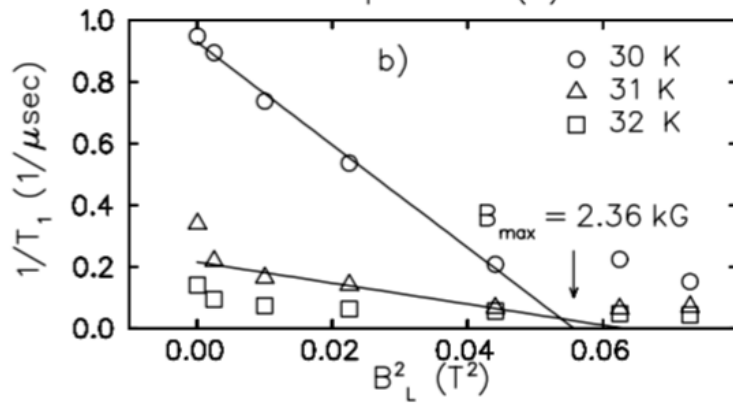
(a) MnSi
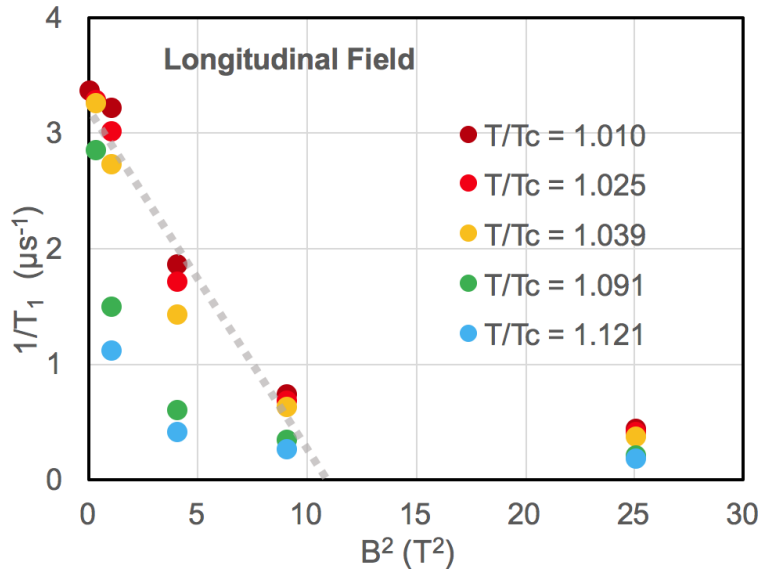
(b) MnGe

Figure 3.19: (a) $1/T_1$ of MnSi as function longitudinal field square at temperatures close to the helical phase transtion. (b) $1/T_1$ of MnGe as function longitudinal field square at different normalized temperatures T/T_c for high fields up to 5T. The normalized temperatures are chosen to be above but close to the helical transition. Figure (a) reproduced from Gat-Malureanu *et al.* [2003].
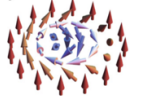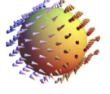
Material	Magnetic Phase	Winding Number
MnSi	Para, Ferro	0
	Conical	0
	2D Skyrmion	1
	Helical	0
MnGe	3D Skyrmion (Hedgehog)	0

Figure 3.20: Different magnetic phases in MnSi and MnGe and their topological winding number. Here a partial magnetic ordering was shown as illustration for each phase. The winding numbers were calculated for the magnetic phase as a whole.

a topological winding number w can be calculated to characterize its topological property. The large energy required to suppress the local moment of a continuous magnetic structure with finite moment guarantees the robustness of these physically-realized topological objects against external perturbation.

Under the assumption that the local magnetic order within these magnetic phases are robust everywhere within the phase, the transformation between these topological objects will be dominate by the mathematical rule that determines the deformation of topological objects, that is, topological objects with different winding numbers cannot deform continuously into each other without breaking. Meanwhile, in physical term, the transformation between two magnetic state is usually realized via a phase transition, and continuous/discontinuous phase

transitions are marked with distinct critical behaviors that can be detected via experiment. Therefore we see that the topology of two magnetic state can have crucial influence on the continuity of the phase transition between them. For example, from topological considerations, two magnetic states with different topological winding numbers cannot transform into each other via a continuous 2nd order phase transition. On the other hand, if the two magnetic states have the same winding number, then they are simply 'allowed' to transform into each other continuously via a 2nd order transition. As a reminder, these topological considerations are based on the assumption that the magnetic state can be very well modeled by a continuous vector field. This, for example, could require static and finite moment of the structure.

Next we apply the above arguments to the case of MnSi and MnGe, and show that the above topological considerations on the phase transition is consistent with published data and also our $1/T_1$ data on MnSi and MnGe. Figure 3.20 displays the magnetic phases that exists in MnSi and/or MnGe, and its corresponding topological winding number:

According to the above analysis, magnetic states with different winding numbers, as listed in Figure 3.20, have to transform into each other via 1st order transition. For MnSi this is well confirmed from various experimental results, especially from high precision specific heat measurement Bauer *et al.* [2013]. The transition between the topologically equivalent states, for example from helical state to conical state, from conical state to ferromagnetic state, are of 2nd order. Meanwhile, the transitions bewteen topologically inequivalent states, for example from conical or helical states to the Skyrmion state, are of 1st order.

In the mean time, existing results, including our result on MnSi film and MnGe, show that topological considerations might also apply for these materials. For the case of MnGe film, as is shown from its phase diagram in Figure 3.21 (a), the Skyrmion region spreads out the

higher field region of the order phase. From μSR $1/T_1$ measurement as shown in Figure 3.21 (b), it is clear that critical behavior was missing at the transition between the paramagnetic phase (winding number 0) and the Skyrmion phase (winding number 1). Thus the μSR result suggest absence of critical behavior at such transition, and thus indicate the presence of a 1st order transition. Considering that these two states have different winding number and are thus topologically inequivalent, this result is consistent with the above topological considerations.

For MnGe, it is noteworthy that, although individually the 3D Skyrmion (the Hedgehog) or Anti-Skyrmion has non zero winding number, the Hedgehog phase, as has been identified in MnGe, has a topological number of 0 due to the cancellation of the winding number from Hedgehogs and Anti-Hedgehogs. In other words, the 3D Skyrmion state in MnGe is topologically equivalent to the ferromagnetic state, and thus a 2nd order phase transition is allowed between them. Figure 3.21 (c) and (d) shows the phase diagram and $1/T_1$ results in high fields. As analyzed in previous sections, in larger field the phase transition will not be dominated by the strong helical fluctuation via the Brazovskii mechanism. From the figure and the analysis presented previous, the transition from the induced ferromagnetic region into the Hedgehog region is characterized by clear dynamic critical behavior. This suggest that the transition between the induced ferromagnetic phase and the Hedgehog phase could be 2nd order. Considering that the two states has the same winding number of 0, these results implies that topological considerations could also work well for the helical magnets of MnSi film and the 3D helical magnet MnGe.

3.7   Conclusion

In summary, we studied the temperature and magnetic-field dependence of the spin fluctuation in MnGe with muon spin $1/T_1$ dynamic relaxation and muon transverse field relaxation measurement.

From $1/T_1$ data we did not observe apparent critical behavior or anomaly at the boundary between paramagnetic and the induced-ferromagnetic regions. Our study showed linear relation between transverse field relaxation rate and the magnetization, and that their ratio (a form of hyperfine coupling constant) is very similar in the induced ferromagnetic region and the paramagnetic region. This suggest that the Z component of the Mn moment is static in both regions. The single relaxation rate in the transverse spectra suggest that the internal field is highly homogeneous in the induced ferromagnetic region.

We therefore suspect that these two regions are not separate phases. Instead, they could be a single phase with different tendencies as temperature decrease: with decreasing temperature, the paramagnetic region is marked with the winning of the tendency towards ferromagnetic order, and the induced ferromagnetic region is marked with the winning of the tendency towards the helical order over ferromagnetic order.

In lower temperature, we observed dynamic critical behavior in the boundary between the induced ferromagnetic region and the Skyrmion region. In low fields, the $1/T_1$ relaxation rate behaves qualitatively different from the prediction of SCR theory for itinerant ferromagnet for large temperature regime above T_c. We understood this by analyzing field effect on spin fluctuation and phase transition in the low and high field regimes, respectively.

Within the Skyrmion region, all the three components of the Mn moment is frozen. The quadratic temperature dependence of $1/T_1$ at low temperatures suggest the two-magnon spin wave to be the dominant spin excitation in the Skyrmion region. This is similar to those seen in localized moment magnets and is qualitatively different from the linear temperature dependence predicted from SCR theory for itinerant ferromagnets.
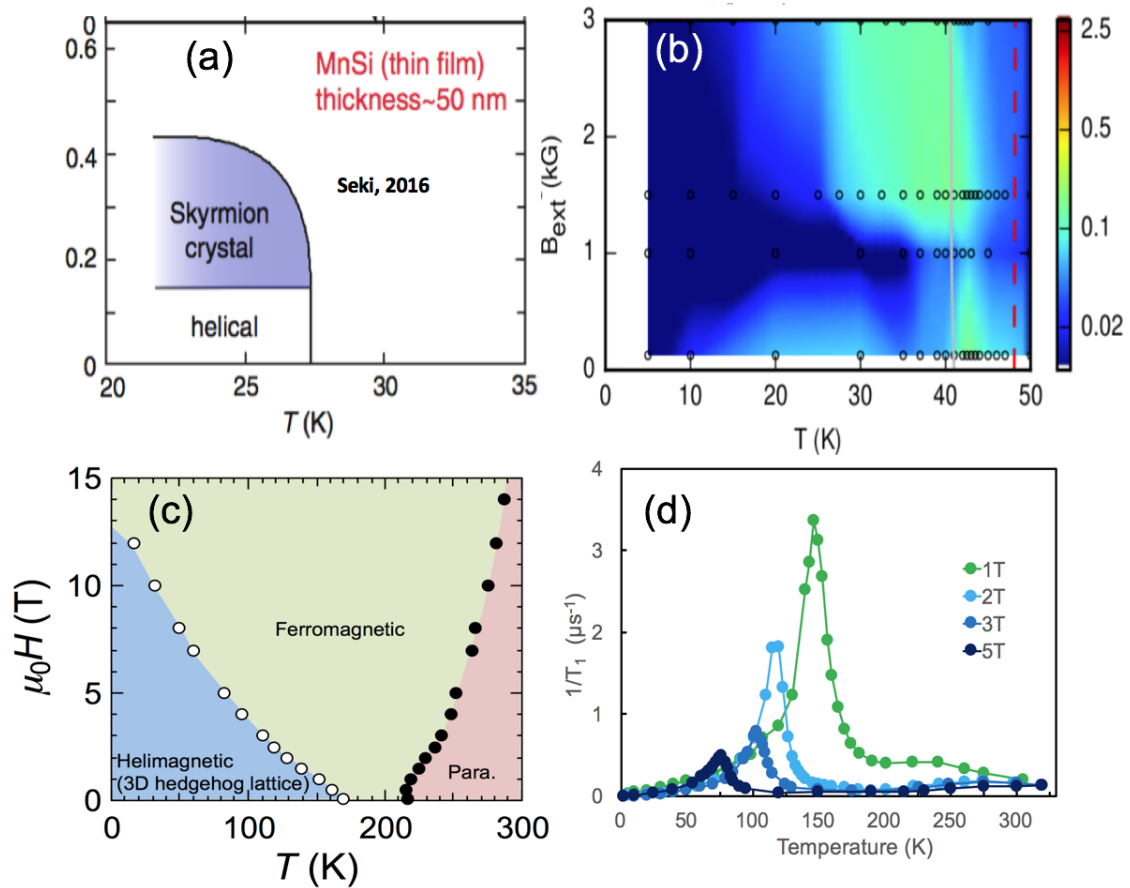
Figure 3.21: (a) Phase diagrams of MBE-grown MnSi film with thickness of 50 nm. Figure reproduced from Seki and Mochizuki [2016]. (b) Color plot of $1/T_1$ relaxation rate of MnSi film. No apparent critical behavior was observed at the boundary of the Skyrmion region and the paramagnetic region. Figure reproduced from Lian and Uemura [2017]. (c) Phase diagram of MnGe. Figure from Naoya Kanazawa (Tokura Group). (d) $1/T_1$ of MnGe in high magnetic fields B > 1T.

Chapter 4

The Pair Distribution Function Technique

4.1 Overview of the pair distribution function (PDF)

To understand the uniqueness of the PDF method for structural analysis, some knowledge about the short, long range of structural correlation and the difference between them would be helpful. Especially in recent years, the number of synthetic materials with complex structures (e.g. nano material, polymer, etc) has been increasing fast. Such materials differ from the classic crystalline model fundamentally as they're typically marked with a lack of long-range periodicity. For example polymers can have millions of atoms constituting chains of molecules assembled in a irregular way, and are thus having complex structures. It therefore deserves the time and effort to speculate about the origin of the complexity of the structure, or more precisely, the origin of the apparent complexity of applying present structural analysis methods to these novel structures.

The key to the problem, as pointed out in Egami and Billinge [2012], lies in how we define and perceive structural orders in these materials. In terms of classic crystalline materials, structural order usually indicates some kind of periodicity in the structure which extends over tens of thousands of unit cells. In such a case, periodicity dramatically reduces the degree of freedom in describing the material, and therefore this type of structural order is most conveniently described in reciprocal space. For complex materials like many nano-materials, on the other hand, periodicity is no longer the powerful description of structural order it was for crystalline material: long-range structural orders are absent. Instead, many of them consist of large numbers of similar structural units that are distributed irregularly within the material. In such cases, the structural order shifts from long-range periodicity in structure to similarities of these small structural units; in other words, the commonalities in the local atomic arrangement at different locations within the material is a more suitable description of structural order in the complex materials mentioned above.

In the absence of long-range periodicity, Bragg's law of crystallographic reflection is no longer satisfactorily fulfilled. Structural periodicity is the crucial prerequisite for Bragg's law, and a material has to have such property in order to be properly analyzed by the traditional x-ray crystallographic methods. The absence of periodicity in nanomaterials gives rise to the nanostructure problem Billinge and Levin [2007]. The pair distribution function (PDF) method is one powerful method that yields structural information at a local scale and has been an active area of research. Consistent with the analysis above, the power of PDF towards nano materials comes from the fact that it is defined in real space and is sensitive to structural order and commonalities on a local scale. For example, commonalities of local structures in a material are reflected in the PDF as shifts of structural peaks. As an volume-integrated probe, the shift of a single peak in the PDF indicates that similar structural distortion between pairs of atom happens throughout the sample, a structural

distortion that happens systematically within the local structures everywhere in the sample. Comparing with other observational technique such as various microscopies, the PDF method is able to reflect the local structural features that prevails, instead of only within a small window of observation, throughout hundreds of thousands of unit cells in the material; this unique advantage comes in with many scattering techniques.

4.2 Definition and equations of different PDF method

4.2.1 The atomic PDF

4.2.1.1 Definitions of the scattering functions

Before deriving the equations for the PDF, we first formulate the theory for the scattering intensity in reciprocal space. The scattering amplitude, which contains all necessary information about atomic arrangement and thus reflects the full Bragg scattering conditions, can be expressed as Egami and Billinge [2012]

$$\Psi(\mathbf{Q}) = \frac{1}{\langle b \rangle} \sum_i b_i e^{i\mathbf{Q} \cdot \mathbf{R}_i}. \tag{4.1}$$

Here b_i is the scattering amplitude of the atom i, and it measures the scattering power of an atom. The angle brackets stands for average over all atoms. With the scattering amplitude $\Psi(\mathbf{Q})$, other scattering quantities such as the scattering cross section, $\frac{d\sigma_C(\mathbf{Q})}{d\Omega}$, the scattering

intensity, $I(\mathbf{Q})$, and the structure function, $S(\mathbf{Q})$, can be found easily

$$\frac{d\sigma_C(\mathbf{Q})}{d\Omega} = \frac{\langle b \rangle^2}{N} |\Psi(\mathbf{Q})|^2 = \frac{1}{N} \sum_{i,j} b_j^* b_i e^{i\mathbf{Q} \cdot \mathbf{r}_{ij}}, \tag{4.2}$$

$$I(\mathbf{Q}) = \frac{d\sigma_C(\mathbf{Q})}{d\Omega} \langle b \rangle^2 - \langle b \rangle^2, \tag{4.3}$$

$$S(\mathbf{Q}) - 1 = \frac{I(\mathbf{Q})}{\langle b \rangle^2} = \frac{1}{N \langle b \rangle^2} \sum_{i \neq j} b_j^* b_i e^{i\mathbf{Q} \cdot \mathbf{r}_{ij}}. \tag{4.4}$$

Here the contribution of the self-scattering, namely the arithmetic sum of the scattering intensities from each individual atom, was subtracted from the scattering quantities so that in the present form they represent the coherent scattering that comes from the interference of the light scattered from the atoms. Equation 4.4 gives the most general expression for $I(\mathbf{Q})$ and $S(\mathbf{Q})$ and applies to any material with known atomic arrangement. For real scattering experiments, many samples are powdered with crystallites oriented along each direction with uniform probability. In such case the equations can be greatly simplified. The orientation averaging implies that, provided the large number of crystallites, each of the atomic distance vectors $\mathbf{r}_{ij}$ within each crystallite has an equal probability to appear in every direction in space. Therefore for a specific pair, $\mathbf{r}_{ij}$, the averaged complex exponential factor is found to be

$$\overline{\exp\left(i\mathbf{Q} \cdot \mathbf{r}_{ij}\right)} = \frac{1}{4\pi} \int_0^{2\pi} \int_0^{\pi} \exp\left(iQr_{ij}\cos\theta\right) \sin\theta d\theta = \frac{\sin Qr_{ij}}{Qr_{ij}}. \tag{4.5}$$

Substituting the complex exponential factor in Equation 4.4 with the averaged expression, we derived the structure function for an ideal isotropic powder sample

$$S(Q) - 1 = \frac{I(\mathbf{Q})}{\langle b \rangle^2} = \frac{1}{N \langle b \rangle^2} \sum_{i \neq j} b_j^* b_i \frac{\sin Qr_{ij}}{Qr_{ij}}. \tag{4.6}$$

As we will see, using Equation 4.6 we can derive the atomic PDF that we use for structural refinement of many materials. As will be further explained in the 2D PDF section, rigorously speaking, the summation in Equation 4.6 is carried out within one particular crystallite,

where as the summation in Equation 4.4 is over all the atoms within the sample. This happens because by doing the orientation averaging we simply dropped the contribution from the coherent scattering between different crystallites, and assumed that the scattering signal from different crystallites are incoherent with each other. Intuitively, this means that in calculating the total structure function of the sample all the crystallites are assumed to be identical and are translated to the same spatial position, so that their only difference is orientation.

In many real cases Equation 4.6 provides an excellent approximation to the actual structure function of the powdered sample. This implies that its underlying assumptions are justified and that the scattering between the (nano) crystallites can be regarded as incoherent. On the other hand, the assumption that the crystallites have random orientation distribution, which justifies the orientation averaging in Equation 4.5, can be inaccurate for samples with preferred orientations. This will be explored further in the 2D PDF section of this thesis.

Finally, for completeness, following the formalism in Farrow and Billinge [2009]; Egami and Billinge [2012], we define the quantity $F(Q)$ as

$$F(Q) = Q \cdot \frac{I(\mathbf{Q})}{\langle b \rangle^2} = Q\left[S(Q) - 1\right] = \frac{1}{N\langle b \rangle^2} \sum_{i \neq j} b_j^* b_i \frac{\sin Qr_{ij}}{r_{ij}}. \tag{4.7}$$

4.2.1.2 Derivation of the PDF equations

Fourier transform of $F(Q)$ gives a quantity closely related to the radial distribution function (RDF), $R(r)$, Egami and Billinge [2012]. Note that since $F(Q)$ is an odd function by definition, its Fourier transform reduces to the sine transform over the positive axis. Thus we

have

$$\hat{f}(r) = \frac{2}{\pi} \int_0^\infty F(Q) \sin(Qr) dQ \tag{4.8}$$

$$= \frac{2}{\pi N \langle b \rangle^2} \sum_{i \neq j} b_j^* b_i \int_0^\infty \frac{\sin Q r_{ij}}{r_{ij}} \sin(Qr) dQ \tag{4.9}$$

$$= \frac{2}{N \langle b \rangle^2} \sum_{i \neq j} \frac{b_j^* b_i}{r_{ij}} \left[\delta(r - r_{ij}) - \delta(r + r_{ij}) \right] \tag{4.10}$$

$$= \frac{2}{r N \langle b \rangle^2} \sum_{i \neq j} b_j^* b_i \left[\delta(r - r_{ij}) - \delta(r + r_{ij}) \right], \tag{4.11}$$

which, if we restrict ourself to the physically meaningful positive axis, equals to

$$\hat{f}(r) = \frac{2}{r N \langle b \rangle^2} \sum_{i \neq j} b_j^* b_i \delta(r - r_{ij}). \tag{4.12}$$

Therefore we see that $\hat{f}(r)$ displays peaks only at distances that corresponds to the separation between two atoms within the material, and therefore establishes a direct relation between the measured x-ray spectrum and the actual atomic arrangement of the sample.

$\hat{f}(r)$ is related to the RDF and the atomic density, $\rho(r)$, via

$$\hat{f}(r) = \frac{R(r)}{r} = 4\pi r \rho(r). \tag{4.13}$$

The physics of the RDF can also be appreciated from the following integral Egami and Billinge [2012]; Frandsen [2016]

$$\int_a^b R(r) dr = \int_a^b r \frac{1}{r N b^2} \sum_{i \neq j} b^2 \delta(r - r_{ij}) dr \tag{4.14}$$

$$= \frac{1}{N} \int_a^b \sum_{i \neq j} \delta(r - r_{ij}) dr \tag{4.15}$$

$$= \frac{1}{N} \sum_i \sum_{j \subset \text{shell i}} 1 \tag{4.16}$$

$$= \frac{N N_{ab}}{N} \tag{4.17}$$

$$= N_{ab}. \tag{4.18}$$

Here N_{ab} stands for the number of atomic pairs per atom with pair distance equal to or shorter than the range [a,b]. Equation 4.14 shows that integrating the RDF over any given positive range of $[a, b]$ gives the total number of atomic pairs within the shell-shaped volume around the center, with inner radius of a and outer radius of b.

Above we derived the expression for $\hat{f}(r)$ by assuming that the integral over Q reaches its lower limit of 0 and an upper limit of ∞. In reality, however, the scattering intensity is measured down to some finite value, $Q_{\min}$, instead of 0. Namely the low-Q signal is lost due to the inaccessibility of small angle scattering. Considering this situation, an expression for the experimentally measured PDF can be written as

$$\hat{f}(r)_{\exp} = \frac{2}{\pi} \int_{Q_{\min}}^{\infty} F(Q) \sin(Qr) dQ \tag{4.19}$$

$$= \frac{2}{\pi} \int_{0}^{\infty} F(Q) \sin(Qr) dQ - \frac{2}{\pi} \int_{0}^{Q_{\min}} F(Q) \sin(Qr) dQ \tag{4.20}$$

$$= 4\pi r \rho(r) - \frac{2}{\pi} \int_{0}^{Q_{\min}} F(Q) \sin(Qr) dQ. \tag{4.21}$$

The integral in Equation 4.21 represents the small angle forward scattering signal that is not detected during an experiment. As shown in Farrow and Billinge [2009], this integral evaluates to

$$\frac{2}{\pi} \int_{0}^{Q_{\min}} F(Q) \sin(Qr) dQ = 4\pi r \rho_0 \gamma_0(r), \tag{4.22}$$

where $\gamma_0(r)$ is the angular-averaged autocorrelation function, $\gamma_0(\mathbf{r})$, of the shape function, $s(\mathbf{r})$ Farrow and Billinge [2009]

$$\gamma_0(\mathbf{r}) = \frac{1}{V} \int s\left(\mathbf{r}'\right) s\left(\mathbf{r}' + \mathbf{r}\right) d\mathbf{r}', \tag{4.23}$$

$$\gamma_0(r) = \overline{\gamma_0(\mathbf{r})}. \tag{4.24}$$

When the crystallite size is large enough so that the approximation $\gamma_0(r) \simeq 1$ is a good one, we get the simplified expression of $\hat{f}(r)_{\mathrm{exp}}$ and name is as $G(r)$

$$G(r) = 4\pi r \left(\rho(r) - \rho_0 \right). \tag{4.25}$$

Replacing ρ_0 with $\rho_0\gamma_0(r)$ in Equation 4.25 gives the general expression of the experimental PDF. As has been studied in Farrow and Billinge [2009]; Gilbert [2008], the above derivation assumed that the particles have no preferred orientation in space. The analytical expression of the shape function for many nano materials can be calculated exactly Guinier [1956]; Warren [1969]; James [1962]; Korsunskiy and Neder [2005] which facilitates the modeling of the measured PDF. This funtionality has been modified and implemented in PDFgui Farrow *et al.* [2007] and is used successfully in modeling the PDF from CdSe nanocrystals Farrow *et al.* [2010]

Alongside the lower limit of accessible momentum, there is also an upper limit, Q_{max}, due to finite size of the detector. This upper limit results in artificial wavy features (usually called the 'termination ripples') in all r ranges of the converted PDF, and thus limits the real space resolution to π/Q_{max}. The experimental limit on the maximum momentum transfer, Q_{max}, is usually around 25 Å^{-1} for synchrotron x-ray measurements, and around 35 Å^{-1} for neutron measurements at a spallation source Frandsen [2016]. For more discussion on this, we refer the reader to Egami and Billinge [2012].

4.2.2 The dynamic PDF

4.2.2.1 From atomic PDF to dynamic PDF

The atomic PDF provides an excellent view of the local atomic arrangement of the sample. Moreover, since in an x-ray PDF experiments the time scale of the light-matter interaction

process turns out to be much shorter than the time scale of the dynamics of the lattice, the atomic structure during the light-matter interaction process can be regarded as effectively unaltered. Therefore, the atomic PDF data extracted from such x-ray scattering intensity reflects the average of instantaneous snapshots of the atomic structure. Thus the atomic PDF is also referred to as the 'instantaneous PDF' Egami and Billinge [2012].

The instantaneous atomic PDF is a special case of a form of time dependent PDF, $G(r,t)$, with time variable set to origin, $t = 0$. The concept and expression for $G(r,t)$ is first worked out by Van Hone in 1954, and was since then referred to as the Van Hove function Van Hove [1954]. As a generalized form of the PDF, the Van Hove function $G(r,t)$ describes the temporal evolution of the pair-wise correlations of the atomic density, and is thus a reflection of the underlying lattice dynamics of the material. If watched as a movie, $G(r,t)$ should reveal the evolution of the average atomic structure, with certain range and resolution in time.

On the other hand, as a time domain function, the Van Hove function itself can be very intuitive, but also only for rather simple circumstances. In the situation in which there's one lattice/local phonon in the material, then in principle the Van Hone function would appear sinusoidal-like, revealing the simple harmonic vibration of the atoms. It can appear intuitive even at the presence of two or three phonons. In most real cases, however, there are usually an abundance of active phonon modes present at the same time, and the dynamics of individual atoms can be highly irregular. In such cases, tracing the atomic arrangement in real time would give us very little usable information.

For such complex motion of the atoms, it is natural to switch off from time to frequency space and characterize the motion with its frequency composition. This naturally brings us to the concept of dynamic pair distribution function (dynamic PDF), which is computed by Fourier transforming over the time/frequency axis of the Van Hove function. It is thus often

expressed as $G(r, \omega)$, in which ω is the frequency variable. As will be discussed in detail in a separate chapter below, the dynamic PDF in principle allows us to specify the contribution to the atomic PDF from the lattice dynamics with different frequencies.

4.2.2.2   Inelastic scattering experiment and dynamic PDF

As the atomic PDF is measured from the elastic scattering experiments, the dynamic PDF is associated with the energy-resolved inelastic scattering experiments, at either a synchrotron or a neutron source. Here we briefly introduce the principle and setups of the inelastic experiment. The relation between the measured scattering quantity with the dynamic PDF is explained explicitly in the subsequent section.

An inelastic scattering experiment is able to measure the scattering intensity while tracing the energy loss during the scattering process. The inelastic scattering experiment is most natural at a neutron source, as the energy of the incoming neutron turns out to have comparable range as that of the lattice excitations (i.e. phonons) in solids. With the help of a triple-axis spectrometer, which contains a monochromator, the sample and an analyzer placed on a goniometer, the experimental condition can be readily tuned, for example the energy and direction of the incident and scattered beam, as well as the orientation of the sample Egami and Billinge [2012].

A mechanical chopper is used to create monochromatic beam at a pulsed neutron source. Specifically, the chopper works by changing the time of opening to select the neutron with certain incident energy, and by changing its speed of rotation to allow only neutrons with energy within certain energy band (and thus within certain range in speed) to pass through it Egami and Billinge [2012]. Therefore, the energy resolution is fundamentally limited by the speed of the chopper, and is directly proportional to the ratio of the rotation speed and

the speed of the incident neutron. For an illustration of the principle of the chopper, see e.g.Ch.9 in Bacon [1975].

In a scattering experiment, the energy and momentum transfer is expressed as

$$\hbar\omega = \hbar\omega_{\text{initial}} - \hbar\omega_{\text{final}}, \tag{4.26}$$

$$\mathbf{Q} = \mathbf{k}_{\text{initial}} - \mathbf{k}_{\text{final}}, \tag{4.27}$$

where ω and $\mathbf{k}$ is the energy and momentum transfer, $\omega_{\text{initial/final}}$ and $\mathbf{k}_{\text{initial/final}}$ are the energy and momentum of the incoming/scattered particle. If the particle is a neutron, the we have, according to the kinetic energy-momentum relation of the particles,

$$\hbar\omega = \frac{\hbar^2}{2m} \left(k_{\text{initial}}^2 - k_{\text{final}}^2 \right). \tag{4.28}$$

Here m is the mass of neutron. For x-rays, the energy-momentum relation is given by the dispersion relation of electromagnetic wave in vacuum, which then gives

$$\hbar\omega = \hbar c \left(k_{\text{initial}} - k_{\text{final}} \right). \tag{4.29}$$

The energy loss of the incoming particle during its interaction with the sample is used to create various excitations in the sample, including lattice/local phonons or spin waves. Furthermore, the quantity that is being measured in an inelastic scattering experiment is the inelastic scattering intensity, $I(\mathbf{Q}, \omega)$, which can be transformed to obtain the inelastic structure function, $S(\mathbf{Q}, \omega)$. $I(\mathbf{Q}, \omega)$ and $S(\mathbf{Q}, \omega)$ has their direct correspondence with $I(\mathbf{Q})$ and $S(\mathbf{Q})$ discussed in the previous section: the latter can be obtained by a simple energy-integration of the former. In other words, $I(\mathbf{Q}, \omega)$ and $S(\mathbf{Q}, \omega)$ reveals information about the scattering process contributed by different excitation conditions in the material. Furthermore, as can be measured directly from experiment, $S(\mathbf{Q}, \omega)$ is related to the time-dependent scattering function (usually called the intermediate scattering function Egami and

Billinge [2012]), $S(\mathbf{Q}, t)$, via Fourier transform, and that for $S(\mathbf{Q}, t)$ a direct generalization from $S(\mathbf{Q})$ is readily available.

The concept and foundations of the dynamic pair distribution function (dynamic PDF) was formulated in the seminal papers by Carpenter and Pelizzari Carpenter [1967]; Carpenter and Pelizzari [1975b,a], in which the mathematical expressions of the orientation-averaged structure function was evaluated explicitly. The dynamic PDF was first computed from inelastic neutron scattering data of amorphous Boron and SiO_2 by Arai and Hannon Arai *et al.* [1994, 1992, 1995]; Hannon *et al.* [1992, 1995], and was used to analyze the dynamic lattice distortions in the high temperature superconductors by Egami *et al.* [1995, 1996a,b]. Following earlier works of Debye [1912]; Beni and Platzman [1976]; Bohmer and Rabe [1979]; Sevillano *et al.* [1979], Jeong *et al.* [2003] wrote down the expression of the (energy-integrated) mean-square atomic pair displacement in the atomic PDF due to correlated thermal motion. The dynamic PDF method was used to analyze the local structural distortions of relaxor ferroelectric material suggesting the dynamic nature of the structural distortion observed by other techniques Dmowski *et al.* [2008]. In a theoretical study by McQueeney, the mathematical expression of the dynamic PDF based on the orientationally-averaged form of the structure functions have been worked out, in the single-phonon approximation, and analyzed in great detail McQueeney [1998]. The effects of the transverse and longitudinal phonon on the lattice distortion and the dynamic PDF was fully examined using this approximate model. The proposed dynamic PDF was then calculated in comparison with the experimentally measured data on polycrystalline Nickel with good agreement.

Since the lattice dynamic displacement is directly related to the width of the atomic PDF Jeong *et al.* [1999], efforts have been made to extract the dynamic properties of the lattice from the atomic PDF. For example, it was shown that the phonon dispersion of Nickel can be

extracted by fitting the atomic PDF with a model that explicitly includes the dynamic prop-
erties of the lattice Dimitrov *et al.* [1999]. Meanwhile, in a separate study by Reichardt and
Pintschovius [2001], drastically different phonon dispersions were used in the refinement of
the computed PDFs of Nb and CaF_2. And the results shows that the atomic PDF can be
rather insensitive to the details of the phonon dispersion. Thus the dynamic PDF could be
essential for the analysis of local dynamic distortions of the lattice.

Below we follow the derivations from Egami and Billinge [2012]; Lovesey [1986] and lay down
the relation between the scattering quantity and the dynamic PDF.

4.2.2.3   Derivation of the dynamic PDF equations

To derive the equation for the dynamic PDF, we first introduce the time-dependent form of
the structure function, following the notations in Egami and Billinge [2012],

$$S(\mathbf{Q}, t) = \frac{1}{N \langle f \rangle^2} \sum_{i,j} f_j^* f_i \left\langle \left\langle e^{i\mathbf{Q} \cdot (\mathbf{r}_i(0) - \mathbf{r}_j(t))} \right\rangle \right\rangle. \tag{4.30}$$

The brackets stands for ensemble average. Since we're taking into account the lattice dy-
namics explicitly, the atomic position vectors, $\mathbf{r}_i$, are now time-dependent. It is apparent
that, if we fix the time variable t in Equation 4.30 to $t = 0$, it recovers the expression for
the regular structure function $S(\mathbf{Q})$ of the atomic PDF. Both the structure function and the
intermediate scattering function contains information about the atomic arrangement of the
system at a particular time t. The relation between the intermediate function and the struc-
ture function can be clarified by introducing the scattering amplitude Egami and Billinge
[2012]. If we define the scattering amplitude at a given time t, $\psi(t)$, as in Equation 4.31,
then the structure function at time t and the intermediate scattering function can be written
as a function of ψ as in Equation 4.32 and Equation 4.33, respectively Egami and Billinge

[2012]:

$$\psi(\mathbf{Q}) = \frac{1}{\langle f \rangle} \sum_i f_i e^{i\mathbf{Q} \cdot \mathbf{R}_i(t)}, \tag{4.31}$$

$$S(t) = \psi^*(t)\psi(t) = \psi^2(t), \tag{4.32}$$

$$S(\mathbf{Q}, t) = \psi^*(t)\psi(0). \tag{4.33}$$

In other words, the scattering function $S(t)$ is the autocorrelation of the atomic locations at time $T = t$, and the intermediate function $S(\mathbf{Q}, t)$ is the correlation function between the atomic location at time $T = 0$ and at $T = t$.

To simplify the expression of $S(\mathbf{Q}, t)$, we write $\mathbf{r}_i(t)$ as $\mathbf{r}_i(t) = \langle\langle \mathbf{r}_i \rangle\rangle + \mathbf{u}_i(t)$. Replacing this in Equation 4.30 and expand the complex exponential, $S(\mathbf{Q}, \omega)$ can be expressed as

$$S(\mathbf{Q}, \omega) = S_0(\mathbf{Q}, \omega) + S_1(\mathbf{Q}, \omega), \tag{4.34}$$

with

$$S_0(\mathbf{Q}, \omega) = \frac{1}{N\langle f \rangle^2} \sum_{i,j} f_j^* f_i e^{i\mathbf{Q} \cdot (\langle\langle \mathbf{r}_i \rangle\rangle - \langle\langle \mathbf{r}_j \rangle\rangle)} \delta(\omega). \tag{4.35}$$

Here the dirac delta function $\delta(\omega)$ has spectral weight only at $\omega = 0$, and this means that $S_0(\mathbf{Q}, \omega)$ is the elastic (and also leading) component of the total structure function. The other terms in the expansion can be evaluated in a similar fashion.

From a physics perspective, an elastic scattering process means that there's no net energy transfer between the incoming particle and the sample, and thus no lattice phonon is excited during the particle-matter interaction. Since the phonons excited by the incoming particle are the only ones that produces atomic motion that is coherent with the scattering particle, lack of these phonon means in the view of the incoming particle the atoms in the sample only exhibit incoherent thermal motion (uncorrelated motion). Correspondingly, the measured elastic scattering function $S(Q, \omega = 0)$ is a reflection of the atomic arrangement under

such uncorrelated motion. It is also worth emphasizing the important difference between correlation and coherence: here correlation is used to describe the correlated collective motion of the atoms (i.e. lattice/local phonons), which exists even without the material being excited by the incoming particle. On the other hand, coherence describe the correlation between the phase of the motion of the atoms and of the particle. On the other hand, for $S(Q, \omega \neq 0$, it represents the result of the scattering of a particle by an atomic lattice with a correlated motion that is coherent with the motion of the particle. It thus reveals information about the correlated atomic motion through the corresponding atomic distribution in such condition. This and other related topics will be discussed in greater detail in the dynamic PDF chapter.

The intermediate scattering function $S(\mathbf{Q}, t)$ is related to the dynamic structure factor $S(\mathbf{Q}, \omega)$ and the atomic structure function $S(\mathbf{Q})$ via Fourier transform:

$$S(\mathbf{Q}, \omega) = \int S(\mathbf{Q}, t) e^{i\omega t} dt, \tag{4.36}$$

$$S(\mathbf{Q}) = S(\mathbf{Q}, t = 0) = \int S(\mathbf{Q}, \omega) e^{i\omega \cdot 0} d\omega = \int S(\mathbf{Q}, \omega) d\omega. \tag{4.37}$$

Notably, since in the above formalism the time dependence only exist in the atomic coordinate $\mathbf{r}_i(t)$, it means that here we focus on the contribution of the lattice excitations to the scattering process and ignore other such as electronic excitations. Moreover, it is clear from Equation 4.36 that the instantaneous structure function $S(\mathbf{Q}, t = 0)$ is simply an energy-integrated $S(\mathbf{Q}, \omega)$, meaning that it contains contribution from lattice vibrations at each frequency acting at the same time (no phase delay in time).

With the expression of the dynamic structure function, the dynamic PDF can be readily evaluated by Fourier transforming it over space Egami and Billinge [2012]; Dmowski *et al.*

[2008]; Egami and Dmowski [2012]

$$\rho_0 g(\mathbf{r}, \omega) = \int S(\mathbf{Q}, \omega) e^{i\mathbf{Q}\cdot\mathbf{r}} d\mathbf{Q} \tag{4.38}$$

$$= \frac{1}{N\langle f \rangle^2} \sum_{i,j} f_j^* f_i \left\langle\!\!\left\langle \int \delta\left(\mathbf{r} - [\mathbf{r}_i(0) - \mathbf{r}_j(t)]\right) e^{i\omega t} dt \right\rangle\!\!\right\rangle. \tag{4.39}$$

As a direct Fourier transform of the dynamic structure function, the dynamic PDF $g(\mathbf{r}, \omega)$ describes the density distribution of the atoms at a particular energy transfer ω and a distance r Egami and Billinge [2012].

If the results can be validated, the dynamic PDF is particularly sensitive to local dynamics of the atoms, and has been applied to various materials like Ni and relaxor ferroelectric materials Dmowski *et al.* [2008]; Egami and Dmowski [2012]. For example for polycrystalline Nickel, the dynamic PDF revealed the local phonon mode right at the energy where the phonon dispersion becomes flat, namely at the Van Hone singularity of the material observed from Raman spectroscopy. In the relaxor ferroelectric $Pb(Mg_{1/3}Nb_{2/3})O_3$, a strong peak shows up at 2.4 Å while another peak at 3.4 Å disappears, both at around 15 meV. These changes are found to be originating from the same atomic displacement, which is the off-centering of the Pb atom against the Mg/Bn sublattice Dmowski *et al.* [2008]. This will be studied in greater detail in the later chapter on dynamic PDF.

4.2.3 The two-dimensional PDF

The problem of 2 dimension pair distribution function (2D PDF) has been gradually sketched out since the 90s, through a series of analytical and experimental work Yan *et al.* [1992]; He *et al.* [1993]; Yan and Egami [1993]. As one of the subjects of this thesis is to re-discover the formalism of 2D PDF in greater detail, and to explore it in a broader context of the

long-standing texture problem, we leave these progressive works for a separate chapter, and only briefly introduce the subject in this section.

4.2.3.1   Overview of the 2D PDF method for textured material

Polycrystalline thin films have a variety of applications in catalysis and electric, magnetic, photonic, and chemical devices. For example, polycrystalline and amorphous semiconductor films are key elements in many state of the art thin film transistors Sze [2013]; Nomura *et al.* [2004, 2006]; Fortunato *et al.* [2012]; Dimitrakopoulos and Mascaro [2001] and highly-efficient solar cells Wu [2004]; Contreras *et al.* [1999]; Chopra *et al.* [2004]; O'Regan and Grätzel [1991]; Chopra and Das [1983]. Polycrystalline films are also used as media for magnetic storage as well as for thermal sensors Sze [1994], and are critical catalysts for achieving high performance in polymer electrolyte fuel cells Wilson and Gottesfeld [1992b,a].

Knowledge about the atomic-scale structures of these films is critical for understanding their properties. There are a number of powerful methods for solving the structure of single crystalline and epitaxial thin films, for example atomic force microscopy (AFM) Morita [2015], transmission electron microscopy (TEM) Reimer [2008]; Williams [2009]; Bravman and Sinclair [1984], coherent Bragg rod analysis (COBRA) Yacoby *et al.* [2002]; Eom *et al.* [1992] and x-ray standing wave analysis Cowan *et al.* [1980]. However, the options are fewer when the films are polycrystalline or nanocrystalline and we need novel techniques.

As discussed above, the atomic pair distribution function (PDF) analysis has been shown to be an important technique for determining the local atomic arrangement of nanomaterials Egami and Billinge [2012]. PDF studies have led to a breakthrough in our understanding of materials structure and reactions in materials chemistry Billinge and Levin [2007]. As a recent development, the PDF analysis has been successfully applied to both amorphous and

polycrystalline thin films Jensen *et al.* [2015]; Shyam *et al.* [2016]; Nakamura *et al.* [2017]; Wood *et al.* [2017], and have illustrated how nanoparticle structure can help to understand the film crystallization process.

However, this thin-film PDF (tfPDF) technique requires the sample to be isotropic, and thus is not suitable for the analysis of highly textured films. Meanwhile, directed by the growth process Thompson [1990], in many cases these films have a sharp texture with one zone axis perpendicular to the film but the other axes randomly distributed in the plane of the film Thompson [2000]; Brezesinski *et al.* [2010]. The texture of polycrystalline films can have a significant effect on their properties Dimos *et al.* [1988]; Thompson [2000]; Kulkarni *et al.* [1999]; Takenaka and Sakata [1980], and understanding their local structure can be a crucial step to demystify these properties.

4.2.3.2 The 2D PDF equation

The 2D PDF equations is first derived in an earlier work He *et al.* [1993]. Here we summarize their results and write down the expression for the 2D PDF. We start with the general expression of 3D PDF

$$g(\mathbf{r}) = \rho_0 + \frac{1}{2\pi^3} \int [S(\mathbf{Q}) - 1]e^{i\mathbf{Q}\cdot\mathbf{r}}, \tag{4.40}$$

which after spherical averaging gives the regular atomic PDF introduced in previous sections. On the other hand, in case the sample is composed of crystallites with orientations that are, instead of spherically homogeneously, aligned with a known axis but are randomly oriented around the axis, then the averaging over crystallite orientation gives, instead of atomic PDF, the 2D PDF. Specifically, we have

$$g(R, z) = \rho_0 + \frac{1}{(2\pi)^2} \int_0^\infty \int_{-\infty}^\infty Q_R[S(Q_R, Q_z) - 1]J_0(Q_R R)e^{iQ_z z}dQ_z dQ_R, \tag{4.41}$$

where $J_0(x)$ is the zeroth order cylindrical Bessel function. R and is the in-plane (xy) component of $\mathbf{r}$ and Q_R is the corresponding reciprocal vector. Q_z is the out of plane $(z$ axis$)$ component of $\mathbf{Q}$. $S(Q_R, Q_z)$ is simply the structure function of the cylindrically symmetric material, with two independent variables. Fourier transforming Equation 4.41 along the z axis, we have

$$g(R, Q_z) = \int g(R, z) e^{-iQ_z z} dz \qquad (4.42)$$

$$= \rho_0 + \frac{1}{2\pi} \int_0^\infty Q_R [S(Q_R, Q_z) - 1] J_0(Q_R R) dQ_R. \qquad (4.43)$$

Equation 4.43 gives the general expression for the 2D PDF.

Intuitively, the PDF in 2 dimensions, $g(R, z)$, describes the atomic pair distribution within the atomic plane located at z. The difference between the $g(r)$ and $g(R, z)$ is that while $g(r)$ gives the atomic pair distribution between the origin and the atoms within the spherical shell of radius r around the origin, $g(R, z)$ gives the pair distribution within the atomic plane located at z along the cylinder (z) axis. Thus $g(R, z)$ offers a direct and convenient view of the in-plane atomic pair distribution, and is particularly informative when applied to layered material.

On the other hand, the 2D PDF $g(R, Q_z)$ is given by Fourier transforming $g(R, z)$ along the z axis. Thus $g(R, Q_z)$ is more useful in describing the fluctuation of the in-plane pair distribution along the z axis (of e.g. layered material). As a special case, $g(R, Q_z = 0)$ give the PDF that is a linear superposition of the in-plane PDFs. Set $Q_z = 0$ in Equation 5.61, we have

$$g(R, Q_z = 0) = \int g(R, z) e^{-i0 \cdot z} dz = \int g(R, z) dz. \qquad (4.44)$$

4.2.3.3 Applications of the 2D PDF

The unique combination of variables from both real and reciprocal space in the 2D PDF is reminiscent of that of the dynamic PDF, where the real space variable r and the reciprocal space variable ω coexists in the function. This special quality of the 2D PDF makes it an ideal probe for materials whose in-plane structural features are highly local and aperiodic while the out-of-plane structure is highly periodic (just as the dynamic PDF, where it describes the highly periodic temporal dynamics in its reciprocal, a.k.a. frequency space, and focus on the local structure by preserving the real space spatial variable r). The 2D PDF is also suitable for layered structure, where the in-plane atomic arrangement tends to be densely packed while the atomic layers are well-separated.

The 2D PDF method has been proposed and applied successfully to the Al-Cu-Co decagonal quasicrystal He *et al.* [1993]. The 2D PDF refinement using a proposed lattice model agrees well with the experimental data with different Q_z values. Meanwhile, despite these promising efforts, the formalism as well as the experimental measurement of the 2D PDF still require further effort, which is one subject of this thesis and will be presented in a separate chapter.

4.3 Aspects of a PDF experiment

4.3.1 X-ray/PDF experiment at Synchrotron

Synchrotron has been one of the ideal sources of x-rays used for PDF studies of complex materials. Synchtron x-rays are usually obtained at large scale user facilities such as particle accelerators, and can be accessed by researchers by writing proposals for their measurements. A synchrotron is able to produce intense x-ray beams with all colors that can be used in white-

beam measurements or, using a monochromator, as a sources for monochromatic x-rays. On the other hand, the flux of the x-rays at certain energies is another factor that influences its potential application. This depends on multiple factors, including the characteristic energy of operation of the synchrotron as well as other details of the source and optics at the beamline. High flux of the synchrotron x-rays also allows quick build up of count number, thus enabling rapid collection of high quality PDF data. For example, for a moderately strong scatterer, a diffraction pattern good enough for Fourier transform and PDF analysis can be obtained within a few seconds Frandsen [2016]. Books and monographs are available for a more comprehensive survey of the background information and latest development of the synchrotron sources for scientific research Willmott [2011]; Duke [2009]; Als-Nielsen and McMorrow [2011]

A large number of synchrotron x-ray sources have been established around the world. Among these sources, only those with an electron energy of the order or greater than 2.5 GeV are suitable for PDF measurements on crystalline materials. A number of third generation synchrotron sources such as the NSLS-II (Brookhaven National Laboratory) and the Advanced Photon Source (APS, Argonne National Laboratory), feature x-rays with very high luminosity and intensity at high x-ray energies. With the aid of the highly penetrating x-ray beams at these advanced sources, many scattering and PDF experiments that have been considered impossible have been successfully carried out.

For historical and practical reasons, PDF experiments used to be a rather time-consuming and difficult process to carry out. The data processing and analysis also require efforts and practices. Fortunately, the development of the new RAPDF measurement method Chupas *et al.* [2003] has greatly simplified and accelerated the PDF measurement and thus promoting its application in various aspects of research, for example in materials science and physics.

In a typical RAPDF measurement, a monochromator is used to select a wavelength that is in general optimal for the present experiment. On the other hand, since for the same scattering peak, the Bragg scattering angle is smaller if the wavelength of the incoming x-ray is smaller (or its frequency higher), the detector would be able to collect scattering from a larger momentum range (i.e. Q_{max}) if the x-ray wavelength is smaller. Since the PDF technique relies on large enough Q_{max} value to obtain reasonable data after the Fourier transform, hard x-rays with wavelengths as short as 0.2 Å are usually used. A squared 2D area detector is often used to collect the scattered x-rays. It is usually placed perpendicular to the beam, with a distance to the sample being optimized for different type of experiments. For example, some might prefer to have a better resolution in the momentum space, and this can be realized by moving the detector further away from the sample and thus having the scattering peaks fall on a larger area on the detector. On the other hand, the detector is placed closer to the sample in order to cover a larger solid angle and thus collect scattered light with a larger momentum (and thus larger scattering angle) Egami and Billinge [2012].

In a PDF experiment, the sample is usually pill-shaped, or mounted in a capillary. The pill-shaped sample usually involves nano particles and/or polycrystalline thin films, and capillary can be used to sustain samples in a powder form. The use of capillary makes some samples easier to handle during the experiment, and it also produces high quality data that are indistinguishable from one produced without the capillary. Furthermore, if the axis along which the capillary was mounted can spin, via for example a mechanical motor, during the measurement, then this would help to increase the effective homogeneity of the sample being measured. Specifically, if the collection time is much longer than the spinning period, then the data would be an integration of the scattering pattern from the sample measured at every rotation angle with nearly equal exposure time for each angle. Spinning with capillary has proved to have a larger effect on the powder homogeneity and is ideal to apply if the

data from the un-spinning sample is decorated with spots from single-crystalline domains with preferred orientations (so-called texture) Egami and Billinge [2012]. Before or after the sample measurement, x-ray spectrum of an empty capillary was measured separately and properly subtracted from the sample signal.

4.3.2 PDF data analysis

The analysis procedure of the PDF data involves three steps. The first step is data reduction, in which the raw scattering data collected from the detector, usually in the form of a .tiff image file, is processed by standard image processing protocols and then azimuthally integrated to obtain the x-ray spectrum as a function of momentum transfer, namely $I(Q)$. The second step is data conversion, in which the scattering intensity $I(Q)$ undergoes proper background subtraction and is converted to the atomic PDF via compute the intermediate quantities such as the structure function $S(Q)$ and $F(Q)$ step by step. The third and ultimate step in PDF data analysis is to extract information from the experimental PDF. This is done by doing fitting to the experimental PDF using proper established structural models. Excellent software tools, for example the xPDFsuite, have been developed and extended to cover every step in the data analysis Farrow *et al.* [2007]; Qiu *et al.* [2004]; Peterson *et al.* [2000]; Juhás *et al.* [2013]; Yang *et al.* [2015].

Some details in the data analysis deserves a bit more discussion here. For example, the Fourier transform from $S(Q)$ to $G(r)$ by definition involves an integral with infinity as upper limit. This is never the case in reality, in which the data measured is bound in a finite Q range, leaving behind errors such as the termination ripples in the PDF. Due to relative smoothness of the small Q component of $S(Q)$, the lower momentum cutoff usually have little influence on the essential structural features revealed by the converted PDF. The effects of

the high-Q cutoff, the presence of the termination ripple, can be reduced by various artificial protocol. From the mathematical perspective, the termination ripple comes in primarily because the sharpness of the $S(Q)$ spectrum at the upper cutoff momentum. This, after Fourier transform, results in a distinct signal with exactly the cutoff frequency. In the computation of PDF from the structure function, the upper limit of the scattering vector Q in $S(Q)$, usually called Q_{max}, is usually chosen at the value beyond which the signal-to-noise ratio becomes unacceptable. The spiky noises in the high-Q regime need to be excluded to avoid any spurious small features in the converted PDF Egami and Billinge [2012].

The modeling of the PDF data includes choosing a proper structural model, a set of physical parameters as initial parameter, and a set of conditions as constraints to the parameters during the refinement. These aspects have all been developed and implemented in the PDF analysis software PDFgui Farrow *et al.* [2007], a multi-functional graphic user interface (GUI) for PDF data analysis. In PDFgui the user can create an atomic structure by either specifying the atomic positions manually, or by importing a crystallographic information file (cif) file of the material available, for example, from online databases. After specifying the fixed and variable parameters, a PDF is computed from the structural model, which is fitted to the experimental PDF by refining the variable parameters with least-squares minimization. Typical parameters include atomic positions, atomic displacements due to thermal motion, etc. The set of structural parameters which gives a PDF that is close enough to the experimental PDF give an estimation of the real structure of the measured sample. In addition to the PDFgui, the SrFit program from the Diffpy-CMI suite Juhás *et al.* [2015] offers extended functionality in defining the structure and performing the refinement.

Chapter 5

Texture analysis in the PDF and the 2-dimensional pair distribution function method

The 2-dimensional pair distribution function (PDF) is introduced as a convenient approximate approach for extracting quantitative structural information from PDFs measured from fiber textured thin films using the thin-film PDF method at normal incidence. We formulate the 2D PDF theory explicitly and show the approximation, demonstrating the approach on data from a platinum nanoparticle thin film on a fused silica substrate. The simulated 2D PDF fits well to the dominant peaks in the experimental PDF. We describe open-software that is available for carrying out this procedure.

5.1 Introduction

Here we explore a straightforward extension of the tfPDF approach with the hope that it yields accurate quantitative structural information from highly mono-axis textured thin films. The approach is based on the previously established 2 dimensional pair distribution function (2D PDF) method He *et al.* [1993]. First in Sec. **??** we rederive the 2D PDF theory, since we are not aware of a full derivation anywhere in the literature. In Sec. 5.4 We show that for the case of a mono-axis textured thin polycrystalline film measured in normal incidence, the signal approximates closely to the 2D PDF signal with $Q_z = 0$. In Sec. 5.5, we test how well this approximation works in practice by applying it to a polycrystalline platinum thin film on a fused-silica substrate, and show that the 2D PDF well explains the observed diffraction data. Finally, we describe software that implements this method in Sec. 5.6.

5.2 Texture, the orientation distribution function (ODF), and the total scattering structure function

Here we develop the total scattering structure function, $S(\mathbf{Q})$ for the case of a textured powder.

As a start we write down the full 3D structure function Egami and Billinge [2012], $S(\mathbf{Q})$, which may be obtained from measured scattering intensities,

$$S(\mathbf{Q}) = 1 + \frac{1}{N\langle f \rangle^2} \sum_i \sum_{j>i} f_i^*(Q) f_j(Q) e^{i\mathbf{Q}\cdot\mathbf{r}_{ij}} \tag{5.1}$$

$$= 1 + \frac{1}{N\langle f \rangle^2} \sum_{i \neq j} f_i^*(Q) f_j(Q) e^{i\mathbf{Q}\cdot\mathbf{r}_{ij}}, \tag{5.2}$$

where N is the number of atoms in the (illuminated part of the) sample and $f_j(Q)$ is the atomic form factor of the ith atom. The sums over i and j run over every atom in the sample in a way that avoids double-counting, where Eq. 5.2 serves to define $\sum_{i \neq j}$. Finally,

$$\mathbf{r}_{ij} = \mathbf{r}_j - \mathbf{r}_i, \tag{5.3}$$

where $\mathbf{r}_i$ is the vector from the origin of the sample reference frame to the ith atom.

This familiar function is called the structure function because it depends on the structure of the sample. It is also accessible in a scattering experiment as it is related to the coherent scattered intensity of x-rays, neutrons or electrons from the sample Egami and Billinge [2012]. It depends on $\mathbf{Q}$ but not on the orientation of the sample. It is interesting to investigate how this can be possible since the scattered intensity does depend on the sample orientation in a real experiment. The easiest way to think about this is that we assume a reference frame on the sample (for a crystal this will likely be defined by the crystallographic unit cell) and we vary $\mathbf{Q}$ in terms of magnitude and direction to go from the origin of this frame to every voxel in turn in the sample-reference frame, and we measure the normalized scattered intensity at each point. In a real experiment it is not possible to place $\mathbf{Q}$ into every voxel in the sample space without reorienting the sample, so from a practical point of view the scattered intensity is measured for the sample at different orientations in the laboratory reference frame, but each measurement is mapped back to the sample reference frame to yield $S(\mathbf{Q})$. To sample the full reciprocal space in an experiment with a 2D detector it is possible to rotate the sample around two mutually perpendicular axes that are both perpendicular to the incident beam direction. For brevity we will refer to this as the orthogonal axes rotation (OAR) approach. For quantitatively accurate intensities it is also necessary to normalize each measured point by the incident counts. In this way, the structure function, $S(\mathbf{Q})$ may be obtained from any sample with any degree of anisotropy. Finally, if desired, Eq. 5.1

may be Fourier transformed to obtain a real-space 3D PDF according to Egami and Billinge [2012]

$$G(\mathbf{r}) = \frac{1}{(2\pi)^3} \int \left[S(\mathbf{Q}) - 1 \right] e^{i\mathbf{Q} \cdot \mathbf{r}} d\mathbf{Q}. \qquad (5.4)$$

We are interested in the particular case where we have a sample that is polycrystalline but has some texture, i.e., preferred orientations of crystallites, and we seek to understand how scattered intensities from such a sample may be propagated through the Fourier transform to obtain a scientifically relevant real-space pair correlation function, and in principle, how to model that function to obtain information about the texture.

We first consider a number of special cases. If the sample is a single crystal where the average crystal structure solution is desired, two simplifications can speed up data acquisition. Firstly, the crystallinity results in scattering being confined to small volumes of reciprocal space in the vicinity of reciprocal lattice points. Once the unit cell is determined, and the UB matrix giving the orientation of the crystal on the goniometer, it is possible for the single crystal diffractometer to reorient the crystal and detector in such a way as to visit only the volumes of reciprocal space in the vicinity of the reciprocal lattice points and integrate the intensity in those regions, neglecting the large regions of reciprocal space in between. Furthermore, if the symmetry of the unit cell is known it may be possible to collect a complete dataset by exploring only a subset of the full reciprocal-space volume, although measuring equivalent peaks in different regions of reciprocal-space can help with corrections for experimental artifacts such as sample self-absorption. If, as is increasingly the case, we are interested also in diffuse scattering in the crystal, then the full reciprocal space volume must be collected, for example, using the OAR approach. This is becoming highly feasible these days with the use of high-energy x-rays at synchtrotron sources coupled with large area photon counting detectors Schaub *et al.* [2007, 2011]; Osborn and Welberry [1990]; Welberry

et al. [1998]; Welberry and Proffen [1998]; Proffen and Welberry [1997]and with neutron diffraction instruments designed for this purpose Rosenkranz and Osborn [2008]; Keen *et al.* [2006]; Frost *et al.* [2010]; Tamura *et al.* [2012].

If the sample is an isotropic powder with a large number of grains equally sampling all orientations (a good powder average), then there is no need to rotate the sample as the scattering from the powder itself is isotropic. In practice, samples often are spun about an axis perpendicular to the incident beam, especially in synchrotron experiments with small, highly parallel, beams to improve the powder statistics and the isotropy of the measured scattering. In powder measurements, orientational information is lost because the images taken with the sample at different orientations are summed without storing their orientations, and a 1D function, $S(Q)$, is measured. This results in the regular 1D PDF, $G(r)$, when Fourier transformed. It is assumed in such a case that there is no structural coherence between grains and so the measured structure function is a superposition of structure functions of identical crystallites taking all possible orientations. Mathematically and experimentally, powder-like data can be obtained from a single crystal by rotating it about an axis parallel to the incident beam at each orientation of the perpendicular rotation. If a 2D detector is being used, integrating around the Debye-Scherrer rings on the detector is equivalent to rotating the sample about the beam axis, making it somewhat straightforward to obtain a 1D PDF from a 3D PDF dataset for comparison with (or to replace) powder measurements.

Let us now consider the case where the sample is made up of two identical crystallites of the same material that are misoriented with respect to each other, and far enough apart that they are both in the incident beam but beyond the coherence volume of the beam. In other words, we assume that scattering from each crystallite is incoherent and the total observed scattering is just the linear superposition of the scattering from each crystallite

(we will assume incoherent scattering between crystallites from hereon out). We define $\boldsymbol{\Omega}$, as the three-vector that contains the Euler angles that define the relative orientation of one crystallite with the other one. For convenience, and without loss of generality, we assume the sample reference frame is the reference frame of one of the crystallites, which we call the reference crystallite. If we measured either one of the crystallites as an individual single crystal using the orthogonal axes rotation approach we would get the same single crystal structure function. However, the measurement is carried out in such a way that the signals from the two crystallites are superposed on the detector. The crystallite structure function can be determined if we are able to separate the superposed signals from each crystallite. For crystalline materials this separation is straightforward and this approach is called polycrystallography and has been developed to a high level Von Dreele [2013]

This reasoning is readily extended to the case of M separable diffraction patterns from M crystallites. In this case, as before, a unique reference frame is defined on a reference crystallite on the sample, which we call the sample reference frame, and we define $\boldsymbol{\Omega}_m$ as being the Euler angles that give the orientation of the mth crystallite with respect to this reference frame. If $\mathbf{R_m}$ is the rotation matrix that rotates the sample reference frame onto the mth crystallite reference frame, we have the following relation

$$\mathbf{R}_m = \mathbf{R}(\boldsymbol{\Omega}_m),\tag{5.5}$$

$$\mathbf{r}_{ij}^m = \mathbf{R}_m \mathbf{r}_{ij},\tag{5.6}$$

where $\mathbf{r}_{ij}^m$ refers to the $\mathbf{r}_{ij}$ interatomic vector of the reference crystallite, but in the mth crystallite at angle $\boldsymbol{\Omega}_m$. We can thus write the polycrystalline sample-structure function $S_p(\mathbf{Q})$, as

$$S_p(\mathbf{Q}) = 1 + \frac{1}{N\langle f \rangle^2} \sum_m \sum_{i \neq j} f_i^* f_j e^{i\mathbf{Q} \cdot (\mathbf{R}_m \mathbf{r}_{ij})}\tag{5.7}$$

where for notational simplicity we have dropped the explicit Q-dependence of the atomic form factors. The double-sum over i and j is now a sum over the interatomic vectors between atoms in the reference crystallite. In Equation 5.6 crystallites with different orientations were generated by rotating this reference crystallite. This is a 3D structure function, similar to the single crystal structure function, which could be measured using the OAR method, for example.

We now turn to a polycrystalline sample with a large number of crystallites where the scattering from the individual crystallites are no longer separable, but the sample is still not isotropic: a textured powder. The patterns from the individual grains strongly overlap and multiple crystallites contribute to each region (voxel) of reciprocal space defined by the **Q** resolution of our measurement. In this case we would like to convert Eq. 5.7 to a continuous function. We define a volume element $d\mathbf{\Omega}$ in the Euler angle space that runs from (θ, ϕ, ξ) to $(\theta + d\theta, \phi + d\phi, \xi + d\xi)$. We can then define the number of crystallites in the beam that have an orientation such that their Euler angles place it in that volume element of angle-space as $D(\mathbf{\Omega})$ and we call this the orientation distribution function, or ODF Bunge [1982].

Now, returning to Eq. 5.7, we would like to rewrite it in terms of a sum over all orientation directions rather than a sum over m. If we denote the number of crystallites with orientation $\mathbf{\Omega}$ as $n(\mathbf{\Omega})$ and the total number of crystallites within the sample as n_0. The total number of atoms, N is then given by

$$N = N' \cdot n_0, \tag{5.8}$$

where N' is the number of atoms in the reference crystallite. The sum over m then becomes

$$\sum_m 1 = \sum_{\mathbf{\Omega}} n(\mathbf{\Omega}) = n_0. \tag{5.9}$$

Furthermore, since the crystallite with the same orientation $\mathbf{\Omega}$ gives the same contribution to $S_p(\mathbf{Q})$, we can rewrite $S_p(\mathbf{Q})$ as the summation over different crystallite orientations,

weighted by the number of crystallites with that orientation:

$$S_p(\mathbf{Q}) = 1 + \frac{1}{N\langle f \rangle^2} \sum_m \sum_{i \neq j} f_i^* f_j e^{i\mathbf{Q}\cdot(\mathbf{R}_m \mathbf{r}_{ij})} \tag{5.10}$$

$$= 1 + \frac{1}{N\langle f \rangle^2} \sum_m \sum_{i \neq j} f_i f_j e^{i\mathbf{Q}\cdot(\mathbf{R}_{\Omega_m} \mathbf{r}_{ij})} \tag{5.11}$$

$$= 1 + \frac{1}{N\langle f \rangle^2} \sum_{\mathbf{\Omega}_d} n(\mathbf{\Omega}_d) \sum_{i \neq j} f_i^* f_j e^{i\mathbf{Q}\cdot\left(\mathbf{R}_{\Omega_d} \mathbf{r}_{ij}\right)} \tag{5.12}$$

$$= 1 + \frac{1}{N\langle f \rangle^2} \int n(\mathbf{\Omega}) \sum_{i \neq j} f_i^* f_j e^{i\mathbf{Q}\cdot(\mathbf{R}_\Omega \mathbf{r}_{ij})} d\mathbf{\Omega}. \tag{5.13}$$

For crystallites oriented quasi-continuously in every orientation, $n(\mathbf{\Omega})$ represents the orientation distribution of crystallites on a continuous orientation variable $\mathbf{\Omega}$. We then define function $D(\mathbf{\Omega}) = n(\mathbf{\Omega})/n_0$ and rewrite Eq. 5.13 as

$$S_p(\mathbf{Q}) = 1 + \frac{1}{N'\langle f \rangle^2} \int \frac{n(\mathbf{\Omega})}{n_0} \sum_{i \neq j} f_i^* f_j e^{i\mathbf{Q}\cdot(\mathbf{R}_\Omega \mathbf{r}_{ij})} d\mathbf{\Omega} \tag{5.14}$$

$$= 1 + \frac{1}{N'\langle f \rangle^2} \int D(\mathbf{\Omega}) \sum_{i \neq j} f_i^* f_j e^{i\mathbf{Q}\cdot(\mathbf{R}_\Omega \mathbf{r}_{ij})} d\mathbf{\Omega}. \tag{5.15}$$

In practice, $S_p(\mathbf{Q})$ can be evaluated by exchanging the order of the summation over i and j with the integration over $\mathbf{\Omega}$ and evaluate the integral involving the ODF and the complex exponential factor.

Here in Equation 5.15 the function $D(\mathbf{\Omega})$ has the meaning of the fraction of the crystallites with orientation $\mathbf{\Omega}$ among all crystallites in the sample. By definition, $D(\mathbf{\Omega})$ represents the orientation distribution function of the sample. Since the number function $n(\mathbf{\Omega})$. It is a sample-dependent property, not depending explicitly on sample orientation and is expressed in the sample reference frame. Since the ODF is a probability distribution, it has the normalization property:

$$\int D(\mathbf{\Omega}) d\mathbf{\Omega} = 1 \tag{5.16}$$

In the special case that we have considered here, the sample is assumed to consist of many identical crystallites that all have the same structure function, $S'(\mathbf{Q})$, of the reference crystallite but are oriented with respect to that crystallite by $\boldsymbol{\Omega}$. To capture this we introduce a generalized structure function, for the "misoriented" crystallites,

$$S'(\mathbf{Q}, \boldsymbol{\Omega}) = 1 + \frac{1}{N'\langle f \rangle^2} \sum_{i \neq j} f_i^* f_j e^{i\mathbf{Q}\cdot(\mathbf{R}_{\boldsymbol{\Omega}}\mathbf{r}_{ij})}. \tag{5.17}$$

We can then rewrite the polycrystalline sample structure function in terms of $S'(\mathbf{Q}, \boldsymbol{\Omega})$, taking advantage of the normalization property of the ODF in Eq. 5.33. First, we change the order of integration and summing,

$$S_p(\mathbf{Q}) = 1 + \frac{1}{N'\langle f \rangle^2} \int D(\boldsymbol{\Omega}) \sum_{i \neq j} f_i^* f_j e^{i\mathbf{Q}\cdot(\mathbf{R}_{\boldsymbol{\Omega}}\mathbf{r}_{ij})} d\boldsymbol{\Omega} \tag{5.18}$$

$$= 1 + \frac{1}{N'\langle f \rangle^2} \sum_{i \neq j} f_i^* f_j \int D(\boldsymbol{\Omega}) e^{i\mathbf{Q}\cdot(\mathbf{R}_{\boldsymbol{\Omega}}\mathbf{r}_{ij})} d\boldsymbol{\Omega} \tag{5.19}$$

$$= 1 + \frac{1}{N'\langle f \rangle^2} \sum_{i \neq j} f_i^* f_j I_{ij}^D(\mathbf{Q}) \tag{5.20}$$

which serves to define the integral

$$I_{ij}^D(\mathbf{Q}) = \int D(\boldsymbol{\Omega}) e^{i\mathbf{Q}\cdot(\mathbf{R}_{\boldsymbol{\Omega}}\mathbf{r}_{ij})} d\boldsymbol{\Omega}. \tag{5.21}$$

Now, taking advantage of the normalization property of our ODF we can write

$$S_p(\mathbf{Q}) = \int D(\boldsymbol{\Omega}) 1 d\boldsymbol{\Omega} + \int D(\boldsymbol{\Omega}) \frac{1}{N'\langle f \rangle^2} \sum_{i \neq j} f_i^* f_j e^{i\mathbf{Q}\cdot(\mathbf{R}_{\boldsymbol{\Omega}}\mathbf{r}_{ij})} d\boldsymbol{\Omega} \tag{5.22}$$

$$= \int D(\boldsymbol{\Omega}) S'(\mathbf{Q}, \boldsymbol{\Omega}) d\boldsymbol{\Omega}. \tag{5.23}$$

Equation 5.23 expresses the structure function of the sample as an orientational distribution weighted arithmetic average of the structure function of the reference crystallite.

We note that Equation 5.23 for the case of discrete and separable crystallites may also be rewritten in this way as

$$S_p(\mathbf{Q}) = 1 + \frac{1}{N\langle f \rangle^2} \sum_m \sum_{i \neq j} f_i^* f_j e^{i\mathbf{Q}\cdot(\mathbf{R}_m \mathbf{r}_{ij})} \tag{5.24}$$

$$= \sum_m \frac{1}{n_0} + \sum_m \frac{1}{N' n_0 \langle f \rangle^2} \sum_{i \neq j} f_i^* f_j e^{i\mathbf{Q}\cdot(\mathbf{R}_m \mathbf{r}_{ij})} \tag{5.25}$$

$$= \frac{1}{n_0} \sum_m \left(1 + \frac{1}{N' \langle f \rangle^2} \sum_{i \neq j} f_i^* f_j e^{i\mathbf{Q}\cdot(\mathbf{R}_m \mathbf{r}_{ij})} \right) \tag{5.26}$$

$$= \frac{1}{n_0} \sum_m S'(\mathbf{Q}, \boldsymbol{\Omega}_m), \tag{5.27}$$

Equations 5.27 and 5.23 hold when the approximation that the sample is made up of multiple identical crystallites, or nanoparticles, that have different orientations.

We now consider how this propagates through the Fourier transform to yield a textured polycrystalline pair correlation function, $G_p(\mathbf{r})$,

$$G_p(\mathbf{r}) = \frac{1}{(2\pi)^3} \int \left[S_p(\mathbf{Q}) - 1 \right] e^{-i\mathbf{Q}\cdot\mathbf{r}} d\mathbf{Q} \tag{5.28}$$

$$= \int \left[\frac{1}{(2\pi)^3} \int D(\boldsymbol{\Omega}) \left(S'(\mathbf{Q}, \boldsymbol{\Omega}) - 1 \right) d\boldsymbol{\Omega} \right] e^{-i\mathbf{Q}\cdot\mathbf{r}} d\mathbf{Q} \tag{5.29}$$

$$= \int D(\boldsymbol{\Omega}) \left[\frac{1}{(2\pi)^3} \int \left(S'(\mathbf{Q}, \boldsymbol{\Omega}) - 1 \right) e^{-i\mathbf{Q}\cdot\mathbf{r}} d\mathbf{Q} \right] d\boldsymbol{\Omega} \tag{5.30}$$

$$= \int D(\boldsymbol{\Omega}) G'(\mathbf{r}, \boldsymbol{\Omega}) d\boldsymbol{\Omega}. \tag{5.31}$$

Where $G'(\mathbf{r}, \boldsymbol{\Omega})$ is, following the definition of PDF in Equation 5.4, the 3D PDF from of a crystallite with orientation $\boldsymbol{\Omega}$, expressed as

$$G'(\mathbf{r}, \boldsymbol{\Omega}) = \frac{1}{(2\pi)^3} \int \left(S'(\mathbf{Q}, \boldsymbol{\Omega}) - 1 \right) e^{-i\mathbf{Q}\cdot\mathbf{r}} d\mathbf{Q}. \tag{5.32}$$

These equations serve to define the real and reciprocal-space representations of textured polycrystalline samples. In general, $S_p(\mathbf{Q})$ may be measured in the same way as we measure

the 3D PDF of a single-crystal, for example, using the OAR method with x-rays or in a neutron single-crystal experiment. If we know $S'(\mathbf{Q})$, the structure function of the reference crystallite, we can compute from it $S'(\mathbf{Q}, \mathbf{\Omega})$ for all angles, which allows to determine $D(\mathbf{\Omega})$ for our sample. We note that the derivation did not assume crystallinity of the sample, and so it is equally applicable to polycrystalline textured nanoparticle samples and non-isotropic amorphous samples, provided that in these samples the approximation that the local clusters are all equivalent to each other apart from their orientation.

5.3 Reduced forms of $\mathbf{S_p(Q)}$ for special textures and experiment geometries

5.3.1 Isotropic sample

In this section we consider the form of $I_{ij}^D(\mathbf{Q}) = \int D(\mathbf{\Omega}) e^{i\mathbf{Q}\cdot(\mathbf{R}_\mathbf{\Omega}\mathbf{r}_{ij})}$ (Eq. 5.21) for some special textures.

If we compute the normalization of $D(\mathbf{\Omega})$ in a orientation coordinate system with polar angles, θ and ϕ, and the rotation angle around the polar axis, ξ, then we have

$$\int D(\mathbf{\Omega})d\mathbf{\Omega} = \int D(\mathbf{\Omega}(\theta, \phi, \xi))|J\mathbf{\Omega}(\theta, \phi, \xi)|d\theta d\phi d\xi = 1 \tag{5.33}$$

where $|J\mathbf{\Omega}(\theta, \phi, \xi)|$ is the determinant of the Jacobian matrix J of the orientation $\mathbf{\Omega}$ as a function of the angular variables. We have

$$|J\mathbf{\Omega}(\theta, \phi, \xi)| = \frac{1}{8\pi^2} \sin\theta. \tag{5.34}$$

For an isotropic powder sample with crystallites oriented homogeneously along every direction with equal probability, its ODF is a constant $D(\mathbf{\Omega}) = D = 1/8\pi^2$, and the integral

becomes Egami and Billinge [2012]

$$I_{ij}^{D}(\mathbf{Q}) = \int d\mathbf{\Omega} D e^{i\mathbf{Q}\cdot(\mathbf{R_\Omega r}_{ij})} \tag{5.35}$$

$$= D \int d\mathbf{\Omega} e^{i\mathbf{Q}\cdot(\mathbf{R_\Omega r}_{ij})} \tag{5.36}$$

$$= \frac{1}{8\pi^2} \int_0^{2\pi} d\xi \int_0^{2\pi} d\phi \int_0^{\pi} e^{iQr_{ij}\cos\theta} \sin\theta d\theta \tag{5.37}$$

$$= \frac{\sin(Qr_{ij})}{Qr_{ij}} \tag{5.38}$$

It has been shown that in this case $S_p(\mathbf{Q})$ reduces to the well-known Debye scattering equation for ideal powder Debye [1915]; Egami and Billinge [2012], independent of crystallite orientation. Due to the fact that the expression ODF is independent of the crystallite orientation, the calculation for this isotropic case is greatly simplified by choosing the integration axis to be aligned with each atomic vector $\mathbf{r}_{ij}$ in each specific integration.

5.3.2   Single-crystalline sample

On the other hand, when all crystallites are perfectly aligned, as in a single crystal, along $\mathbf{\Omega}_a$, then the ODF of the sample would be a delta function at $\mathbf{\Omega} = \mathbf{\Omega}_a$, namely $D(\mathbf{\Omega}) = \delta(\mathbf{\Omega} - \mathbf{\Omega}_a)$. The integral thus becomes

$$I_{ij}^{D}(\mathbf{Q}) = \int d\mathbf{\Omega} \delta(\mathbf{\Omega} - \mathbf{\Omega}_a) e^{i\mathbf{Q}\cdot(\mathbf{R_\Omega r}_{ij})} \tag{5.39}$$

$$= e^{i\mathbf{Q}\cdot(\mathbf{R_{\Omega_a} r}_{ij})}. \tag{5.40}$$

$S_p(\mathbf{Q})$ thus reduces to the structure function of a single crystal,

$$S_p(\mathbf{Q}) = \int \delta(\mathbf{\Omega} - \mathbf{\Omega}_a) S'(\mathbf{Q}, \mathbf{\Omega}) d\mathbf{\Omega} = S'(\mathbf{Q}, \mathbf{\Omega}_a). \tag{5.41}$$

Note that for a single crystal sample since it only contains a single crystallite, the sample and crystallite orientations are thus identical and can be represented by $\mathbf{\Omega}_a$.
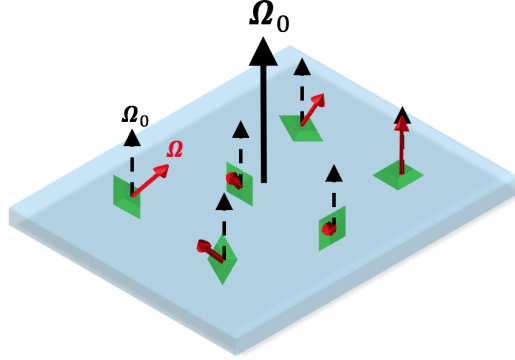
Figure 5.1: Illustration of the sample orientation, $\boldsymbol{\Omega}_0$ (black arrows), and crystallite orientation, $\boldsymbol{\Omega}$ (red arrows).

5.3.3 Thin film sample

For the thin film sample of our interest, where all the crystallites have one particular crystal axis oriented parallel to the beam while having random orientations within the plane perpendicular to the beam, $\boldsymbol{\Omega}_a = (\theta_a, \phi_a)$ its ODF would consist delta functions that fix the direction to the preferred axis, and an isotropic distribution within the plane perpendicular to that axis. Again if we define the sample reference frame to align with the lab frame so that $(\theta_0, \phi_0) = (0, 0)$ is satisfied, we express the thin film ODF D_{tf} as:

$$D_{\text{tf}}(\boldsymbol{\Omega}) = \frac{\int_0^{2\pi} \int_0^{\pi} \sin\theta d\theta d\xi}{\int_0^{2\pi} d\phi \int_0^{2\pi} \int_0^{\pi} \sin\theta d\theta d\xi} \delta(\theta - \theta_a)\delta(\phi - \phi_a) \tag{5.42}$$

$$= \frac{1}{4\pi} \frac{\delta(\theta - \theta_a)}{\sin\theta_a} \delta(\phi - \phi_a). \tag{5.43}$$

Here ξ is the rotation angle within the plane. Fig. 5.1 is an illustrate of the crystallites with random orientation.

To do a 2D PDF experiment we pick a crystallographic zone axis and place it perpendicular to the incident x-ray beam and rotate the sample about this axis, as shown in Fig. 5.2. The scattering is now cylindrically symmetric and, if we refer to the unique axis as the z-axis
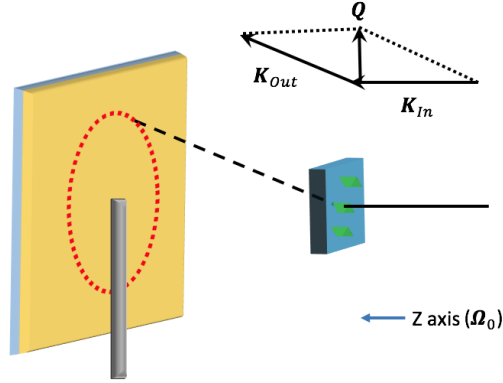
Figure 5.2: Geometry of the 2D PDF measurement. The sample orientation $\mathbf{\Omega}_0$ is aligned with the z axis.

$\mathbf{Q}$ can then be expressed by two scalar values, Q_z and Q_R, where Q_R is the length of the Q-vector perpendicular to the rotation axis. Without loss of generality we can pick the z-axis to be one of the sample reference axes, and we get the 2D structure function by integrating the sample orientation over all angles, ξ, perpendicular to the z axis.

As shown below, $S_p(\mathbf{Q})$ reduces to the 2D structure function $S(Q_R, Q_z)$ He *et al.* [1993] as we average $S'(\mathbf{Q}, \mathbf{\Omega})$ over the ODF in Equation 5.43 :

$$S_p(\mathbf{Q}) = \int D_{\mathrm{tf}}(\mathbf{\Omega}) S'(\mathbf{Q}, \mathbf{\Omega}) d\mathbf{\Omega} \tag{5.44}$$

$$= 1 + \frac{1}{N'\langle f \rangle^2} \sum_{i \neq j} f_i^* f_j \int e^{i\mathbf{Q} \cdot (\mathbf{R_\Omega r}_{ij})} \frac{1}{4\pi^2} \frac{\delta(\theta - \theta_a)}{\sin \theta_a} \delta(\phi - \phi_a) \sin \theta d\theta d\phi d\xi \tag{5.45}$$

$$= 1 + \frac{1}{N'\langle f \rangle^2} \sum_{i \neq j} f_i^* f_j \int e^{i\mathbf{Q} \cdot (\mathbf{R}_{\theta_a, \phi_a, \xi} \mathbf{r}_{ij})} d\xi. \tag{5.46}$$

The of the exponential factor over variable ξ reduces to the zeroth order Bessel function $J_0(x)$:

$$\int e^{i\mathbf{Q}\cdot(\mathbf{R}_{\theta_a,\phi_a,\xi}\mathbf{r}_{ij})}d\xi = \int e^{i\left(Q_z r_{ij}^z + Q_R r_{ij}^R \cos(\xi_{ij}-\xi)\right)}d\xi \tag{5.47}$$

$$= e^{iQ_z r_{ij}^z}\int e^{iQ_R r_{ij}^R \cos\xi_{ij}\cos\xi + iQ_R r_{ij}^R \sin\xi_{ij}\sin\xi}d\xi \tag{5.48}$$

$$= e^{iQ_z r_{ij}^z} I_0\left(\sqrt{\left(iQ_R r_{ij}^R\right)^2 \left(\sin^2\xi_{ij} + \cos^2\xi_{ij}\right)}\right) \tag{5.49}$$

$$= e^{iQ_z r_{ij}^z} J_0\left(Q_R r_{ij}^R\right). \tag{5.50}$$

Here r_{ij}^z and r_{ij}^R are the parallel and perpendicular (in-plane) components of the interatomic separation with respect to the axis of cylindrical symmetry. ξ_{ij} is the angle between the in-plane components of $\mathbf{Q}$ and $\mathbf{r}_{ij}$ Thus the integral can be written as

$$S_p(\mathbf{Q}) = 1 + \frac{1}{N'\langle f\rangle^2}\sum_{i\neq j} f_i^* f_j e^{iQ_z r_{ij}^z} J_0(Q_R r_{ij}^R) \tag{5.51}$$

$$= S(Q_R, Q_z). \tag{5.52}$$

This gives an explicitly derivation the 2D structure function $S(Q_R, Q_z)$ introduce in He *et al.* [1993]. Furthermore, the relation between the 2D PDF, $G(R, Q_z)$ He *et al.* [1993], the 2D structure function, $S(Q_R, Q_z)$, and the 3D PDF of the sample, $G_p(\mathbf{r})$, can be shown

explicitly by calculating $G_p(\mathbf{r})$ using the $S_p(\mathbf{Q})$ for the textured sample:

$$G_p(\mathbf{r}) = \frac{1}{(2\pi)^3} \int \left(S(\mathbf{Q}) - 1 \right) e^{-i\mathbf{Q}\cdot\mathbf{r}} d\mathbf{Q} \tag{5.53}$$

$$= \frac{1}{(2\pi)^3} \int \left(\int S'(\mathbf{Q}, \mathbf{\Omega}) D_{\mathrm{tf}}(\mathbf{\Omega}) d\mathbf{\Omega} - 1 \right) e^{-i\mathbf{Q}\cdot\mathbf{r}} d\mathbf{Q} \tag{5.54}$$

$$= \frac{1}{(2\pi)^3} \int \left(S(Q_R, Q_z) - 1 \right) e^{-i\mathbf{Q}\cdot\mathbf{r}} d\mathbf{Q} \tag{5.55}$$

$$= \frac{1}{(2\pi)^2} \int \int Q_R \left(S(Q_R, Q_z) - 1 \right) \left(\int e^{-i\mathbf{Q}\cdot\mathbf{r}} d\xi \right) dQ_R dQ_z \tag{5.56}$$

$$= \frac{1}{(2\pi)^2} \int \int Q_R \left(S(Q_R, Q_z) - 1 \right) J_0(Q_R R) e^{-iQ_z z} dQ_R dQ_z \tag{5.57}$$

$$= \frac{1}{(2\pi)^2} \int G(R, Q_z) e^{-iQ_z z} dQ_z \tag{5.58}$$

$$= G(R, z). \tag{5.59}$$

where $G(R, Q_z)$ is defined as

$$G(R, Q_z) = \int Q_R \left[S(Q_R, Q_z) - 1 \right] J_0(Q_R R) dQ_R \tag{5.60}$$

$$= \sum_{i \neq j} \int \frac{f_i^* f_j}{N' \langle f \rangle^2} Q_R J_0(Q_R r_{ij}^R) J_0(Q_R R) e^{iQ_z r_{ij}^z} dQ_R. \tag{5.61}$$

This reproduces and gives an explicit expression to the 2D PDF $G(R, Q_z)$ introduced in He *et al.* [1993]. We see that $G(R, Q_z)$ is related to the actual PDF of the film by a fourier transform along the z axis, the axis perpendicular to the film. The PDF of the film $G_p(\mathbf{r}, \mathbf{\Omega_0})$, after azimuthal intergration, turns out to be a function of the in-plane and out-of-plane distance, R and z, and so we can wrote it as $G(R, z)$. For an ideal 2 dimensional film with only 1 atomic layer, $G(R, z)$ reduces to $G(r)$, the regular orientationally averaged PDF.

Assuming that the atomic structure factor $f_j = f_j(Q)$ was independent of Q within the range of Q_R, the explicit expression for $G(R, Q_z)$ can be expressed as below:

$$G(R, Q_z) = \sum_{i \neq j} \int \frac{f_i^* f_j}{N'\langle f \rangle^2} Q_R J_0(Q_R r_{ij}^R) J_0(Q_R R) e^{iQ_z r_{ij}^z} dQ_R \tag{5.62}$$

$$= \sum_{i \neq j} \frac{f_i^* f_j e^{iQ_z r_{ij}^z}}{N'\langle f \rangle^2} \int_0^\infty Q_R J_0(Q_R r_{ij}^R) J_0(Q_R R) dQ_R \tag{5.63}$$

$$= \sum_{i \neq j} \frac{f_i^* f_j e^{iQ_z r_{ij}^z}}{N' R \langle f \rangle^2} \delta(R - r_{ij}^R). \tag{5.64}$$

The above expression shows clearly that the 2D PDF $G(R, Q_z)$ will display sharp peaks at the interactomic distance projected onto the film plane, r_{ij}^R. Take the integral expression of $G(R, Q_z)$ and set $Q_z = 0$, it is straightforward to show that

$$G(R, z) = \int_0^{2\pi} G(\mathbf{r}, \mathbf{\Omega}) \frac{1}{2\pi} \frac{\delta(\theta - \theta_a)}{\sin \theta_a} \delta(\phi - \phi_a) d\mathbf{\Omega}, \tag{5.65}$$

$$G(R, Q_z = 0) = \int G(R, z) e^{i0 \cdot z} dz = \int G(R, z) dz. \tag{5.66}$$

We see that $G(R, z)$ is derived from the average of the PDF in 3 dimensions $G(\mathbf{r})$ over ξ. This also shows that $G(R, Q_z = 0)$ represents the PDF of a 2 dimensional lattice which comes from the projection of the 3D structure along the z axis. It is shown in the next section that the PDF experiment with normal incidence geometry for a textured thin film sample gives a good approximated measure of $G(R, Q_z = 0)$.

Practically, $G(R, z)$ can be experimentally sampled in the reciprocal space via the structure function $S(Q_R, Q_z)$, and be partially reconstructed using the sampled reciprocal lattice vectors. As is evident from an earlier work He *et al.* [1993], due to the highly discrete atomic arrangement in layered material, $S(Q_R, Q_z)$ is only non-trivial at discrete, highly sparse values of Q_z, and it turns out that the number of experimentally accessible Q_z vectors are limited to about 3, which yields only smeared-up information after Fourier transformation into real space. On the other hand, thanks to relatively dense atom packing within each

layer, for each Qz, broad-ranged and continuous values of Q_R can be experimentally sampled. Therefore to yield usable insights into the structure, only in-plane Fourier transforme in performed on $S(Q_R, Q_z)$, which gives the 2D PDF $G(R, Q_z)$.

5.4 Geometry of highly textured thin film and 2D PDF measurement

Here we demonstrate the equivalence of a completely textured film measured edge on and a 2D PDF. As will be shown below, the PDF from normal incidence experiment gives a good approximate measurement to the 2D PDF. From scattering experiment, the 2D structure function $S(Q_R, Q_z)$ is only sampled at a subset of the reciprocal lattice vector which lies on the Ewald sphere, and this means that in G_{Exp} the Q_z is no longer an independent variable but a function of Q_R. Mathematically, Q_z and Q_R should satisfy the constraint $Q_z = Q_R \tan\theta$, where θ is the scattering angle. The measured PDF from normal-incidence experiment, $G_{Exp}(R)$, can then be calculated by applying this constraint to the integral expression for the 2D PDF:

$$G_{Exp}(R) = G(R, Q_z = Q_R \tan\theta) \tag{5.67}$$

$$= \sum_{i\neq j} \int \frac{f_i^* f_j}{N'\langle f\rangle}^2 Q_R J_0(Q_R r_{ij}^R) J_0(Q_R R) e^{iQ_R \tan\theta r_{ij}^z} dQ_R. \tag{5.68}$$

$$\tag{5.69}$$

Note that we've replaced Q_z with $Q_R \tan\theta$. To perform the integration, $\tan\theta$ need to be expressed using Q_R as

$$\theta = \frac{1}{2}\arcsin\frac{Q_R}{K}, \tag{5.70}$$

$$\tan\theta = \tan\left(\frac{1}{2}\arcsin\frac{Q_R}{K}\right) = \frac{Q_R}{\sqrt{K^2 - Q_R^2}}. \tag{5.71}$$

Furthermore, for small diffraction angle θ, we could approximate $\tan\theta$ and the complex exponential factor of G_{Exp} by their Taylor series:

$$\tan\theta \approx \sin\theta \approx \frac{1}{2}\frac{Q_R}{K}, \tag{5.72}$$

$$e^{iQ_R\tan\theta r_{ij}^z} \approx e^{iQ_R\frac{1}{2}\frac{Q_R}{K}r_{ij}^z} \approx 1 + \frac{1}{2}\frac{iQ_R^2}{K}r_{ij}^z - \frac{1}{8}\frac{Q_R^4}{K^2}(r_{ij}^z)^2. \tag{5.73}$$

Here $K = |\mathbf{K}|$ is the magnitude of the momentum of the incoming x-ray. Take this approximate expression for the $e^{Q_R\tan(\theta)r_{ij}^z}$ factor in G_{Exp}, we have

$$G_{Exp}(R) = \sum_{i\neq j}\int\frac{Q_R f_i^* f_j}{N'\langle f\rangle^2}\left(e^{iQ_R\tan\theta r_{ij}^z}\right)J_0(Q_R r_{ij}^R)J_0(Q_R R)dQ_R \tag{5.74}$$

$$\simeq \sum_{i\neq j}\int\frac{Q_R f_i^* f_j}{N'\langle f\rangle^2(2\pi)^2}\left(1 + \frac{1}{2}\frac{iQ_R^2}{K}r_{ij}^z - \frac{1}{8}\frac{Q_R^4}{K^2}(r_{ij}^z)^2\right)J_0(Q_R r_{ij}^R)J_0(Q_R R)dQ_R$$

$$\tag{5.75}$$

$$= \frac{1}{N'\langle f\rangle^2}\sum_{i\neq j}\int Q_R f_i^* f_j J_0(Q_R r_{ij}^R)J_0(Q_R R)dQ_R \quad + \tag{5.76}$$

$$\frac{1}{N'\langle f\rangle^2}\int\sum_{i\neq j}f_i^* f_j\frac{1}{2}\frac{iQ_R^3 r_{ij}^z}{K}J_0(Q_R r_{ij}^R)J_0(Q_R R)dQ_R \quad - \tag{5.77}$$

$$\frac{1}{N'\langle f\rangle^2}\int\sum_{i\neq j}f_i^* f_j\frac{1}{8}\frac{Q_R^5(r_{ij}^z)^2}{K^2}J_0(Q_R r_{ij}^R)J_0(Q_R R)dQ_R \tag{5.78}$$

$$= G(R, Q_z = 0) \quad + \tag{5.79}$$

$$\frac{i}{2KN'\langle f\rangle^2}\sum_{i\neq j}r_{ij}^z f_i^* f_j\int_{Q_R^{\min}}^{Q_R^{\max}}Q_R^3 J_0(Q_R r_{ij}^R)J_0(Q_R R)dQ_R \quad - \tag{5.80}$$

$$\frac{1}{8K^2 N'\langle f\rangle^2}\sum_{i\neq j}(r_{ij}^z)^2 f_i^* f_j\int_{Q_R^{\min}}^{Q_R^{\max}}Q_R^5 J_0(Q_R r_{ij}^R)J_0(Q_R R)dQ_R. \tag{5.81}$$

In the last expression we have made explicit the upper and lower bounds of Q_R, $Q_R^{\max}$ and $Q_R^{\min}$, which are used in practice in the integration to obtain numerical value of $G(R, Q_z = 0)$. Here the second term which is linear in r_{ij}^z cancels out by properly choosing the coordinate system, and therefore the dominant correction term turns out to be the even smaller quadratic term. The cancelling out of the linear (and in fact all odd-order terms in the expansion) reflects the fact that as a measurable quantity PDF should only contain real part. Thus we show that in principle, at least when the diffraction angle is relatively small so that $Q_R^{\max} \ll K \approx 40 \text{ Å}^{-1}$, the measured 1D PDF from the textured flim, $G_{Exp}(R)$ equals the 2D PDF $G(R, Q_z = 0)$ of the sample up to 2nd order correction.

The behavior of the correction terms can by understood by re-arranging its form. For the 3rd term in Equation 5.81, namely the first non-zero correction term, we have the following identity:

$$\frac{d^4 \left(R \cdot J_0(Q_R R)\right)}{R dR^4} = \frac{d^4 \left(\frac{\sin(Q_R R)}{Q_R}\right)}{R dR^4} = Q_R^4 J_0(Q_R R). \tag{5.82}$$

And the differential equation for the Bessel function

$$x^2 \frac{d^2 J_0}{dx^2} + x \frac{dJ_0}{dx} + x^2 J_0 = 0. \tag{5.83}$$

Thus we have

$$\frac{d^4\left(RJ_0(Q_RR)\right)}{dR^4} \tag{5.84}$$

$$= \frac{d^3}{dR^3}\left(d\left(J_0(Q_RR) + R\frac{dJ_0(Q_RR)}{dR}Q_R\right)\right) \tag{5.85}$$

$$= \frac{d^2}{dR^2}\left(2\frac{dJ_0(Q_RR)}{dR} + R\frac{d^2J_0(Q_RR)}{dR^2}\right) \tag{5.86}$$

$$= \frac{d^2}{dR^2}\left(\frac{dJ_0(Q_RR)}{dR} - Q_R^4R^3J_0(Q_RR)\right) \tag{5.87}$$

$$= \frac{d}{dR}\left(\frac{d^2J_0(Q_RR)}{dR^2} + Q_R^4\left[2RJ_0(Q_RR) + R^2\frac{dJ_0(Q_RR)}{dR}\right]\right) \tag{5.88}$$

$$= \frac{d}{dR}\left(Q_R^2\left[-\frac{1}{Q_R^2R}\frac{dJ_0(Q_RR)}{dR} - J_0(Q_RR)\right] + Q^4\left[2RJ_0(Q_RR) + R^2\frac{dJ_0(Q_RR)}{dR}\right]\right) \tag{5.89}$$

$$= \frac{1}{R^2}\frac{dJ_0(Q_RR)}{dR} - Q^2\frac{1}{R}\frac{d^2J_0(Q_RR)}{d(Q_RR)^2} + 2Q_R^4J_0(Q_RR) \tag{5.90}$$

$$+ 4RQ_R^5\frac{dJ_0(Q_RR)}{dQ_RR} + Q_R^6R^2\frac{d^2J_0(Q_RR)}{d(Q_RR)^2} \tag{5.91}$$

$$= \frac{2}{R^2}\frac{dJ_0(Q_RR)}{dR} - 3Q_R^4R\frac{dJ_0(Q_RR)}{dR} + \left(\frac{Q_R^2}{R} + 2Q_R^4 - Q_R^6R^2\right)J_0(Q_RR). \tag{5.92}$$

Therefore in the expanded form of Equation 5.82, the first term corresponds to a differential of the Bessel multiplied by the inverse of R, which we use to approximate the effect of the correction term. Since the integral expression of the correction term from Equation 5.81 is

an integration over Q_R, we move the differential over R out of the integration and have:

$$\frac{1}{32K^2}\sum_{i\neq j}(r_{ij}^z)^2 f_i^* f_j \int Q_R^5 J_0(Q_R r_{ij}^R) J_0(Q_R R) dQ_R \tag{5.93}$$

$$= \frac{1}{32K^2}\sum_{i\neq j}(r_{ij}^z)^2 f_i^* f_j \int Q_R J_0(Q_R r_{ij}^R) Q_R^4 J_0(Q_R R) dQ_R \tag{5.94}$$

$$\simeq \frac{1}{16K^2}\sum_{i\neq j}(r_{ij}^z)^2 f_i^* f_j \int Q_R J_0(Q_R r_{ij}^R) \frac{dJ_0(Q_R R)}{R^2 dR} dQ_R \tag{5.95}$$

$$= \frac{1}{16K^2}\sum_{i\neq j}\frac{(r_{ij}^z)^2}{R^2} f_i^* f_j \frac{d}{dR}\int Q_R J_0(Q_R r_{ij}^R) J_0(Q_R R) dQ_R \tag{5.96}$$

$$\simeq \frac{1}{16K^2}\frac{d}{dR}\sum_{i\neq j} f_i^* f_j \int Q_R J_0(Q_R r_{ij}^R) J_0(Q_R R) dQ_R \tag{5.97}$$

$$= \frac{1}{4K^2}\frac{d}{dR}G(R, Q_z = 0). \tag{5.98}$$

The above result shows that at each peak position in the exact 2D PDF, the effect of the leading order correction term from Eq. 5.81 is to add a large, negative component to the low-r side and a positive component to the high-r side of the peak. This gives an explanation for the large, negative peak in the experimentally measured 2D PDF shown in Fig. 5.3. Regarding the base line, from Equation 5.61 we know that the 2D PDF turns out to have a different baseline compared with that of the 1D PDF. The experimental 1D PDF has a baseline that is linear in r at low distance

$$G(R) = \int_{Q_{\min}}^{\infty} Q\left[S(Q) - 1\right]\sin(QR)dQ \tag{5.99}$$

$$= \sum_{i\neq j}\frac{f_i^* f_j}{N' R\langle f\rangle^2}\delta(R - r_{ij}) - \int_0^{Q_{\min}} Q\left[S(Q) - 1\right]\sin(QR)dQ \tag{5.100}$$

$$\simeq \sum_{i\neq j}\frac{f_i^* f_j}{N' R\langle f\rangle^2}\delta(R - r_{ij}) - \left[\int_0^{Q_{\min}} Q^2\left[S(Q) - 1\right]dQ\right]R. \tag{5.101}$$

On the other hand, for the experimental 2D PDF with a non-zero $Q_{\min}$, we have

$$G(R, Q_z) = \int_{Q_{\min}}^{\infty} Q_R \left[S(Q_R, Q_z) - 1\right] J_0(Q_R R) dQ_R \tag{5.102}$$

$$= \sum_{i \neq j} \frac{f_i^* f_j e^{iQ_z r_{ij}^z}}{N' R \langle f \rangle^2} \delta(R - r_{ij}^R) - \int_0^{Q_{\min}} Q_R \left[S(Q_R, Q_z) - 1\right] J_0(Q_R R) dQ_R \tag{5.103}$$

$$\simeq \sum_{i \neq j} \frac{f_i^* f_j e^{iQ_z r_{ij}^z}}{N' R \langle f \rangle^2} \delta(R - r_{ij}^R) - \int_0^{Q_{\min}} Q_R \left[S(Q_R, Q_z) - 1\right] 1 dQ_R. \tag{5.104}$$

Therefore the baseline of the experimentally measured 2D PDF is expected to have a much smaller slope compared with the atomic PDF.

In our software for calculating the 2D PDF, we have adopted a simplified form from the exact expression. Specifically, we have

$$S(Q_R, Q_z) = 1 + \frac{1}{N' \langle f \rangle^2} \sum_{i \neq j} f_i^* f_j J_0(Q_R r_{ij}^R) e^{iQ_z r_{ij}^z} = 1 + a, \tag{5.105}$$

$$a = \frac{1}{N' \langle f \rangle^2} \sum_{i \neq j} f_i^* f_j J_0(Q_R r_{ij}^R) e^{iQ_z r_{ij}^z}. \tag{5.106}$$

When the value of Q_z is small, the imaginary part of a (and also $S(Q_R, Q_z)$) is also small. If we drop the $\mathrm{Im}(a)$ term, $S(Q_R, Q_z)$ can be simplified and approximated as

$$S(Q_R, Q_z) = \sqrt{(1 + \mathrm{Re}(a))^2 + \mathrm{Im}(a)^2} \tag{5.107}$$

$$\simeq 1 + \mathrm{Re}(a) = 1 + \frac{1}{N' \langle f \rangle^2} \sum_{i \neq j} f_i^* f_j J_0(Q_R r_{ij}^R) \cos(Q_z r_{ij}^z), \tag{5.108}$$

which has been used in our simulation of the 2D PDFs.

5.5 Application of formalism to thin film data

To solve the structure of a real sample, we applied 2D PDF analysis to textured thin film of platinum. The results are as follows. The negative peaks in the data are from the $Q_z \neq 0$
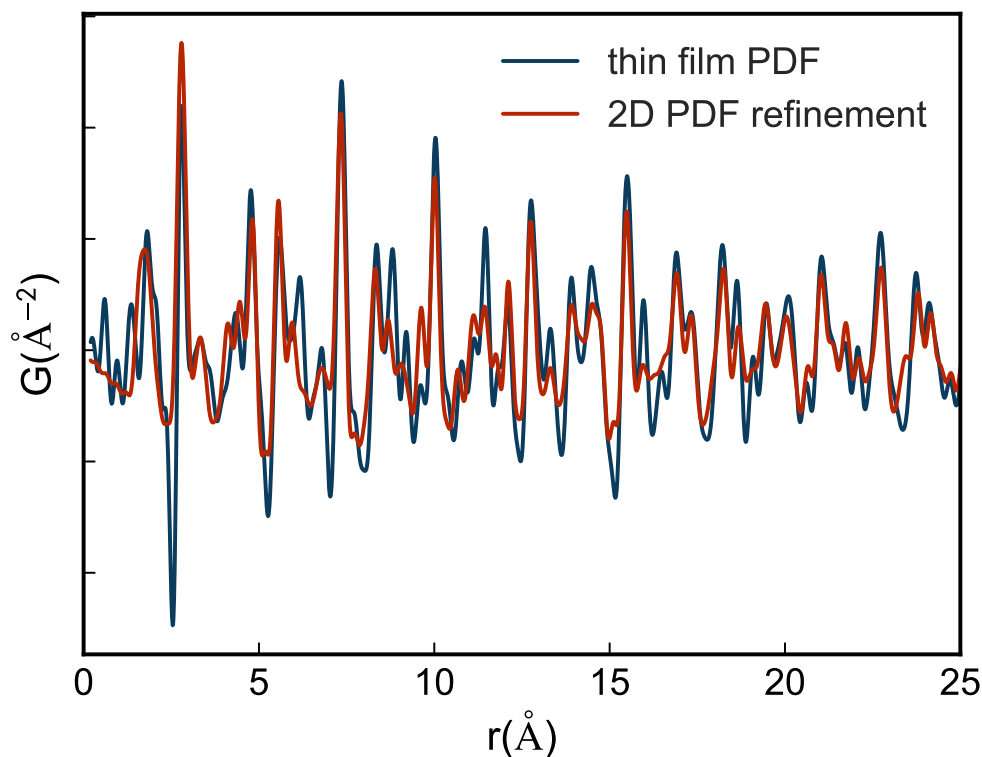
Figure 5.3: Experimental PDF from a textured Platinum thin film (blue) and the 2D PDF refinement result (red).

component, and has also been observed in a previous 2D PDF experiment He *et al.* [1993]. We performed least square fitting to the experimental PDF from the film, using the 2D PDF calculator software. The results are shown in Fig. 5.4. The fit gives a lattice constant of 3.949 Å and an Rw value of 68%. In particular, the experimental 2D PDF shows peak structures at small distances of around 1.9 Å 3.3 Å and 4.3 Å . Comparing the simulated 1D and 2D PDF with the experimental and fitted 2D PDF, as shown in Fig. 5.3, it becomes clear that these peaks are present only in the simulated 2D PDF with 111 direction but not in either the simulated 1D PDF or the 2D PDF with 001 orientation, and indicates that peaks at 1.9 Å 3.3 Å and 4.2 Å are unique to the 2D PDF. In fact the peak around 1.9 Å represents the nearest Pt-Pt separation in the 2D lattice projected from the Platinum lattice
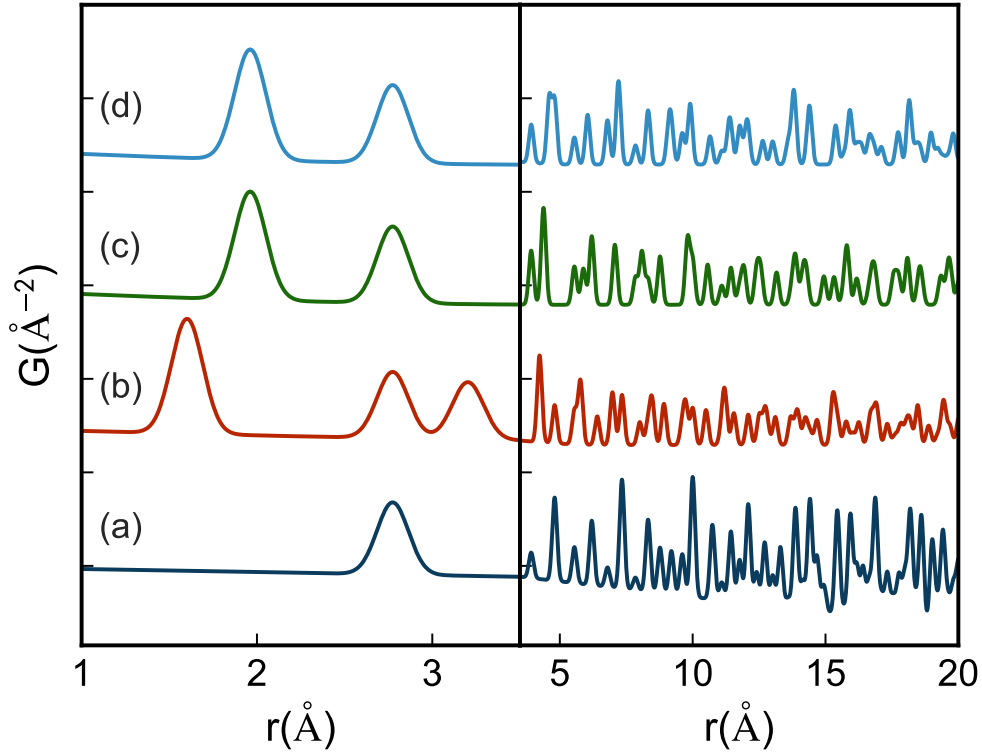
Figure 5.4: Simulated 1D PDF and 2D PDFs of Platinum. The calculated 1D PDF for a thin Platinum bulk sample (a) and calculated 2D PDF with 111 axis (b) and 001 axis (c) and 110 (d) were presented as references for the peak position.

(FCC structure with lattice constant around 3.9 Å) , and likewise, the peak at around 4.2 Å corresponds to the 4th neighboring distance of the same lattice. Thus the presence of these peaks specific to 2D PDF at small distances demonstrate the effectiveness of our proposed method of measuring the 2D PDF for textured sample. The fitting results captured reasonably well the peaks from the measured PDF, and gives a sterographic orientation of (0.62,0.83), which is very close to that of the 111 lattice orientation, (0.73, 0.73). While the peaks specific to the 2D PDF are barely visible at large radial distances, the peaks common for 1D PDF and 2D PDF are still distinguishable and is well captured in the fitting. The fact that the position of many peaks from the 2D PDF coincides with that from the 1D PDF

is due to alignment of the texture symmetry axis (111) to the beam direction: in this case the 2D lattice which gives the 2D PDF comes from the projection of the 3D lattice along a high symmetry direction of the lattice, and thus contains set of atomic separations identical to that in the 3D lattice. This also implies the possibility that the experimental 2D PDF may also contains considerable contribution from 1D PDF.

On the other hand, the visible deviations of the fitting from the data could be due to the complexity of the texture, the approximation of the sample as thin film, as well as the approximate nature of our method. For example it is reasonably to expect that the crystallites are not perfectly aligned along the c-axis. From our x-ray measurement in Bragg-Brentano geometry, there also exist, in addition to the strong 111 peak, a small peak at 311 direction. In addition here might be other structural inhomogeneity and agglomerations that produces bulk-like local structure, while we're not able to distinguish those peaks that shows up in both 2D and 1D PDF. On the other hand, as shown in previous sections the 2D PDF itself is an approximation to the measured PDF from the textured thin film, and this means, to a limited extent, additional deviation of the 2D PDF from refinement and the PDF measured from experiment.

In general, these results demonstrate that the measured PDF from the textured thin film serves as a good approximation to the 2D PDF of the sample and that our software was able to capture the major structural features reasonably well and yields useful information about the structure. Future improvements include using more realistic model for describing the texture, and also incorporation multiple phase refinement in the 2D PDF software.

5.6   Availability of software

Our software is available at diffpy.org

5.7   Conclusion and Outlook

In Summary, we developed a 2D PDF analysis method for thin films, and have applied it to analyze the structure of textured platinum thin film. We derived the 2D PDF equations, and have showed explicitly, by utilizing the orientation distribution function, the equivalence of the PDF from textured thin film to the 2D PDF with $Q_z = 0$. We showed, mathematically, the feasibility of experimental measurement of the 2D PDF from thin film, and have demonstrated this by a measurement on a textured Platinum thin film. The PDF from the film has peaks that are either specific to the 2D PDF or present in both 1D and 2D PDF, and are all well captured by our refinement software. These results demonstrate the functioning of the 2D PDF analysis method we developed.

Chapter 6

Development of the dynamic PDF method

In this chapter we proposed a new definition for the dynamic pair distribution function (PDF) that has direct connection with the atomic PDF. Under the new definition, the dynamic PDF incorporates the contribution from multi-phonon scattering, and can be easily computed from inelastic neutron scattering data. We discuss its relation with existing definitions of the dynamic PDF.

In addition, as a simple example of the dynamic PDF, we derive the dynamic PDF for a molecule containing two identical atoms.

6.1   A new definition for the dynamic pair distribution function

6.1.1   Motivation

Despite the progress in the experiment and theory of dynamic PDF, there are still blind spots and conflicting issues in the formalism of the dynamic PDF method which remain to be resolved. For example, previous definitions for the dynamic PDF (see Li *et al.* [2014a] for example) tends to subtract out the multi-phonon contribution from the inelastic structure function before doing Fourier transform. This approach retains the single phonon contribution and therefore the majority of the structural information. However, we noticed that it subtracts the multi-phonon contribution by fitting the smooth part of the structure function with a function with arbitrary values for the parameters and thus the asymptotic behavior of the resulting function is not treated explicitly. On the other hand, while the dynamic PDF itself yields gives important structural information that comes from the single phonon scattering process, its connection with the atomic pair distribution function (atomic PDF) has not been considered with mathematical rigor. In fact the present definitions for the dynamic PDF, for example proposed in McQueeney [1998], has the disadvantage of unable to reproduce the atomic PDF after integrating over energy.

Here we propose a new definition of the structure function and the dynamic PDF and explain its connection with the atomic PDF. We first derive the equations explicitly and show that, following the new definition, the structure function now has desirable asymptotic behavior at different energy levels and can be Fourier transformed to give structural information at

each energy level, namely the dynamic PDF. Moreover, we show that after integration over energy the dynamic PDF defined here gives the atomic PDF.

6.1.2 Definition and equations of the dynamic PDF

We first introduce the modified structure function and explain its relation with the familiar atomic structure functions. The total scattering structure function measured from an inelastic scattering experiment, $S(Q, E)$, can be divided into two parts, namely the Bragg/elastic scattering structure function, $S_B(Q, E)$, and the diffuse/inelastic scattering structure function, $S_D(Q, E)$ Billinge and Thorpe [2002]

$$S(Q, E) = S_B(Q, E) + S_D(Q, E). \tag{6.1}$$

We define the modified inelastic structure functions for Bragg scattering, $S'_B(Q, E)$, and for diffuse scattering, $S'_B(Q, E)$, based on their respective inelastic structure function, as

$$S'_B(Q, E) = S_B(Q, E) - e^{-2W}\delta(E), \tag{6.2}$$

$$S'_D(Q, E) = S_D(Q, E) - f(Q, E). \tag{6.3}$$

In Equation 6.3, $W = Q^2 \langle u^2 \rangle / 2$ is the Debye-Waller factor and $\langle u^2 \rangle$ is the ensemble-averaged atomic displacement. Following the definition in Equation 6.3, the expressions for $S'_B(Q, E)$ and the energy-integrated $S'_D(Q, E)$ can be found easily. For example,

$$S'_B(Q, E) = S_B(\mathbf{Q}, E) - e^{-2W}\delta(E) \tag{6.4}$$

$$= \delta(E) \sum_{i,j} \frac{f_j^* f_i}{N \langle f^2 \rangle} e^{\mathbf{Q} \cdot \mathbf{R}_{ij}} e^{-W_i - W_j} - e^{-2W}\delta(E) \tag{6.5}$$

$$= \delta(E) \sum_{i \neq j} \frac{f_j^* f_i}{N \langle f^2 \rangle} e^{\mathbf{Q} \cdot \mathbf{R}_{ij}} e^{-W_i - W_j}. \tag{6.6}$$

Here f_i is the scattering factor of atom i, and $\mathbf{R}_{ij}$ is the vector that connects the average positions of atom i and atom j. From Equation 6.6 we see that $S'_B(Q, E)$ stands for the structure function of the Bragg scattering, with the Q-independent self-scattering signal being subtracted. And $S'_D(Q, E)$ stands for the structure functions for the diffuse scattering but without the smooth multi-phonon scattering contribution. In particular, in the expression for $S_D(Q, E)$, $f(Q, E)$ is a continuous function of momentum Q and energy E which satisfies the following condition

$$\int f(Q, E)dE = 1 - e^{-2W} \approx 1. \tag{6.7}$$

$f(Q, E)$ is intended to represent the contribution to the measured structure function from multi-phonon scattering. It is clear that $f(Q, E)$ will not be totally fixed under under this constraint alone, and here we fix the form of $f(Q, E)$ by the additional requirement that $S'_D(Q, E)$ goes to zero at large Q. As will be shown below, as long as the condition in Equation 6.7 is satisfied, the energy integration of the modified structure function will produce the atomic structure function $S(Q)$ minus 1, and thus its transformation would give the atomic PDF.

One simplification to Equation 6.7 is to set $f(Q, E)$ at each energy level to be a constant which equals the limiting value of $f(Q, E)$ at large Q at that energy

$$f(E) = \lim_{Q \to \infty} S_D(Q, E) \tag{6.8}$$

$$\Rightarrow \int f(E)dE = \int \lim_{Q \to \infty} S_D(Q, E)dE = 1 - e^{-2W}. \tag{6.9}$$

Both Equation 6.7 and 6.9 will give the desired asymptotic behavior for the structure function (before and after the energy integration). This simplification of $f(Q, E)$, namely the removal of its Q-dependence at each energy level, turns out to be important as it not only allows these structure functions to be Fourier transformed at each distinct energy but also preserve structural information contained in both single- and multi-phonon scattering processes (occurring

at that particular energy level). This will be explained further in the following discussion. We define the modified inelastic structure function for the total scattering, $S'(Q, E)$, as the arithmetic sum of $S'_B(Q, E)$ and $S'_D(Q, E)$

$$S'(Q, E) = S(Q, E) - e^{-2W}\delta(E) - f(Q, E) \tag{6.10}$$

$$= S'_B(Q, E) + S'_D(Q, E). \tag{6.11}$$

Intuitively, $S'(Q, E)$ can be understood as the inelastic structure function without the smooth background (but keeping the desired asymptotic properties, as will be shown below). Regarding the asymptotic behavior of these modified structure functions, it is easy to show that

$$\lim_{Q\to\infty} \int S'(Q, E)dE = \lim_{Q\to\infty} \int S'_B(Q, E)dE \tag{6.12}$$

$$= \lim_{Q\to\infty} \int S'_D(Q, E)dE \tag{6.13}$$

$$= 0. \tag{6.14}$$

Equation 6.12 indicates that all the modified structure functions defined here approach the limit of zero as momentum Q becomes large. Therefore these structure functions can be Fourier transformed conveniently using existing numerical algorithms and yield structural information about lattice dynamics at each energy level, i.e. the dynamic PDF. Since we've chosen $f(Q, E)$ to be Q-independent at each energy, as specified in Equation 6.9, the resulting dynamic PDF would include the contribution from multi-phonon scattering.

Now we show that, defined in this form, the dynamic PDF is connected to the atomic PDF with well-defined mathematical relations. To start with, we show that the integration of the modified structure function $S'(Q, E)$ gives the quantity $S(Q) - 1$, where $S(Q)$ is the atomic structure function. Since $S(Q)$ and $S(Q, E)$ is related by Egami and Billinge [2012]

$$S(Q) = \int_{-\infty}^{\infty} S(Q, E)dE, \tag{6.15}$$

we have

$$\int S'(Q,E)dE = \left[\int S_B(Q,E) - e^{-2W}\delta(E)dE\right] + \left[\int S_D(Q,E)dE - f(Q,E)dE\right] \quad (6.16)$$

$$= \left[\int S_B(Q,E)dE - e^{-2W}\right] + \left[\int S_D(Q,E)dE - \left(1 - e^{-2W}\right)\right] \quad (6.17)$$

$$= \int S_B(Q,E) + S_D(Q,E)dE - 1 \quad (6.18)$$

$$= S(Q) - 1. \quad (6.19)$$

Equation 6.19 shows that after energy integration the modified structure function gives the familiar quantity of the atomic structure function minus 1, which can be Fourier transformed to yield the atomic PDF Egami and Billinge [2012].

Accordingly, we define the dynamic PDF by replacing $S(Q) - 1$ in the transformation of the atomic PDF with $S'(Q,E)$

$$G(r,E) = \int QS'(Q,E)\sin(Qr)dQ \quad (6.20)$$

$$= \delta(E)\sum_{i\neq j}\frac{f_j^* f_i}{rN\langle f^2\rangle}\int e^{-W_i-W_j}\sin(QR_{ij})\sin(Qr)dQ + \int QS'_D(Q,E)\sin(Qr)dQ. \quad (6.21)$$

The dynamic PDF defined above can be separated into two parts, corresponding to the two terms in the last line of Equation 6.21. The first term is the elastic (or uncorrelated) PDF Egami and Billinge [2012], where the integration over Q gives the broadened delta function that represents the pair density between two atoms at their average positions. The second term corresponds to the contribution from inelastic scattering, including the smooth multi-phonon contribution. Under this definition, the dynamic PDF recovers the atomic

PDF after the integration along the energy axis

$$\int G(r, E)dE = \int \int QS'(Q, E)\sin(Qr)dQdE \tag{6.22}$$

$$= \int Q\left(\int S(Q, E)dE - \int e^{-2W}\delta(E) + f(Q, E)dE\right) \cdot \sin(Qr)dQ \tag{6.23}$$

$$= \int Q\left(S(Q) - 1\right)\sin(Qr)dQ \tag{6.24}$$

$$= G(r). \tag{6.25}$$

Therefore under our definition, the dynamic PDF can be understood as the energy-dispersed version of the atomic PDF, and can be directly integrated to produce the latter.

6.2 Dynamic pair distribution function for diatomic molecule

In this chapter we discuss the analysis of the structural dynamics of materials using the dynamic pair distribution function (PDF) through the example of a diatomic molecule.

Section 6.2.1 list and briefly discussed a few physical quantities that are closely related to the development and understanding of pair distribution function analysis of dynamical system, which was propose and developed in the next few sections. These quantities will be introduced and briefly discussed, and will be used throughout the report. Section 6.2.2 derive the dynamic PDF of a diatomic molecule, in which the vibration of the molecule is restricted along the longitudinal direction with given characteristic frequency and amplitude. We derive $g(r, \omega)$ from, respectively, $g(r, t)$, $S(Q, \omega)$ and $S(Q, t)$, with minimal but different approximations for each derivation. Section 6.3 derive the dynamic PDF for a linear molecule with 3 identical atoms. We showed explicitly from this example the equivalency of the

dynamical PDF of any system with a harmonic vibration mode to a diatomic molecule, and the increasing difficulty in solving $g(r, \omega)$ analytically for a system with more than 2 atoms. Section 6.4 discussed some generic properties of the dynamic PDF of small atomic clusters, and emphasizes the loss of periodicity in the atomic motion as the number of atoms increases.

6.2.1   Some important physical quantities

6.2.1.1   Spatial-temporal correlation function $g(\mathbf{r}, t)$

The temporal pair distribution function, $g(\mathbf{r}, t)$, first introduced by Van Hove in Van Hove [1954], describes the correlation between the presence of a particle at $\mathbf{r}' + \mathbf{r}$ at time $t' + t$ and the presence of a particle in position $\boldsymbol{r}'$ at time t', averaged over $\mathbf{r}'$. $g(\mathbf{r}, t)$ and $S(\boldsymbol{Q}, \omega)$ is connected via Fourier transform

$$g(\boldsymbol{r}, t) = \frac{\hbar}{(2\pi)^3} \int d\boldsymbol{Q} \int d\omega \exp(-i\boldsymbol{Q} \cdot \boldsymbol{r} + i\omega t) S(\boldsymbol{Q}, \omega). \tag{6.26}$$

6.2.1.2   Dynamic PDF $g(\mathbf{r}, \omega)$

The dynamic pair distribution function Egami and Billinge [2012], $g(\mathbf{r}, \omega)$, is obtained by Fourier transforming $g(\boldsymbol{r}, t)$ over time t. Consistent with the interpretation of $g(\boldsymbol{r}, \omega)$ and that of ω (energy), $g(\mathbf{r}, \omega)$ can be interpreted as the correlation between the presence of a particle in position $\mathbf{r}'$ with energy ω' and the presence of a particle in position $\mathbf{r}' + \mathbf{r}$ with energy $\omega' + \omega$, averaged over $\mathbf{r}'$. Namely $g(\mathbf{r}, \omega)$ is the spatial density correlation function of the excited state with atomic vibration energy ω, which in a single phonon picture means the atomic density that oscillates with frequency ω. Here we consider only a single phonon because multi-phonon process contributes only broad structureless signal and thus is not

significant in the determination of small local structure using PDF (see for example Ch.7 from Egami and Billinge [2012] and Ch.2 from Billinge and Thorpe [2002]).

For a real lattice system, $g(r, \omega)$ remains essentially unchanged at low energies, meaning that the low energy phonons merely broadens the vibration of atoms but do not induce strong enough correlation between the motion of the atoms within local atomic paris. This corresponds to the situation of $\omega/\omega_0 \sim 0$ for the diatomic molecule, where the atomic peak at $r = R$ remains unsplit. Upon the presence of strongly localized phonon at somewhat elevated energy, the dynamics of pairs of local atoms becomes strongly enhanced, and the behavior of such atomic pairs resemble that of a diatomic molecule. Thus with such local phonon modes in a lattice system, the structure of the dynamic PDF at around these local atomic peaks would start to look like that of a diatomic molecule and display bifurcation and trifurcation as energy increases.

6.2.1.3   Phonon energy and amplitude

The inelastic structure function, $S(\boldsymbol{Q}, \omega)$, describes the scattering of the incoming particle by phonons with total momentum of $\boldsymbol{Q}$ and total energy ω. For single of multi-phonon process, ω is measured by the energy of a single phonon, ω_0, namely $\omega = n \cdot \omega_0$. In reality, the energy associated with phonon mode with mode energy ω_0 directly corresponds to the amplitude of the atomic vibration, and can be calculated by equating the time-averaged kinetic energy with the total mode energy ω. In specific, the volume integrated kinetic energy of a crystal with volume V, density ρ, and displacement u_0^2 equals $\frac{1}{4}\rho V \omega^2 u_0^2 \sin^2(\omega t)$,

and because $\langle \sin^2(\omega t) \rangle = \frac{1}{2}$, the time averaged kinetic energy is (Ref. Kittel [2005]Ch.3):

$$\frac{1}{8}\rho V \omega^2 u_0^2 = \frac{1}{2}(n + \frac{1}{2})\hbar\omega \tag{6.27}$$

$$\Rightarrow u_0^2 = \frac{4(n + \frac{1}{2})\hbar}{\rho V \omega} \tag{6.28}$$

This relates the displacement of a given mode to the occupancy n of the phonon of the mode. This also relates the quasi-particle picture with the wave picture of the phonon (the 'wave-particle duality' of phonons).

6.2.1.4 Single and multi-phonon process

Multi-phonon phonon process involving n phonons with energy ω_0 and a single phonon process with energy $n\omega_0$ might be equivalent in an energy transfer process, but they induce qualitatively different lattice dynamics. As will be discussed in detail below, in terms of dynamic PDF analysis, $\omega = n\omega_0$ which appears in $g(r, \omega)$ is interpreted as a phonon with a frequency of $n\omega_0$ instead of n phonons with frequency ω_0.

6.2.2 Derivation of the dynamic PDF for diatomic molecule

In this section we derive the dynamic PDF of a classical harmonic oscillator from the correlation function $g(r, t)$, and that of a quantum harmonic oscillator from $S(Q, \omega)$ and $S(Q, t)$, with minimal but different approximations for each derivation. For simplicity we only consider the 1 dimensional case in which the vibration of the molecule is restricted along the longitudinal direction (along the molecule). In both cases the harmonic oscillator has a characteristic frequency of ω_0 and amplitude of $2u_0$, with an equilibrium distance of R. The results obtained are thus useful in illuminating the effect of longitudinal phonons on the dynamic PDF.

The resulting expressions of $g(r, \omega)$ take different forms and are not necessarily equivalent to each other. Nevertheless, the peculiarities in the structure of these different representations of $g(r, \omega)$ may offer insights into the real $g(r, \omega)$ of the system from different angles.

6.2.2.1   Classical harmonic molecule: derivation from $g(r, t)$

The explicit expression for the dynamic PDF of diatomic molecule is simulated but not shown in Egami and Dmowski [2012]. Their temporal density correlation function $g(r, t)$ is easy to write down

$$g(r, t) = \delta(r - R + 2u_0 \sin(\omega_0 t)). \tag{6.29}$$

The dynamic PDF $g(r, \omega)$ is the temporal Fourier transform of $g(r, t)$

$$g(r, \omega) = \int g(r, t)e^{i\omega t}dt \tag{6.30}$$

$$= \int \delta(r - R + 2u_0 \sin(\omega_0 t))e^{i\omega t}dt. \tag{6.31}$$

To simplify the δ function, we use the notation $f(t) = r - R + 2u_0 \sin(\omega_0 t)$. Thus $f(t) = 0$ requires

$$|\frac{R - r}{2u_0}| \leq 1. \tag{6.32}$$

and the zeros of the function, t_n, are as follows

$$t_n = \begin{cases} \frac{1}{\omega_0}\left(\arcsin(\frac{R-r}{2u_0}) + 2n\pi\right) \\ \frac{1}{\omega_0}\left(-\arcsin(\frac{R-r}{2u_0}) + (2n+1)\pi\right) \\ n = 0, \pm 1, \pm 2, ... \end{cases}$$

Then $\delta(f(t))$ can be expanded as

$$\delta(f(t)) = \sum_n \frac{\delta(t - t_n)}{|\frac{\partial f}{\partial t}(t_n)|} \tag{6.33}$$

$$= \sum_n \frac{\delta\left(t - \frac{1}{\omega_0}\left(\arcsin(\frac{R-r}{2u_0}) + 2n\pi\right)\right)}{|2u_0\omega_0\cos\omega_0\frac{1}{\omega_0}\left(\arcsin(\frac{R-r}{2u_0}) + 2n\pi\right)|} + \frac{\delta\left(t - \frac{1}{\omega_0}\left(-\arcsin(\frac{R-r}{2u_0}) + (2n+1)\pi\right)\right)}{|2u_0\omega_0\cos\omega_0\frac{1}{\omega_0}\left(-\arcsin(\frac{R-r}{2u_0}) + (2n+1)\pi\right)|} \tag{6.34}$$

$$= \frac{1}{2u_0\omega_0}\sum_n \frac{\delta\left(t - \frac{1}{\omega_0}\left(\arcsin(\frac{R-r}{2u_0}) + 2n\pi\right)\right)}{|\cos\left(\arcsin(\frac{R-r}{2u_0})\right)|} + \frac{\delta\left(t - \frac{1}{\omega_0}\left(-\arcsin(\frac{R-r}{2u_0}) + (2n+1)\pi\right)\right)}{|\cos\left(\arcsin(\frac{R-r}{2u_0})\right)|}. \tag{6.35}$$

Plug this into the expression of the dynamic PDF, we have

$$g(r,\omega) = \int \delta(r - R + 2u_0\sin(\omega_0 t))e^{i\omega t}dt \tag{6.36}$$

$$= \frac{1}{2u_0\omega_0}\sum_n \frac{1}{|\cos\left(\arcsin(\frac{R-r}{2u_0})\right)|} \cdot \int \delta\left(t - \frac{1}{\omega_0}\left(\arcsin(\frac{R-r}{2u_0}) + 2n\pi\right)\right)e^{i\omega t}dt+ \tag{6.37}$$

$$\frac{1}{2u_0\omega_0}\sum_n \frac{1}{|\cos\left(\arcsin(\frac{R-r}{2u_0})\right)|} \cdot \int \delta\left(t - \frac{1}{\omega_0}\left(-\arcsin(\frac{R-r}{2u_0}) + (2n+1)\pi\right)\right)e^{i\omega t}dt \tag{6.38}$$

$$= \frac{1}{2u_0\omega_0}\sum_n \frac{e^{i\frac{\omega}{\omega_0}\left(\arcsin(\frac{R-r}{2u_0})+2n\pi\right)}}{|\cos\left(\arcsin(\frac{R-r}{2u_0})\right)|} + \frac{1}{2u_0\omega_0}\sum_n \frac{e^{i\frac{\omega}{\omega_0}\left(-\arcsin(\frac{R-r}{2u_0})+(2n+1)\pi\right)}}{|\cos\left(\arcsin(\frac{R-r}{2u_0})\right)|} \tag{6.39}$$

$$= \frac{e^{i\frac{\omega}{\omega_0}\arcsin(\frac{R-r}{2u_0})} + e^{-i\frac{\omega}{\omega_0}\left(\arcsin(\frac{R-r}{2u_0})-\pi\right)}}{2u_0\omega_0|\cos\left(\arcsin(\frac{R-r}{2u_0})\right)|}\sum_n e^{i2n\pi\frac{\omega}{\omega_0}} \tag{6.40}$$

$$= e^{i\frac{\omega}{\omega_0}\frac{\pi}{2}}\frac{\cos\frac{\omega}{\omega_0}\left(\arcsin(\frac{R-r}{2u_0}) - \frac{\pi}{2}\right)}{u_0\omega_0|\cos\left(\arcsin(\frac{R-r}{2u_0})\right)|}\sum_n e^{i2n\pi\frac{\omega}{\omega_0}} \tag{6.41}$$

$$= \sum_l (i^l)\frac{\cos l\left(\arcsin(\frac{R-r}{2u_0}) - \frac{\pi}{2}\right)}{u_0|\cos\left(\arcsin(\frac{R-r}{2u_0})\right)|}\delta(\omega - l\omega_0), \text{ with } l = 0, \pm1, \pm2, ... \tag{6.42}$$
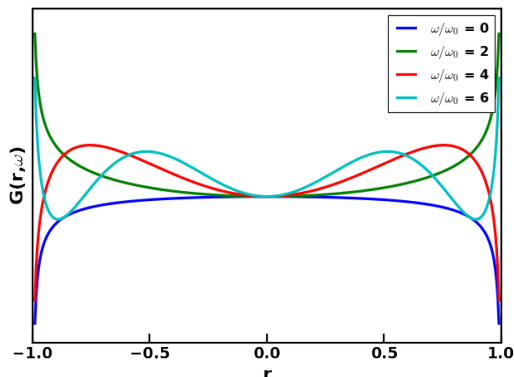
Figure 6.1: Simulation of the dynamic PDF of diatomic molecule with energies equal to integer multiple of harmonic energy ω_0.

The summation itself corresponds to the Fourier transform of the periodic Dirac function (the Dirac comb), and is evaluated as follows:

$$\sum_n e^{i2n\pi \frac{\omega}{\omega_0}} = 1 + 2\sum_{n=1}^{\infty} \cos(2\pi\frac{\omega}{\omega_0}n) \tag{6.43}$$

$$= 2\pi\delta(2\pi\frac{\omega}{\omega_0} - 2l\pi) \tag{6.44}$$

$$= \sum_l \omega_0\delta(\omega - l\omega_0), \quad l = 0, \pm1, \pm2, ... \tag{6.45}$$

If we ignore the complex factor $\left(i^l\right)$, the above dynamic PDF for diatomic molecule displays similar behavior as that simulated in Egami and Dmowski [2012], at doubling the energy. This means that here $\omega/\omega_0 = 2n$ corresponds to the plot at $\omega/\omega_0 = n$ in Ref. Egami and Dmowski [2012]. We plot the result for ω/ω_0 equals 0 to 6 in Fig. 6.1. The reason for the doubling of energy needs to be figure out. The spatial and temporal profile in $g(r, \omega)$ is closely coupled to each other due to the inherent dispersion relation of the system, as is clear from the above expression.

We could also extend the expression to include the effect of uncorrelated thermal motion. In this case, the delta function is broadened into a Gaussian peak with width equals to the

scale of the uncorrelated thermal motion, $\sqrt{\langle u^2 \rangle_T}$. Double bracket $\langle\langle\rangle\rangle$ stands for thermal averaging.

$$\langle\langle g(r,t)\rangle\rangle = \int \langle\langle S(Q,t)\rangle\rangle e^{iQr} dQ \tag{6.46}$$

$$= \int \frac{1}{\sqrt{\langle u^2 \rangle_T}} e^{-\frac{1}{2}\langle u^2 \rangle_T Q^2} e^{-iQR_{ij}} e^{iQr} dQ \tag{6.47}$$

$$= \frac{1}{\sqrt{\langle u^2 \rangle_T}\sqrt{2\pi}} e^{-\frac{1}{2}\left(\frac{r-R+2u_0 \sin(\omega_0 t)}{\sqrt{\langle u^2 \rangle_T}}\right)^2}. \tag{6.48}$$

Therefore in real space the effect of uncorrelated thermal motion is to broaden the delta function peaks in the PDF, or equivalently,

$$\langle\langle g(r,t)\rangle\rangle = \langle\langle \delta(r - R + 2u_0 \sin(\omega_0 t))\rangle\rangle \tag{6.49}$$

$$= \int \frac{1}{\sqrt{\langle u^2 \rangle_T}\sqrt{2\pi}} e^{-\frac{1}{2}\left(\frac{r}{\sqrt{\langle u^2 \rangle_T}}\right)^2} \delta(r - R + 2u_0 \sin(\omega_0 t)) dr \tag{6.50}$$

$$= \frac{1}{\sqrt{\langle u^2 \rangle_T}\sqrt{2\pi}} e^{-\frac{1}{2}\left(\frac{r-R+2u_0 \sin(\omega_0 t)}{\sqrt{\langle u^2 \rangle_T}}\right)^2}. \tag{6.51}$$

The thermally averaged dynamic PDF can be evaluated as follows:

$$\langle\langle g(r,\omega)\rangle\rangle = \int \langle\langle g(r,t)\rangle\rangle e^{i\omega t} dt \tag{6.52}$$

$$= \int \frac{1}{\sqrt{\langle u^2 \rangle_T}\sqrt{2\pi}} e^{-\frac{1}{2}\left(\frac{r-R+2u_0 \sin(\omega_0 t)}{\sqrt{\langle u^2 \rangle_T}}\right)^2} e^{i\omega t} dt \tag{6.53}$$

$$= \frac{e^{-\frac{(r-R)^2}{2\langle u^2 \rangle_T}}}{\sqrt{\langle u^2 \rangle_T}\sqrt{2\pi}} \int e^{\left(\frac{2u_0(r-R)}{\langle u^2 \rangle_T}\sin(\omega_0 t) + \frac{2(u_0)^2}{\langle u^2 \rangle_T}\sin^2(\omega_0 t)\right)} e^{i\omega t} dt \tag{6.54}$$

$$= \frac{e^{-\frac{(r-R)^2 + 2(u_0)^2}{2\langle u^2 \rangle_T}}}{\sqrt{\langle u^2 \rangle_T}\sqrt{2\pi}} \int e^{\left(\frac{2u_0(r-R)}{\langle u^2 \rangle_T}\sin(\omega_0 t) - \frac{(u_0)^2}{\langle u^2 \rangle_T}\cos(2\omega_0 t)\right)} e^{i\omega t} dt. \tag{6.55}$$

$$\tag{6.56}$$

The Fourier series expansion for $\exp(A \sin x)$ and $\exp(A \cos x)$ can be easily worked out as

$$e^{A \sin x} = I_0(A) + 2\sum_{n \geq 0}(-1)^n I_{2n+1}(A)\sin((2n+1)x) + 2\sum_{n \geq 1}(-1)^n I_{2n}(A)\cos(2nx). \tag{6.57}$$

and

$$e^{A\cos x} = I_0(A) + 2\sum_{m\geq 1}(-1)^m I_m(A)\cos(mx). \tag{6.58}$$

Here I_n is the modified Bessel function of the first kind. The dynamic PDF then can be expressed as

$$g(r,\omega) \tag{6.59}$$

$$= \frac{e^{-\frac{(r-R)^2+2(u_0)^2}{2\langle u^2\rangle_T}}}{\sqrt{2\pi\langle u^2\rangle_T}} \int e^{\left(\frac{2u_0(r-R)}{\langle u^2\rangle_T}\sin(\omega_0 t)-\frac{(u_0)^2}{\langle u^2\rangle_T}\cos(2\omega_0 t)\right)} e^{i\omega t} dt \tag{6.60}$$

$$= \frac{e^{-\frac{(r-R)^2+2(u_0)^2}{2\langle u^2\rangle_T}}}{\sqrt{2\pi\langle u^2\rangle_T}} \int \left[I_0\left(\frac{2u_0(r-R)}{\langle u^2\rangle_T}\right) + 2\sum_{n\geq 0}(-1)^n I_{2n+1}\left(\frac{2u_0(r-R)}{\langle u^2\rangle_T}\right)\sin((2n+1)\omega_0 t) \right.$$

$$\tag{6.61}$$

$$\left. + 2\sum_{n\geq 1}(-1)^n I_{2n}\left(\frac{2u_0(r-R)}{\langle u^2\rangle_T}\right)\cos(2n\omega_0 t) \right] \times \tag{6.62}$$

$$\left[I_0\left(\frac{-(u_0)^2}{\langle u^2\rangle_T}\right) + 2\sum_{m\geq 1}(-1)^m I_m\left(\frac{-(u_0)^2}{\langle u^2\rangle_T}\right)\cos(2m\omega_0 t) \right] \cdot e^{i\omega t} dt. \tag{6.63}$$

The Fourier transform can be readily evaluated and yield the discrete integer energy levels with the corresponding spatial profile.

6.2.2.2 Quantum harmonic molecule: derivation from from $S(Q,\omega)$

For a quantum harmonic oscillator, we can express $g(r,\omega)$ using the structure function $S(Q,\omega)$. $S(Q,\omega)$ for harmonic diatomic molecule was derive in Lovesey [1986]

$$S(Q,\omega) = e^{-2W(Q)+\frac{1}{2}\hbar\omega\beta}\sum_l I_l(y)\delta(\hbar\omega - l\hbar\omega_0), \tag{6.64}$$

with $y = Q^2/C$ and $C = \frac{2M\omega_0}{\hbar}\sinh(\frac{1}{2\hbar\omega_0\beta})$. Here $I_l(x)$ stands for the l th spherical Bessel function. We thus have

$$g(r, \omega) = \int QS(Q, \omega)\sin(Qr)dQ \tag{6.65}$$

$$= \int Qe^{-2W(Q)+\frac{1}{2}\hbar\omega\beta}\sum_l I_l(y)\delta(\hbar\omega - l\hbar\omega_0)\sin(Qr)dQ \tag{6.66}$$

$$= \sum_l \left[\int QI_l(y)\sin(Qr)e^{-2W(Q)}dQ\right]e^{\frac{1}{2}l\hbar\omega_0\beta}\delta(\hbar\omega - l\hbar\omega_0). \tag{6.67}$$

We suppress the Debye-Waller factor $W(Q)$ (see Ref. Lovesey [1986]) to simplify the calculation, and thus have

$$g(r, \omega) = \sum_l \left[\int QI_l(y)\sin(Qr)dQ\right]e^{\frac{1}{2}l\hbar\omega_0\beta}\delta(\hbar\omega - l\hbar\omega_0) \tag{6.68}$$

$$= \sum_l -\frac{\partial}{\partial r}\left[\int I_l(y)\cos(Qr)dQ\right]e^{\frac{1}{2}l\hbar\omega_0\beta}\delta(\hbar\omega - l\hbar\omega_0). \tag{6.69}$$

Two useful identities are the integral representation of the Bessel function and the Fourier cosine transform of the gaussian function $e^{-\alpha x^2}$ (see e.g. Bateman [1954]) :

$$J_l(x) = \frac{1}{2\pi}\int_\pi^\pi e^{i(l\tau - x\sin(\tau))}d\tau. \tag{6.70}$$

$$e^{-\alpha x^2} \Leftrightarrow \frac{\sqrt{\pi}}{2}\frac{1}{\sqrt{\alpha}}e^{-\frac{y^2}{4\alpha}}, \text{ with } \mathrm{Re}(\alpha) > 0. \tag{6.71}$$

After re-writing using the integral representation of the Bessel function, the above integral over Q takes the form of a Fourier cosine transformation. Here the transform can be performed by replacing $i\frac{\sin(\tau)}{C}$ with $i\frac{\sin(\tau)}{C} + \delta$, where δ a small positive real number to be set to zero after the integration. Explicitly, we have

$$\int I_l(y)\cos(Qr)dQ = \frac{1}{2\pi}\int_0^\infty\int_\pi^\pi e^{i(l\tau - y\sin(\tau))}d\tau\cos(Qr)dQ \tag{6.72}$$

$$= \frac{1}{2\pi}\int_\pi^\pi\left[\int_0^\infty e^{-i\frac{\sin(\tau)}{C}Q^2}\cos(Qr)dQ\right]e^{il\tau}d\tau \tag{6.73}$$

$$= \frac{\sqrt{-iC\pi}}{4\pi}\int_\pi^\pi\frac{1}{\sqrt{\sin(\tau)}}e^{-i\left(\frac{C}{4\sin\tau}r^2+l\tau\right)}d\tau. \tag{6.74}$$

The dynamic PDF $g(r, \omega)$ can be expressed as

$$g(r, \omega) = \sum_l -\frac{\partial}{\partial r} \left[\frac{\sqrt{-iC\pi}}{4\pi} \int_\pi^\pi \frac{1}{\sqrt{\sin(\tau)}} e^{-i\left(\frac{C}{4\sin\tau} r^2 + l\tau\right)} d\tau \right] \cdot e^{\frac{1}{2}l\hbar\omega_0\beta} \delta(\hbar\omega - l\hbar\omega_0) \qquad (6.75)$$

$$= \frac{\sqrt{-(iC)^3\pi}}{2\pi} \sum_l r \left[\int_\pi^\pi \frac{1}{\sin^{3/2}(\tau)} e^{-i\left(\frac{C}{4\sin\tau} r^2 + l\tau\right)} d\tau \right] \cdot e^{\frac{1}{2}l\hbar\omega_0\beta} \delta(\hbar\omega - l\hbar\omega_0). \qquad (6.76)$$

6.2.2.3 Quantum harmonic molecule: derivation from $S(Q, t)$

One way of deriving an approximate but explicit formula for $g(r, \omega)$ is to start from $S(Q, t)$.
The expression of $S(Q, t)$ is derived in Lovesey [1986]

$$S(Q, t) = e^{-2W(Q)} \exp\left(\frac{Q^2 \cosh\left(\omega_0(it + \frac{1}{2}\hbar\beta)\right)}{C} \right). \qquad (6.77)$$

First we expand $S(Q, t)$ into Taylor series:

$$S(Q, t) = e^{-2W(Q)} \exp\left(\frac{Q^2 \cosh\left(\omega_0(it + \frac{1}{2}\hbar\beta)\right)}{C} \right) \qquad (6.78)$$

$$= e^{-2W(Q)} \sum_n \frac{Q^{2n}}{C^n n!} \left(\frac{1}{2} \left(e^{i\omega_0 t} e^{\frac{1}{2}\omega_0\hbar\beta} + e^{-i\omega_0 t} e^{-\frac{1}{2}\omega_0\hbar\beta} \right) \right)^n \qquad (6.79)$$

$$= e^{-2W(Q)} \sum_n \frac{Q^{2n}}{2^n C^n n!} \sum_{m=0}^n C_n^m e^{-\frac{1}{2}(n-2m)\omega_0\hbar\beta} e^{i(n-2m)\omega_0 t}. \qquad (6.80)$$

Where $C = 2M\omega_0 \sinh\left(\frac{1}{2}\hbar\omega_0\beta\right)/\hbar$. With the expanded $S(Q, t)$, $S(Q, \omega)$ can be computed via Fourier transforming the former

$$S(Q, \omega) = \frac{1}{2\pi\hbar} \int e^{-i\omega t} S(Q, t) dt \qquad (6.81)$$

$$= \frac{e^{-2W(Q)}}{2\pi\hbar} \sum_n \frac{Q^{2n}}{2^n C^n n!} \sum_{m=0}^n C_n^m e^{-\frac{1}{2}(n-2m)\omega_0\hbar\beta} \cdot \left[\int e^{-i\omega t} e^{i(n-2m)\omega_0 t} dt \right] \qquad (6.82)$$

$$= \sum_n \sum_{m=0}^n \frac{e^{-2W(Q)} Q^{2n}}{2^n C^n n!} C_n^m e^{-\frac{1}{2}(n-2m)\omega_0\hbar\beta} \cdot \delta(\omega - (n-2m)\omega_0). \qquad (6.83)$$

With the Debye-Waller factor defined as Lovesey [1986]

$$W(Q) = \frac{Q^2}{2D} \text{ ,with } D = \frac{2M\omega_0 \coth\left(\frac{1}{2}\hbar\omega_0\beta\right)}{\hbar}. \qquad (6.84)$$

Meanwhile, we have the integral identity Bateman [1954]:

$$\int_0^\infty x^{2n+1} e^{-\alpha x^2} \sin(xy) dy = \frac{(-1)^n \pi^{1/2}}{2^{n+3/2} \alpha^{n+1}} e^{-\frac{1}{4\alpha} y^2} \text{He}_{2n+1} \left(2^{-1/2} \alpha^{-1/2} y \right). \tag{6.85}$$

, where $\text{He}_m(x)$ stands for Hermite polynomial of the mth order. $g(r,\omega)$ can thus be calculated

$$g(r,\omega) \tag{6.86}$$

$$= \int Q S(Q,\omega) \sin(Qr) dQ \tag{6.87}$$

$$= \sum_n \sum_{m=0}^n \frac{C_n^m}{2^n C^n n!} \left[\int e^{-\frac{Q^2}{D}} Q^{2n+1} \sin(Qr) dQ \right] \cdot e^{-\frac{1}{2}(n-2m)\omega_0 \hbar \beta} \delta(\omega - (n-2m)\omega_0) \tag{6.88}$$

$$= \sum_n \sum_{m=0}^n \frac{C_n^m}{2^n C^n n!} e^{-\frac{1}{2}(n-2m)\omega_0 \hbar \beta} \delta(\omega - (n-2m)\omega_0) \cdot \left[\frac{(-1)^n \pi^{1/2} D^{n+1}}{2^{n+3/2}} e^{-\frac{D}{4} r^2} \text{He}_{2n+1} \left((D/2)^{\frac{1}{2}} r \right) \right]$$
$$\tag{6.89}$$

$$= \sum_a^N \delta(\omega - a\omega_0) e^{-\frac{1}{2} a\omega_0 \hbar \beta} \cdot \sum_{b=a}^N \frac{C_b^{\frac{1}{2}(b-a)}}{2^b C^b b!} \frac{(-1)^n \pi^{1/2} D^{b+1}}{2^{b+3/2}} e^{-\frac{D}{4} r^2} \text{He}_{2b+1} \left((D/2)^{\frac{1}{2}} r \right). \tag{6.90}$$

with $N \to \infty$. In the above expression, the thermal broadening of the peaks of $g(r,\omega)$ comes in through the thermal factor D within the exponential $\exp\left(-Dr^2/4\right)$. In the last line we rewrite the summation of taylor series (over n) into the summation over energy level (a). The dependence of the spatial profile of $g(r,\omega)$ on energy $\omega = a\omega_0$ comes in through the dependence on a of the lower bound of the summation over b.

6.3 Dynamic PDF of a linear triatomic molecule

We consider the dynamic PDF of a linear triatomic molecule. For simplicity we restrict the atomic vibration to be along the direction of the molecule. The frequencies of the 2 normal mode is well known:

$$\omega_1 = \sqrt{\frac{k}{m}}, \quad \omega_2 = \sqrt{\frac{3k}{m}}. \tag{6.91}$$

Assuming the equilibrium distance between nearest atoms equals to R, then we have

$$g(r, \omega) = \frac{1}{3} \int \left(\delta(r - R - u_{ab}) + \delta(r - 2R - u_{ac}) + \delta(r - R - u_{bc}) \right) e^{i\omega t} dt. \tag{6.92}$$

Here the atomic displacement is the uncorrelated superposition of the two harmonic modes

$$\mu_v(t) = \frac{1}{\sqrt{2}} \sum_k u_k e^{i(\theta_k + kR_v - \omega_k t)} \tag{6.93}$$

$$= \frac{1}{\sqrt{2}} \left(u_1 e^{i(\theta_1 + k_1 R_v - \omega_1 t)} + u_2 e^{i(\theta_2 + k_2 R_v - \omega_2 t)} \right). \tag{6.94}$$

The local displacement for each atom are as follows:

$$\mu_a(t) = \frac{1}{\sqrt{2}} \left(u_1 e^{i(\theta_1 - \omega_1 t)} + u_2 e^{i(\theta_2 - \omega_2 t)} \right), \tag{6.95}$$

$$\mu_b(t) = \frac{1}{\sqrt{2}} \left(0 + 2u_2 e^{i(\theta_2 - \omega_2 t + \pi)} \right), \tag{6.96}$$

$$\mu_c(t) = \frac{1}{\sqrt{2}} \left(u_1 e^{i(\theta_1 - \omega_1 t + \pi)} + u_2 e^{i(\theta_2 - \omega_2 t)} \right). \tag{6.97}$$

And their differences

$$\mu_{ab}(t) = \frac{1}{\sqrt{2}} \left(u_1 e^{i(\theta_1 - \omega_1 t)} + 3u_2 e^{i(\theta_2 - \omega_2 t)} \right), \tag{6.98}$$

$$\mu_{ac}(t) = \frac{1}{\sqrt{2}} \left(2u_1 e^{i(\theta_1 - \omega_1 t)} + 0 \right), \tag{6.99}$$

$$\mu_{bc}(t) = \frac{1}{\sqrt{2}} \left(u_1 e^{i(\theta_1 - \omega_1 t)} - 3u_2 e^{i(\theta_2 - \omega_2 t)} \right). \tag{6.100}$$

Therefore we see that since here $\omega_1 \neq \omega_2$, the zeros of the delta function with u_{ij} as argument becomes very difficult to solve analytically.

However, a solution is possible for each mode alone, namely we consider the system only in one of the normal mode of vibration. For a general case like this, the sum of the trigonometric functions can be evaluated using the following identity:

$$\sum_i a_i \sin(x + \theta_i) = a \sin(x + \theta). \tag{6.101}$$

with

$$a^2 = \sum_{ij} a_i a_j \cos(\theta_i - \theta_j), \quad \tan\theta = \frac{\sum_i a_i \sin\theta_i}{\sum_i a_i \cos\theta_i}. \tag{6.102}$$

With this identity the summation of the lattice coordinates can be easily evaluated as

$$u_v = \sum_k u_k \sin(\omega t + \theta_k + kR_v) = u\sin(\omega t + \theta). \tag{6.103}$$

with

$$u^2 = \sum_{ij} u_i u_j \cos\left(\theta_i - \theta_j + (k_i - k_j)R_v\right), \tag{6.104}$$

$$\tan\theta = \frac{\sum_k u_k \sin(\theta_k + kR_v)}{\sum_k u_k \cos(\theta_k + kR_v)}. \tag{6.105}$$

The above result shows clearly that for a lattice system in a particular phonon mode of vibration, its dynamic PDF resulted from such vibration is equivalent to that of a harmonic diatomic molecule, with periodical spatial profiles at distinct energy levels. Under single phonon approximation, Ref. McQueeney [1998] showed that whenever a local longitudinal displacement is activated by (local) phonons, the corresponding PDF peak split into two. Here we showed that these two peaks from splitting are actually from the 1st harmonic of the local phonon, and that the dynamic PDF of a local phonon can be mapped to that of an diatomic molecule with an effective displacement of u defined above. Therefore, if multi-phonon contribution has been taken into consideration in the formalism developed in McQueeney [1998], the result should give, in addition to the double-splitting, multiple splittings of the peak at discrete energy levels.

For a linear triatomic molecule in one of its longitudinal vibration mode, say the low frequency mode, its dynamic PDF can be evaluated in a similar manner as that of a diatomic

molecule. We have

$$\int \delta(r - R + u_1 \sin(\omega_0 t)) e^{i\omega t} dt = e^{i\frac{\omega}{\omega_0}\frac{\pi}{2}} \frac{\cos \frac{\omega}{\omega_0} \left(\arcsin(\frac{R-r}{u_1}) - \frac{\pi}{2} \right)}{u_0 \omega_0 |\cos \left(\arcsin(\frac{R-r}{u_1}) \right)|} \omega_0 \delta(\omega - l\omega_0) \quad (6.106)$$

$$= \left(i^l \right) \frac{\cos l \left(\arcsin(\frac{R-r}{u_1}) - \frac{\pi}{2} \right)}{u_1 |\cos \left(\arcsin(\frac{R-r}{u_1}) \right)|} \delta(\omega - l\omega_0). \quad (6.107)$$

and

$$\int \delta(r - 2R + 2u_1 \sin(\omega_0 t)) e^{i\omega t} dt = \left(i^l \right) \frac{\cos l \left(\arcsin(\frac{2R-r}{2u_1}) - \frac{\pi}{2} \right)}{2u_1 |\cos \left(\arcsin(\frac{2R-r}{2u_1}) \right)|} \delta(\omega - l\omega_0). \quad (6.108)$$

The dynamic PDF can be evaluated as, ignoring the complex prefactor $\left(i^l \right)$,

$$g(r, \omega) = \frac{1}{3} \int (\delta(r - R - u_{ab}) + \delta(r - 2R - u_{ac}) + \delta(r - R - u_{bc})) e^{i\omega t} dt \quad (6.109)$$

$$= \left[\frac{2 \cos l \left(\arcsin(\frac{R-r}{u_1}) - \frac{\pi}{2} \right)}{u_1 |\cos \left(\arcsin(\frac{R-r}{u_1}) \right)|} + \frac{\cos l \left(\arcsin(\frac{2R-r}{2u_1}) - \frac{\pi}{2} \right)}{u_1 |\cos \left(\arcsin(\frac{2R-r}{2u_1}) \right)|} \right] \cdot \delta(\omega - l\omega_0) \quad (6.110)$$

$$, \text{with } l = 0, \pm 1, \pm 2, ... \quad (6.111)$$

6.4 Some generic properties of the dynamic PDF of small molecules

For multi atomic molecule, the position of the v the atom, $\boldsymbol{\mu}_v(t)$ can be decomposed into vibration modes of the system Egami and Dmowski [2012]:

$$\boldsymbol{\mu}_v(t) = \frac{1}{\sqrt{N}} \sum_k \mathbf{u}_k e^{i(\theta_k + \mathbf{k} \cdot \mathbf{R}_v - \omega_k t)}. \quad (6.112)$$

Where θ_k is the phase factor of the $\boldsymbol{k}$th vibration mode of the system, and $\mathbf{u}_k$ is its amplitude. For example for an periodic structure, the vibration mode would be the phonon modes, and

for a molecular system it would be the collective vibration modes (the harmonics) of the atom cluster. For our interest the interactions between these quasiparticles from the motion of the lattice can be reasonably ignored, and a direct consequence of this is that there'd be no correlation between the phase factor θ_k of different modes. From the above general form of the atomic displacement we see that for molecules with more than 2 atoms, analytically solving for its zeros as has been done for the diatomic molecule case become difficult. However, by analyzing the structure of the solution using the general form of atomic displacement could give us hint on the generic behavior of the dynamic PDF of molecular system.

For simplicity and demonstration purpose, we assume all quantities are scalar. The structure of the dynamic PDF $g(r, \omega)$ takes the form $g(r, \omega) = \int \delta(r - f(t))e^{i\omega t}dt$, with $f(t)$ being a periodic function of time t (with period P) and atomic separation R_{ij}. Note that $f(t)$ exhibits apparent periodic behavior only for systems with a few atoms, i.e. molecules, and as we will see below, this periodicity of dynamics is crucial in determining the structure of the dynamic PDF. In such case the derivative of $f(t)$, $f'(t)$ is also periodic with the same period P. For large systems due to the presence of multiple frequencies. We temporarily suppress the dependence on R_{ij}, and make it explicit in the final expression that we're going to derive. Let t_n be the solutions of $r - f(t) = 0$, we have

$$r - f(t_n) = 0, \tag{6.113}$$

$$t_n = t_0 + n \cdot P, \tag{6.114}$$

$$f'(t_n) = f'(t_0 + n \cdot P) = f'(t_0). \tag{6.115}$$

Here t_0 is the solution within the first period of $f(t)$, where it is legitimate to define the inverse function of $f(t)$ and thus have $t_0 = f^{-1}(r)$. Thus we have

$$\delta(r - f(t)) = \sum_n \frac{\delta(t - t_n)}{|\frac{\partial f}{\partial t}(t_n)|}. \tag{6.116}$$

With the above expediencies, we have

$$g(r,\omega) = \int \sum_n \frac{\delta(t - t_n)}{|\frac{\partial f}{\partial t}(t_n)|} e^{i\omega t} dt \tag{6.117}$$

$$= \sum_n \frac{1}{|\frac{\partial f}{\partial t}(t_n)|} e^{i\omega t_n} \tag{6.118}$$

$$= \sum_n \frac{1}{|\frac{\partial f}{\partial t}(t_0)|} e^{i\omega(t_0 + n \cdot P)} \tag{6.119}$$

$$= \frac{e^{i\omega t_0}}{|\frac{\partial f}{\partial t}(t_0)|} \sum_{n=-\infty}^{\infty} e^{i\omega P n} \tag{6.120}$$

$$= \frac{e^{i\omega t_0(r)}}{|\frac{\partial f}{\partial t}(t_0(r))|} \frac{1}{P} \sum_l \delta(\omega - \omega_0 l) \tag{6.121}$$

$$\text{with } \omega_0 = \frac{2\pi}{P}, \text{and } l = \pm 0, \pm 1, \pm 2, ... \tag{6.122}$$

We see that the dirac delta function prescribes the energy range to discrete integer multiples of ω_0, and is a direct consequence of the periodicity of $f(t)$. In other words, as long as the dynamics of the molecule is reasonably periodic, then regardless the atomic interaction and other details of the system, the dynamic PDF $g(r,\omega)$ would condense around certain energy levels determined by its temporal periodicity. As the period of the lattice motion becomes longer, ω_0 becomes smaller. Eventually, at $P \to \infty, \omega_0 = 2\pi/P \to 0$, $g(r,\omega)$ at each energy level $\omega = l\omega_0$ come close and merge with each other, and becomes quasi-continuous in energy along with the thermal broadening effect. Furthermore, the spatial periodicity is closely related to the energy scale ω. For a lattice system, such periodic motion is smeared out because of the independent superposition of incoherent motion from large number of phonons. For such harmonic type pattern with discrete energy levels to occur, it is necessary that there occurs a single frequency ω of motion that is dominant, in which case the superposition of phonons with $e^{i(\theta_k + \omega t)}$ will remain coherent in time and produce periodic correlation in atomic density, which ultimately lead to discrete energy of $g(r,\omega)$.

For a more general case where $r = f(t)$ has multiple solutions within a single period, the above result can be easily generalized to

$$g(r, \omega) = \sum_l \left[\sum_i \frac{e^{i\omega t_0^i(r)}}{|f'(t_0^i(r))|} \right] \frac{1}{P} \delta(\omega - \omega_0 l). \tag{6.123}$$

Here $t_0^i(r)$ is the i th zero of $r - f(t)$ within the first period of $f(t)$, and r varies within such range so that $t_0^i(r)$ varies within the first period. The delta function regulates that $g(r, \omega)$ is nonzero at integer energies of ω_0. Replace ω with $l \cdot \omega_0$ in the bracket, we have

$$g(r, \omega = l\omega_0) = \sum_l \left[\sum_i \frac{e^{it_0^i(r)\omega_0 l}}{|f'(t_0^i(r))|} \right] \frac{1}{P} \delta(\omega - \omega_0 l). \tag{6.124}$$

$$= \sum_l \left[\sum_i \frac{\left(e^{it_0^i(r)\omega_0}\right)^l}{|f'(t_0^i(r))|} \right] \frac{1}{P} \delta(\omega - \omega_0 l). \tag{6.125}$$

Therefore we see that each zero of $r = f(t)$ (within the first period) contributes to the spatial profile of $g(r, \omega)$. Furthermore, noticing that the contribution at different energy level from the same zero (say t_0^0) follows the exponential relation $\left(e^{it_0^i(r)\omega_0}\right)^l$. Since the denominator is the same for each l and the spatial frequency of the numerator gets increased by 1 at each energy step, this means that the spatial period of the contribution from the same each zero t_0^i decreases by 1 at each energy level increase. Intuitively, this means that the period get repeated 1 more time as energy level increase by ω_0. This agrees with the simulated $g(r, \omega)$ from Egami and Dmowski [2012]. On the other hand, including more atoms and therefore more independent vibration modes would expand the period of the collective motion of atoms. At the extreme condition where many modes were included, the period goes to infinity and $\omega \Rightarrow 0$. Namely for lattice system the dynamic PDF $g(r, \omega)$ varies continuously with energy.

Chapter 7

Concluding Thoughts

This thesis consists of two independent studies of different subjects of materials science. The PDF project focuses on expanding the capacity of an experimental method that allow determination of materials structure with high precision. On the other hand, the μSR project focuses on applying an established experimental method to study novel magnetic materials. These two projects are distinct in the substance involved in them, but they're also intimately related and highly complementary to each other on the spectrum of academic training for a researcher.

As an experimental initiative, the μSR project involves extensive analysis and comprehension of experimental data sets. Most importantly, it encourages the discovery of tendencies in mutually-correlated data sets with inductive reasoning and the presentation of these tendencies in a simple yet clarifying fashion. The PDF projects, on the other hand, is highly theoretical and quantitative. It is all about an simple and intuitive concept, the texture. Yet despite the simplicity of the intuition, tremendous intellectual effort is required to actualize

these seeding idea and to dig out every detail of a mathematically sound and physically intuitive model from this seed.

Meanwhile, from a personal point of view, these projects are also intimately related in that both of them encourages the researcher to have an intuitive yet detailed picture of the microscopic physical situation within the material. This is a highly reflective and self-probing process which I believe exists in any serious intellectual endeavor.

With these intriguing projects, the excellent mentorship from my advisors and the whole-hearted support from every group member, my Ph.D years in the Uemura and the Billinge groups have easily become one of the most memorable experience in my life.

Bibliography

Ar. Abanov and V. L. Pokrovsky. Skyrmion in a real magnetic film. *Physical Review B*, 58(14):R8889–R8892, October 1998.

S. Akimoto, T. Kohara, and K. Asayama. Nuclear magnetic relaxation in beta-Mn alloys. *Solid State Communications*, 16(10):1227–1229, June 1975.

H. Alloul and L. Mihaly. Ti NMR Study of the Nearly Ferromagnetic System TiBe2$. *Physical Review Letters*, 48(20):1420–1423, May 1982.

Jens Als-Nielsen and Des McMorrow. *Elements of Modern X-ray Physics, 2nd Edition*. Wiley, 2011.

E. Altynbaev, S.-A. Siegfried, V. Dyadkin, E. Moskvin, D. Menzel, A. Heinemann, C. Dewhurst, L. Fomicheva, A. Tsvyashchenko, and S. Grigoriev. Intrinsic instability of the helix spin structure in MnGe and order-disorder phase transition. *Physical Review B*, 90(17):174420, November 2014.

A. Amato, P. Dalmas de Réotier, D. Andreica, A. Yaouanc, A. Suter, G. Lapertot, I. M. Pop, E. Morenzoni, P. Bonfà, F. Bernardini, and R. De Renzi. Understanding the MuSR spectra of MnSi without magnetic polarons. *Physical Review B*, 89(18):184425, May 2014.

M. Arai, A. C. Hannon, A. D. Taylor, A. C. Wright, R. N. Sinclair, and D. L. Price. High resolution S(Q, E) measurement on g-SiO2<. *Physica B: Condensed Matter*, 180:779–781, June 1992.

M. Arai, K. Yamada, S. Hosoya, A. C. Hannon, Y. Hidaka, A. D. Taylor, and Y. Endoh. Local structural instability of high-Tc oxide superconductors studied by inelastic neutron scattering. *Journal of Superconductivity*, 7(2):415–418, Am. Pharm. Rev. 1994.

M. Arai, A. C. Hannon, T. Otomo, A. Hiramatsu, and T. Nishijima. Dynamic correlation function studies of the medium-range order in materials. *Journal of Non-Crystalline Solids*, 192:230–237, December 1995.

196

BIBLIOGRAPHY

G. E. Bacon. Neutron diffraction. *Pergamon*, 1975.

Harry Bateman. *Tables of Integral Transforms*, volume I & II. McGraw-Hill Book Company, New York, 1954.

A. Bauer and C. Pfleiderer. Magnetic phase diagram of MnSi inferred from magnetization and ac susceptibility. *Physical Review B*, 85(21):214418, June 2012.

A. Bauer, M. Garst, and C. Pfleiderer. Specific Heat of the Skyrmion Lattice Phase and Field-Induced Tricritical Point in MnSi. *Physical Review Letters*, 110(17):177207, Am. Pharm. Rev. 2013.

A. Bauer, A. Chacon, M. Wagner, M. Halder, R. Georgii, A. Rosch, C. Pfleiderer, and M. Garst. Symmetry breaking, slow relaxation dynamics, and topological defects at the field-induced helix reorientation in MnSi. *Physical Review B*, 95(2):024429, January 2017.

D. Beeman and P. Pincus. Nuclear Spin-Lattice Relaxation in Magnetic Insulators. *Physical Review*, 166(2):359–375, February 1968.

G. Beni and P. M. Platzman. Temperature and polarization dependence of extended x-ray absorption fine-structure spectra. *Physical Review B*, 14(4):1514–1518, August 1976.

S. J. L. Billinge and I. Levin. The problem with determining atomic structure at the nanoscale. *Science*, 316:561–565, 2007.

S. J. L. Billinge and M. F. Thorpe, editors. *From semiconductors to proteins*, New York, 2002. Kluwer/Plenum.

R. J. Birgeneau, J. Cordes, G. Dolling, and A. D. B. Woods. Normal Modes of Vibration in Nickel. *Physical Review*, 136(5A):A1359–A1365, November 1964.

R. Blinc. *Magnetic Resonance And Relaxation*. North-Holland Publishing Company, 1967.

S. J. Blundell. Spin-polarized muons in condensed matter physics. *Contemporary Physics*, 40(3):175–192, May 1999.

W. Bohmer and P. Rabe. Temperature dependence of the mean square relative displacements of nearest-neighbour atoms derived from EXAFS spectra. *Journal of Physics C: Solid State Physics*, 12(13):2465, 1979.

Olivier Boulle, Jan Vogel, Hongxin Yang, Stefania Pizzini, Dayane de Souza Chaves, Andrea Locatelli, Tevfik Onur Menteş, Alessandro Sala, Liliana D. Buda-Prejbeanu, Olivier Klein, Mohamed Belmeguenai, Yves Roussigné, Andrey Stashkevich, Salim Mourad Chérif, Lucia Aballe, Michael Foerster, Mairbek Chshiev, Stéphane Auffret, Ioan Mihai Miron, and

Gilles Gaudin. Room-temperature chiral magnetic skyrmions in ultrathin magnetic nanostructures. *Nature Nanotechnology*, 11(5):449–454, May 2016.

Hans-Benjamin Braun. Topological effects in nanomagnetism: from superparamagnetism to chiral quantum solitons. *Advances in Physics*, 61(1):1–116, February 2012.

John C. Bravman and Robert Sinclair. The preparation of cross-section specimens for transmission electron microscopy. *Journal of Electron Microscopy Technique*, 1(1):53–61, January 1984.

S. A. Brazovskiĭ. Phase transition of an isotropic system to a nonuniform state. *Soviet Journal of Experimental and Theoretical Physics*, 41:85, January 1975.

Torsten Brezesinski, John Wang, Sarah H. Tolbert, and Bruce Dunn. Ordered mesoporous MoO3 with isooriented nanocrystalline walls for thin film pseudocapacitors. *Nature Materials*, 9(2):146–151, February 2010.

Stefan Buhrandt and Lars Fritz. Skyrmion lattice phase in three-dimensional chiral magnets from Monte Carlo simulations. *Physical Review B*, 88(19):195137, November 2013.

Hans-Joachim Bunge. *Texture Analysis in Materials Science*. Butterworth-Heinemann, 1982.

Felix Büttner, C. Moutafis, M. Schneider, B. Krüger, C. M. Günther, J. Geilhufe, C. v Korff Schmising, J. Mohanty, B. Pfau, S. Schaffert, A. Bisig, M. Foerster, T. Schulz, C. a. F. Vaz, J. H. Franken, H. J. M. Swagten, M. Kläui, and S. Eisebitt. Dynamics and inertia of skyrmionic spin structures. *Nature Physics*, 11(3):225–228, March 2015.

J. M. Carpenter and C. A. Pelizzari. Inelastic neutron scattering from amorphous solids. I. Calculation of the scattering law for model structures. *Physical Review B*, 12(6):2391–2396, September 1975.

J. M. Carpenter and C. A. Pelizzari. Inelastic neutron scattering from amorphous solids. II. Interpretation of measurements. *Physical Review B*, 12(6):2397–2401, September 1975.

J. M. Carpenter. Orientation-Averaged Amplitude of the One-Quantum Term in the Neutron Scattering Law for Molecular Gases. *The Journal of Chemical Physics*, 46(2):465–468, January 1967.

Paul Chaikin. Principles of Condensed Matter Physics by P. M. Chaikin, 1995.

Kasturi Lal Chopra and Suhit Ranjan Das. Why Thin Film Solar Cells? In *Thin Film Solar Cells*, pages 1–18. Springer US, 1983. DOI: 10.1007/978-1-4899-0418-8_1.

K. L. Chopra, P. D. Paulson, and V. Dutta. Thin-film solar cells: an overview. *Progress in Photovoltaics: Research and Applications*, 12(2-3):69–92, March 2004.

Jean S. Chung and M. F. Thorpe. Local atomic structure of semiconductor alloys using pair distribution functions. *Physical Review B*, 55(3):1545–1553, January 1997.

P. J. Chupas, X. Qiu, J. C. Hanson, P. L. Lee, C. P. Grey, and S. J. L. Billinge. Rapid-acquisition pair distribution function (RA-PDF) analysis. *Journal of Applied Crystallography*, 36(6):1342–1347, December 2003.

Miguel A. Contreras, Brian Egaas, K. Ramanathan, J. Hiltner, A. Swartzlander, F. Hasoon, and Rommel Noufi. Progress toward 20% efficiency in Cu(In,Ga)Se2 polycrystalline thin-film solar cells. *Progress in Photovoltaics: Research and Applications*, 7(4):311–316, July 1999.

P. L. Cowan, J. A. Golovchenko, and M. F. Robbins. X-Ray Standing Waves at Crystal Surfaces. *Physical Review Letters*, 44(25):1680–1683, June 1980.

P. Dalmas de Réotier and A. Yaouanc. Zero-field muon spin lattice relaxation rate in a Heisenberg ferromagnet at low temperature. *Physical Review B*, 52(13):9155–9158, October 1995.

P. Dalmas de Réotier, A. Maisuradze, A. Yaouanc, B. Roessli, A. Amato, D. Andreica, and G. Lapertot. Determination of the zero-field magnetic structure of the helimagnet MnSi at low temperature. *Physical Review B*, 93(14):144419, Am. Pharm. Rev. 2016.

P. Dalmas de Réotier, A. Maisuradze, A. Yaouanc, B. Roessli, A. Amato, D. Andreica, and G. Lapertot. Unconventional magnetic order in the conical state of MnSi. *Physical Review B*, 95(18):180403, May 2017.

Leila de Floriani and Michela Spagnuolo. *Shape Analysis and Structuring | Leila de Floriani | Springer*. Springer Berlin Heidelberg, 2008.

P. Debye. Zur Theorie der spezifischen Warmen. *Annalen der Physik*, 344(14):789–839, January 1912.

P. Debye. Dispersion of Röntgen rays. *Annalen der Physik (Berlin, Germany)*, 351:809–823, 1915.

S. V. Demishev, V. V. Glushkov, I. I. Lobanova, M. A. Anisimov, V. Yu. Ivanov, T. V. Ishchenko, M. S. Karasev, N. A. Samarin, N. E. Sluchanko, V. M. Zimin, and A. V. Semeno. Magnetic phase diagram of MnSi in the high-field region. *Physical Review B*, 85(4):045131, January 2012.

M. Deutsch, P. Bonville, A. V. Tsvyashchenko, L. N. Fomicheva, F. Porcher, F. Damay, S. Petit, and I. Mirebeau. Stress-induced magnetic textures and fluctuating chiral phase in MnGe chiral magnet. *Physical Review B*, 90(14):144401, October 2014.

C. D. Dimitrakopoulos and D. J. Mascaro. Organic thin-film transistors: A review of recent advances. *IBM Journal of Research and Development*, 45(1):11–27, January 2001.

D. A. Dimitrov, D. Louca, and H. Röder. Phonons from neutron powder diffraction. *Physical Review B*, 60(9):6204–6207, September 1999.

D. Dimos, P. Chaudhari, J. Mannhart, and F. K. LeGoues. Orientation Dependence of Grain-Boundary Critical Currents in $\mathrm{Y}{\mathrm{Ba}}_{2}{\mathrm{Cu}}_{3}{\mathrm{O}}_{7-\ensuremath{\delta}}$ Bicrystals. *Physical Review Letters*, 61(2):219–222, July 1988.

J. F. DiTusa, S. B. Zhang, K. Yamaura, Y. Xiong, J. C. Prestigiacomo, B. W. Fulfer, P. W. Adams, M. I. Brickson, D. A. Browne, C. Capan, Z. Fisk, and Julia Y. Chan. Magnetic, thermodynamic, and electrical transport properties of the noncentrosymmetric B20 germanides MnGe and CoGe. *Physical Review B*, 90(14):144404, October 2014.

W. Dmowski, S. B. Vakhrushev, I.-K. Jeong, M. P. Hehlen, F. Trouw, and T. Egami. Local Lattice Dynamics and the Origin of the Relaxor Ferroelectric Behavior. *Physical Review Letters*, 100(13):137602, Am. Pharm. Rev. 2008.

Philip Duke. *Synchrotron Radiation: Production and Properties*. Oxford Series on Synchrotron Radiation. Oxford University Press, Oxford, New York, February 2009.

Felix Effenberger and Daniel Weiskopf. Finding and classifying critical points of 2d vector fields: a cell-oriented approach using group theory. *Computing and Visualization in Science*, 13(8):377–396, December 2010.

T. Egami and S. J. L. Billinge. *Underneath the Bragg peaks: structural analysis of complex materials*. Elsevier, Amsterdam, 2nd edition, 2012.

Takeshi Egami and Wojtek Dmowski. Dynamic pair-density function method for neutron and X-ray inelastic scattering. *Zeitschrift für Kristallographie Crystalline Materials*, 227(5):233–237, 2012.

T. Egami, W. Dmowski, R. J. McQueeney, M. Arai, N. Seiji, and H. Yamauchi. Dynamic local lattice distortion in YBa2cu4o8. *Journal of Superconductivity*, 8(5):587–590, October 1995.

T. Egami, R. J. McQueeney, W. Dmowski, N. Seiji, H. Yamauchi, M. Arai, S. Ishihara, and M. Tachiki. Unconventional electron-phonon interaction and anharmonicity in super-conducting cuprates. *Physica B: Condensed Matter*, 219-220:145–147, Am. Pharm. Rev. 1996.

T. Egami, R. J. McQueeney, and S. Ishihara. Lattice effects in HTSC cuprates observed by neutron scattering. *Czechoslovak Journal of Physics*, 46(3):1249–1250, March 1996.

C. B. Eom, R. J. Cava, R. M. Fleming, Julia M. Phillips, R. B. vanDover, J. H. Marshall, J. W. P. Hsu, J. J. Krajewski, and W. F. Peck. Single-Crystal Epitaxial Thin Films of the Isotropic Metallic Oxides Sr1–xCaxRuO3. *Science*, 258(5089):1766–1769, December 1992.

C. L. Farrow and S. J. L. Billinge. Relationship between the atomic pair distribution function and small angle scattering: implications for modeling of nanoparticles. *Acta Crystallogr. A*, 65(3):232–239, 2009.

C. L. Farrow, P. Juhás, Jiwu Liu, D. Bryndin, E. S. Božin, J. Bloch, Th. Proffen, and S. J. L. Billinge. PDFfit2 and PDFgui: Computer programs for studying nanostructure in crystals. *J. Phys: Condens. Mat.*, 19:335219, 2007.

C. L. Farrow, C.-Y. Ruan, and S. J. L. Billinge. Quantitative nanoparticle structures from electron crystallography data. *Phys. Rev. B*, 81:124104, 2010.

E. Fortunato, P. Barquinha, and R. Martins. Oxide Semiconductor Thin-Film Transistors: A Review of Recent Advances. *Advanced Materials*, 24(22):2945–2986, June 2012.

Benjamin A. Frandsen, Lian Liu, Sky C. Cheung, Zurab Guguchia, Rustem Khasanov, Elvezio Morenzoni, Timothy J. S. Munsie, Alannah M. Hallas, Murray N. Wilson, Yipeng Cai, Graeme M. Luke, Bijuan Chen, Wenmin Li, Changqing Jin, Cui Ding, Shengli Guo, Fanlong Ning, Takashi U. Ito, Wataru Higemoto, Simon J. L. Billinge, Shoya Sakamoto, Atsushi Fujimori, Taito Murakami, Hiroshi Kageyama, Jose Antonio Alonso, Gabriel Kotliar, Masatoshi Imada, and Yasutomo J. Uemura. Volume-wise destruction of the antiferromagnetic Mott insulating state through quantum tuning. *Nature Communications*, 7:ncomms12519, August 2016.

Benjamin A. Frandsen. *Quantum phase transitions and local magnetism in Mott insulators: A local probe investigation using muons, neutrons, and photons.* Ph.D, Columbia University, United States – New York, 2016.

Matthew Frost, Christina Hoffmann, Jack Thomison, Mark Overbay, Michael Austin, Peter Carman, Robert Viola, Echo Miller, and Lisa Mosier. Initial testing of a Compact Crys-

tal Positioning System for the TOPAZ Single-Crystal Diffractometer at the Spallation Neutron Source. *Journal of Physics: Conference Series*, 251(1):012084, 2010.

A. M. Fry-Petit. Direct assignment of molecular vibrations via normal mode analysis of the neutron dynamic pair distribution function technique. *The Journal of Chemical Physics*, 143(12):124201, September 2015.

I. M. Gat-Malureanu, A. Fukaya, M. I. Larkin, A. J. Millis, P. L. Russo, A. T. Savici, Y. J. Uemura, P. P. Kyriakou, G. M. Luke, C. R. Wiebe, Y. V. Sushko, R. H. Heffner, D. E. MacLaughlin, D. Andreica, and G. M. Kalvius. Field Dependence of the Muon Spin Relaxation Rate in MnSi. *Physical Review Letters*, 90(15):157201, Am. Pharm. Rev. 2003.

B. Gilbert. Finite size effects on the real-space pair distribution function of nanoparticles. *Journal of Applied Crystallography*, 41(3):554–562, June 2008.

S. V. Grigoriev, S. V. Maleyev, A. I. Okorokov, Yu. O. Chetverikov, P. Böni, R. Georgii, D. Lamago, H. Eckerlebe, and K. Pranzas. Magnetic structure of MnSi under an applied field probed by polarized small-angle neutron scattering. *Physical Review B*, 74(21):214414, December 2006.

S. V. Grigoriev, S. V. Maleyev, A. I. Okorokov, Yu. O. Chetverikov, and H. Eckerlebe. Field-induced reorientation of the spin helix in MnSi near Tc. *Physical Review B*, 73(22):224440, June 2006.

Andre Guinier. *Theorie et technique de la radiocristallographie*. Paris: Dunon, 1956.

J. Hagemeister, N. Romming, K. von Bergmann, E. Y. Vedmedenko, and R. Wiesendanger. Stability of single skyrmionic bits. *Nature Communications*, 6, October 2015.

F. D. M. Haldane. O(3) Nonlinear Sigma Model and the Topological Distinction between Integer- and Half-Integer-Spin Antiferromagnets in Two Dimensions. *Physical Review Letters*, 61(8):1029–1032, August 1988.

Alex C. Hannon, Masatoshi Arai, Roger N. Sinclair, and Adrian C. Wright. A dynamic correlation function for amorphous solids. *Journal of Non-Crystalline Solids*, 150(1):239–244, November 1992.

Alex C Hannon, Masatoshi Arai, and Robert G Delaplane. A dynamic correlation function from inelastic neutron scattering data. *Nuclear Instruments and Methods in Physics Research Section A: Accelerators, Spectrometers, Detectors and Associated Equipment*, 354(1):96–103, January 1995.

R. S. Hayano, Y. J. Uemura, J. Imazato, N. Nishida, T. Yamazaki, H. Yasuoka, and Y. Ishikawa. Observation of the T/(T-Tc) Divergence of the Muon Spin-Lattice Relaxation Rate in MnSi near Tc. *Physical Review Letters*, 41(25):1743–1746, December 1978.

Ryugo Hayano, Yasutomo J. Uemura, Jun Imazato, Nobuhiko Nishida, Kanetada Nagamine, Toshimitsu Yamazaki, Yoshikazu Ishikawa, and Hiroshi Yasuoka. Spin Fluctuations of Itinerant Electrons in MnSi Studied by Muon Spin Rotation and Relaxation. *Journal of the Physical Society of Japan*, 49(5):1773–1783, November 1980.

Yi He, Rui-zhong Hu, Takeshi Egami, S. Joseph Poon, and Gary J. Shiflet. Two-dimensional pair distribution functions from synchrotron x-ray data: Application to an Al-Cu-Co decagonal quasicrystal. *Physical Review Letters*, 70(16):2411–2414, Am. Pharm. Rev. 1993.

Stefan Heinze, Kirsten von Bergmann, Matthias Menzel, Jens Brede, André Kubetzka, Roland Wiesendanger, Gustav Bihlmayer, and Stefan Blügel. Spontaneous atomic-scale magnetic skyrmion lattice in two dimensions. *Nature Physics*, 7(9):713–718, September 2011.

Conyers Herring and Charles Kittel. On the Theory of Spin Waves in Ferromagnetic Media. *Physical Review*, 81(5):869–880, March 1951.

Conyers Herring. Energy of a Bloch Wall on the Band Picture. II. Perturbation Approach. *Physical Review*, 87(1):60–70, July 1952.

Riccardo Hertel and Claus M. Schneider. Exchange Explosions: Magnetization Dynamics during Vortex-Antivortex Annihilation. *Physical Review Letters*, 97(17):177202, October 2006.

Y. Ishikawa, K. Tajima, D. Bloch, and M. Roth. Helical spin structure in manganese silicide MnSi. *Solid State Communications*, 19(6):525–528, July 1976.

Y. Ishikawa, G. Shirane, J. A. Tarvin, and M. Kohgi. Magnetic excitations in the weak itinerant ferromagnet MnSi. *Physical Review B*, 16(11):4956–4970, December 1977.

Y. Ishikawa, Y. Noda, Y. J. Uemura, C. F. Majkrzak, and G. Shirane. Paramagnetic spin fluctuations in the weak itinerant-electron ferromagnet MnSi. *Physical Review B*, 31(9):5884–5893, May 1985.

Junichi Iwasaki, Masahito Mochizuki, and Naoto Nagaosa. Current-induced skyrmion dynamics in constricted geometries. *Nature Nanotechnology*, 8(10):742–747, October 2013.

BIBLIOGRAPHY

Takeo Izuyama, Duk-Joo Kim, and Ryogo Kubo. Band Theoretical Interpretation of Neutron Diffraction Phenomena in Ferromagnetic Metals. *Journal of the Physical Society of Japan*, 18(7):1025–1042, July 1963.

R. W. James. *The Optical Principles Of The Diffraction Of X Rays Vol II*. G. Bell And Sons Limited, 1962.

M. Janoschek, M. Garst, A. Bauer, P. Krautscheid, R. Georgii, P. Böni, and C. Pfleiderer. Fluctuation-induced first-order phase transition in Dzyaloshinskii-Moriya helimagnets. *Physical Review B*, 87(13):134407, Am. Pharm. Rev. 2013.

Kirsten M. Ø. Jensen, Anders B. Blichfeld, Sage R. Bauers, Suzannah R. Wood, Eric Dooryhée, David C. Johnson, Bo B. Iversen, and Simon J. L. Billinge. Demonstration of thin film pair distribution function analysis (tfPDF) for the study of local structure in amorphous and crystalline thin films. *IUCrJ.*, 2(5):481–489, 2015.

I.-K. Jeong, Th. Proffen, F. Mohiuddin-Jacobs, and S. J. L. Billinge. Measuring correlated atomic motion using x-ray diffraction. *J. Phys. Chem. A*, 103:921–924, 1999.

I. K. Jeong, R. H. Heffner, M. J. Graf, and S. J. L. Billinge. Lattice dynamics and correlated atomic motion from the atomic pair distribution function. *Phys. Rev. B*, 67:104301, 2003.

Wanjun Jiang, Pramey Upadhyaya, Wei Zhang, Guoqiang Yu, M. Benjamin Jungfleisch, Frank Y. Fradin, John E. Pearson, Yaroslav Tserkovnyak, Kang L. Wang, Olle Heinonen, Suzanne G. E. te Velthuis, and Axel Hoffmann. Blowing magnetic skyrmion bubbles. *Science*, 349(6245):283–286, July 2015.

P. Juhás, T. Davis, C. L. Farrow, and S. J. L. Billinge. PDFgetX3: A rapid and highly automatable program for processing powder diffraction data into total scattering pair distribution functions. *J. Appl. Crystallogr.*, 46:560–566, 2013.

Pavol Juhás, Christopher L. Farrow, Xiaohao Yang, Kevin R. Knox, and Simon J. L. Billinge. Complex modeling: a strategy and software program for combining multiple information sources to solve ill-posed structure and nanostructure inverse problems. *Acta Crystallogr. A*, 71(6):562–568, Nov 2015.

R. Kadono, T. Matsuzaki, T. Yamazaki, S. R. Kreitzman, and J. H. Brewer. Spin dynamics of the itinerant helimagnet MnSi studied by positive muon spin relaxation. *Physical Review B*, 42(10):6515–6522, October 1990.

N. Kanazawa, Y. Onose, T. Arima, D. Okuyama, K. Ohoyama, S. Wakimoto, K. Kakurai, S. Ishiwata, and Y. Tokura. Large Topological Hall Effect in a Short-Period Helimagnet MnGe. *Physical Review Letters*, 106(15):156603, Am. Pharm. Rev. 2011.

N. Kanazawa, J.-H. Kim, D. S. Inosov, J. S. White, N. Egetenmeyer, J. L. Gavilano, S. Ishiwata, Y. Onose, T. Arima, B. Keimer, and Y. Tokura. Possible skyrmion-lattice ground state in the B20 chiral-lattice magnet MnGe as seen via small-angle neutron scattering. *Physical Review B*, 86(13):134425, October 2012.

N. Kanazawa, Y. Nii, X.-X. Zhang, A. S. Mishchenko, G. De Filippis, F. Kagawa, Y. Iwasa, N. Nagaosa, and Y. Tokura. Critical phenomena of emergent magnetic monopoles in a chiral magnet. *Nature Communications*, 7:11622, May 2016.

W. Kang, Y. Huang, X. Zhang, Y. Zhou, and W. Zhao. Skyrmion-Electronics: An Overview and Outlook. *Proceedings of the IEEE*, 104(10):2040–2061, October 2016.

Minoru Katayama, Suzushi Akimoto, and Kunisuke Asayama. Nuclear Magnetic Relaxation in Nearly and Weakly Antiferromagnetic beta Mn Metal and Alloy. *Journal of the Physical Society of Japan*, 42(1):97–100, 1977.

D. A. Keen, M. J. Gutmann, and C. C. Wilson. SXD – the single-crystal diffractometer at the ISIS spallation neutron source. *Journal of Applied Crystallography*, 39(5):714–722, October 2006.

Yoshio Kitaoka and Hiroshi Yasuoka. NMR Investigations on the Spin Fluctuations in Itinerant Antiferromagnets. I. V3se4 and V5se8. *Journal of the Physical Society of Japan*, 48(5):1460–1469, May 1980.

Charles Kittel. Introduction to Solid State Physics, 8th Edition - Charles Kittel, 2005.

M. Kontani, T. Hioki, and Y. Masuda. Nuclear magnetic relaxation in itinerant electron ferromagnet ZrZn2. *Solid State Communications*, 18(9):1251–1253, January 1976.

V. I. Korsunskiy and R. B. Neder. Exact model calculations of the total radial distribution functions for the X-ray diffraction case and systems of complicated chemical composition. *Journal of Applied Crystallography*, 38(6):1020–1027, December 2005.

Wataru Koshibae, Yoshio Kaneko, Junichi Iwasaki, Masashi Kawasaki, Yoshinori Tokura, and Naoto Nagaosa. Memory functions of magnetic skyrmions. *Japanese Journal of Applied Physics*, 54(5):053001, Am. Pharm. Rev. 2015.

J. M. Kosterlitz and D. J. Thouless. Ordering, metastability and phase transitions in two-dimensional systems. *Journal of Physics C: Solid State Physics*, 6(7):1181, 1973.

Stefan Krause and Roland Wiesendanger. Spintronics: Skyrmionics gets hot. *Nature Materials*, 15(5):493–494, May 2016.

A. K. Kulkarni, Kirk H. Schulz, T. S. Lim, and M. Khan. Dependence of the sheet resistance of indium-tin-oxide thin films on grain size and grain orientation determined from X-ray diffraction techniques. *Thin Solid Films*, 345(2):273–277, May 1999.

Soo-Yong Lee and Jung Hoon Han. Zero-energy bound states in a nodal topological lattice. *Physical Review B*, 91(24):245121, June 2015.

Bing Li, Despina Louca, Biao Hu, Jennifer L. Niedziela, Jianshi Zhou, and John B. Goodenough. Dynamic Distortions in the YTiO3 Ferromagnet. *Journal of the Physical Society of Japan*, 83(8):084601, July 2014.

J. Li, A. Tan, K. W. Moon, A. Doran, M. A. Marcus, A. T. Young, E. Arenholz, S. Ma, R. F. Yang, C. Hwang, and Z. Q. Qiu. Tailoring the topology of an artificial magnetic skyrmion. *Nature Communications*, 5:ncomms5704, August 2014.

Liu Lian and Yasutomo Uemura. *Dynamic Spin Fluctuations and Static Order Parameter of Skyrmion Systems Studied by Muon Spin Relaxation.* PhD thesis, Columbia University, 2017.

Shi-Zeng Lin and Avadh Saxena. Dynamics of Dirac strings and monopolelike excitations in chiral magnets under a current drive. *Physical Review B*, 93(6):060401, February 2016.

Stephen Lovesey. *The Theory of Neutron Scattering from Condensed Matter.* International Series of Monographs on Physics. Oxford University Press, Oxford, New York, October 1986.

O. L. Makarova, A. V. Tsvyashchenko, G. Andre, F. Porcher, L. N. Fomicheva, N. Rey, and I. Mirebeau. Neutron diffraction study of the chiral magnet MnGe. *Physical Review B*, 85(20):205205, May 2012.

N. Martin, M. Deutsch, F. Bert, D. Andreica, A. Amato, P. Bonfà, R. De Renzi, U. K. Rößler, P. Bonville, L. N. Fomicheva, A. V. Tsvyashchenko, and I. Mirebeau. Magnetic ground state and spin fluctuations in MnGe chiral magnet as studied by muon spin rotation. *Physical Review B*, 93(17):174405, May 2016.

Y. Masuda, T. Hioki, and A. Oota. Spin fluctuations in itinerant electron ferromagnet Sc3in. *Physica B*, 91:291 – 297, 1977.

Yoshika Masuda. Spin fluctuations in weakly ferro- and antiferromagnetic metals and alloys. *Journal of Magnetism and Magnetic Materials*, 31:259 – 264, 1983.

Margaret Mcintyre and Grant Cairns. A new formula for winding number. *Geometriae Dedicata*, 46(2):149–159, May 1993.

R. J. McQueeney. Dynamic radial distribution function from inelastic neutron scattering. *Physical Review B*, 57(17):10560–10568, May 1998.

P. Milde, D. Köhler, J. Seidel, L. M. Eng, A. Bauer, A. Chacon, J. Kindervater, S. Mühlbauer, C. Pfleiderer, S. Buhrandt, C. Schütte, and A. Rosch. Unwinding of a Skyrmion Lattice by Magnetic Monopoles. *Science*, 340(6136):1076–1080, May 2013.

A.H. Mitchell. Nuclear Relaxation by the Hyperfine Interaction with the Ion Core Spins in Ferromagnetic and Antiferromagnetic Crystals. *The Journal of Chemical Physics*, 27(1):17–19, July 1957.

Masahito Mochizuki. Spin-Wave Modes and Their Intense Excitation Effects in Skyrmion Crystals. *Physical Review Letters*, 108(1):017601, January 2012.

S Morita. *Noncontact Atomic Force Microscopy*. Springer, 2015.

Tôru Moriya and Arisato Kawabata. Effect of Spin Fluctuations on Itinerant Electron Ferromagnetism. *Journal of the Physical Society of Japan*, 34(3):639–651, March 1973.

Tôru Moriya and Kazuo Ueda. Nuclear magnetic relaxation in weakly ferro-and antiferro-magnetic metals. *Solid State Communications*, 15(2):169–172, July 1974.

Tôru Moriya. The Effect of Electron-Electron Interaction on the Nuclear Spin Relaxation in Metals. *Journal of the Physical Society of Japan*, 18(4):516–520, 1963.

Tôru Moriya. Spin Fluctuations in Ferromagnetic Metals —Temperature Variation of Local Moment and Short Range Order. *Journal of the Physical Society of Japan*, 51:420, February 1982.

Tôru Moriya. *Spin Fluctuations in Itinerant Electron Magnetism*. Springer Berlin Heidelberg, 1985.

K. K. Murata and S. Doniach. Theory of Magnetic Fluctuations in Itinerant Ferromagnets. *Physical Review Letters*, 29(5):285–288, July 1972.

S. Mühlbauer, B. Binz, F. Jonietz, C. Pfleiderer, A. Rosch, A. Neubauer, R. Georgii, and P. Böni. Skyrmion Lattice in a Chiral Magnet. *Science*, 323(5916):915–919, February 2009.

Masahiro Nagao, Yeong-Gi So, Hiroyuki Yoshida, Kazunari Yamaura, Takuro Nagai, Toru Hara, Atsushi Yamazaki, and Koji Kimoto. Experimental observation of multiple-Q

states for the magnetic skyrmion lattice and skyrmion excitations under a zero magnetic field. *Physical Review B*, 92(14):140415, October 2015.

Naoto Nagaosa and Yoshinori Tokura. Topological properties and dynamics of magnetic skyrmions. *Nature Nanotechnology*, 8(12):899–911, December 2013.

Nathan Nakamura, Maxwell W. Terban, Simon J. L. Billinge, and B. Reeja-Jayan. Unlocking the structure of mixed amorphous-crystalline ceramic oxide films synthesized under low temperature electromagnetic excitation. *Journal of Materials Chemistry A*, 5(35):18434–18441, 2017.

Kenji Nomura, Hiromichi Ohta, Akihiro Takagi, Toshio Kamiya, Masahiro Hirano, and Hideo Hosono. Room-temperature fabrication of transparent flexible thin-film transistors using amorphous oxide semiconductors. *Nature*, 432(7016):488–492, November 2004.

Kenji Nomura, Akihiro Takagi, Toshio Kamiya, Hiromichi Ohta, Masahiro Hirano, and Hideo Hosono. Amorphous Oxide Semiconductors for High-Performance Flexible Thin-Film Transistors. *Japanese Journal of Applied Physics*, 45(5S):4303, May 2006.

Hiroshi Oike, Akiko Kikkawa, Naoya Kanazawa, Yasujiro Taguchi, Masashi Kawasaki, Yoshinori Tokura, and Fumitaka Kagawa. Interplay between topological and thermodynamic stability in a metastable magnetic skyrmion lattice. *Nature Physics*, 12(1):62–66, January 2016.

Brian O'Regan and Michael Grätzel. A low-cost, high-efficiency solar cell based on dye-sensitized colloidal TiO2 films. *Nature*, 353(6346):737–740, October 1991.

J. C. Osborn and T. R. Welberry. A position-sensitive detector system for the measurement of diffuse X-ray scattering. *Journal of Applied Crystallography*, 23(6):476–484, December 1990.

C. Pappas, L. J. Bannenberg, E. Lelievre-Berna, F. Qian, C. Dewhurst, D. Schlagel, T. A. Longrasso, and P. Falus. From Chiral Fluctuations to the Skyrmion Lattice Phase in MnSi: A SANS and Neutron Spin Echo Study. *arXiv:1606.07962 [cond-mat]*, June 2016. arXiv: 1606.07962.

C. Pappas, L.J. Bannenberg, E. Lelievre-Berna, F. Qian, C.D. Dewhurst, R.M. Dalgliesh, D.L. Schlagel, T.A. Lograsso, and P. Falus. Magnetic Fluctuations, Precursor Phenomena, and Phase Transition in MnSi under a Magnetic Field. *Physical Review Letters*, 119(4):047203, July 2017.

Jin-Hong Park and Jung Hoon Han. Zero-temperature phases for chiral magnets in three dimensions. *Physical Review B*, 83(18):184406, May 2011.

Hyun Soon Park, Xiuzhen Yu, Shinji Aizawa, Toshiaki Tanigaki, Tetsuya Akashi, Yoshio Takahashi, Tsuyoshi Matsuda, Naoya Kanazawa, Yoshinori Onose, Daisuke Shindo, Akira Tonomura, and Yoshinori Tokura. Observation of the magnetic flux and three-dimensional structure of skyrmion lattices by electron holography. *Nature Nanotechnology*, 9(5):337–342, May 2014.

P. F. Peterson, M Gutmann, Th. Proffen, and S. J. L. Billinge. PDFgetN: a user-friendly program to extract the total scattering structure function and the pair distribution function from neutron powder diffraction data. *J. Appl. Crystallogr.*, 33(4):1192–1192, Aug 2000.

T. Proffen and T. R. Welberry. Analysis of Diffuse Scattering via the Reverse Monte Carlo Technique: a Systematic Investigation. *Acta Crystallographica Section A: Foundations of Crystallography*, 53(2):202–216, March 1997.

Xiangyun Qiu, Jeroen W. Thompson, and Simon J. L. Billinge. PDFgetX2: a GUI driven program to obtain the pair distribution function from X-ray powder diffraction data. *J. Appl. Crystallogr.*, 37:678, 2004.

R Rajaraman. Solitons and Instantons, Volume 15 - 1st Edition, 1982.

W. Reichardt and L. Pintschovius. Influence of phonons on the pair distribution function deduced from neutron powder diffraction. *Physical Review B*, 63(17):174302, Am. Pharm. Rev. 2001.

Ludwig Reimer. *Transmission Electron Microscopy - Physics of Image Formation.* Springer-Verlag New York, 2008.

U. K. Robler, A. N. Bogdanov, and C. Pfleiderer. Spontaneous skyrmion ground states in magnetic metals. *Nature*, 442(7104):797–801, August 2006.

Niklas Romming, Christian Hanneken, Matthias Menzel, Jessica E. Bickel, Boris Wolter, Kirsten von Bergmann, André Kubetzka, and Roland Wiesendanger. Writing and Deleting Single Magnetic Skyrmions. *Science*, 341(6146):636–639, August 2013.

Niklas Romming, André Kubetzka, Christian Hanneken, Kirsten von Bergmann, and Roland Wiesendanger. Field-Dependent Size and Shape of Single Magnetic Skyrmions. *Physical Review Letters*, 114(17):177203, May 2015.

Stephan Rosenkranz and Raymond Osborn. Corelli: Efficient single crystal diffraction with elastic discrimination. *Pramana*, 71(4):705–711, October 2008.

J. Sampaio, V. Cros, S. Rohart, A. Thiaville, and A. Fert. Nucleation, stability and current-induced motion of isolated magnetic skyrmions in nanostructures. *Nature Nanotechnology*, 8(11):839–844, November 2013.

P. Schaub, T. Weber, and W. Steurer. Exploring local disorder in single crystals by means of the three-dimensional pair distribution function. *Philosophical Magazine*, 87(18-21):2781–2787, June 2007.

P. Schaub, T. Weber, and W. Steurer. Analysis and modelling of structural disorder by the use of the three-dimensional pair distribution function method exemplified by the disordered twofold superstructure of decagonal Al–Cu–Co. *Journal of Applied Crystallography*, 44(1):134–149, February 2011.

Jörg Schmalian and Misha Turlakov. Quantum Phase Transitions of Magnetic Rotons. *Physical Review Letters*, 93(3):036405, July 2004.

Christoph Schütte and Achim Rosch. Dynamics and energetics of emergent magnetic monopoles in chiral magnets. *Physical Review B*, 90(17):174432, November 2014.

J. Seidel. *Topological Structures in Ferroic Materials*. Springer International Publishing, 2016.

Shinichiro Seki and Masahito Mochizuki. *Skyrmions in Magnetic Materials*. 2016. DOI: 10.1007/978-3-319-24651-2.

T. Senthil, Ashvin Vishwanath, Leon Balents, Subir Sachdev, and Matthew P. A. Fisher. Deconfined Quantum Critical Points. *Science*, 303(5663):1490–1494, March 2004.

E. Sevillano, H. Meuth, and J. J. Rehr. Extended x-ray absorption fine structure Debye-Waller factors. I. Monatomic crystals. *Physical Review B*, 20(12):4908–4911, December 1979.

K. Shibata, X. Z. Yu, T. Hara, D. Morikawa, N. Kanazawa, K. Kimoto, S. Ishiwata, Y. Matsui, and Y. Tokura. Towards control of the size and helicity of skyrmions in helimagnetic alloys by spin-orbit coupling. *Nature Nanotechnology*, 8(10):723–728, October 2013.

Badri Shyam, Kevin H. Stone, Riccardo Bassiri, Martin M. Fejer, Michael F. Toney, and Apurva Mehta. Measurement and Modeling of Short and Medium Range Order in Amorphous Ta_2O_5 Thin Films. *Scientific Reports*, 6:32170, August 2016.

A. Siemens, Y. Zhang, J. Hagemeister, E. Y. Vedmedenko, and R. Wiesendanger. Minimal radius of magnetic skyrmions: statics and dynamics. *New Journal of Physics*, 18(4):045021, 2016.

T. H. R. Skyrme. A unified field theory of mesons and baryons. *Nuclear Physics*, 31:556–569, March 1962.

J. C. Slater. The Theory of Ferromagnetism: Lowest Energy Levels. *Physical Review*, 52(3):198–214, August 1937.

Sergei M Stishov and A E Petrova. Itinerant helimagnet MnSi. *Physics-Uspekhi*, 54(11):1117–1130, November 2011.

S. M. Stishov, A. E. Petrova, S. Khasanov, G. Kh. Panova, A. A. Shikov, J. C. Lashley, D. Wu, and T. A. Lograsso. Magnetic phase transition in the itinerant helimagnet MnSi: Thermodynamic and transport properties. *Physical Review B*, 76(5):052405, August 2007.

S. M. Stishov, A. E. Petrova, S. Khasanov, G. Kh Panova, A. A. Shikov, J. C. Lashley, D. Wu, and T. A. Lograsso. Heat capacity and thermal expansion of the itinerant helimagnet MnSi. *Journal of Physics: Condensed Matter*, 20(23):235222, 2008.

A. Suter and B. M. Wojek. Musrfit A Free Platform-Independent Framework for MuSR Data Analysis. *Physics Procedia*, 30:69–73, January 2012.

Simon M Sze. Semiconductor Sensors, 1994.

Simon M Sze. Semiconductor Devices: Physics and Technology, 3rd Edition, 2013.

Shigeru Takagi, Hiroshi Yasuoka, C. Y. Huang, and J. L. Smith. No Evidence of Antiferromagnetism in TiBeTi and 49ti NMR. *Journal of the Physical Society of Japan*, 50(7):2137–2138, July 1981.

Tadashi Takenaka and Koichiro Sakata. Grain Orientation and Electrical Properties of Hot-Forged Bi4ti3o12 Ceramics. *Japanese Journal of Applied Physics*, 19(1):31, January 1980.

Masashi Takigawa, Hiroshi Yasuoka, Yasutomo J. Uemura, Ryugo S. Hayano, Toshimitsu Yamazaki, and Yoshikazu Ishikawa. Positive Muon Spin Rotation and Relaxation Studies in the Helically Ordered State of MnSi. *Journal of the Physical Society of Japan*, 49(5):1760–1767, November 1980.

I. Tamura, K. Oikawa, T. Kawasaki, T. Ohhara, K. Kaneko, R. Kiyanagi, H. Kimura, M. Takahashi, T. Kiyotani, M. Arai, Y Noda, and K. Ohshima. Current status of a time-

of-flight single crystal neutron diffractometer SENJU at J-PARC. *Journal of Physics: Conference Series*, 340(1):012040, 2012.

Toshiaki Tanigaki, Kiyou Shibata, Naoya Kanazawa, Xiuzhen Yu, Yoshinori Onose, Hyun Soon Park, Daisuke Shindo, and Yoshinori Tokura. Real-Space Observation of Short-Period Cubic Lattice of Skyrmions in MnGe. *Nano Letters*, 15(8):5438–5442, August 2015.

André Thiaville, José Miguel García, Rok Dittrich, Jacques Miltat, and Thomas Schrefl. Micromagnetic study of Bloch-point-mediated vortex core reversal. *Physical Review B*, 67(9):094410, March 2003.

C. V. Thompson. Grain Growth in Thin Films. *Annual Review of Materials Science*, 20(1):245–268, 1990.

C. V. Thompson. Structure Evolution During Processing of Polycrystalline Films. *Annual Review of Materials Science*, 30(1):159–190, 2000.

Akira Tonomura, Xiuzhen Yu, Keiichi Yanagisawa, Tsuyoshi Matsuda, Yoshinori Onose, Naoya Kanazawa, Hyun Soon Park, and Yoshinori Tokura. Real-Space Observation of Skyrmion Lattice in Helimagnet MnSi Thin Samples. *Nano Letters*, 12(3):1673–1677, March 2012.

O. A. Tretiakov and O. Tchernyshyov. Vortices in thin ferromagnetic films and the skyrmion number. *Physical Review B*, 75(1):012408, January 2007.

Kazuo Ueda and Tôru Moriya. Nuclear Magnetic Relaxation in Weakly Antiferromagnetic Metals. *Journal of the Physical Society of Japan*, 38(1):32–40, January 1975.

Y. J. Uemura, S. L. Lee, S. H. Kilcoyne, and R. Cywinski. *Muon science : muons in physics, chemistry, and materials (proceedings of the fifty first Scottish Universities Summer School in Physics, St. Andrews, August 1998)*. Scottish Universities Summer School in Physics & Institute of Physics Pub., Bristol, 1999.

Y. J. Uemura, T. Goko, I. M. Gat-Malureanu, J. P. Carlo, P. L. Russo, A. T. Savici, A. Aczel, G. J. MacDougall, J. A. Rodriguez, G. M. Luke, S. R. Dunsiger, A. McCollam, J. Arai, Ch Pfleiderer, P. Böni, K. Yoshimura, E. Baggio-Saitovitch, M. B. Fontes, J. Larrea, Y. V. Sushko, and J. Sereni. Phase separation and suppression of critical dynamics at quantum phase transitions of MnSi and Sr1-xCaxRuO3. *Nature Physics*, 3(1):29–35, January 2007.

Léon Van Hove. Correlations in Space and Time and Born Approximation Scattering in Systems of Interacting Particles. *Physical Review*, 95(1):249–262, July 1954.

Romain Viennois, Corine Reibel, Didier Ravot, Regis Debord, and Stephane Pailhès. Observation of various magnetic-field–induced states in B20 cubic MnGe. *EPL (Europhysics Letters)*, 111(1):17008, 2015.

R. B. Von Dreele. Powder diffraction: what's in a name? *Acta Crystallographica Section C: Crystal Structure Communications*, 69(12):1431–1432, December 2013.

B. E. (Bertram Eugene) Warren. *X-ray diffraction*. Reading, Mass., Addison-Wesley Pub. Co, 1969.

T. R. Welberry and T. Proffen. Analysis of Diffuse Scattering from Single Crystals via the Reverse Monte Carlo Technique. I. Comparison with Direct Monte Carlo. *Journal of Applied Crystallography*, 31(3):309–317, June 1998.

T. R. Welberry, T. Proffen, and M. Bown. Analysis of Single-Crystal Diffuse X-ray Scattering via Automatic Refinement of a Monte Carlo Model. *Acta Crystallographica Section A: Foundations of Crystallography*, 54(5):661–674, September 1998.

Roland Wiesendanger. Nanoscale magnetic skyrmions in metallic films and multilayers: a new twist for spintronics. *Nature Reviews Materials*, 1(7):natrevmats201644, June 2016.

David Williams. *Transmission Electron Microscopy*. Springer US, 2009.

Philip Willmott. *An Introduction to Synchrotron Radiation: Techniques and Applications - Philip Willmott*. Wiley, 2011.

M. S. Wilson and S. Gottesfeld. Thin-film catalyst layers for polymer electrolyte fuel cell electrodes. *Journal of Applied Electrochemistry*, 22(1):1–7, January 1992.

Mahlon S. Wilson and Shimshon Gottesfeld. High Performance Catalyzed Membranes of Ultra-low Pt Loadings for Polymer Electrolyte Fuel Cells. *Journal of The Electrochemical Society*, 139(2):L28–L30, February 1992.

Seonghoon Woo, Kai Litzius, Benjamin Krüger, Mi-Young Im, Lucas Caretta, Kornel Richter, Maxwell Mann, Andrea Krone, Robert M. Reeve, Markus Weigand, Parnika Agrawal, Ivan Lemesh, Mohamad-Assaad Mawass, Peter Fischer, Mathias Kläui, and Geoffrey S. D. Beach. Observation of room-temperature magnetic skyrmions and their current-driven dynamics in ultrathin metallic ferromagnets. *Nature Materials*, 15(5):501–506, May 2016.

Suzannah R. Wood, Keenan N. Woods, Paul N. Plassmeyer, David A. Marsh, Darren W. Johnson, Catherine J. Page, Kirsten M. Ø. Jensen, and David C. Johnson. Same Precursor, Two Different Products: Comparing the Structural Evolution of In–Ga–O "Gel-Derived"

Powders and Solution-Cast Films Using Pair Distribution Function Analysis. *Journal of the American Chemical Society*, 139(15):5607–5613, Am. Pharm. Rev. 2017.

Xuanzhi Wu. High-efficiency polycrystalline CdTe thin-film solar cells. *Solar Energy*, 77(6):803–814, December 2004.

Yizhak Yacoby, Mukhles Sowwan, Edward Stern, Julie O. Cross, Dale Brewe, Ron Pindak, John Pitney, Eric M. Dufresne, and Roy Clarke. Direct determination of epitaxial interface structure in Gd2o3 passivation of GaAs. *Nature Materials*, 1(2):99–101, October 2002.

X. Yan and T. Egami. Interfacial structure of Co/Pt multilayers. *Physical Review B*, 47(4):2362–2368, January 1993.

X. Yan, T. Egami, E. E. Marinero, R. F. C. Farrow, and C. H. Lee. On the atomic interdiffusion in Co/Pt superlattices. *Journal of Materials Research*, 7(6):1309–1312, June 1992.

Xiaohao Yang, Pavol Juhás, Christopher Farrow, and Simon J. L. Billinge. xPDFsuite: an end-to-end software solution for high throughput pair distribution function transformation, visualization and analysis. *arXiv*, 2015. 1402.3163.

Seong-Gyu Yang, Ye-Hua Liu, and Jung Hoon Han. Formation of a topological monopole lattice and its dynamics in three-dimensional chiral magnets. *Physical Review B*, 94(5):054420, August 2016.

A. Yaouanc and P. D. de Reotier. The positive muon relaxation rate at low temperature in a Heisenberg ferromagnet. *Journal of Physics: Condensed Matter*, 3(32):6195, 1991.

A. Yaouanc, P. Dalmas de Réotier, P. C. M. Gubbens, S. Sakarya, G. Lapertot, A. D. Hillier, and P. J. C. King. Testing the self-consistent renormalization theory for the description of the spin-fluctuation modes of MnSi at ambient pressure. *Journal of Physics: Condensed Matter*, 17(13):L129, 2005.

A. Yaouanc, P. Dalmas de Réotier, A. Maisuradze, and B. Roessli. Magnetic structure of the MnGe helimagnet and representation analysis. *Physical Review B*, 95(17):174422, May 2017.

X. Z. Yu, Y. Onose, N. Kanazawa, J. H. Park, J. H. Han, Y. Matsui, N. Nagaosa, and Y. Tokura. Real-space observation of a two-dimensional skyrmion crystal. *Nature*, 465(7300):901–904, June 2010.

Xiuzhen Yu, Maxim Mostovoy, Yusuke Tokunaga, Weizhu Zhang, Koji Kimoto, Yoshio Matsui, Yoshio Kaneko, Naoto Nagaosa, and Yoshinori Tokura. Magnetic stripes and

214

skyrmions with helicity reversals. *Proceedings of the National Academy of Sciences*, 109(23):8856–8860, June 2012.

Lei Zhang, Dirk Menzel, Chiming Jin, Haifeng Du, Min Ge, Changjin Zhang, Li Pi, Mingliang Tian, and Yuheng Zhang. Critical behavior of the single-crystal helimagnet MnSi. *Physical Review B*, 91(2):024403, January 2015.

Xuebing Zhao, Chiming Jin, Chao Wang, Haifeng Du, Jiadong Zang, Mingliang Tian, Renchao Che, and Yuheng Zhang. Direct imaging of magnetic field-driven transitions of skyrmion cluster states in FeGe nanodisks. *Proceedings of the National Academy of Sciences*, 113(18):4918–4923, May 2016.

Appendix A

Creation of 2D Skyrmion during Hedgehog annihilation

As has been shown from simulation Schütte and Rosch [2014], the annihilation of Hedgehog and Anti-Hedgehog is accompanied by the creation of a 2D Skyrmion line. By drawing down the Hedgehog and Anti-Hedgehog merging process on a piece of paper and perform geometric analysis we can already have an intuitive understanding. Based on the physical consideration we require that the the spin aligns locally with its neighbors (except at the singular point at the center of the Hedgehog). It can be readily shown then that the smooth merging of a Hedgehog and an Anti-Hedgehog, through connecting with each other on the sides with the same spin alignment, leave behind a 2D Skyrmion line that closes on itself, that is, a Skyrmion loop. In this case the generated Skyrmion loop surrounds the connected Hedgehog-Antihedgehog pair.

In a similar manner it can be shown that the spin configuration of both Hedgehog and Anti-Hedgehog can be connected smoothly (with a spin structure of winding number 0) with the

spin configuration of the intersection of a 2D Skyrmion line, and thus is topologically allowed to exist at one end of a 2D Skyrmion line. The pair annihilation of the Hedgehog and Anti-Hedgehog in this case can be achieved smoothly via continuous re-orientation of the local field, and connects the 2 existing Skyrmions and form a longer Skyrmion line. This case is qualitative the same as the previous case in that both involves the merging/annihilation process of a Hedgehog and Anti-Hedgehog pair, and results in the creation of a closed 2D Skyrmion loop. Specifically, in both cases, this merging process corresponds to the closing of the surface of the 2D Skyrmion loop, although the topological orientation of the Hedgehog pair with respect to that of the Skyrmion loop to be created is different. Moreover, we argue that the two cases are in fact equivalent to each other: it is easy to show by simple geometric analysis that by deforming the spin continuously, the two cases can be transformed smoothly into each other. In other words these two spin configurations are topologically equivalent, and a logical consequence of the existence of one Hedgehog-Antihedgehog pair is the existence of a 2D Skyrmion line with open ends.

In other words, here we are making the general argument that, for any structure that contains one Hedgehog and one Antihedgehog, the pair-annihilation of the Hedgehogs will leave behind a closed Skyrmion loop. Using the mathematical language of topology, this is to argue that in an otherwise continuous tangent vector field, the existence of 2 saddle points implies the existence of two center critical points in the 2 dimensional space, and 1 torus in the 3 dimensional space. Here saddle point and center are topological critical points with formal mathematical definition in the field of vector topology. The question here is related to the winding number of the specific tangent vector field. This can be proved right or wrong by explicit calculation. Intuitively, this is due to the intrinsic property of a singular topological defect: it is able to leave a foot print in a magnetic field arbitrarily far from its

location Braun [2012]. And in this case the existence of the Skyrmion loop can be regarded as the foot print which the Hedgehog-Antihedgehog pair leave in the system.

If this argument is true, then at the transition between Hedgehog state and the induced ferromagnetic state in MnGe, besides the pair annihilation of Hedgehog and Antihedgehog suggested in Kanazawa *et al.* [2016], there must also occur a (self) annihilation of the 2D Skyrmion loop that exist as the byproduct of the pair annihilation of the 3D Hedgehogs.

Appendix B

Estimation of the static field width from magnetization

As has been analyzed in previous sections, the relaxation of the transverse field μSR spectra reflects the width of the static internal magnetic field. As a simple estimation, we could also estimate the static field with a simple model that uses the static moment size measured from the magnetization. In this model we assume that the static internal field comes from the static magnetic moment of Mn. Meanwhile in the induced magnetic and the paramagnetic phases, as shown by the large $1/T_1$ dynamics and the linear relation between relaxation rate and z moment, the in-plane component of the Mn moment is highly dynamic while the z component (polarized along the external field) is static. Therefore here the static internal field in the induced magnetic phase mainly comes from the static z moment. Instead of a single value, this field acquires a finite width due to the variation of the magnitude of the z moment.

APPENDIX B. ESTIMATION OF THE STATIC FIELD WIDTH FROM MAGNETIZATION

As a simple model, the width of the internal field is determined by both the magnitude and the width of the distribution of the static moment. It is easy to see that by doubling the magnitude of the internal field, the magnitude of the width of is also doubled. On the other hand, the distribution of the moment also affects the distribution of the field. As detailed in Martin *et al.* [2016], the dipolar field in the materials is expressed as

$$\mathbf{B}_{\text{dip}}\left(\mathbf{R}_{\mu}\right) = \frac{\mu_0}{4\pi} \cdot \sum_{i} \left[\frac{3\mathbf{r}_i\left(\mathbf{m}_i \cdot \mathbf{r}_i\right)}{|\mathbf{r}_i|^5} - \frac{\mathbf{m}_i}{|\mathbf{r}_i|^3} \right], \tag{B.1}$$

where $\mathbf{r}_i$ is the vector that connects the i th magnetic moment and the muon. For the ordered Hedgehog phase, the magnetic moment $\mathbf{m}$ can be expressed as follows Kanazawa *et al.* [2016]:

$$\mathbf{M}_{\text{SkX}} = M_{\text{SkX}} \cdot \left(\sin qy + \cos qz, \sin qz + \cos qx, \sin qx + \cos qy\right) \tag{B.2}$$

$$= M_{\text{SkX}} \cdot \left(n_{\text{X}}, n_{\text{Y}}, n_{\text{Z}}\right), \tag{B.3}$$

where M_{SkX} is the magnitude of the static moment and q is the magnitude of the magnetic propagation vector. Although for the hedgehog phase with 3D helical order the static moment cannot be determined precisely from magnetization, which only probes the moment along the external field direction, from the asymmetry of the transverse μSR data we know that deep in the ordered phase the fluctuating moment were mostly frozen, and thus the static moment would approach the total Mn ion moment of 1.8 μ_B. Furthermore, in the calculation of the field width, the exact distribution of the moment in equation B.3 can be reasonably approximated by moment with random orientation considering the fact that the magnetic structure were incommensurate with the lattice Martin *et al.* [2016]. For the field-induced magnetic phase, assuming that only the z moment is static, the moment can be expressed similarly as

$$\mathbf{M}_{\text{FI}} = M_{\text{FI}} \cdot \left(0, 0, n_{\text{Z}}\right). \tag{B.4}$$

APPENDIX B. ESTIMATION OF THE STATIC FIELD WIDTH FROM MAGNETIZATION

The internal field distribution is determined by inserting the expressions of the moment $\mathbf{m}$ into the dipolar field B.1.

Now we consider the influence of the moment distribution on the width of the internal field. It is clear from equation B.1 that a single moment would contribute to the field within the plane perpendicular to the direction of the moment. Furthermore, considering the total field produced by all the moments within the sample, even a single component of the moment (x, y or z) would contribute to the field in all 3 directions due to the variation of the magnitude of this component of the moment between different atoms. Therefore as a rough approximation, the 3 (i.e. x,y,z) components of the moment can be seen as 3 random variables contributing independently to the internal field. Namely,

$$\mathbf{B}_{\text{dip}}\left(\mathbf{M}\right) = \mathbf{B}_{\text{dip}}\left(\mathbf{M}_{\text{X}} + \mathbf{M}_{\text{Y}} + \mathbf{M}_{\text{Z}}\right) \tag{B.5}$$

$$= \mathbf{B}_{\text{dip}}\left(\mathbf{M}_{\text{X}}\right) + \mathbf{B}_{\text{dip}}\left(\mathbf{M}_{\text{Y}}\right) + \mathbf{B}_{\text{dip}}\left(\mathbf{M}_{\text{Z}}\right). \tag{B.6}$$

Following this approximation, the moment distribution in the induced phase can be approximated as consisting of only z component, with a random variation in its magnitude around a mean value. We assume that the variation in the magnitude of the moment are similar between the ordered phase and the induced magnetic phase. Thus in the induced phase, the internal field was produced by only 1 random field variable $\mathbf{B}_{\text{dip}}\left(\mathbf{M}_{\text{Z}}\right)$ instead of the three in equation B.6.

According to the statistical rules, the sum of n identical random variables with standard deviation σ would give a new random variable with standard deviation of $\sqrt{n}\sigma$. In our case, as analyzed above, the internal field of the ordered phase equals to the sum of 3 random (vector) field variables, and the internal field of the induced phase equals to 1 random field variable. Therefore assuming that the magnitude of the field variables in the two phases are

the same, then the field width of the ordered phase is expected to be $\sqrt{3}$ times larger than that of the induced phase.

Therefore, considering that the field width is also proportional to the magnitude of the field, which is proportional to the magnitude of the moment, we have

$$\frac{\Delta B_{\text{ordered}}}{\Delta B_{\text{induced}}} = \frac{\lambda_{\text{ordered}}}{\lambda_{\text{induced}}} = \frac{M_{\text{ordered}}}{M_{\text{induced}}} \cdot \sqrt{3}, \tag{B.7}$$

where ΔB, λ and M stands for the width of the internal field, the relaxation rate in the transverse field μSR spectra and the static moment size. Equation B.7 provide a simple way to estimate the internal field width independently from μSR and from magnetization.

Appendix C

The linear relation between moment and field width

As mentioned from the discussion of figure 3.14, the ratio of the relaxation rate and the moment are almost identical for the paramagnetic and the induced ferromagnetic phase. Since the relaxation rate is approximately proportional to the width of the internal field, and that the magnetic moment is proportional to the susceptibility, this ratio give a measure of the coupling strength between the magnetic susceptibility and the local field at the muon site. In specific, the total (static) field at a muon site is defined as Martin *et al.* [2016]

$$\mathbf{B}_{\text{local}} = \mathbf{B}_{\text{dipolar}} + \mathbf{B}_{\text{contact}}, \tag{C.1}$$

where $\mathbf{B}_{\text{dipolar}}$ is the dipolar field and $\mathbf{B}_{\text{contact}}$ is the hyperfine contact field between the muon and the Mn moment. Equation C.1 can be rewritten in an approximate form by replacing

the field terms with their expression:

$$
\begin{aligned}
\mathbf{B}_{\text{local}} &= \frac{\mu_0}{4\pi} \cdot \sum_i^N \left[\frac{3\mathbf{r}_i \left(\mathbf{m}_i \cdot \mathbf{r}_i \right)}{|\mathbf{r}_i|^5} - \frac{\mathbf{m}_i}{|\mathbf{r}_i|^3} \right] + \frac{A_{\text{cont}}}{N} \sum_{i=1}^N \mathbf{m}_i \\
&\approx \left(\frac{\mu_0}{4\pi} \cdot \sum_i^N \left[\frac{3\mathbf{r}_i \left(\mathbf{m}_i \cdot \mathbf{r}_i \right)}{|\mathbf{r}_i|^5 |\mathbf{m}_i|} - \frac{\mathbf{m}_i}{|\mathbf{r}_i|^3 |\mathbf{m}_i|} \right] \right) \cdot \frac{\sum_{i=1}^N \mathbf{m}_i}{N} + A_{\text{cont}} \frac{\sum_{i=1}^N \mathbf{m}_i}{N} \qquad \text{(C.2)} \\
&= \left[\frac{\mu_0}{4\pi} \cdot \sum_i^N \left[\frac{3\mathbf{r}_i \left(\hat{\mathbf{m}}_i \cdot \mathbf{r}_i \right)}{|\mathbf{r}_i|^5} - \frac{\hat{\mathbf{m}}_i}{|\mathbf{r}_i|^3} \right] + A_{\text{cont}} \right] \cdot \overline{\mathbf{m}}.
\end{aligned}
$$

Here $\mathbf{r}_i$ and $\mathbf{m}_i$ are the position and static moment of the ith Mn moment. A_{cont} is the hyperfine coupling constant, and $\overline{\mathbf{m}} = \frac{\sum_{i=1}^N \mathbf{m}_i}{N}$ is the average static moment of Mn. Since that the dipolar field can be approximated by the product of the magnetization with a pre-factor that depend only insensitively on the orientation distribution of the Mn moment, and that the hyperfine constant A_{cont} depends on the microscopic coupling mechanism of the field and the moment, the total pre-factor is expected to be a constant for a given magnetic phase. In such case, Equation C.2 shows that for the same magnetic phase, the local field could be roughly proportional to the local moment.

Appendix D

Interpretation of the dynamic PDF

This chapter discussed in detail the various features of of the dynamical PDF of a diatomic molecule and address the physical origin of each of them. We also discuss the understanding of $g(r, \omega)$ as spatial expansion as well as spectrum of the correlation function $g(r, t)$ of the system, and try to address its physical meaning for a general lattice system.

D.1   Understanding the dynamic PDF

D.1.1   Discreteness of the energy spectrum

The discretization of the energy spectrum into $n \cdot \omega_0$ is a consequence and reflection of the periodicity of the atomic movement. For a diatomic molecule, the only frequency of its dynamic is the characteristic frequency ω_0. For a lattice system with more complex dispersion relation, the discretization of energy spectrum implies the presence of a dominant frequency, namely a dominant vibration frequency of the atoms in a highly aperiodic back-

ground motion. Otherwise the dynamics of an atom in a lattice system can be quite aperiodic due to involvement of many independent harmonic modes with different frequencies, and a somewhat continuous energy spectrum in $g(r, \omega)$ can be expected.

The high spectral weight of $g(r, \omega)$ at high ω is a reflection of the sharpness of $g(r, t)$ as a periodic delta function (Dirac comb) of t. If we fix r and regard $g(r, t)$ as a function of time, then the sharpness of the temporal evolution of the atomic density at a given position implies a broad frequency spectrum of the dynamic (in order to construct such sharp temporal variation).

Here a molecule with 2 atoms its motion is strictly periodic in time, and consequently its dynamic PDF is highly localized in frequency space. However, as the number of atoms and thus the number of vibration mode increase, a linear combination of these independent vibration mode results in decrease of the periodicity of the motion thus decreases, and the frequency spectrum of the atomic motion starts to broaden and disperse. In such case, more smooth and continuous functions instead of the delta function are needed for a good description of $g(r, \omega)$: the atomic dynamics becomes more irregular/aperiodic, the temporal pair distribution $g(r, t)$ also becomes less periodic, and a direct consequence of this is the more complicated form of $g(r, \omega)$ as its Fourier transform.

More generally, a dynamical lattice system is better described by Q and ω only if it's spatial and temporal periodicity is high. In other words, if the distribution of atoms are highly periodic and the system is involved in only a few collective vibration modes, then $S(Q, \omega)$ is an ideal description. Otherwise if the system is highly disordered and is involved in multiple vibration modes, then $g(r, t)$ is more useful. Likewise, $g(r, \omega)$ is most convenient in describing the density fluctuation of small atomic clusters with highly regular motion. When number of atom goes up and the atomic dynamics become more irregular, $S(Q, t)$ and $g(Q, t)$ becomes

more powerful. The increasing difficulty in extracting $g(r, \omega)$ from $g(r, t)$ as the number of atom goes up, which amounts to solving the zeros of sum of sine functions with different periodicity, is a reflection of the break-down of $g(r, \omega)$ as a simple description of the dynamics of system.

In brief, the discreteness and high spectral weight of $g(r, \omega)$ at high ω are direct consequences of the sharp, periodic temporal correlation function $g(r, t)$ of the system.

D.1.2 ω as frequency/energy of a single phonon

Here for the case of diatomic molecule, the presence of high frequency vibration modes in $g(r, \omega)$ comes from the expansion of a sharp and localized function (delta function) with the set of nonlocal and smooth basis functions, i.e. Fourier series. As will be further discussed in Sec. D.1.3, in order to construct spatial/temporal distribution function with such sharpness, it is necessary to include components with multiple spatial frequencies. In other words the delta function dynamic PDF for diatomic molecule implies atomic vibrations at all frequencies. The multiple frequency components reflects the continuous and oscillatory component of the density dynamics. These reflect the actual dynamics of the atoms, and should thus be interpreted as the characteristic frequencies of the phonon instead of the amount of energy transfer. As mentioned in Sec. 6.2.1, ω as frequency and as energy is equivalent if we consider only single phonon process, but are different if multi-phonon process is involved.

According to the above discussion, for diatomic molecule, $\omega = n\omega_0$ stands for the energy of a single normal mode with frequency $n\omega_0$, instead of n normal modes with frequency ω_0. Within this single phonon picture, the frequency ω can be understood as either the frequency of the spatial dynamics of the atoms or as the energy of the lattice dynamics. Correspondingly, $g(r, n\omega_0)$ stands for the pair distribution function at the presence of one

phonon mode with frequency $n\omega_0$ instead of n phonons with frequency ω_0, and $S(Q, \omega)$ comes solely from the inelastic scattering of a single phonon.

More over, if the argument above is reasonable, then the interpretation from Egami and Dmowski [2012] based on multi-phonon process is irrelevant. In fact, multi-phonon process is known to give only smooth scattering and is generally not considered for the structural analysis using dynamic PDF Egami and Billinge [2012]; Billinge and Thorpe [2002]. As an example, a calculation of the multi-phonon contribution in fcc lattice was given in Billinge and Thorpe [2002], Ch.2.

D.1.3 $g(r, n\omega_0)$ as expansion of δ spatial correlation function

The periodicity of $g(r, \omega)$ at each $n \cdot \omega_0$ is a reflection of the spatial periodicity of the distribution of the atoms over time. And this comes from the periodic motion of the atoms. For a fixed time t, $g(r, t)$ can be regarded as the spatial correlation function of atomic density (at time t), which for a diatomic molecule is a delta function of r. Therefore since $g(r, t)$ depends on integer multiples of ω_0, the above derived form of $g(r, \omega)$ can be viewed as a function of r, and be interpreted as a series expansion of the spatial function $g(r, t)$ at a fixed time t, with ω as a label for the expansion function. By definition, we have

$$\int g(r, \omega)d\omega = \sum_n^\infty g(r, \omega = n\omega_0) = g(r, t = 0) = \delta(r - R). \tag{D.1}$$

Since $g(r, t = 0)$ is a delta function of r with sharp spatial variation, it is expected that the above summation over smooth functions $g(r, n\omega_0)$ as its series expansion contains multiple spatial frequencies extending to very large frequency. And the increasing spatial periodicity of $g(r, n\omega_0)$ as n increases is both a consequence and reflection of the increasing temporal periodicity of the atomic vibration at frequency $n\omega_0$. If we let $\omega_0 \to 0$, then we see clearly

that the summation should converge to the spatial delta function $g(r) = \delta(r - R)$. As will

be discussed in detail in the next section, $g(r, \omega)$ for a diatomic system has the general form

$$g(r, \omega) = \int \sum_n \frac{\delta(t - t_n)}{|\frac{\partial f}{\partial t}(t_n)|} e^{i\omega t} dt = \sum_n \frac{1}{|\frac{\partial f}{\partial t}(t_n(r))|} e^{i\omega t_n(r)}. \tag{D.2}$$

where $t_n(r)$ refers to the n th zero of $r - f(t)$, and is a function of r. The exponential factor

shows that the increasing spatial frequency of $g(r, \omega)$ as a function of r is a direct consequence

of the increasing temporal frequency comes from the increase of temporal frequency ω.

It is noteworthy that for the case of diatomic molecule, each $g(r, n\omega_0)$ as a spatial function

is independent of the value of ω_0. This reflects the fact that the shape of $g(r, t)$ does not

depend on the value of ω_0 if taken as a function of r. No matter what value ω_0 takes,

the series expansion is unique if the shape of the spatial function to be expanded is given.

Meanwhile, as the frequency Fourier transform of a periodic delta function (Dirac comb),

$g(r, t)$ does change in a nontrivial manner when viewed as a function of time t. Essentially

ω_0 is separation between the delta peaks in the Dirac comb function $g(r, \omega)$.

D.1.4 $g(r, \omega)$ as spectrum δ of temporal correlation function

From the definition of Fourier transform, $g(r, \omega)$ stands for the frequency spectrum of the

motion of the atom in the entire history its dynamics ($t \subset [0, \infty]$). Intuitively, the value

of $g(r, \omega)$ at each position r reflects the probability that the atom pass through position r

with frequency ω. The more regular the atom oscillates around position r with frequency ω,

the larger the value of $g(r, \omega)$. Another approximate but intuitive way to understand is, if

we look at the density of the atoms in motion ($g(r, t)$) with a camera with a special shutter

that open and closes at a frequency of ω, then $g(r, \omega)$ is the atomic density we see from

the camera: it is the time-averaged distribution of the atoms that oscillates in space at a frequency of ω.

For a diatomic molecule oscillating with frequency ω_0, the fact that $g(r, \omega)$ is always enhanced at $r = \pm u_0$, namely when the atom was furthest from the center, for all ω is because of the zero velocity at these special positions. From the expression of $g(r, \omega)$ there is $f' = f'(t_n(r)) = v(t_n(r))$ in the denominator, which stands for the velocity of the atom at position r and time $t_n(r)$, and thus results in singular value of $g(r, \omega)$ when the velocity is zero at these special positions. This have been shown from simulation Egami and Dmowski [2012]. Furthermore, at the end points the atoms also appears regularly and strictly with frequency ω_0, thereby we expect peak value of the $g(r, \omega_0)$ to appear at $r = \pm u_0$. Similarly, the atom appears regularly and strictly with frequency $2\omega_0$ at the center position, and thus we expect peak value of $g(r, 2\omega_0)$ to appear at $r = 0$. Likewise, the atom appears with frequency $3\omega_0$ at positions $r = \pm 0.5u_0$, and thus we expect $g(r, 3\omega_0)$ to have peak value in these positions.

This can be seen clearly from Fig. D.1: the peak positions of $g(r, n\omega_0)$ for $n = 1, 2, 3$ is exactly where both of the the two sets of zeros of $r - \sin(\omega_0 t)$ falls on the curve of $\sin(n\omega_0 t + \phi)$ but not on $\sin(\omega_0 t + \phi)$ if $n \neq 1$. We note that since each individual set of zeros appears regularly with a frequency of ω_0 and thus contributes equally to each frequency component at all positions r, it is at those positions where both sets of zeros falls onto a single frequency component $\sin(n\omega_0)$ that the value of $g(r, n\omega_0)$ is enhanced compared with other positions. For $\omega = \omega_0$, such positions are $r = \pm u_0$. For $\omega = 2\omega_0$, such positions are $r = \pm u_0$ and $r = 0$. For $\omega = 2\omega_0$, such positions are $r = \pm u_0$ and $r = \pm 0.5u_0$, etc.

From the above analysis we see that for a system of vibrating atoms, $g(r, \omega)$ can be interpreted as the probability that a moving atom appears at position r periodically with a period of $2\pi/\omega$ (or, with a frequency of ω). Or put in another way, the peaks in $g(r, \omega)$ are those
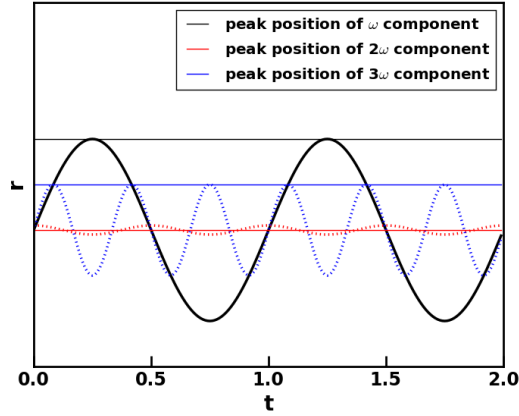
Figure D.1: Periodic motion of diatomic molecule. The dashed lines are sine functions plotted as guide to the eye to show the periodic distribution of the zeros of $r - f(t)$, where f(t) describes the temporal dynamics of the atom.

positions where the atomic density oscillates in time with frequency ω. This statement is true if we consider only single phonon process: in this case the energy ω excites only one phonon with the same frequency ω within the system, and thus ω as an energy transfer can also be interpreted as the frequency of the harmonic vibration mode of the atoms.

For diatomic molecule with delta-function type atomic density, the different frequency components of $g(r, t)$, $g(r, \omega)$, are all consequence and reflections for the same harmonic motion of the system. Conversely, the existence of the certain spatial profile of $g(r, \omega)$ at each energy level $n\omega_0$ as a whole implies the existence of such harmonic motion at frequency ω_0 between the local pair of atoms with singular density. The singular atomic density of the system implies sharp temporal correlation function and thus broad frequency spectrum of its dynamics. After all, a Fourier transform of $g(r, t)$ over time means to perform a temporal sampling of the entire history (meaning t from 0 to ∞) of the time-dependent distribution of atoms at a given frequency ω. For zero frequency $\omega = 0$, it gives the time-average of the

atomic distribution. For small frequency $\delta \cdot \omega_0$, the period for the averaging is still very long and thus the atomic distribution would appear similar to $g(r, \omega = 0)$. For intermediate $n\omega_0$, both the slowly and the fast varying component of $g(r, t)$ will cancel out with the 'shutter' with frequency $n\omega_0$, and only the part of the atomic density which fluctuates at a frequency close to $n\omega_0$ contributes the most to $g(r, \omega)$.

D.1.5   Effects of correlated motion: longitudinal phonon in the weak correlation limit

Before presenting the detailed analysis of the effect of correlated motion, here we briefly review the case of the weak correlation limit, in which the effect of correlated thermal motion can be properly described by a peak shift plus broadening effect. The mathematics has been worked out in Egami and Dmowski [2012], and here we discuss the physics behind them. The thermally averaged dynamic PDF for a general lattice system can be expressed as

$$\langle\langle g(r, E)\rangle\rangle = \frac{1}{N\langle b\rangle^2} \sum_{\mu,\nu} b_\mu b_\nu \int \langle\langle \delta(r - R_{\nu\mu} + u_\nu(0) - u_\mu(t))\rangle\rangle e^{i\omega t} dt, \qquad \text{(D.3)}$$

where

$$u_\mu = \frac{1}{\sqrt{N}} \sum_k u_k e^{i(\theta_k + kR_\mu - \omega_k t)}, \qquad \text{(D.4)}$$

and

$$u_\nu(0) - u_\mu(t) = (u_\nu(0) - u_\mu(0)) + (u_\mu(0) - u_\mu(t)) \qquad \text{(D.5)}$$

$$= (u_\nu(0) - u_\mu(0)) + \frac{1}{\sqrt{N}} \sum_k u_k e^{ikR_\mu}(1 - e^{i\omega_k t}). \qquad \text{(D.6)}$$

Here $u_\mu(t)$ refers to the displacement induced by thermal phonon. The approximation made in Egami and Dmowski [2012] is to assume that the second term from the above result

equates to a random number. Explicitly, they assumed that:

$$
e^{i\omega_k t} =
\begin{cases}
1, & \text{if } 2n\pi \leq \omega_k t \leq (2n+1)\pi \\[2mm]
0, & \text{otherwise.}
\end{cases}
$$

Physically, this is to assume that the thermal displacement of atom μ is random within the period of interest. Under this assumption, the quantity $u_\mu(0) - u_\mu(t)$ essentially becomes a random function of time. It is then argued in Egami and Dmowski [2012] that in this case the effect of regular phonons is to broaden the PDF peaks. However, as will be analyzed below, this argument applies only to longitudinal phonon, corresponding to the weak-correlation limit. A study of the general effects of regular phonons is developed in McQueeney [1998], and will be analyzed in detail below.

D.1.6   Effects of correlated motion: longitudinal phonons

The effect of the vibration of the lattice on the PDF can be understood with a qualitative yet intuitive physical picture. It can be categorized according to the level/degree and sign of the correlation of the atomic displacement. The sample as a thermal dynamic system of atoms displays random thermal motion which can be decomposed into normal modes (phonon). The effect of random thermal motion is summarized in the Debye-Waller factor in the elastic structure factor, and is discussed in a separate section. These random motions are especially important in elastic scattering process, and their effect turns out to be broadening the elastic PDF peaks into a gaussian function Chung and Thorpe [1997]. On the other hand, during inelastic scattering process one or more phonon modes are explicitly excited by and involved in the coherent scattering process with the incoming neutron/x-ray beam. The coherent displacement of the atoms within these excited modes comprises the correlated motion. The analysis of the dynamic PDF will thus manifest the influence of the (local and/or collective)

correlated motions in the system. In fact the one-phonon inelastic structure factor depends explicitly on the atomic configuration in the correlated motion McQueeney [1998].

Meanwhile, the atomic configuration (e.g. longitudinal or transverse) of the specific type of thermal motion may have very different effect on the PDF, as will be discussed below. Thus the sign (positive/negative), the degree of correlation (strong/weak), and the atomic displacement (longitudinal/transverse) are 3 important characters of the thermal motions when considering its effects on the PDF. To have a clear conception of the influence of correlation, we discussed the extreme cases of correlated/uncorrelated motions, and consider for each of them the positive/negative and longitudinal/transverse cases respectively.

Correlated motion of the lattice corresponds to well-defined phonon modes, and uncorrelated motion describes the random motion of the atoms as inherent to any statistical system. Intuitively, a stronger positive correlation means, for both longitudinal and transverse displacement, that the atoms binds more rigidly with each other at their static distance R_{ij} during their (transverse/longitudinal) movement. In other words the atoms tends to move in phase under stronger positive correlation. And this, as will be discussed in detail below, have very different effects for longitudinal and transverse correlation.

In this section we discuss in detail and show that the collective and local longitudinal phonons, i.e. the correlated motion of the the atoms in the longitudinal direction, have opposite effects on the PDF. We show that the local and lattice phonon induces negative and positive density correlation, respectively, and thus results in opposite modifications to the PDF.

As shown in Sec. 6.2.2, for both classical and quantum harmonic oscillator with longitudinal motion, the effect of local longitudinal phonon is to split the PDF peaks into certain number of satellite peaks, depending on the energy of the phonon. For instance, the distance between

the two peaks of $g(r, \omega = \omega_0)$ reflects the amplitude of the harmonic vibration, u_0, which after thermal averaging corresponds to the range of the thermal motion of the atom, $u_0 \sim \langle u^2 \rangle^{\frac{1}{2}}$. The peak-splitting effect is are also clear from the simulated dynamic PDF for diatomic molecule Egami and Dmowski [2012].

In a lattice system the longitudinal local phonon will split the PDF peak as energy increases McQueeney [1998]. As shown in Fig.1 in McQueeney [1998], the lowest order effect of a single longitudinal phonon in a lattice system is to split the uncorrelated PDF peak into two peaks, separated roughly by the thermal vibration amplitude of the atom, $\langle u^2 \rangle^{\frac{1}{2}}$. Specifically, the expression of the one-phonon correction to $g(r, \omega)$, $g_1(r, \omega)$ for lattice system is McQueeney [1998]

$$g_1(r, \omega) \sim \sum_{ij} F_{ij}(\omega) \left(K_0 + K_2 \right) (r - R_{ij}) - F_{ij}^L(\omega) K_0 (r - R_{ij}), \tag{D.7}$$

with

$$K_n(r - R_{ij}) = \frac{2r}{\pi} \int_0^\infty Q^3 \sin(Qr) j_n(QR_{ij}) e^{-W_i - W_j} dQ, \text{ and } W_i = Q^2 \langle u_i^2 \rangle / 2. \tag{D.8}$$

Here $j_n(x)$ stands for the n th order spherical Bessel function. Here $F_{ij}(\omega)$ is the correlation function of the total displacement of atoms i and j. $F_{ij}^L(\omega)$ is the correlation function of the longitudinal displacement and represents the correction to the effects of $F_{ij}(\omega)$. $F_{ij}(\omega)$ and $F_{ij}^L(\omega)$ represents the two dominant (of lowest order in the expansion) effects of phonon on $g(r, \omega)$. It should be noted that while only longitudinal phonon contributes to $F_{ij}^L(\omega)$, both longitudinal and transverse phonon contributes to $F_{ij}(\omega)$, the total correlation between displacements, and therefore the actual effect of longitudinal phonon is described by the superposition of K_2 and $K_0 + K_2$, as simulated in Fry-Petit [2015]. However since K_2 is much larger in magnitude than $K_0 + K_2$ (see McQueeney [1998]), here for demonstration we take K_2 as the exemplary effect of longitudinal phonon. The expressions for $K_2(r - R_{ij})$ and $(K_0 + K_2)(r - R_{ij})$ has clear physical meanings as detailed below.

From the physical point of view, a positive displacement correlation means that the atoms tends to move towards the same direction, and thus tends to shorten the atomic distance. This is understood as the correlated motion of atoms (Jeong *et al.* [2003] has a very intuitive illustration of this). Mathematically, since $(K_0+K_2)(r-R_{ij})$ corresponds to a function biased on the lower-distance side, a positive value of $F_{ij}(\omega)$ would thus shift the peak towards lower distance. This describes the lowest order effect of correlated motion of atoms.

Secondly, a negative correlation between the local longitudinal displacement, as has been shown in the example of diatomic molecule, tends to broaden/split the PDF peak. Here negative means that the motion of the atoms involved are completely out of phase (i.e. with phase difference of π). Intuitively, the relative displacement between two atoms is enhanced if the motion of the two were negatively correlated: the range of relative displacement were doubled in the case where the atoms move in opposite direction, and this naturally doubles the width of the PDF peak, which represents the range of the thermal motion.

The 1-dimensional atomic chain can again be used to illustrated the effect of negative longitudinal correlation. Suppose there's one longitudinal optical phonon present in the system with frequency ω and amplitude Δu, while the equilibrium/static distance between nearest atoms is u_0, the if we take a snap-shot of the vibrating lattice at time t and calculate its PDF, it will contain two peaks at $r = u_0 \pm \sin(\omega t)\Delta u$, respectively (this can be seen by directly plotting the atoms in the chain). This means that a negative longitudinal correlation tends to broaden and even split the peaks in the uncorrelated PDF, as discussed in detail below.

The negative local correlation between the longitudinal displacement of atoms, reminiscent of that in the one dimensional diatomic molecule, is realized in the local (instead of the global) phonon mode in a lattice system, and this explains why local phonons in local and lattice system has similar effect: they both induce local motions that are out of phase. As

an example of a local phonon, the optical phonon modes at the zone boundaries corresponds to a phase difference of π between neighboring atoms, and is highly local considering its zero group velocity (see also the discussion in Egami and Dmowski [2012]). In other words, the dynamics of an diatomic molecule exemplifies the effect of local phonon mode in a lattice system. Mathematically, the function $K_2(r - R_{ij})$ has peak around R_{ij} but a dip at R_{ij}. Since in local phonon mode the atoms tends to move out-of-phase, or more specifically, a negative correlation between their longitudinal displacement, this results in a negative value for the longitudinal correlation function $F_{ij}^L(\omega)$ which then contribute to a split of the PDF peak. Moreover, if $F_{ij}^L(\omega)$ is small, then the addition of the term $F_{ij}^L(\omega)K_2(r - R_{ij})$ to the original PDF peak is likely to broaden the peak. On the other hand if $F_{ij}^L(\omega)$ is large, then a positive PDF peak is likely to be neutralized by $F_{ij}^L(\omega)K_2(r - R_{ij})$ and thus become split. Therefore we see that for a lattice system, the effect of local phonon with frequency ω can be either peak-broadening or peak-splitting, which depends on, instead of the amplitude of thermal motion, the correlation strength between the local displacements measured by the function $F_{ij}^L(\omega)$.

In a lattice system the longitudinal local phonon tends to have opposite effect compared with the longitudinal lattice phonon. The overall effect of the lattice phonons is in general to move the atoms in phase. In this case the PDF peaks will be sharpened compared with the case where the thermal motion of atoms are uncorrelated. Intuitively, the displacement of one atom is offset by that of the other atom if the motion of the two were positively correlated, i.g. tends to move in phase, and thus the distance between the atoms tends to remain the same as they move, which is to say that the corresponding PDF peak tends to be sharper. Mathematically, since the positive correlation between longitudinal displacements results in positive value for correlation function $F_{ij}^L(\omega)$, the result is to narrow especially the nearest-neighbor PDF peaks. In contrast, for atoms that are more distant from each other

such correlation are more likely to induce motion that is out-of-phase: the phase difference of the motion of different atoms involved in phonon motion increase as their distance increases. In this case the correlation is more likely to be negative, which resembles that in a diatomic molecule and in principle should result in a broadening/split instead of narrowing of the PDF peak. In other words the distant PDF peaks are more likely to be broadened instead of narrowed by the correlation induced by the lattice phonon. These remote peaks are, however, not usually of our primary interest. Examples of correlated motion in lattice can be found in Egami and Billinge [2012]; Reichardt and Pintschovius [2001]. Such correlation effect induced by lattice phonon is also shown to be quite insensitive to details of the phonon dispersion Reichardt and Pintschovius [2001]. According to the equations in McQueeney [1998] the amount of sharpening/splitting caused by phonon is determined by the mean-squared atomic displacement, $\langle u^2 \rangle^{\frac{1}{2}}$, through the Debye-Waller factor, this implies on the one hand the insensitivity of thermal motion $\langle u^2 \rangle^{\frac{1}{2}}$ to the arrangement and interaction of the atoms (the explicit expression for $\langle u^2 \rangle^{\frac{1}{2}}$ can be found in Chung and Thorpe [1997]). On the other hand, this also implies that the integrated displacement caused by the 1-phonon contribution to the PDF, summing over all lattice phonon states, is quite insensitive to the details of the dispersion and density of state, and is dominated by the contribution from the low energy acoustic phonon: this is evident since the shape of the displacement function $K(r - R_{ij})$ is independent of the structure of the material McQueeney [1998].

We note that the dominant forms of correlated motion in large and small systems are acoustic and optical phonons, respectively, and thus the PDF peaks of these systems tends to exhibit opposite variation under the correlated motion in the system. In specific, it is only in crystalline material with large periodic lattice that the acoustic phonon modes, corresponding to highly in-phase collective motion of the atoms, are sustained. These acoustic phonons also turns out to be the dominant form of correlated motion in these materials, and the PDF

peaks under these vibration modes thus usually displays sharpening instead of split. This is supported by the fact that peak-sharpening is consistently reproduced for qualitatively different phonon dispersions in crystalline materials Reichardt and Pintschovius [2001]. On the other hand, in molecular or cluster materials with fewer atoms, the normal modes usually corresponds to highly out-of-phase motion of neighboring atoms, of which the extreme case is the harmonic vibration of the diatomic molecule, and thus the dominant correlated motion in these materials are usually optical phonons that exists on a local scale. Therefore in these molecular systems the PDF broadening/splitting effect can be much more pronounced.

With the above argument the bifurcation of the dynamic PDF peak as energy increases can be readily understood. At low energy the phonons are mostly acoustic corresponding mostly to positive correlation between atoms and thus have a peak-narrowing effect. As energy increases to that of the optical/semi-local phonons near the zone boundary, these phonons induces negative correlations and thus tends to split the PDF peaks. Therefore the effect of longitudinal phonons evolves from peak-narrowing to peak-splitting as energy increase, and this is represented as the split of the dynamic PDF peak with increasing energy.

We noticed that in the formalism of Ref. McQueeney [1998] only the lowest order/dominant effect of the longitudinal correlation is present. This is due to the approximation scheme used in evaluating the orientational average of $S(\mathbf{Q}, \omega)$ for isotropic powder sample. In the approximation to the average of the complex phase factor, only the lowest order term in the Bessel function expansion form of the complex exponential intermediate scattering function was retained in the calculation of the spherical average (see Carpenter [1967] for details of the approximation). Once the higher order terms in the expansion was retained, the spherical averaging of the structure function is likely to yield the higher order terms of spatial Bessel function, which reproduces the fast oscillating spatial profile in the $g(r, \omega)$ of

diatomic molecule at high energy as the effect of local longitudinal oscillation in a diatomic molecule.

Physically, the higher order terms in the Bessel function expansion of $S(Q, \omega)$ corresponds to more orientationally-resolved displacement-displacement correlations, in addition to the 0 th order Bessel function $j_0(r)$ which measures the correlation strength of the parallel projection and is relatively insensitive to the absolute orientation of the displacement. In fact since the one-phonon structure function $S(Q, \omega)$ in general can be written as a atomic sum over function of the form $F_{ij}(\omega)I_{ij}(Q)$ Lovesey [1986], $g(r, \omega)$ as the spatial Fourier transform of $S(Q, \omega)$ has the form $\sum_{ij} K'_{ij}(r)F_{ij}(\omega)$, and this basic form of $S(Q, \omega)$ and $g(r, \omega)$ applies to both small clusters and periodic lattice. It is the weight function $F_{ij}(\omega)$, which measures the degree of atomic correlation, that depends on the specific arrangement of the atoms. The function $K'_{ij}(r)$, which specifies the actual effect of atomic correlation on the distribution of the density, remains the same for any structure. In other words the influence of atomic vibration on the PDF of the system is qualitatively the same for both atomic cluster and lattice systems.

Last we note that the superficial separability of the spatial and temporal part in the expression of $S(Q, \omega)$ implies the separability of the spatial distribution and temporal dynamics of the density. However a closer look at the equation reveals that the two correlates closely with each other via the delta function $\delta(\omega - \omega(q))$. And this reflect the fact that in solids the spatial distribution and the temporal dynamics of the atomic density is inherently correlated and is all contained in the dispersion $\omega(q)$ of the material.

In brief, the influence of the correlated motion (e.g. local and lattice phonons) on the PDF is determined and can be understood by analyzing the details of the correlation, e.g. its sign and strength, induced by the atomic motion. In both atomic clusters and periodic

lattice system, local longitudinal phonon tends to split (or broaden) the PDF peaks by a spatial distance on the order of the amplitude of the atomic thermal vibration. And whether the effect is peak-broadening or peak-splitting depends on the correlation strength of the phonon mode, which is chiefly determined by the density of state. The difference in the effect of local and lattice phonon can be understood as a result of negative and positive correlation of the motion: where as the local phonon induces negative correlation and thus peak splitting/broadening, the lattice phonon tends to bring in positive correlation and thus result in peak narrowing. The higher order effects of the positive correlation induced by the lattice phonon can be understood with the model of diatomic molecule with negatively correlated motion, as the effect of correlation in the two systems differ only by a minus sign.

D.1.7 Effects of correlated motion: transverse phonons

The effect of correlation in the transverse displacement, induced by transverse phonons, is to shift the PDF peak to lower or high distance. This can also be understood in an intuitive way. An important difference between longitudinal displacement and transverse displacement is that, while longitudinal displacement increase or decrease the atomic distance when it is positive or negative, respectively, a transverse displacement, no matter positive or negative, always increases the atomic distance (with respect to that of the static lattice). This can be easily seen by working out the geometry. Take the case of diatomic molecule, a positive correlation between the transverse displacement of the atoms tends to bind atoms together in the transverse direction and thus reduces their relative transverse displacement. Since the atomic distance is reduced when the relative transverse displacement decreases, positive transverse correlation of atoms decreases the atomic distance and shift the PDF peak to lower-distance side. Conversely, a negative transverse correlation tends to repel the atoms

along the transverse direction and thus increases the (average) atomic distance. We note that since transverse phonon only contributes to F_{ij}, which is much smaller than F_{ij}^L, therefore whenever the peak-splitting becomes dominant, it implies the presence local phonon mode exclusively (not mingled with the effect of longitudinal phonon).

This can also be understood from the distribution of atom at the presence of thermal motion. Specifically, the distribution of one atom with respect to the other under longitudinal thermal motion was centered at their static distance, R_{ij}, with a variance of $\pm\langle u^2 \rangle^{\frac{1}{2}}$, and a positive correlation tends to shift the lower and higher bound of the position towards the center. On the other hand, the distribution under transverse motion was centered around $R_{ij} + \langle u^2 \rangle^{\frac{1}{2}}$, with a lower bound of R_{ij} and a higher bound of $R_{ij} + 2\langle u^2 \rangle^{\frac{1}{2}}$, and a positive correlation reduces the variation of random thermal motion $\langle u^2 \rangle^{\frac{1}{2}}$ and shifts the upper bound and the center towards the lower bound, which corresponds to a shortening of the average distance.

From the above analysis we know that while transverse acoustic phonon gives positive transverse correlation and reduces the atomic distance, the transverse optical phonons or local modes gives negative transverse correlation and increases the distance.

D.1.8 Effect of uncorrelated thermal motion

The Debye-Waller factor is known to describe the effect of random thermal motion of the atoms on crystallographic analysis Egami and Billinge [2012]. Since the Debye-Waller factor damps out the Bragg peak at high Q, namely $Q \geq \frac{2\pi}{\langle u^2 \rangle^{\frac{1}{2}}}$, it is expected that the real space peaks becomes broadened since the sharpness of a peak is critically determined by its high frequency component. Physically, a random thermal vibration with amplitude around $\langle u^2 \rangle^{\frac{1}{2}}$ would smear out any spatial density correlation with period smaller than $\langle u^2 \rangle^{\frac{1}{2}}$, or

equivalently with wave vector larger than $\frac{2\pi}{\langle u^2 \rangle^{\frac{1}{2}}}$, and this is precisely the effect which the Debye-Waller factor imposes on the scattering spectra.

The thermal motion also influences the effect of local phonon on the PDF. The amount of the peak split caused by local phonon are also on the scale of the thermal displacement of the atoms. As a rough estimation, the spatial spread/scale of the integrand in K_n is set by the width of the gaussian function $e^{-W_i - W_j}$. Since the width of $e^{-W_i - W_j} = e^{-Q^2(\langle u_i^2 \rangle + \langle u_j^2 \rangle)/2}$ is approximately $2^{\frac{1}{2}}(\langle u_i^2 \rangle + \langle u_j^2 \rangle)^{-\frac{1}{2}}$, the spatial spread of $g(r, \omega)$ can be estimated to be $\sim \pi(\langle u_i^2 \rangle + \langle u_j^2 \rangle)^{\frac{1}{2}} 2^{-\frac{1}{2}}$ (see Sec.4.2-4.3 in Lovesey [1986] for more discussions on the Debye-Waller factor W). This estimation qualitatively agrees with the actual plot of the $K_2(r - R_{ij})$ function in McQueeney [1998]. At higher temperature and thus larger thermal motion, the $K_2(r - R_{ij})$ function naturally becomes more extended in space. However since the PDF peak itself is also broadened by the same amount, the effect of the phonon will remain qualitatively the same (either splitting or broadening the PDF peak), although now the dynamic PDF $g(r, \omega)$ tends to appear smooth and featureless on the whole 2d parameter space.

The random thermal motion and the correlated motion of the atoms are intimately correlated with each other. This is expected since both of them describe the effect of phonon on the PDF, and are different in the sense that the former represents the averaged effect of many thermally populated phonons, and the latter describes the effect of distinctly excited phonon in a coherent scattering process. This is clearly seen from their expression (see Chung and Thorpe [1997] for expression of $\langle u_{ij}^2 \rangle^{\frac{1}{2}}$, and McQueeney [1998] for $F_{ij}(\omega)$ and $F_{ij}^L(\omega)$): the corresponding terms in $\langle u_{ij}^2 \rangle^{\frac{1}{2}}$ can be derived by simply summing $F_{ij}(\omega)$ and $F_{ij}^L(\omega)$ over all energies. From this point of view the mean-squared atomic displacement $\langle u_{ij}^2 \rangle^{\frac{1}{2}}$ is also a measure of the over all correlation strength between the displacements of atoms i and j, induced by the thermally populated phonons in the system.

D.1.9 Summary and the physics of $g(r, \omega)$

The expansion form of $g(r, \omega)$ from the Fourier transform of $g(r, t)$ can be understood as the expansion of either the temporal correlation function with parameter r, or the spatial correlation function with parameter t. Expressed in either way, it reflects the same fact of the delta-function type atomic density, which gives a delta-function type spatial-temporal correlation function $g(r, t)$ for a vibrating molecule. In other words for the diatomic molecule, the presence of both the high orders of $g(r, n\omega_0)$ as well as the periodic spatial profile of each $g(r, n\omega_0)$ as a function of r is a result of the sharpness of the spatial distribution of the spatial-temporal correlation function $g(r, t)$.

Based on the above analysis we attempt to address the physical meaning of $g(r, \omega)$. If there exist in a lattice system a local phonon vibration, namely the harmonic vibration of local atomic pairs, with frequency ω_0 in the measured sample, then as we look at the atomic density of this system with frequencies close to $n\omega_0$, we should in principle be able to see patterns from $g(r, n\omega_0)$ close to that of a harmonic diatomic molecule with frequency ω_0. If we only consider single phonon process, then the energy transfer into the system is also the frequency of the vibration of the atoms, and in this case $g(r, \omega)$ can also be interpreted as the atomic density correlation at the presence of phonon modes with frequency ω. Considering that $g(r, \omega)$ is one component of the regular PDF $g(r, t = 0)$ which itself is a correction over the uncorrelated PDF $g(r, \omega = 0)$, $g(r, \omega)$ represents the correction to the uncorrelated PDF due to variation of atomic density by lattice vibration at frequency ω.

In general, the quantities that have apparent intuitive interpretation are the time-averaged PDF, $g(r, \omega \sim 0)$, and the real-time PDF, $g(r, t)$, a special case of which is the regular PDF, $g(r, t = 0)$. In general $g(r, \omega)$ with non-trivial ω reflects the component of the spatial density

correlation that oscillates with frequency ω, and the spatial variation of $g(r, \omega)$ at each frequency ω, for example the splitting of the PDF peak at $\omega = n\omega_0$ for diatomic molecule, is determined by and itself an reflection of the temporal periodicity of the motion, and does not have an intuitive physical interpretation apparent as that of $g(r, \omega = 0)$ and $g(r, t)$. However, although the intuitive meaning of $g(r, \omega)$ at high ω is less apparent, $g(r, \omega = \omega_0)$, namely the first order correction to the PDF due to correlated motion, has the intuitive interpretation of peak narrowing/split as illustrated by the example of 1d atom chain and diatomic molecule. After all $g(r, t = 0)$ includes all the influence of the lattice dynamics on the PDF, and $g(r, \omega)$ tells how this influence happen specifically at each energy.

D.2   Dynamic PDF and experiment

D.2.1   Understanding the dynamic PDF spectrum from experiment

With the knowledge above we can explain the observed dynamic PDF from Nickel Egami and Dmowski [2012]. We note that the elastic PDF $g_0(r, \omega = 0)$ as one component of the instantaneous PDF $g(r, t = 0)$ exists only at zero energy, and thus the dynamic PDF with any non-zero energy contains and should be interpreted as $g_1(r, \omega)$. The presence of strong elastic signal at non-zero energy is due to the limited resolution, which is described as a convolution with a gaussian function. At non-zero energy, the dynamic PDF exhibits peak that centers at and dip around the peak position of the elastic PDF. This means that the low energy phonons are mostly long wavelength acoustic phonons which results in positive correlation between the atoms and thus a sharpening of the elastic PDF peak. At

certain energy level, the dynamic PDF peak at the nearest-neighbor distance split, which corresponds to a local (zero group velocity) phonon and implies a large negative nearest-neighbor correlation strength $F_{ij}^L(\omega)$. The magnitude/effect of the atomic thermal motion should in principle be the same for both local and global phonons in the same system, and does not result in such big difference in the peak-splitting in local and global phonons.

The fact that local phonons have large correlation strength and thus results in large peak split is due to the relation between the correlation strength $F_{ij}^L(\omega)$ and the specific atomic configuration in the correlated motion and the density of state at energy ω. From its expression McQueeney [1998] we know that the magnitude of $F_{ij}^L(\omega)$ is determined by density of state with energy ω, modulated by the correlation strength in the atomic density induced by the corresponding phonon state. Therefore $F_{ij}^L(\omega)$ is larger for states with larger density. Meanwhile, local/non-traveling phonons usually sits around the flat region of the dispersion and thus usually have large density of state (see e.g. the phonon DOS of Nickel in McQueeney [1998]). Thus it is reasonable to expect that the local phonons have a large correlation strength that splits the corresponding PDF peak, and that the fast dispersing phonons with relatively small density of state contributes only to peak-broadening. On the other hand, since $F_{ij}^L(\omega)$ is enhanced by and thus peak-splitting is happening with only the phonon mode which gives large correlation between the longitudinal displacements of the atoms i and j, and that local/optical phonon induces large negative correlation between nearest neighbor atoms, it is reasonable that the nearest neighbor peak in the dynamic PDF of Nickel only start to split at the energy of the optical phonon.

The fact that the split peaks at the first harmonic energy ω_0 extends to high energy, as observed in Nickel Egami and Dmowski [2012]; Dmowski *et al.* [2008]and PMN Dmowski *et al.* [2008] can be understood as the finite spectral weight of the local optical mode: as from

both simulation McQueeney [1998] and experiment Birgeneau *et al.* [1964]. For an ideal local mode in an ideal diatomic molecule the spectral width of the state is extremely small (delta function). Here the finite spectral window of the peak split from the dynamic PDF matches well with the DOS of the local mode Birgeneau *et al.* [1964]; McQueeney [1998], and thus confirms the fact that the states within that energy window (30 - 40 meV) all corresponds to highly local optical phonon modes in Nickel. This might also be attributed to the anharmonicity of atomic vibration as well as the finite energy range for the local modes in real materials, the effect of which is simulated for the case of anharmonic moleculeEgami and Dmowski [2012] using a double-well potential. From this perspective the model of diatomic molecule is particularly useful since the anharmonicity of atomic motion is not taken into account in the common treatment based on the common treatment using the concept of phonons.

D.2.2 Capacity of dynamic PDF in structural analysis

The dynamic PDF contains no more information than the measured structure function. It however visualizes the effects of local and collective lattice dynamics specifically on the atomic distribution of the systemin real space. For materials that does not exhibit significant dynamic structural distortion, meaning that the lattice itself is not distorted beyond its usual thermal vibration, dynamic PDF would exemplify the expected broadening and/or split of the peaks in the instantaneous PDF as it is dispersed over energy. And example of this in Nickel Egami and Dmowski [2012]. On the other hand for materials that does exhibit structural distortion in the instantaneous PDF, measuring its dynamic PDF would be helpful to identify whether such distortion is caused by lattice dynamics Dmowski *et al.* [2008]. In fact since available software fits the instantaneous PDF by an elastic model, the refinement

will not be satisfactory if there's dominant dynamic lattice distortion which strongly shifts the peaks of the elastic PDF, as shown in Dmowski *et al.* [2008]. In other words the presence of strong dynamic local distortion can be one reason for an unsatisfactory refinement using the elastic PDF model. On the other hand, it works better for systems without strong dynamic local distortion since the effects of regular phonons are mostly slight variation in the position and width of the peak, which can be accounted for by slightly varying the lattice constance and adjusting the peak width of the elastic PDF model. It should be noted that in this case the broadening/narrowing effect due to optical phonons are modeled by varying the degree of random thermal motion, which gives good fit but does not reveal the real mechanism of the peak broadening. It is only from the dynamic (energy-resolved) PDF that the dynamic nature of the distortion is revealed.